DEVELOPMENT AND CHARACTERIZATION OF CHARGED MEMBRANES FOR SEPARATION STUDIES

By

AVISHEK PAL

CHEM01200904023

Bhabha Atomic Research Centre, Mumbai

A thesis submitted to the
Board of Studies in Chemical Sciences

In partial fulfillment of requirements
for the degree of

DOCTOR OF PHILOSOPHY

of

HOMI BHABHA NATIONAL INSTITUTE

June, 2016

HOMI BHABHA NATIONAL INSTITUTE

Recommendations of the Viva Voce Board

As members of the Viva Voce Board, we certify that we have read the dissertation prepared by **Avishek Pal** entitled ***"Development and Characterization of Charged Membranes for Separation Studies"*** and recommend that it may be accepted as fulfilling the dissertation requirement for the Degree of Doctor of Philosophy.

Chairman - Prof. (Dr.) M. Kumar Manmohan Kumar **Date:** 06-06-2016

Guide – Prof. (Dr.) R. C. Bindal **Date:** 06/06/16

Examiner – Prof. Shobha Shukla Shobha Shukla **Date:** 6/6/16

Member - Dr. A. K. Ghosh **Date:** 06/06/2016

Member - Prof. (Dr.) Y. K. Bhardwaj YK Bhardwaj **Date:** 06/06/2016

Technical Advisor - Dr. A. K. Pandey Pandey **Date:** 6/6/16

Final approval and acceptance of this thesis is contingent upon the candidate's submission of the final copies of the thesis to HBNI.

I/We hereby certify that I/we have read this thesis prepared under my/our direction and recommend that it may be accepted as fulfilling the thesis requirement.

Date: 6-6-2016

Place: Mumbai

Guide

डॉ. आर . सी . बिंदल / Dr. R.C. Bindal
अध्यक्ष, झिल्ली विकास अनुभाग
Head, Membrane Development Section
रसायन इंजीनियरी वर्ग
Chemical Engg. Group
बी.ए.आर.सी. / B.A.R.C.

STATEMENT BY AUTHOR

This dissertation entitled "***Development and Characterization of Charged Membranes for Separation Studies***" has been submitted in partial fulfillment of requirements for an advanced degree at Homi Bhabha National Institute (HBNI) and is deposited in the library to be made available to borrowers under rules of the HBNI.

Brief quotations from this dissertation are allowable without special permission, provided that accurate acknowledgement of source is made. Requests for permission for extended quotation from or reproduction of this manuscript in whole or in part may be granted by the Competent Authority of HBNI when in his or her judgment the proposed use of the material is in the interests of scholarship. In all other instances, however, permission must be obtained from the author.

Avishek Pal 6-6-2016

Avishek Pal

DECLARATION

I, hereby declare that the investigations presented in the current thesis entitled "***Development and Characterization of Charged Membranes for Separation Studies***" have been carried out by me. The research work is original and has not been submitted earlier as a whole or in part for a degree / diploma at this or any other Institution / University.

Avishek Pal 6-6-2016

Avishek Pal

List of Publications arising from the thesis

Patents

1. T. K. Dey, **Avishek Pal**, R. C. Bindal and P. K. Tewari, Charged thin film composite nanofiltration membrane and process of its production, *Indian Patent*, **2014**, *Application No.: 1902/MUM/2014.*

2. T. K. Dey, **Avishek Pal**, R. C. Bindal and P. K. Tewari, Nanofiltration membranes with surface negative charge for fractional separation of mono and multivalent ionic species, *Indian Patent,* **2015,** *Application No.: 2095/MUM/2015.*

Journals

1. **Avishek Pal**, T. K. Dey, Anshu Singhal, R. C. Bindal and P. K. Tewari, Nano-ZnO impregnated inorganic–polymer hybrid thin film nanocomposite nanofiltration membranes: an investigation of variation in structure, morphology and transport properties, *RSC Advances,* **2015**, *5,* 34134–34151.

2. **Avishek Pal**, T. K. Dey and R. C. Bindal, Intrinsic dependence of hydrophilic and electrokinetic features of positively charged thin film composite nanofiltration membranes on molecular weights of poly(ethyleneimine)s, *Polymer,* **2016**, *93,* 99 –114.

Conferences

1. **Avishek Pal**, T. K. Dey, R. C. Bindal, S. Prabhakar and P. K. Tewari, Effect of compositional variations of amine component, containing 2, 4 – diamino benzene sulfonic acid and piperazine, on the performance of negatively charged thin film composite nanofiltration membranes, *National conference on water purification technologies and management (InDACON) – Navi Mumbai, India,* **2012**, SIII-3.

2. **Avishek Pal**, T. K. Dey, R. C. Bindal, S. Prabhakar and P. K. Tewari, Study of separation characteristics of indigenously developed negatively charged nanofiltration membranes towards single and binary mixed electrolyte systems, *National conference on water purification technologies and management (InDACON) – Navi Mumbai, India*, **2012**, pp. SIII-12.

3. **Avishek Pal**, T. K. Dey, R. C. Bindal, S. Prabhakar and P. K. Tewari, Effect of acid chlorides as reactant on the morphology and performance of negatively charged thin film

composite nanofiltration membranes, *DAE-BRNS symposium on emerging trends in separation science and technology (SESTEC) – Mumbai, India*, **2012**, pp. 52.

4. **Avishek Pal**, T. K. Dey, R. C. Bindal and P. K. Tewari, Impact of curing conditions on surface features of thin film composite nanofiltration membranes: An AFM - SEM study, *Third international multicomponent polymer conference (IMPC) – Kerala, India*, **2012**, pp. 74.

5. **Avishek Pal**, T. K. Dey, R. C. Bindal and P. K. Tewari, Influence of electrolytes on the electro-kinetic behaviours of charged nanofiltration membrane, *International conference on water desalination, treatment and management (InDACON) – Jaipur, India*, **2013**, pp. 43.

6. **Avishek Pal**, T. K. Dey, R. C. Bindal and P. K. Tewari, Preparation and physicochemical characterization of a crosslinked & quaternized polyamide network based positively charged thin film composite nanofiltration membrane, *DAE-BRNS symposium on emerging trends in separation science and technology (SESTEC) – Mumbai, India*, **2014**, pp. 223.

7. **Avishek Pal**, T. K. Dey, R. C. Bindal and P. K. Tewari, Fractionation of a simulated composite stream containing uranyl nitrate and ammonium nitrate by an indigenously developed negatively charged thin film composite nanofiltration membrane, *DAE-BRNS symposium on emerging trends in separation science and technology (SESTEC) – Mumbai, India*, **2014**, pp. 224.

8. **Avishek Pal**, T. K. Dey, R. C. Bindal and P. K. Tewari, Analysis of amplitude parameter-linked surface topographies of nanofiltration membranes using atomic force microscopy, *International conference on innovative technologies and management for water security (InDACON) – Chennai, India*, **2014**, pp. 353–361.

9. **Avishek Pal**, T. K. Dey, R. C. Bindal and P. K. Tewari, Dependence of performance of positively charged nanofiltration membranes on molecular weight of poly(ethyleneimine), *Trombay symposium on desalination and water reuse (TSDWR) – Mumbai, India*, **2015**, pp. 265-269.

DEDICATED

TO

MY PARENTS

ACKNOWLEDGEMENTS

The successful completion of the current thesis would not have been accomplished without the sincere and supportive encouragement of numerous people, which precisely includes my well wishers, my friends and the department (***Membrane Development Section, Chemical Engineering group, Bhabha Atomic Research Centre***) colleagues, who contributed in many direct or indirect ways. First and Foremost, I would like to express my sincere gratitude to my research guide **– *Prof.* (*Dr.) R. C. Bindal*** for giving continuous support, motivation and enthusiasm during the course of my PhD. Further, I would like to acknowledge the valuable technical support of ***Dr. T. K. Dey***, who as an advisor, with his continuous encouragement and meticulous scientific discussions helped me in overcoming several hurdles that faced during the course of research works. I also owe my deep sense of gratitude for the strong motivation, support and the worthy faith of ***Dr. P. K. Tewari***. My sincere thanks are due to ***Dr. Hemant Sodaye*** and ***Mr. Soumitra Kar*** for all their precious help, simulating discussions and tremendous co-operations. Besides these peoples, I would like to thank the revered members of my doctoral committee *i.e.*, ***Prof. (Dr.) Lalit Varshney***, ***Prof. (Dr.) Manmohan Kumar***, ***Prof. (Dr.) Y. K. Bharadwaj***, ***Dr. A. K. Pandey***, ***Dr. S. Prabhakar*** and ***Dr. A. K. Ghosh*** for their valuable times, encouragement, thoughtful ideas and critical evaluation during the course of Ph.D.

I am heartily thankful to ***Dr. Anshu Singhal*** (Chemistry Division) for her help, co-operation and suggestions as collaborator during the course of one of my research work. I would also like to express my sincere appreciation to the members of MDS *i.e.*, ***Mr. M. S. Kamble, Mr. U. R. More, Mr. R. Brhamne, Mr. Amit Singha, Mrs. Lokhandaye*** and ***Mrs. Gauri*** for their continuous in-field support and encouragement in carrying out the entire research works.

I feel blessed to get a new energetic community of many good friends, who become the constant source of laughter, joy and support in my personal as well as professional life. Thus, I would like to thank all such friends - ***Vivek***, ***Dilip***, ***Ahmed***, ***Yusuf***, ***Sumit***, ***Ayan***, ***Jerina***, ***Monika***, ***Vasundhara***, ***Suman***, ***Shagufta*** and ***Shikha***, who always stood by me with their warm friendship and lend constant encouragement and support in sailing through all the hardships. I would like to acknowledge all the ***teachers***; I learnt from since my childhood, I would not have been here without their grooming through guidance, priceless blessings and support.

Finally, I would like to acknowledge the people who mean the world to me, my family, where ***my parents*** with their unconditional love, support, faith and encouragement have inspired in all pursuits of life. I owe all my accomplishments to them. I would also like to thank all my ***relatives***, ***brothers and sisters*** for their constant encouragement and support. Last but not the least, I would like to thank everybody who was important in the successful realization of this thesis, as well as apologize that I could not mention everyone personally.

Avishek Pal

LIST OF ABBREVIATIONS

Atomic Force Microscopy	**AFM**
Attenuated Total Reflectance	**ATR**
Average roughness	**R_a**
Branched poly(ethyleneimine)	**BPEI**
Coefficient of kurtosis	**R_{Ku}**
Contact angle	θ
Electrokinetic surface charge densities	**σ_s**
Energy dispersive X-ray	**EDX**
Fourier Transform Infrared	**FT IR**
Glycidyltrimethylammonium chloride	**GTACl**
Ion exchange capacities	**IEC**
Molecular weight cut off	**MWCO**
Nanofiltration	**NF**
N-methyl -2- pyrrolidone	**NMP**
Nuclear Magnetic Resonance	**NMR**
Percentage of solute rejection	**SR**
Piperazine	**PIP**
Porosity	ø
Polysulfone	**Psf**
Reverse Osmosis	**RO**
Root mean square roughness	**R_q**
Scanning Electron Microscopy	**SEM**

Steady-state solvent flux	J_W
Streaming potential	V_{st}
Steady-state pure water flux	**PWF**
Surface skewness	$\mathbf{R_{Sk}}$
Surface free energy	**SFE**
Ten point height	$\mathbf{R_{10Z}}$
Terephthaloyl chloride	**TPC**
Thin Film Composite	**TFC**
Thin Film Nanocomposite	**TFN**
Trimesoyl chloride	**TMC**
Ultrafiltration	**UF**
X-ray Photoelectron Spectroscopy	**XPS**
Zeta potential	ζ
4,4$^{/}$-diamino stilbene-2,2$^{/}$- disulfonic acid	**DASDSA**
2,2$^{/}$-benzidene disulfonic acid	**BDSA**
2, 4 - diamino benzene sulfonic acid	**DABSA**

CONTENTS

CHAPTER – 2 **Structure - topography - morphology - performance relationship of non-crosslinked and crosslinked co-polyamide based negatively charged TFC NF membranes**

CHAPTER – 3 Development and characterization of negatively charged TFC NF membranes, derived employing diaryl diamines with multiple sulfonic acid groups

CHAPTER – 4 **Variation in physicochemical features and separation characteristics of positively charged TFC NF membranes with change in molecular architectures of quaternized poly(ethyleneimine amide)s**

CHAPTER – 5 **Nano-ZnO impregnated thin film nanocomposite NF membranes: An investigation of variation in structure, morphology and transport properties**

SYNOPSIS

Progressive developments of high-performance as well as innovative membrane based separation processes stand essential for sustainable growth of the industries which could become beneficial to the society, and subsequently have drawn the attention of the separation scientists for quite a long time. In the present scenario, adoption of such suitable efficient processes for separation, concentration and purification of molecular mixtures are thus major concerns in wide range of chemical industries, precisely in obtaining high grade products in the food and pharmaceutical industries, delivering high quality water in the communities and industries, removing or recovering the toxic or valuable species from the industrial effluents, separating the toxic organic residues generated from the textile and dye manufacturing industries, removing the large amount of non-biodegradable inorganic salts having low to high potential of environmental hazards as generated in mining and mineral processing industries etc.

In the arena of pressure driven membrane processes, plenty of synthetic polymeric membranes function as semipermeable interphases between two adjacent phases and regulate the transport of ionic constituents from one phase into the other across the selective barrier, following specific transport mechanisms. Nanofiltration (NF), being one such versatile pressure driven membrane process acquires an immense importance by exerting more potential in wide spectrum of applications of the separation industries [1]. In the course of pressure driven NF processes, charged membranes are employed in achieving differential rejections towards wet streams comprising of ionic constituents of varying valances or fractionation of mixed ionic streams, utilizing their unique feature of transport selectivity. Unlike the neutral NF membranes which, in general, allow the passage of smaller monovalent ions and retain the larger multivalent ones, in most cases, NF membranes bear either negatively charged or positively charged functionalities in their polymeric surfaces or matrices and behave as electrically charged layers when come in contact with electrolyte solutions, depending on the interaction patterns between charge of the membrane and charge of the ionic constituents under considerations. Thus, the two different dominant classes of charged NF membranes include – negatively charged NF membranes (comprising of fixed negatively charged sites and mobile positively charged sites, repelling the anions and concomitantly allowing the preferential passage of the cations of an electrolyte solution through the membrane, in the course of separation) and positively charged NF membranes (comprising of fixed positively charged sites and mobile negatively charged sites, repelling the cations and allowing the preferential passage of the anions of an electrolyte solution through the membrane, alongside during separation) [2].

Literature survey & assessment of prior studies: The earlier research efforts on development of various negatively charged NF membranes reveal that the most commonly used processes for generation of such charged membranes with various polymeric constitutions include interfacial polymerization [3], grafting of polymers to introduce charge and making membranes using them by phase separation technique [4], modification of preformed membranes by radiation grafting [5], coating of charged polymer layer over another substrate [6], applying multilayer polyelectrolytes (alternative layers of oppositely charged polyelectrolytes) over an existing substrate membrane [7], coating or filling of charged gels in the porous structure of the membrane [8] etc.

Prior efforts by the researchers towards development of positively charged NF membranes following different ways provide various polymeric constitutions with modified structural and physicochemical features, which include bromination followed by *in situ* amine crosslinking method [9], interfacial polymerization through crosslinking process [10], phase inversion [11], phase inversion followed by *in situ* amination [12], *in situ* amination followed by phase inversion [13-15], sol-gel process [16], UV-induced graft polymerization [17], UV-induced graft polymerization followed by quaternization through crosslinking process [18], method of glutaraldehyde crosslinking [19] etc. In recent years, the highly branched dendritic architectures of hyperbranched polymers associated with unique chemical and physical properties [20] have gained the attention of the membranologists for development of another novel classes of such NF membranes [21-23], employing the advantageous availability of plenty terminal functional sites in them.

***Motivation behind the proposed research area*:** The tremendous applications of charged NF membranes in separation industries trigger off the primary search for the novel synthetic polymeric membranes and the facile methods of membrane manufacturing from those materials. The predominant types of NF membranes are polymeric in nature and relevantly polymers with different constitutions have become the preferred options to many researchers for the development of NF membranes because of their easy tunability, wide ranging options available as membrane materials and possibility of easy scale up. In view of this, inclusion of charges in the polymeric structure of NF membranes during the process of manufacture, thereby eliminating the post fabrication modification step seems to become an interesting alternative of other conventional manufacturing processes, though quite challenging for the researchers.

Among various categories of NF membranes, thin film composite (TFC) type, comprising of ultra-thin polymeric skin layer with negatively or positively charged functionalities, fabricated on a chemically different thicker polymeric asymmetric porous layer as support substrate draws much attention due to their superior surface features and transport mechanisms. The surface features of such TFC type NF membranes vary with the process parameters like monomeric nature, composition and concentration; membrane preparative conditions like polymerization time, reaction temperature, curing type, curing duration and its' extent, degree of functionalization and also with the consequent effect of polymeric crosslinking density, porosity, segmental orientation and their distribution over the surfaces. A knowledge of structural, morphological and topographical features along with the hydrophilic-electrokinetic attributes of a membrane are thus of great importance. Selection of a facile method through an in depth investigation of the process parameters and subsequent optimization of the physicochemical properties becomes enormously significant since they exclusively supervise the macroscopical behaviors of the membranes, such as high rejection capability towards specific solutes and better throughput towards the solvent.

Keeping in mind about such necessity in development of high-performance novel charged membrane materials as a crucial step towards a sustainable industrial growth, which could become beneficial for a large domain of the society, Membrane Development Section of Bhabha Atomic Research Center adopted a programme of developing indigenous charged nanofiltration membranes for scale-up applications as a part of XI-/XII- Plan Project of Govt. of India. Since, the core of every membrane based separation processes depends on the membrane itself, an effort with a strong motivation, thus, was propagated during the tenure of the proposed research work for development of indigenous charged nanofiltration membranes.

The current thesis entitled "***Development and Characterization of Charged Membranes for Separation Studies***" has been divided into six chapters. A brief description of the different chapters is given below.

SYNOPSIS

Chapter – 1*:** In this chapter, entitled "Introduction***" the background of rising demands for the charged membranes as dominant separation devices has been illustrated. The subject of advantageous features of membrane based separation processes, more particularly the emergent charged membranes have been dealt with in details to highlight the scientific pursuit of the separation scientists in understanding the unique mechanism of interaction of the charged membranes and electrolytes with varying ionic constituents, in addition to the various factors affecting the macroscopical behaviors of such membranes. This has been followed by a review of the existing literatures in the field of charged membranes to search for the deficient areas, exploring the various methods and chemical modifications towards formation of such charged membranes. The chapter also includes brief fundamental descriptions of the different instrumental techniques employed in characterizing the intrinsic physicochemical features of the developed charged membranes. The chapter concludes with a motivation, substantiating the ground for getting involved in the research works which has been carried out as a part of the present thesis.

Chapter – 2: In the present chapter, entitled "***Structure - topography - morphology - performance relationship of non-crosslinked and crosslinked co-polyamide based negatively charged TFC NF membranes***" we report the developments and comprehensive physicochemical characterizations of negatively charged TFC type NF membranes, derived employing *in situ* interfacial polycondensation process, where the monomeric combination of reactive diamines comprises a cyclo-aliphatic diamine *i.e.*, piperazine (PIP) and an aromatic diamine with negatively charged moieties *i.e.*, 2, 4 - diamino benzene sulfonic acid. The poly-functional acid chloride monomers employed are either trimesoyl chloride (TMC) or terephthaloyl chloride (TPC), functioning as reactant cum crosslinking agent. The variations in structural features of the skin layers' co-polyamides with alteration of the crosslinking agents *i.e.*, TMC and TPC, as analyzed through Attenuated Total Reflectance (ATR) – Fourier Transform Infrared (FT IR) and solid state (^{13}C) nuclear magnetic resonance (NMR) spectroscopic techniques have been discussed in details. The impacts of varying curing temperatures on membranes' skin surface topographies have been analyzed by atomic force microscopy (AFM). The changes in membranes' skin layer morphology with variation in curing durations have also been assessed by scanning electron microscopy (SEM). In the course of these studies, the nanofiltration performances of the membranes have been correlated with the variations in membranes' physicochemical features on change of the reactants' compositions, polymerization time and post-reaction curing conditions, during formations of the membranes. The negatively charged TFC-NF membranes exhibited high degree of selectivity towards solutes having ionic constituents of varying valences, by showing a differential rejection pattern in the order of $Na_2SO_4 > MgSO_4 > MgCl_2 > NaCl$.

Chapter – 3: This chapter, entitled "***Development and characterization of negatively charged TFC NF membranes derived employing diaryl diamines with multiple sulfonic acid groups***" includes an in depth study on development of a series of TFC type NF membranes with polyamide and co-polyamide type skin layers bearing high density of negative charges. The innovativeness in the research work pertains to the use of unique combinations of reactive diaryl diamine monomers along with a poly-functional acid chloride monomer (TMC) functioning as reactant cum crosslinking agent. Binary as well as ternary monomeric compositions have been employed to develop these membranes, wherein the former compositions involved the use of one bi-functional diaryl diamine monomer *i.e.*, either $4,4^{/}$-diamino stilbene-$2,2^{/}$-disulfonic acid

(DASDSA) or 2,2$^{/}$-benzidene disulfonic acid (BDSA), which serves as source of the negatively charged sites (sulfonic acid groups, $-SO_3H$) and the later compositions involved a cyclo-aliphatic diamine, piperazine (PIP) as a co-monomer along with either of the charge bearing diaryl diamine monomer, during *in situ* interfacial polycondensation or co-polycondensation processes, respectively.

ATR-FTIR has been employed to investigate the structural variations of the different kinds of polyamides and co-polyamides, formed as skin layers of the membranes. Quantitative analysis of the surface roughness parameters by AFM techniques revealed the variations in topographical characteristics of the membranes' surfaces. SEM analyses of skin surfaces of the membranes further revealed the finer changes happening in the skin layer morphology on formations of the membranes with different polymeric constitutions. Variations in hydrophilic and electrokinetic features of the membranes illustrated the intrinsic roles of the charge bearing diaryl diamine monomers. Evaluation of nanofiltration performances depicted the variant behaviors of the membranes towards various single solute feed systems as the membranes derived from binary monomeric compositions follow the differential rejection patterns in the order $Na_2SO_4 > MgSO_4 > NaCl > MgCl_2$, whereas, the membranes derived from ternary monomeric compositions follow the differential rejection patterns in the order of $Na_2SO_4 > MgSO_4 > MgCl_2 > NaCl$, with high rejections for sulfate containing solutes and low rejections for chloride containing solutes, which is typical of negatively charged NF membranes.

Chapter – 4: In this chapter, entitled "***Variation in physicochemical features and separation characteristics of positively charged TFC NF membranes with change in molecular***

architectures of quaternized poly(ethyleneimine amide)s" the details of development and characterization of a novel class of positively charged TFC type NF (TFC-PCNF) membranes, having crosslinked molecular architectures of poly(ethyleneimine amide)s have been illustrated. The TFC-PCNF membranes were developed through *in situ* interfacial polymerization process, employing functionalized branched amine-rich polycationic polymer *i.e.*, branched poly(ethyleneimine) (BPEI) of varying molecular weights (*i.e.*, 10k, 50k-100k and 600k-100k D) and trimesoyl chloride (TMC) as a reactant cum crosslinking agent. Prior to the polymerization stage, glycidyltrimethylammonium chloride (GTACl) was used to accomplish the functionalization through quaternization of the constituent BPEIs.

Mechanistic details of formation of the quaternized BPEIs, evaluated by employing ^{1}H–NMR and FTIR spectroscopic techniques have revealed that facile quaternization of BPEIs by GTACl involved formation of termolecular-oxirane/amine/hydroxyl complex. The study also substantiated that such formation followed an *in situ* autocatalytic approach during the consecutive non-catalytic and catalytic steps, where inclusion of the hydroxypropyl trimethylammonium groups as quaternized functional-moieties happened in the amine sites of the BPEIs' backbone. Structural features of the crosslinked-quaternized poly(ethyleneimine amide)s, synthesized as thin skin layers of the TFC-PCNF membranes have been analyzed by FTIR and XPS studies. The variations in hydrophilic features of TFC-PCNF membranes, observed through contact angle measurements have implied that the structural orientation as well as organization of the resultant rigid crosslinked poly(ethyleneimine amide) got affected by the enhancement in M.W. of BPEI, since increase in branching density of polymeric backbone of the quaternized BPEI induced constrained mobility in the chain segments and thus, consequently restricted the migration of polar terminal functional-moieties from the interior to the periphery of the skin layer polymer. The effect of inclusion of the quaternized functional-moieties on packing patterns of the polymer chains in structures of crosslinked poly(ethyleneimine amide)s has signified the extent of differential hindrance in segmental orientations depending on the resultant variation in spacing of the moieties. Analysis of the trends in electrokinetic features of the TFC-PCNF membranes, observed through streaming potential measurements, with variation of pH has enlightened that absolute ζ values enhanced with lowering of pH followed by decline at even higher acidic environment. This further depicted the reduction of effective streaming current through diffusive back flow of the streaming current due to dragging of the tangentially driven counter-ions from the hydrodynamic slipping plane to the bulk of the membranes stationary positively charged layer. However, at progressively enhanced pH condition, non-specific adsorption of the excess counter-ions as well as concentration build up of the counter-ions with subsequent compression in the electrical double layer thickness have resulted in screening of the surface positive charges with severe reduction in the positive absolute ζ values of the membranes. Cross-flow permeation study with respect to varying solutes has depicted that the TFC-PCNF membranes followed a rejection trend of $MgCl_2 > MgSO_4 > Na_2SO_4 > NaCl$, under iso-osmotic environment of solutes. The higher rejections of $MgCl_2$ and $MgSO_4$ profoundly indicated the role of Donnan exclusion. The higher rejection efficiency for Na_2SO_4 over NaCl signified the additional and overcompensating contribution of size exclusion phenomena, exhibiting the role of skin layer pore structure formed by the crosslinked architecture of the poly(ethyleneimine amide) in restricting the transport of larger sized hydrated anionic constituents as compared to the smaller sized ones.

Chapter – 5: This chapter, entitled "***Nano-ZnO impregnated thin film nanocomposite NF membranes: An investigation of variation in structure, morphology and transport properties***" comprises the details of development and physicochemical characterizations of inorganic–polymer hybrid thin film nanocomposite NF (TFN-NF) membranes, prepared by *in situ* interfacial polymerization of branched poly(ethyleneimine) and trimesoyl chloride, with simultaneous impregnation of the as synthesized hexagonal wurtzite nanocrystals of ZnO (nano-ZnO), either through aqueous or organic phase. The effects of variation in route specific introduction of nano-ZnO into the skin layer polymer matrix of positively charged TFN-NF membranes, through either aqueous (Aq-ZnO:TFN-NF) or organic (Org-ZnO:TFN-NF) phase, during *in situ* interfacial polymerization of reactive monomers have been analyzed in details. The nano-ZnO was synthesized by thermal decomposition of anhydrous $Zn(acac)_2$ in n-octylamine at temperature as low as 110 ^oC and then characterized by X-ray powder diffraction (XRD) analysis, XPS as well as FTIR and Raman spectroscopy. Structural characterizations by XPS and ATR FTIR have probed the interactions of the nano-ZnO and its co-existence in the hybrid nanocomposite material, highlighting the electronic and molecular level interactions happening in the nanocomposite polyamide skin layers of the membranes and their dependence on nano-ZnO concentration as well as the mode of its introduction. Morphological characterizations by SEM revealed the formation of distinct patterns and coils in the skin surfaces of Aq-ZnO:TFN-NF class of membranes. However, the nanomaterials remained distributed as discrete clusters at varying extent within the skin layers of Org-ZnO:TFN-NF class of membranes. Topographical characterizations by AFM showed the variation of surface roughness parameters with change in the precursor medium of introduction of nano-ZnO, revealing that the uniformity in distribution of the nano-ZnO was less in the skin surfaces of Org-ZnO:TFN-NF membranes than the Aq-ZnO:TFN-NF membranes.

Energy dispersive X-ray quantified the elemental contribution of nanomaterials in the membrane skin layers. Nanofiltration performance towards different solutes, providing differential rejections in the order of $MgCl_2 > NaCl \geq Na_2SO_4$, revealed membranes' distinct positively charged surface features. Introduction of nano-ZnO improved the solvent fluxes of the membranes significantly, particularly in the Aq-ZnO:TFN-NF set of membranes. The study has attempted to establish correlations between the factors leading to dynamic membrane formation and the resulting physicochemical features as well as transport properties.

Chapter – 6: In this chapter, entitled "***Conclusions, implications and future perspectives***" the results of the entire works carried out in favor of the proposed area of research, as a part of the thesis have been summarized. This chapter concisely illustrates the advantageous applicability of the developed, both negatively and positively charged TFC type NF membranes. A glimpse of the correlations drawn between the intrinsic physicochemical features of the investigated charged membranes and their transport characteristics has also been reviewed in brief. An illustration has also been made stating that how the present developments of the charged NF membranes, as discussed in subsequent chapters (**Chapter - 2 to 5**) provided facile methods towards development of novel membranes, which have the potential applicability for a broad range of commercial to in-house applications.

References:

[1] A. Bhattacharya, P. Ghosh, Nanofiltration and reverse osmosis membranes: theory and application in separation of electrolytes, *Rev. Chem. Eng.*, **2004**, *20*, 111.

[2] R.J. Peterson, Composite reverse osmosis and nanofiltration membranes, *J. Membr. Sci.*, **1993**, *83*, 81–150.

[3] W.J. Lau, A.F. Ismail, N. Misdan, M.A. Kassim; A recent progress in thin film composite membrane: A review; *Desalination*, **2012**, *287*, 190–199.

[4] Wang *et al.*, Internal hydrophilic membranes from blended anionic copolymers, US Patent no. 6,258,272.

[5] Method for preparing negatively charged nanofiltration membrane through grafting induced after plasma radiation, Chinese Patent no.102068912.

[6] Moya *et al.*, Porous composite membrane and process, US Patent no. 5,629,084.

[7] Sclenoff *et al.*, Polyelectrolyte complex films for analytical and membrane separation of chiral compounds, US Patent no. 7,101,947.

[8] Childs *et al*., Composite materials comprising supported porous gels containing metal-affinity ligands, US Patent no. 7,604,749.

[9] X. Tongwen, Y. Weihua, A novel positively charged composite membranes for nanofiltration prepared from poly(2,6-dimethyl-1,4-phenylene oxide) by *in situ* amines crosslinking, *J. Membr. Sci.*, **2003**, *215*, 25–32.

[10] R. Du, J. Zhao, Properties of poly (*N*,*N*-dimethylaminoethyl methacrylate)/polysulfone positively charged composite nanofiltration membrane, *J. Membr. Sci.*, **2004**, *239*, 183–188.

[11] Q. Zhang, H. Wang, S. Zhang, L. Dai, Positively charged nanofiltration membrane based on cardo poly(arylene ethersulfone) with pendant tertiary amine groups, *J. Membr. Sci.*, **2011**, *375*, 191–197.

[12] Y. Su, X. Jian, S. Zhang, G. Wang, Preparation and characterization of quaternized poly(phthalazinone ether sulfone ketone) NF membranes, *J. Membr. Sci*., **2004**, *241*, 225–233.

[13] B. Tang, T. Xu, M. Gong, W. Yang, A novel positively charged asymmetry membranes from poly(2,6-dimethyl-1,4-phenylene oxide) by benzyl bromination and *in situ* amination: membrane preparation and characterization, *J. Membr. Sci*., **2005**, *248*, 119–125.

[14] B. Tang, T. Xu, W. Yang, A novel positively charged asymmetry membranes from poly(2,6-dimethyl-1,4-phenylene oxide) by benzyl bromination and *in situ* amination Part II: Effect of charged group species on membrane performance and morphologies, *J. Membr. Sci*., **2006**, *268* 123–131.

[15] B. Tang, T. Xu, P. Sun, W. Yang, A novel of positively charged asymmetry membrane prepared from poly(2,6-dimethyl-1,4-phenylene oxide) by *in situ* amination Part III. Effect of benzyl and aryl bromination degrees of polymer on membrane performance and morphologies, *J. Membr. Sci*., **2006**, *279*, 192–199.

[16] S. Zhang, T. Xu, C. Wu, Synthesis and characterizations of novel, positively charged hybrid membranes from poly(2,6-dimethyl-1,4-phenylene oxide), *J. Membr. Sci*., **2006**, *269*, 142–151.

[17] H. Deng, Y. Xu, Q. Chen, X. Wei, B. Zhu, High flux positively charged nanofiltration membranes prepared by UV-initiated graft polymerization of methacrylatoethyl trimethyl ammonium chloride (DMC) onto polysulfone membranes, *J. Membr. Sci*., **2011**, *366*, 363–372.

[18] X. Li, L. Zhu, Y. Xu, Z. Yi, B. Zhu, A novel positively charged nanofiltration membrane prepared from N,N-dimethylaminoethyl methacrylate by quaternization crosslinking, *J. Membr*. *Sci*., **2011**, *374*, 33–42.

[19] Y. Ji, Q. An, Q. Zhao, H. Chen, C. Gao, Preparation of novel positively charged copolymer membranes for nanofiltration, *J. Membr. Sci*., **2011**, *376*, 254–265.

[20] C. Gao, D. Yan, Hyperbranched polymers: from synthesis to applications, *Prog. Polym. Sci*., **2004**, *29*, 183–275.

[21] Y.-C. Chiang, Y.-Z. Hsub, R.-C. Ruaan, C.-J. Chuang, K.-L. Tung, Nanofiltration membranes synthesized from hyperbranched polyethyleneimine, *J. Membr. Sci*., **2009**, *326*, 19–26.

[22] X.-Z. Wei, L.-P. Zhu, H.-Y. Deng, Y.-Y. Xu, B.-K. Zhu, Z.-M. Huang, New type of nanofiltration membrane based on crosslinked hyperbranched polymers, *J. Membr. Sci*., **2008**, *323*, 278–287.

[23] T. K. Dey, R. C. Bindal, S. Prabhakar, P. K.Tewari, Development, characterization and performance evaluation of positively charged thin film composite nanofiltration membrane containing fixed quaternary ammonium moieties, *Sep. Sci. Technol*., **2011**, *46*, 933–943.

LIST OF FIGURES

CHAPTER – 1

CHAPTER – 2

CHAPTER – 3

CHAPTER – 4

CHAPTER – 5

LIST OF TABLES

CHAPTER –1

Introduction

CHAPTER–1

1. 1. Overview of the processes employed for separation of masses

Separation is a mass transfer process, employed to convert a mixture of substances into two or more distinct product mixtures, at least one of which is enriched in one or more of the mixture's constituents. In some cases, a separation may fully fractionate the mixture into its pure constituents. Separations are carried out based on differences in properties like size, shape, mass, or chemical affinity between the constituents of a mixture, and are often classified according to the particular differences they use to achieve separation. However, when no single difference can be employed to accomplish a desired separation, multiple processes will often be performed in conjunction to achieve the desired output.

The separation, concentration, and purification of molecular mixtures are major problems in the chemical industries. Efficient separation processes are also needed to obtain high value products in the food and pharmaceutical industries, to supply high quality water in communities and industries, and to remove or recover toxic or valuable components from industrial effluents. For these purposes, multiple conventional separation processes are used industrially, such as –

adsorption (adhesion of atoms, ions or molecules from a gas, liquid, or dissolved solid to a surface, which creates a film of the adsorbate on the surface of the adsorbent),

centrifugation (separation based on density differences; which involves the use of the centrifugation for the sedimentation of mixtures with a centrifuge),

distillation (a method of separating mixtures based on differences in volatilities of components in a boiling liquid mixture),

crystallization (process of formation of solid crystals precipitating from a solution, melts or more rarely deposited directly from a gas, or in other way a chemical solid–liquid separation technique, in which mass transfer of a solute from the liquid solution to a pure solid crystalline phase occurs),

drying (a mass transfer process which removes liquid from a solid by vaporization),

electrophoresis (separation of organic molecules based on their different interaction with a gel under an electric potential which is the motion of dispersed particles relative to a fluid under the influence of a spatially uniform electric field),

evaporation **(**a type of vaporization of a liquid that occurs only on the surface of a liquid),

extraction (leaching or solid extraction is used to dissolve soluble matter from its mixture with an insoluble solid; liquid-liquid extraction is used to separate two miscible liquids by the use of solvent that preferentially dissolves one of them),

flocculation (separation of a solid from a liquid in a colloid, by use of a flocculent, which promotes the solid clumping into flocs),

filtration **(**removal of large particulates suspended in fluids by mesh, bag and paper filters),

fractional distillation (a process where the compound is heated and, as each of its constituent components comes to a boiling point, its vapors are separated and cooled, so it can be removed in its pure form),

ion exchange (a reversible chemical reaction between two substances, usually a relatively insoluble solid and a solution, during which ions of equal charge may be interchanged),

magnetic separation **(**a process in which magnetically susceptible material is extracted from a mixture using a magnetic force),

precipitation (the formation of a solid in a solution during a chemical reaction),

sedimentation (the tendency for particles in suspension to settle out of the fluid in which they are entrained, and come to rest against a barrier).

1. 2. Potential of membrane as a separation device

A synthetic membrane, made of by chemical entities is a physical interphase between two adjacent phases and regulates the transport of various constituents from one phase into the other across the selective barrier which gets controlled in a specific manner of physicochemical interaction. A membrane separation system separates an influent stream into two streams known as permeate and concentrate. Permeate is the portion of the fluid that has passed through the semi-permeable membrane, whereas the concentrate stream contains the constituents that have been rejected by the membrane.

From the last few decades, membrane induced separation processes have become more advantageous because of their eco-friendliness over the conventional separation techniques in various aspects such as separation without phase change (except pervaporation), isothermal operation at low temperatures, low energy consumption, flexibility in equipment design as well as operations since the systems are modular, minimum space requirements for plant operation, easy up scaling and down scaling of membrane process, separation ability for a wide range of molecular weight components in the process stream, offering lower costs and lower maintenance, improvement of final product quality, effectiveness in processing dilute solutions. Therefore, with view of the above mentioned promising aspects, generation of synthetic membranes as separation tool has drawn the attention of the separation scientists for quite a long time and also gained an important place in chemical technology due to its usefulness in a broad range of applications [1].

An overview of the different membrane processes, distinguished based on driving forces are enlisted in Table 1. 1.

Table 1. 1

Driving forces and respective membrane separation processes.

Driving force	*Membrane separation processes*
Pressure difference	Microfiltration (MF), Ultrafiltration (UF), Nanofiltration (NF), Reverse osmosis (RO)
Chemical potential difference	Pervaporation, Dialysis, Gas separation, Vapor permeation, Liquid membranes
Electrical potential difference	Electro-dialysis, Membrane electrophoresis, Membrane electrolysis
Temperature difference	Membrane distillation

Among different pressure driven membrane based separation techniques, the process that would be as promising as a superior technique over other such membrane processes, is nanofiltration membrane process [2], which stands in between reverse osmosis and ultrafiltration membrane processes and the membrane is considered as loose RO or tighter UF membrane. In case of this membrane processes, particularly membrane materials with charged surface act as a selective barrier in treating hardness of low brackish water for the production of potable water, removing organic and inorganic compounds, viruses and bacterias, managing the exclusion of pesticides etc. During treatment of brackish water, nanofiltration shows the advantage of being ion selective towards mixed streams constituting varying mono- and multi-valent ionic species, depending on the nature of charge of the membranes. Further, when NF can remove undesirable materials in single-step, then conventional separation processes might need several steps to do so, as a consequence, nanofiltration can be considered as more resourceful and cheaper. Another competitive process to nanofiltration is reverse osmosis because of its higher rejection ability than nanofiltration. Nonetheless, RO requires higher trans-membrane pressure than NF which becomes unbeneficial due to higher operating costs. In addition, sometimes minerals need to be added to the treated water because of nonselective nature of reverse osmosis process, which further increases the cost of product. The membrane materials employed for nanofiltration processes in treating brackish water have also the promising potential to be used in food and pharmaceutical industries [24, 25], dairy industries [26], textile industries [27], biotechnological industries [28] etc. for selective removal of contaminants. More particularly, they found suitable for fractional separation involving high value products, such as in pharmaceuticals, for recovery of drug molecules from broths containing high concentration of salts, separation and purification of valuables from fermentation broths, resolution of racemic mixtures of amino acids and other biotechnological applications. With the ability to perform in a wide arena of separation industries, charged nanofiltration membranes draw more attention and favor over conventional pressure driven desalinating techniques, because the later cannot perform such kind of selective removals in one and continuous stage of operation and require additional processes to complete the desired task.

1. 3. Motivation and need of the present research work

Aggressive research works are being carried out by the membranologists for the development of new synthetic membrane materials with superior properties for nanofiltration processes. Researchers are coming out with novel techniques to solve the issues associated with the technology. The major challenge posed by the membranes like fouling, stability of membranes in harsh environments, improvement of solute rejections, selectivity or differential rejection ability and fluxes, improving the lifespan of the membranes seem to be attracting more attention of the researches.

The tremendous applications of charged NF membranes in separation industries trigger off the primary search for the novel synthetic polymeric membranes and the facile methods of membrane manufacturing from those materials. The predominant types of NF membranes are polymeric in nature and relevantly polymers with different constitutions have become the preferred options to many researchers for the development of NF membranes because of their easy tunability, wide ranging options available as membrane materials and possibility of easy scale up. In view of this, inclusion of charges in the polymeric structure of NF membranes during the process of manufacture, thereby eliminating the post fabrication modification step seems to become an interesting alternative of other conventional manufacturing processes, though quite challenging for the researchers.

Among various categories of NF membranes, thin film composite (TFC) type, comprising of ultra-thin polymeric skin layer with negatively or positively charged functionalities, fabricated on a chemically different thicker polymeric asymmetric porous layer as support substrate draws much attention due to their superior surface features and transport mechanisms. The surface features of such TFC type NF membranes vary with the process parameters like monomeric nature, composition and concentration; membrane preparative conditions like polymerization time, reaction temperature, curing type, curing duration and its' extent, degree of functionalization and also with the consequent effect of polymeric crosslinking density, porosity, segmental orientation and their distribution over the surfaces. A knowledge of structural, morphological and topographical features along with the hydrophilic-electrokinetic attributes of a membrane are thus of great importance. Selection of a facile method through an in depth investigation of the process parameters and subsequent optimization of the physicochemical properties becomes enormously significant since they exclusively supervise the macroscopical behaviors of the membranes, such as high rejection capability towards specific solutes and better throughput towards the solvent.

Keeping in mind about such necessity in development of high-performance novel charged membrane materials as a crucial step towards a sustainable industrial growth, which could become beneficial for a large domain of the society, Membrane Development Section of Bhabha Atomic Research Center adopted a programme of developing indigenous charged nanofiltration membranes for scale-up applications as a part of XI-/XII- Plan Project of Govt. of India. Since, the core of every membrane based separation processes depends on the membrane itself, an effort with a strong motivation, thus, was propagated during the tenure of the proposed research work for development of indigenous charged nanofiltration membranes.

1. 4. Thesis Objective

Progressive developments of high-performance as well as innovative membrane based separation processes stand essential for sustainable growth of the industries which could become beneficial to the society, and subsequently have drawn the attention of the separation scientists for quite a long time. In the present scenario, adoption of such suitable efficient processes for separation, concentration and purification of molecular mixtures are thus major concerns in wide range of chemical industries, precisely in obtaining high grade products in the food and pharmaceutical industries, delivering high quality water in the communities and industries, removing or recovering the toxic or valuable species from the industrial effluents, separating the toxic organic residues generated from the textile and dye manufacturing industries, removing the large amount of non-biodegradable inorganic salts having low to high potential of environmental hazards as generated in mining and mineral processing industries etc.

In the arena of pressure driven membrane processes, plenty of synthetic polymeric membranes function as semipermeable interphases between two adjacent phases and regulate the transport of ionic constituents from one phase into the other across the selective barrier, following specific transport mechanisms. Nanofiltration (NF), being one such versatile pressure driven membrane process acquires an immense importance by exerting more potential in wide spectrum of applications of the separation industries [1]. In the course of pressure driven NF processes, charged membranes are employed in achieving differential rejections towards wet streams comprising of ionic constituents of varying valances or fractionation of mixed ionic streams, utilizing their unique feature of transport selectivity. Unlike the neutral NF membranes which, in general, allow the passage of smaller monovalent ions and retain the larger multivalent ones, in most cases, NF membranes bear either negatively charged or positively charged functionalities in their polymeric surfaces or matrices and behave as electrically charged layers when come in contact with electrolyte solutions, depending on the interaction patterns between charge of the membrane and charge of the ionic constituents under considerations. Thus, the two different dominant classes of charged NF membranes include – negatively charged NF membranes (comprising of fixed negatively charged sites and mobile positively charged sites, repelling the anions and concomitantly allowing the preferential passage of the cations of an electrolyte solution through the membrane, in the course of separation) and positively charged NF membranes (comprising of fixed positively charged sites and mobile negatively charged sites, repelling the cations and allowing the preferential passage of the anions of an electrolyte solution through the membrane, alongside during separation) [2].

The earlier research efforts on development of various negatively charged NF membranes reveal that the most commonly used processes for generation of such charged membranes with various polymeric constitutions include interfacial polymerization [3], grafting of polymers to introduce charge and making membranes using them by phase separation technique [4], modification of preformed membranes by radiation grafting [5], coating of charged polymer layer over another substrate [6], applying multilayer polyelectrolytes (alternative layers of oppositely charged polyelectrolytes) over an existing substrate membrane [7], coating or filling of charged gels in the porous structure of the membrane [8] etc.

Prior efforts by the researchers towards development of positively charged NF membranes following different ways provide various polymeric constitutions with modified structural and physicochemical features, which include bromination followed by *in situ* amine crosslinking method [9], interfacial polymerization through crosslinking process [10], phase inversion [11], phase inversion followed by *in situ* amination [12], *in situ* amination followed by phase inversion [13-15], sol-gel process [16], UV-induced graft polymerization [17], UV-induced graft polymerization followed by quaternization through crosslinking process [18], method of glutaraldehyde crosslinking [19] etc. In recent years, the highly branched dendritic architectures of hyperbranched polymers associated with unique chemical and physical properties [20] have gained the attention of the membranologists for development of another novel classes of such NF membranes [21-23], employing the advantageous availability of plenty terminal functional sites in them.

1. 5. Perspectives of charged membranes

1.5.1. Charged membrane materials

In the diversity of membrane technology, charged membrane based separations become progressively more promising in various fields of separation industries due to the unique transport selectivity or retention properties of the membranes towards certain charged solutes. Membranes employed for such separation processes provide further advantages like reduction of fouling phenomena due to their variant structural aspects. A charged membrane is a class of semipermeable polymeric membranes having charge (either positive or negative) bearing functionality either in the surface or in the matrix, which in contact with an electrolyte solution carries an electric charge. There are two different classes of charged membranes, such as –

Positively charged membranes – fixed positively charged functionalities & mobile negatively charged functionalities; in electrolyte solution either the membrane will exchange the anions of the electrolyte with its negatively charged sites or they will allow the anions to pass through preferentially.

Negatively charged membranes – fixed negatively charged functionalities and mobile positively charged functionalities; in electrolyte solution either the membrane will exchange the cations of the electrolyte with its positively charged sites or they will allow the cations to pass through preferentially.

The charged nature of the membranes generates an electrical potential, which is maximum at the surface and decreases on moving through the liquid away from the surface, thereby affecting the distribution of ions in the liquid. Ions from the liquid that have opposite charge to the charge of the membrane surface, conventionally called as the counter-ions adsorb or get attracted to the membrane. The ions immediately adjacent to the surface are nearly immobile and formed a layer, which is known as Stern layer, since the opposite charges are strongly interacting. Further, moving away from the solid surface, the electrostatic attraction of the solid decreases and the ions remain more mobile, thus forming the diffuse layer which is composed of both co- and counter-ions. In bulk solution, the ions of both signs are in a random motion. The Stern layer and diffuse layer are the principle of the electrical double layer model that describes the distribution of charges at the solid-liquid interface. Because of the difference in charge between the diffuse layer and the solid surface, movement of one relative to the other will cause charge separation and generate a potential difference, or alternatively, application of an external electrical potential will cause movement of one relative to the other. This relative movement of the constituents of liquid with respect to the solid surface occurs at the surface of shear and the potential at this surface of shear is known as the electrokinetic phenomena.

1.5.1.1. Materials and processes towards negatively charged membranes

Several routes are adopted by researchers to prepare charged membranes. The most commonly used ones include grafting of polymers to introduce charge and making membranes from those polymers by phase separation technique, modification of preformed membranes by grafting using radiation or by chemical means, coating of charged polymer layer over another substrate, applying multilayer polyelectrolytes (alternative layers of oppositely charged polyelectrolytes) over an existing substrate membrane, coating or filling of charged gels in the porous structure of the membrane.

Chemical grafting and blending is one of the popular ways of making charge bearing membranes. US patent 6,258,272 discloses a method of making membranes by first making sulfonated polymers or copolymers and blending them with polysulfone polymer to make phase inversion membranes of charged type [4].

Modification by grafting of suitable chemical functionalities on an existing membrane is another route of making charged membranes. CN102068912 describes a method for the preparation of negative charge bearing nanofiltration membranes starting from a polysulfone or polyvinyledene difluoride membrane and modifying them by grafting, using monomers and crosslinkers, aided by low temperature plasma [5]. The post fabrication radiation grafting assisted by UV, gamma or electron beams may not lead to uniform modification of the existing membrane. The control over pore size and their distribution is not satisfactory. Further, these processes may damage the polymer backbone of the original membrane during the radiation treatment step, making it weak. Commercial production needs a lot of facilities like radiation source, etc. and the process is cumbersome.

Another method of producing charge bearing membrane is coating of charged polymeric layer over another membrane substrate. US patent 5,629,084 describes about manufacturing of negatively charge bearing membranes by coating with a self crosslinking polymer layer over an existing membrane substrate [6].

Layer by layer coating of polyelectrolyte complexes is a method for producing charged membranes where polymer layers, alternately of opposite charges, are deposited one over another, on a support membrane. US patent 7,101,947 discloses about making of charge bearing membranes by depositing alternative layers of positively charged polyelectrolyte and negatively charged poly electrolyte to obtain a membrane for separation of chiral compounds [7]. Material incompatibility of the generally hydrophobic support membrane and the immediate layer adjacent to it is another drawback of this type of membranes.

Gel filling is another route adopted by researchers to make charge bearing membranes, wherein charged gel polymers are filled into the porous structures of the substrate membranes. In this process pores of the substrates are filled with either cationic or anionic monomers along with crosslinker and initiators and polymerizing it with UV radiation. US patent 7,604,749 discloses about making of charge bearing membranes by gel filling process [8]. Membranes prepared with gel filling process are suitable for only low pressure applications and with feed solutions of low salinities in nanofiltration.

The most preferred method for making thin film composite (TFC) membranes is *in situ* interfacial polymerization technique, wherein the ultrathin discriminating layer is deposited on a suitable substrate employing reactive chemicals [3].

Thus, various processes reportedly used for preparation of negatively charged nanofiltration membranes generally involve post fabrication modification such as by radiation induced grafting, coating of charged polymer layer over a micro porous substrate or filling of charged gels in the micro pores of a substrate membrane, etc. All these processes suffer from various deficiencies particularly their non-amenability to scale up for commercial productions.

1.5.1.2. Materials and processes towards positively charged membranes

With progressive findings of polymeric materials for production of potential NF membranes, membranologists find opportunity to enlarge the area of research on such membrane systems for extensive industrial applications. Prior efforts by the researchers towards development of positively charged NF membranes following different ways provided various polymeric constitutions with modified structural and physicochemical features. The different ways towards tuning of macroscopical features of such NF membranes included bromination followed by *in situ* amine crosslinking method [9], interfacial polymerization through crosslinking process [10], phase inversion [11], phase inversion followed by *in situ* amination [12], *in situ* amination followed by phase inversion [13-15], sol-gel process [16], UV-induced graft polymerization [17], UV-induced graft polymerization followed by quaternization though crosslinking process [18] and method of glutaraldehyde crosslinking [19] etc. In recent years, the highly branched dendritic architectures of hyperbranched polymers associated with unique chemical and physical properties [20] have gained the attention of the membranologists for development of novel classes of membrane matrices. A group of researchers like Y.-C. Chiang et al. [21] and X.-Z.

Wei et al. [22] reported the development of various nanofiltration membranes from a hyperbranched polymer like poly(ethyleneimine), employing the advantageous availability of plenty terminal functional groups in it. In an attempt, made by T. K. Dey et al. [23], TFC type positively charged NF membranes were successfully developed by *in situ* interfacial polymerization process, employing glycidyltrimethyl ammonium chloride (GTACl) functionalized branched poly(ethyleneimine) having quaternized amine sites, as amine monomer and terephthaloyl chloride (TPC), as acid chloride monomer. There, an extensive illustration was made on the variation in performances of the charged NF membranes with respect to the effect of functionalization as well as degree of functionalization of the branched poly(ethyleneimine) and membrane preparative conditions like curing temperature, duration of curing and reactant concentration.

1.5.2. Chemistry behind interaction between charged membrane and charged solutes

The unique separation mechanism of charged NF membrane is usually illustrated in terms of charge and/or size effects [1]. Transport of uncharged solutes takes place by convection phenomena due to a pressure gradient and by diffusion mechanism due to a concentration gradient across the membrane. However, a sieving mechanism is also responsible for the retention of uncharged solutes. For charged components like ionic solutes or macromolecules, an electrostatic interaction (attractive or repulsive) takes place between the component and the membrane, as most nanofiltration membranes are either positively or negatively charged. The variation of charge thus plays an important role in nanofiltration performances. Due to the special feature of the NF membranes’ surfaces (mostly having fixed negative or positive surface charge), these membranes exhibit selectivity towards feed solution comprising of varying ionic solutes, where the extent of separation is influenced by the steric effect (due to small pore radius) and the charge on the surface of the pore (Donnan exclusion phenomena). At low concentration of ionic solute, the multivalent ions are separated by the NF membrane to a higher degree than monovalent ions, since the passage of the latter happens more freely through pore of the membrane. Since, the electrokinetic phenomenon involved during the course of nanofiltration process is remarkably affected by the physico-chemistry of the solution, thus, by alteration of the physico-chemistry of the feed solution with optimum conditions for charge interaction between the ionic constituents and membrane may lead to a high efficiency of the process.

1.5.2.1. Influence of membranes' surface charge on retention of ionic solutes

Polymeric charged membranes acquire either negative or positive surface charges, depending on the nature of the polymers and the chemical environment of the feed solution. Membranes' performance in terms of selectivity or differential rejection ability towards charged molecules as well as ionic solutes depends on the extent of the surface charges of the membrane. When a polymeric membrane with charged functionalities residing on the exterior surface as well as on the interior pore surface comes in contact with aqueous solution comprising of ionic constituents, then surface charge gets generated through different charging mechanisms such as dissociation of functional groups, adsorption of ions from solution and adsorption of polyelectrolytes, ionic surfactants and charged macromolecules.

These surface charges of membrane have an influence over the distribution of ions in the solution due to the requirement of electro-neutrality of the system. This leads to formation of an electrical double layer at the interface between charged surface of the membrane and layer of a neutralizing excess of counter-ions in the adjacent solution. When a charged membrane is placed in an ionic solution, because of the presence of a fixed membrane charge, the ionic concentrations in the membrane become unequal to those in the solution and consequently equilibrium arises between the membrane and the solution. The mobile counter-ions' (bearing opposite sign of charge with respect to the fixed charge in the membrane) concentration remains higher in the membrane phase than in the bulk solution, while the mobile co-ions' (bearing same sign of charge as the fixed membrane charge) concentration becomes lower in the membrane phase than in the bulk solution [24]. These concentration differences cannot be leveled out by diffusion as electroneutrality would then be disturbed, owing to the electric-charge bearing properties of the mobile ions. The fluxes of counter-ions towards the bulk of solution and of co-ions towards the membrane surface result in an accumulation of varying charge nature in both the phases. Therefore, the diffusing ions experience a potential difference between the two phases. Such potential difference is termed as "Donnan potential", which effectively draws counter-ions back into the membrane and co-ions back into the solution with an eventual establishment of equilibrium between the electric field and the tendency of the ions to eliminate concentration differences by diffusion. During establishment of such equilibrium, the co-ions as well as the solute itself, for maintaining the electroneutrality, get repelled from the membrane surface. This electrolyte exclusion from the membrane is known as Donnan exclusion, which varies proportionally with the magnitude of the Donnan potential.

1.5.2.2. Influence of solutes' charge behavior on retention of ionic solutes

The rejection behavior of a charged membrane is dependent on the volume concentration of the fixed ionic groups of the membrane surface *i.e.*, charge density of the membrane and hence the Donnan potential [25]. However, the electrostatic repulsive interaction between the membrane and the ionic solutes also depend on the extent of charge present on the solutes. Therefore, increasing or decreasing efficiency of electrolyte exclusions by a membrane can be ascribed to the magnitude of solute charge or more specifically the magnitude of charge of counter-ions and co-ions of the ionic solute. Counter-ions of high charge density (small size and/or high valence) and co-ions of low charge density minimize solutes' exclusion. This reduced effect of repulsion by the charged membrane surface is due to a concurrent occurrence of maximum attraction and minimum repulsion by the membranes fixed charged sites to the counter-ions and co-ions, respectively. Donnan efficiency or magnitude of Donnan potential of a membrane gets reduced if an association happens between the fixed charged sites of the membrane surface and counter-ions of the solution, forming an ion-pair with subsequent diminish of the effective charge density of the former. At high charge density for the multivalent counter-ions, there may occur reversal of membranes fixed charges. Since, the selectivity of a charged membrane is governed by the membrane-solute and solute-solute interactions, the counter-ions with high charge density and of small size preferentially approach the membrane.

1.5.3. Factors affecting charge properties of the membranes

1.5.3.1. Dependency of membranes' charge on pH of feed solution

The skin layers of most TFC membranes, carries a negative charge to minimize the adsorption of negatively charged foulants present in membrane feed solutions and increase the rejection of dissolved solutes. The negative charge on the membrane surface is usually caused by the tethered sulfonic and/or carboxylic acid groups or the residual carboxylic acid groups that get de-protonated at neutral pH condition. Studies on membranes' surface charge as quantified by zeta potential measurements reveal that pH had an effect upon the charge of a membrane due to the dissociation of functional groups [26]. Zeta potentials for most membranes have been observed in many studies to become increasingly more negative as pH is increased and functional groups get de-protonated. A polymeric NF membrane typically consists of hydrophobic functional groups (alkyl or aromatic chains) which alternate to hydrophilic functional groups ($-CONH_2$, $-COOH$, $-NH_2$, $-SO_3^-H^+$, $-R_3N^+$,etc). The extent of hydrophilic functional groups' dissociation is indeed strongly pH dependent. The active part of the polymer (which is involved in charge determination) is assumed as the sum of two different group sites: the hydrophilic sites which are considered to give rise to the pH dependent "fixed" charge (sign depends on the result of the prevailing mechanism among the concomitant "protonation" and "de-protonation" of functional groups) and the hydrophobic sites which are considered to give rise only to competitive adsorption. At low pH environment, the high proton concentration in the solution predominantly leads to the protonation of the hydrophilic sites, making the charge of membrane positive. However, at high pH environment, the low proton concentration in the solution leads to the de-protonation of these hydrophilic sites, making the membrane charge more negative. Thus, a drastic variation in absolute values as well as sign of the zeta potential can be seen under the influence of pH and accordingly membranes' surface charge density also gets changed. In general, with the increase of pH value, the surface charge density of a negatively charged membrane tends to decrease from positive to negative value, regardless of the ionic strength or any kind of impurities present in the solution.

1.5.3.2. Dependency of membranes' charge on variation of feed solutions' ionic strength

Both the concentration and the valence of ions present in the feed solution affect the surface charge of the membrane [24]. The adsorption of ions on the charged sites of the membrane, at higher concentration of ionic solutes can cause a change in the membranes' actual charge behavior, thus affecting the retention of the solute. Concentration of the ions in the solution may thus take different roles in the formation of electrical double layer. Due to these reasons, ions of multi-valence seem to be more effective in influencing the membrane charge property. The increase of the ionic strength produces a shielding effect through screening of charge, making responsible for the decrease of the membrane negative charge along the surface. The membrane charge density also depends very much on the type of solute and the solute concentration. Decrease in the zeta potential of a charged membrane by interaction with a solution of high ionic strength is regarded as the reduction of electrostatic force.

1.6. Concise description of the techniques employed for characterization of membranes

Comprehensive characterization of a membrane following different methods, as a subsequent step of membrane preparation stages is of utmost interest, which is required to be carried out in determining the physicochemical features of a given membrane acquiring the appropriate knowledge about the structural and morphological features of the membranes' polymer material. This further helps in choosing the appropriate membrane for a specific application, controlling the membrane quality and predicting the membranes' separation performance for various substances.

1.6.1. Structural characterization of charged membranes

1.6.1.1. Attenuated Total Reflectance-Fourier Transform Infrared (ATR – FTIR) spectroscopy

As a reliable technique for the characterization, identification and quantification of structural features of any polymeric system, infrared (IR) spectroscopy has always shown its' usefulness. An important advantage of this spectroscopic technique is its' ability to analyze material under a very wide range of conditions including solids, liquids and gases. The principle of FTIR relies on the fact that the most molecules absorb light in the infra-red region of the electromagnetic spectrum where the absorption corresponds specifically to the bonds present in the molecule. The background emission spectrum of the IR source is first recorded, followed by the emission spectrum of the IR source with the sample in place. The ratio of the sample spectrum to the background spectrum is directly related to the sample's absorption spectrum. The resultant absorption spectrum, originated from the bonds' natural vibrational frequencies indicates the presence of various chemical bonds and functional groups of the sample under investigation. It is particularly useful for identification of organic molecular groups and compounds due to the range of functional groups, side chains and crosslinks involved, all of which will have characteristic vibrational frequencies in the infra-red range.

The Attenuated Total Reflectance (ATR) is the most widely used FTIR sampling tool. The technique of ATR particularly has become one of the best choices to study the structure and organization of membranes' material-chemistry in different relevant conditions. The ATR mode associated with the spectrometer generally allows qualitative or quantitative analysis of samples with little or no sample preparation which enhances the speed of sample analysis. In transmission spectroscopy, the IR beam passes through the sample and the effective path length is determined by the thickness of the sample and its orientation to the directional plane of the IR beam. But the benefit of ATR sampling comes from the very thin sampling path length or depth of penetration of the IR beam into the sample. This is in contrast to traditional FTIR sampling by transmission where the sample must be diluted with IR transparent salt, pressed into a pellet or pressed to a thin film, prior to analysis to prevent totally absorbing bands in the infrared spectrum. In ATR mode of sampling, the IR beam incidents into a crystal of relatively higher refractive index (ZnSe crystal, 45^o angle of incidence and refractive index of 2.4) and reflects from the internal surface of the crystal and creates an evanescent wave which projects orthogonally into the sample in intimate contact with the ATR crystal. Some of the energy of the evanescent wave is absorbed by the sample and the reflected radiation (some now absorbed by the sample) is returned to the detector. The schematic representation of ATR phenomenon is shown below in Fig. 1. 1:

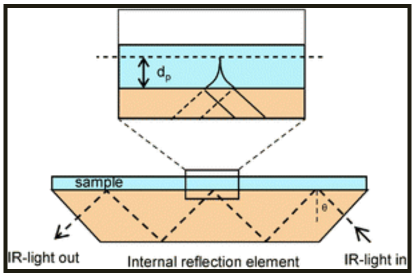

Fig. 1. 1 Schematic of ATR.

The penetration depth of the light depends on the refractive indices of the internal reflection element (n_1) and sample (n_2), wavelength (λ) and the angle of incidence (θ) according to Eq. 1:

$$d_p = \frac{\lambda}{2\pi n_1 \sqrt{\left(\sin^2\theta - \frac{n_2^2}{n_1^2}\right)}} \qquad (1)$$

From this equation, it can be seen that the penetration depth depends on the wavelength. Consequently, ATR spectra differ from transmission spectra of the same material in the sense that at higher wave numbers (*i.e.*, smaller λ) the intensity in ATR becomes smaller than in transmission mode.

Generally, most spectrometers calculate an ATR-absorbance spectrum normalizing for the penetration depth (which proportional to the wavelength) according to Eq. 2:

$$ATR = -\log\left(\frac{I_t}{I_0}\right)\frac{const.}{\lambda} \qquad (2)$$

While the analysis of samples by ATR is easy, it is interesting and useful to be aware of each of the experimental factors like refractive indices of the ATR crystal and the sample, angle of incidence of the IR beam, critical angle, depth of penetration, wavelength of the IR beam, effective path length, number of reflections and quality of the sample contact with ATR crystal characteristics, which affect the final spectrum.

1.6.1.2. Nuclear magnetic resonance (NMR) spectroscopy

A nuclear magnetic resonance spectrum results from the interaction of the observed nuclear spin with its' magnetic environment. The nuclear spin interacts with the external magnetic field (Zeeman interaction), with its' electronic environment (chemical shift, quadrupolar coupling etc) and further with the neighboring nuclei (dipolar and scalar couplings etc.). Some interactions are isotropic while others are anisotropic. Solid-state NMR (SS-NMR) spectroscopy is a kind of NMR spectroscopy, which characterizes the presence of anisotropic (directionally dependent) interactions. In general, these interactions are orientation dependent. In media with no or little mobility (*e.g.* crystals, powders, large membrane vesicles, molecular aggregates), anisotropic interactions have a substantial influence on the behavior of a system of nuclear spins. In contrast, in a classical liquid-state NMR experiment, Brownian motion leads to an averaging of anisotropic interactions. Anisotropic interactions modify the nuclear spin energy levels (and hence the resonance frequency) of all sites in a molecule, and often contribute to a line-broadening effect in NMR spectra. However, there is a range of situations when their presence can either not be avoided, or is even particularly desired, as they encode structural parameters, such as orientation information, on the molecule of interest.

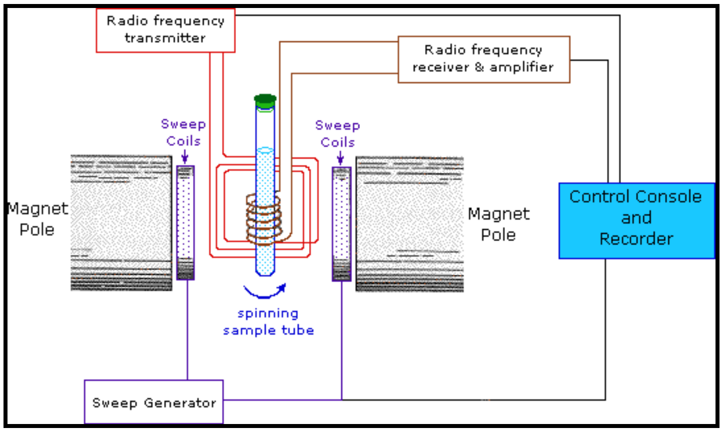

Fig. 1. 2 Schematic of NMR.

High-resolution conditions in solids can be established by reducing the effect of anisotropic interactions and increasing the signal-to-noise ratio using Magic Angle Spinning (MAS), macroscopic sample orientation, combinations of both of these techniques, enhancement of mobility by highly viscous sample conditions, and a variety of radio frequency (RF) irradiation patterns. While the latter allows decoupling of interactions in spin space, the others facilitate averaging of interactions in real space. MAS consists of placing the sample in a rotor spinning about an axis tilted at the magic angle, thereby giving all anisotropic interactions an additional time dependence. Depending on the spinning speed, non-homogeneous interactions can be partly or totally suppressed. In addition, line-broadening effects from microscopic inhomogeneities can be reduced by appropriate methods of sample preparation.

1.6.1.3. X-ray photoelectron spectroscopy

The technique of X-ray photoelectron spectroscopy (pictorially presented in Fig. 1. 3) has now become widely used for surface characterization of membranes through quantitative estimations of the elements composing the surfaces. In X-ray photoelectron spectroscopy (XPS) electrons emitted after the interaction between primary X-rays or electrons and a sample are detected. The amount of electrons having escaped from the sample without energy loss is typically measured in the range of 20 to 2000 eV. The data is represented as a graph of intensity versus electrons' binding energy. Due to the impact of the primary beam (X-ray photon, mostly from an Al-Kα or Mg-Kα primary source), the atoms in the sample are ionized and electrons are liberated from the surface, as a result of the photoemission process. XPS relies on soft X-rays as the source of primary radiation, which is necessary to provoke ionization of the atoms. In XPS low energy electrons are measured, giving rise to comparable depth and sensitivity values and only a lateral resolution of a few to 100 μm can be reached. This type of measurements is necessarily performed under high vacuum conditions. Thus, the technique of XPS cannot be considered as non-destructive technique although the analyses themselves are not destructive in nature.

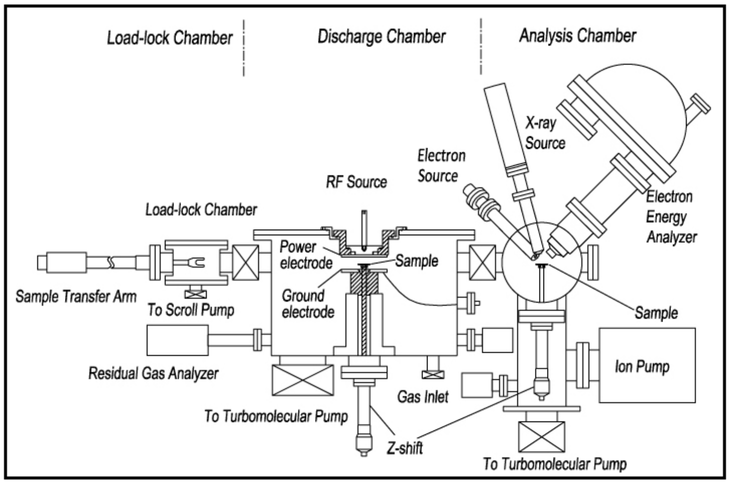

Fig. 1. 3 Schematic of XPS operation.

1.6.2. Topographical - morphological characterization of charged membranes

1.6.2.1. Atomic force microscopy

The surface topography of any membrane material has been characterized using the technique of atomic force microscopy (AFM), which can provide two as well as three-dimensional informations regarding surface features. An important advantageous outcome of AFM operation is thus the study of surface properties of membranes, the ability to quantify the surface topography and then correlation of them to membranes' performances.

The AFM can produce topographical images by scanning a microscopic tip, attached at the end of a cantilever over a surface. The cantilever is typically of silicon nitride with a tip radius of curvature on the order of nanometers. When the tip is brought into proximity of a sample surface, forces between the tip and the sample lead to a deflection of the cantilever according to Hooks law. Depending on the situation, forces that are measured in AFM include mechanical contact force, van der Waals forces, capillary forces, chemical forces, electrostatic forces, magnetic forces, solvation forces etc. If the tip is scanned at a constant height, a risk would exist that the tip collides with the surface, causing damage. Hence, in most cases a feedback mechanism is employed to adjust the tip-to-sample distance to maintain a constant force between the tip and the sample. Traditionally, the sample is mounted on a piezoelectric tube that can move the sample in the z direction for maintaining a constant force, and the x and y directions for scanning the sample. Alternatively a 'tripod' configuration of three piezo crystals may be employed, with each responsible for scanning in the x, y and z directions. This eliminates some of the distortion effects seen with a tube scanner. In newer designs, the tip is mounted on a vertical piezo scanner while the sample is being scanned in X and Y using another piezo block. The resulting map of the area $z = f(x, y)$ represents the topography of the sample. Typically, the deflection is measured using a laser spot reflected from the top surface of the cantilever into an array of photodiodes. This photodetector measures the difference in light intensities between the upper and lower photodiodes and then converts this signal into a voltage. This method enables a computer to generate a three-dimensional map of the surface topography.

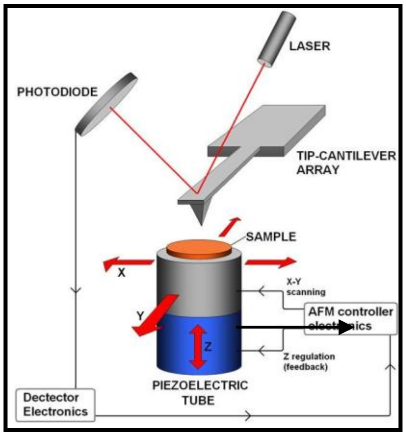

Fig. 1. 4 Schematic of AFM operation.

There are three commonly used AFM techniques: contact mode, noncontact mode and tapping mode. In **contact mode**, the tip scans the sample in close contact with the surface. This means that the inter-atomic force between the sample and the tip is repulsive, with a typical value of 10^{-7} N. Problems with contact mode are caused by excessive tracking forces applied to the sample by the probe. Therefore, contact mode AFM cannot be applied to soft surfaces, such as polymeric membranes. In situations where tip contact might alter the sample, **non-contact** *mode* is used. In this mode the tip moves about 50–150 Å above the sample surface. Attractive inter-atomic forces between the tip and the sample are detected, and topographic images are constructed by scanning the tip above the surface. The attractive forces from the sample are, however, substantially weaker (10^{-13} N) than the forces used in contact mode. Therefore, the cantilever is driven to vibrate near its’ resonant frequency by means of a piezoelectric element and changes in the resonant frequency as a result of tip–surface force interaction are measured (dynamic detection method). Problems with noncontact mode can be caused by a contaminant layer (present on the sample), which interferes with the cantilever oscillation and results in low resolution. **Tapping mode** of AFM allows high-resolution topographic imaging of sample surfaces by alternately bringing the tip into contact with the surface to provide high resolution and then lifting it off the surface to avoid dragging the tip across the surface. Tapping mode imaging is again implemented by oscillating the cantilever assembly at or near the cantilevers resonant frequency using a piezoelectric crystal. The piezo motion causes the cantilever to oscillate with a large amplitude (typically greater than 20 nm) when the tip is not in contact with the surface. The oscillating tip is then moved toward the surface until it begins to gently touch or tap the surface. During scanning, the vertically oscillating tip alternately contacts the surface and lifts off, generally at a frequency of 50,000–500,000 cycles per second. As the oscillating cantilever begins to intermittently contact the surface, the cantilever oscillation is reduced due to energy loss caused by the tip contacting the surface. The reduction in oscillation amplitude is used to identify and measure surface features.

Three dimensional surface topographic technique provides specific 3D roughness parameters, which are classified in the following categories as: *amplitude parameters* (based on overall height of the surface) like average roughness (R_a), root mean square roughness (R_q), Ten point height (R_{10z}), Skewness (R_{Sk}) and Kurtosis (R_{Ku}); *spatial parameters* (based on frequencies of occurrence of surface characteristics) like texture direction of a surface (R_{td}) and texture direction index (R_{tdi}); *hybrid parameter* (based on the combination of height of the formations and frequencies of occurrence of the surface) like surface area ratio (R_{dr}) and *functional parameters* (based on special functioning properties like bearing, sealing and lubricant retaining capabilities) like peak material volume (V_{mp}), core material volume (V_{mc}), core void volume (V_{vc}), valley void volume (V_{vv}), surface bearing index (R_{bi}), core fluid retention index, (R_{ci}) and valley fluid retention index (R_{vi}). A brief theoretical overview of the various amplitude parameters, extracted from the 2D and 3D topographic image analysis, are the major indicators in characterizing the surface topography by implying the amplitude related properties of a surface. These are used to measure the vertical characteristics of the membranes’ surface by computing the surface deviations from the mean plane. The topographic image extracted through AFM corresponds to a measured height value, *z(x,y)* for a given surface area, A, in a surface plane, x-y. Each height value is allied to a pair of surface coordinates, (x,y), and the image is depicted by a matrix with *N* number of rows and *M* number of columns which corresponds to the surface (x,y) points being the matrix elements the height *z(x,y)*.

The average roughness (R_a) parameter represents the average absolute deviation of the roughness from the mean plane, the plane for which the volumes enclosed by the image above and below are equal and is represented by the mathematical expression of Eq. 3:

$$R_a(N,M) = \frac{1}{NM}\sum_{x=1}^{N}\sum_{y=1}^{M}\left(z(x,y) - \bar{z}(N,M)\right) \qquad (3)$$

The root mean square (rms) roughness (R_q) represents the standard deviation of the distribution of surface heights within a given area and is more sensitive statistically than the average roughness values to describe the variation of a membranes’ surface roughness. This is mathematically represented as Eq. 4:

$$R_q(N,M) = \sqrt{\frac{1}{NM}\sum_{x=1}^{N}\sum_{y=1}^{M}\left(z(x,y) - \bar{z}(N,M)\right)^2} \qquad (4)$$

The ten point height (R_{10Z}), defined by ISO system as difference in height between the average of the five highest peaks and the five lowest valleys relative to the mean plane is mathematically represented as Eq. 5:

$$R_{10z}(ISO) = \frac{1}{n}\left(\sum_{i=1}^{n} p_i - \sum_{i=1}^{n} v_i\right) \qquad (5)$$

Where p_i and v_i represent the height of the ith peak and depth of the ith valley respectively. n is the number of samples along the assessment length.

Statistically skewness is defined as a measure of the asymmetry of the probability distribution of a real valued random variable [27]. It is related to the third moment of a distribution. The skewness of a surface, R_{Sk}, used to measure the symmetry of the profile about the mean plane, is sensitive and responsive to the occasional presence of deep valleys or high peaks in the surface profile. A symmetrical height distribution, *i.e.*, with as many peaks as valleys, provides a surface with zero skewness whereas surface profile with peaks removed or deep valleys provides surface with negative skewness and that with valleys filled in or with high peaks endows a surface with positive skewness. The evaluation of R_{Sk} for membranes becomes important when two membrane surface profiles with same R_a or R_q are distinguished based on variation of shapes. The mathematical description of surface skewness of a profile is given by Eq. 6:

$$R_{Sk} = \frac{1}{NR_q^3}\sum_{i=1}^{N}\left(Z_i - \overline{Z}\right)^3 \qquad (6)$$

The statistical definition of Kurtosis gives a measure of the shape of the probability distribution of a real valued random variable. It is closely related to the fourth moment of a distribution. Kurtosis coefficient, R_{Ku} of a surface topographic analysis describes the sharpness of the probability density of a surface profile. It characterizes the relative peakedness or flatness of a distribution compared to the normal distribution. A positive R_{Ku} indicates a relatively peaked distribution and a negative R_{Ku} indicates a relatively flat distribution. If $R_{Ku} > 3$, the distribution curve is said to be leptokurtic distribution which is sharper than a normal distribution, with values concentrated around the mean with the occasional high peak or deep valley. This means high probability for extreme values. If, $R_{Ku} < 3$, the distribution curve is said to be platykurtic distribution which is flatter than a normal distribution with a wider distribution of peaks. In such case, the probability for extreme values is less than for a normal distribution, and the values are wider spread around the mean. If R_{Ku} = 3, the distribution curve is of Gaussian type and said to be mesokurtic distribution. The mathematical description for coefficient of kurtosis of a profile is given by Eq. 7:

$$R_{Ku} = \frac{1}{NR_q^4} \sum_{i=1}^{N} \left(Z_i - \overline{Z} \right)^4 \tag{7}$$

1.6.2.2. Scanning electron microscopy

A scanning electron microscope (SEM) is a type of electron microscope that can acquire images of a sample by scanning it with a high-energy beam of electrons in a raster scan pattern. The electrons interact with the atoms that make up the sample producing signals that contain information about the sample's surface topography, composition, and other properties such as electrical conductivity.

The types of signals produced by an SEM include secondary electrons, back-scattered electrons (BSE), characteristic X-rays, light (cathodoluminescence), specimen current and transmitted electrons, shown below pictorially in Fig. 1. 5 & 1.6.

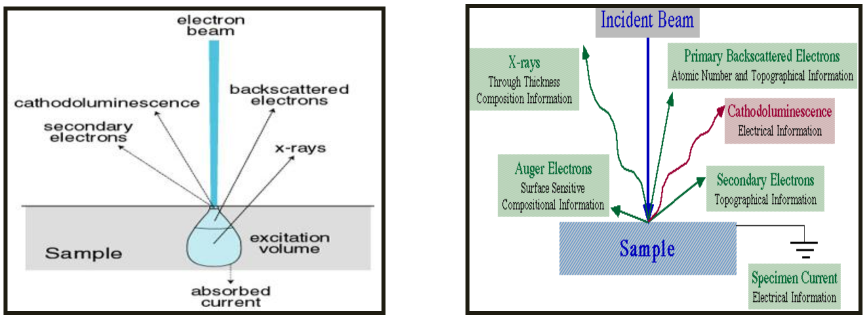

Fig. 1. 5 & 1. 6 Schematic diagram of electronic interaction with sample and generation of signals.

Secondary electron detectors are common in all SEMs, but it is rare that a single machine would have detectors for all possible signals. The signals result from interactions of the electron beam with atoms at or near the surface of the sample. In the most common or standard detection mode, secondary electron imaging or SEI, the SEM can produce very high-resolution images of a sample surface, revealing details less than 1 nm in size. Due to the very narrow electron beam, SEM micrographs have a large depth of field yielding a characteristic three-dimensional appearance useful for understanding the surface structure of a sample. A wide range of magnifications is possible, from about 10 times (about equivalent to that of a powerful hand-lens) to more than 500,000 times, about 250 times the magnification limit of the best light microscopes. Back-scattered electrons (BSE) are beam electrons that are reflected from the sample by elastic scattering. BSE are often used in analytical SEM along with the spectra made from the characteristic X-rays. Since the intensity of the BSE signal is strongly related to the atomic number (Z) of the specimen, BSE images can provide information about the distribution of different elements in the sample. For the same reason, BSE imaging can image colloidal gold immuno-labels of 5 or 10 nm diameter which would otherwise be difficult or impossible to detect in secondary electron images in biological specimens. Characteristic X-rays are emitted when the electron beam removes an inner shell electron from the sample, causing a higher energy electron to fill the shell and release energy. These characteristic X-rays are used to identify the composition and measure the abundance of elements in the sample.

In a typical SEM, an electron beam is thermionically emitted from an electron gun having energy ranging from 0.5 keV to 40 keV and fitted with a tungsten filament cathode. Tungsten is normally used in thermionic electron guns because it has the highest melting point and lowest vapor pressure of all metals, thereby allowing it to be heated for electron emission, and because of its low cost. Other types of electron emitters include lanthanum hexaboride (LaB_6) cathodes, which can be used in a standard tungsten filament SEM if the vacuum system is upgraded and field emission guns (FEG), which may be of the cold-cathode type using tungsten single crystal emitters or the thermally-assisted Schottky type, using emitters of zirconium oxide.

The electron beam is typically focused by one or two condenser lenses (as shown in Fig. 1. 7) to a spot about 0.4 nm to 5 nm in diameter. The beam passes through pairs of scanning coils or pairs of deflector plates in the electron column, typically in the final lens, which deflect the beam in the *x* and *y* axes so that it scans in a raster fashion over a rectangular area of the sample surface.

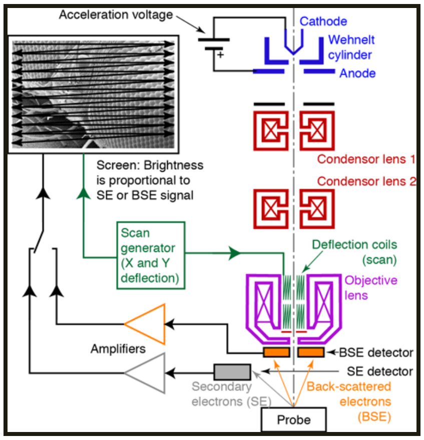

Fig. 1. 7 Schematic diagram of SEM.

When the primary electron beam interacts with the sample, the electrons lose energy by repeated random scattering and absorption within a teardrop-shaped volume of the specimen known as the interaction volume, which extends from less than 100 nm to around 5 µm into the surface. The size of the interaction volume depends on the electron's landing energy, the atomic number of the specimen and the specimen's density. The energy exchange between the electron beam and the sample results in the reflection of high-energy electrons by elastic scattering, emission of secondary electrons by inelastic scattering and the emission of electromagnetic radiation, each of which can be detected by specialized detectors. The beam current absorbed by the specimen can also be detected and used to create images of the distribution of specimen current. Electronic amplifiers of various types are used to amplify the signals which are displayed as variations in brightness on a cathode ray tube. The raster scanning of the CRT display is synchronized with that of the beam on the specimen in the microscope, and the resulting image is therefore a distribution map of the intensity of the signal being emitted from the scanned area of the specimen. The image may be captured by photography from a high resolution cathode ray tube, but in modern machines is digitally captured and displayed on a computer monitor and saved to a computer's hard disk.

1.6.2.3. Elemental analysis of membrane surfaces – Energy Dispersive X-ray

The technique of EDX makes use of the X-ray spectrum which is emitted by a solid sample after bombardment with a focused beam of electrons to obtain a localized chemical analysis. All elements from atomic number 4 (Be) to 92 (U) can be detected in principle, though not all instruments are equipped for 'light' elements ($Z < 10$). Qualitative analysis involves the identification of the characteristic lines appeared in the spectrum and is fairly straightforward owing to the simplicity of X-ray spectra. Quantitative analysis (determination of the concentrations of the elements present in the sample) entails measuring line intensities for each element in the sample and for the same elements in calibration standards of known composition. By scanning the beam in a television-like raster and displaying the intensity of a selected X-ray line, element distribution images or 'maps' can also be produced. Also, images produced by electrons collected from the sample reveal surface topography or mean atomic number differences according to the mode selected. The SEM which is closely related to the electron probe, is designed primarily for producing electron images, but can also be used for element mapping, and even point analysis, if an X-ray spectrometer is added. Thus, quantitative surface elemental analysis and mapping have been performed by an energy dispersive X-ray spectrometer (EDX) coupled to the SEM and a micro analysis system (INCA Oxford Instruments, UK), employing a certain accelerating voltage at specific magnification, where the instrument is equipped with an ultrathin beryllium window and 20 mm^2 Si detector.

1.6.3. Evaluation of surface charge properties of membranes

The electrokinetic features of the membranes have been evaluated by streaming potential analysis, employing ZetaCAD electrokinetic analyzer (CAD Inst., France). The streaming potential analyzer consisted of a quartz-cell configuration (Fig. 1. 8) is capable of holding two flat sheet membranes in such a way that the membranes are remained separated by spacers and the skin layers are faced each other creating a slit channel for tangential flow of electrolytic solution across the membranes.

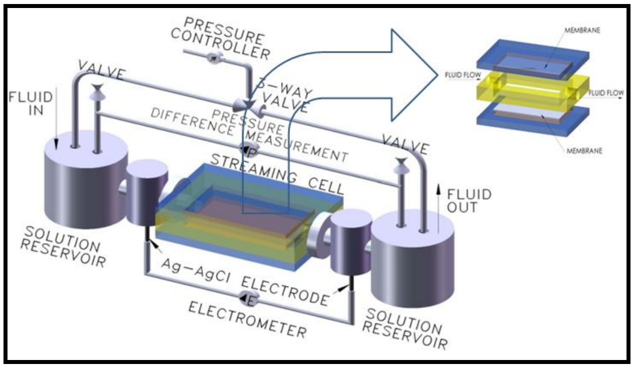

Fig. 1. 8 Schematic diagram of streaming potential analyzer set-up.

The electrical potential difference, generated due to the bidirectional flow of electrolyte (KCl) solution under pressure gradient across the membrane was measured by Ag/AgCl electrodes, equipped with the cell. Zeta potentials of the membranes under varying pH environments, ranging from pH 3 to 11 were evaluated utilizing the streaming potential values and the relationship between the measurable streaming potential (V_{st}) and the zeta potential (ζ), which is expressed by the Helmholtz-Smoluchowski equation (Eq. 8).

$$\mathrm{V_{st}} = \frac{\varepsilon}{\lambda\eta}\zeta \tag{8}$$

Where, ε is the dielectric constant ($\varepsilon = \varepsilon_0\varepsilon_r$, being ε_r the relative dielectric constant and ε_0 the vacuum permittivity), η and λ are the viscosity and conductivity of the electrolyte medium. An average value of zeta potential from three replicates was reported and the measurement error was found to be ± 0.5 mV.

The values of ζ of the membranes as determined with respect to the variation of pH can further be employed to calculate electrokinetic surface charge densities (σ_s) at the shear planes of the membranes as a function of the respective pH environments [28], using Eq. 9.

$$\sigma_s = \frac{\varepsilon\zeta}{\lambda_{Deb}} \tag{9}$$

The Debye-length (λ_{Deb}) was derived according to the Eq. 10.

$$\lambda_{Deb} = \sqrt{\frac{\varepsilon RT}{2F^2 I}} \tag{10}$$

Where, R, T and F denote the gas constant, absolute temperature and Faraday constant, respectively; and I represents the ionic strength of the electrolyte medium, calculated from the molar concentration (C_i in M) of the ith ion of the electrolyte and the charge number (z_i) of that ion, expressed in Eq. 11 as:

$$I = \sum_i Z_i^2 C_i \tag{11}$$

For electrokinetic measurements under varying pH environments, HCl and NaOH are used to adjust the pH values which led to presence of excess of similar counter-ions (Cl^-) at acidic pH and additional dissimilar counter-ion (OH^-) at alkaline pH, respectively.

The ion exchange capacities (IEC) of charged (negatively charged) membranes have been determined by placing the membranes in 0.1N HCl for 24 hr to convert all the negatively charged sites in H^+ form, and then after several wash with water to remove the traces of HCl from the membrane's surface. Thereafter, the membranes are cut in small pieces, placed in 500 ml flask having 200 ml of 0.1N NaOH solution. The samples are left in the solution for another 24 hrs. After that 5 ml of the aliquot is pipetted and titrated against standard HCl (0.1N).

$$\text{Memb.}^{-}\,\text{Na}^{+} + \text{H}^{+} \rightarrow \text{Memb.}^{-}\,\text{H}^{+} + \text{Na}^{+}$$

$$\text{Memb.}^{-}\,\text{H}^{+} + \text{Na}^{+}\,\text{OH}^{-} \rightarrow \text{Memb.}^{-}\,\text{Na}^{+} + \text{H}_2\text{O}$$

The ion exchange capacity is estimated from Eq. 12

$$\text{IEC} = (N_{NaOH}\,.\,V_{NaOH}) - (40.\,N_{HCl}.\,V_{HCl}) / m_{dry} \qquad (12)$$

Where, V_{NaOH} & N_{NaOH} are the volume & normality of NaOH taken initially for exchange with the membrane; N_{HCl} & V_{HCl} are the volume & normality of HCl consumed by the aliquot NaOH after the exchange process. m_{dry} is the mass of the dry membrane.

1.6.4. Determination of hydrophilic behaviors of charged membranes - contact angle measurements

In surface science, an instrument generally called a Contact Angle Goniometer or Drop Shape Analyzer is used to measure the static contact angle and surface tension of a solid surface with respect to polar or non-polar solvents. Static contact angle measurement has been conducted using sessile drop method at ambient temperature. A contact angle measuring instrument (DSA 100 of KRUSS Gmbh, Germany) with DSA 1 v 1.92 software uses cameras and software to capture and analyze the drop shape. The contact angle (θ) is defined as the angle formed by a liquid at the three phase boundary where the liquid, vapor and solid intersect. The contact angle depends on the interfacial tensions between the vapor & liquid, liquid & solid and vapor & solid, shown below in the Fig. 1. 9

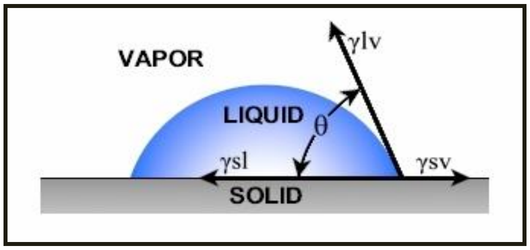

Fig. 1. 9 Contact angle of a liquid sample on a solid surface.

Another perspective that describes contact angles uses cohesion vs. adhesion. Cohesion is the force between the liquid molecules which hold the liquid together. Adhesion is the force between the liquid molecules and the solid molecules. The contact angle is a quantitative measure that tells the user the ratio of cohesion vs. adhesion. If the contact angle is near zero, meaning the liquid droplet spreads completely on the solid surface, adhesive forces are dominating. If the contact angle is very high, meaning the liquid droplet bead up on the solid surface as water does on a freshly waxed car, cohesive forces are dominating. Higher is the contact angle of a surface lower will be the tendency of that surface to get wet which means the surface is hydrophobic in nature. Similarly lower contact angle value reflects the hydrophilic nature of the surface.

Since in equilibrium the chemical potential of the three phases should be equal so if the solid–vapor interfacial energy (*i.e.*, surface free energy) is denoted as γ_{sv}, the solid–liquid interfacial energy as γ_{sl} and the liquid–vapor interfacial energy (*i.e.*, surface tension) as γ_{lv}, then an equation that must be satisfied in equilibrium is known as Youngs equation which is given by Eq. 13

$$\gamma_{sv} - \gamma_{sl} - \gamma_{lv} \cos\theta_c = 0 \qquad (13)$$

Where, θ_c is the equilibrium contact angle.

The image (Fig. 1. 10) shows how the wettability of surface varies with change in contact angle.

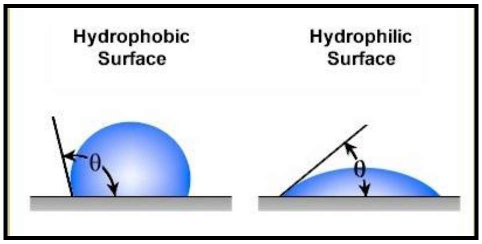

Fig. 1. 10 Pictorial representation of wettability of a surface with change in contact angle.

While static contact angles give static information about the interfacial tensions between the solid, liquid and gas, advancing and receding contact angles give some information about the dynamic interaction of the liquid, solid and gas. An advancing contact angle is determined by pushing a droplet out of a pipette onto a solid. When the liquid initially meets the solid it will form some contact angle. As the pipette injects more liquid through the pipette, the droplet will increase in volume, the contact angle will increase, but its three phase boundary will remain stationary until it suddenly jumps outward. The contact angle the droplet had immediately before jumping outward is termed the advancing contact angle. The receding contact angle is however measured by sucking the liquid back out of the droplet. The droplet will decrease in volume, the contact angle will decrease, but its three phase boundary will remain stationary until it suddenly jumps inward. The contact angle the droplet had immediately before jumping inward is termed the receding contact angle.

The following schematic diagram (Fig. 1. 11) gives an impression about the difference in behavior between the advancing and receding contact angle measurements:

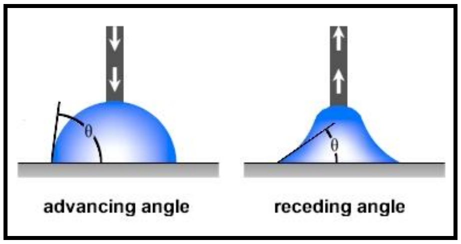

Fig. 1. 11 Pictorial representation of advancing and receding contact angle measurements.

The difference between advancing and receding contact angles is termed contact angle hysteresis which can be used to characterize surface heterogeneity, roughness, and mobility.

The contact angle is also employed to assess the hydrophilicity and surface free energy (SFE) with its polar and dispersive components of the active skin layers of the membranes. For this purpose, three different solvents (water, ethylene glycol and diiodomethane) with known surface tension values (γ_s, γ_s^p and γ_s^d, Table 1. 2) have been employed.

Table 1. 2

Polar (γ_s^p) and dispersive (γ_s^d) components of the surface tension (γ_s) values (subscript s stands for solvent; superscript p and d refer to the polar and dispersive components, respectively) of the probe solvents: water, ethylene glycol and diiodomethane [20].

Solvent	γ_s (mN/m)	γ_s^p (mN/m)	γ_s^d (mN/m)
Water	72.8	51.0	21.8
Ethylene glycol	48.0	19.0	29.0
Diiodomethane	50.8	–	50.8

Fowkes method [29] is applied to calculate the SFE along with the polar and dispersive components of the membranes’ surfaces from the surface tension values of the probe solvents and contact angle values of the membranes with respect to those solvents. Wetting envelopes are also constructed for the membranes’ surfaces by reversing the method applied to determine the polar and dispersive part of SFE. The closed contour or envelope, with coordinate system made from polar and dispersive part of the SFE defines the line where the condition of contact angle 0^o ($\cos \theta = 1$) is satisfied.

1.6.5. Performance evaluation of membranes

1.6.5.1. Evaluation of characteristic features of base membrane

For measurement of porosity of the base membrane, gravimetric method has been applied. There, a circular piece of the Psf membrane with an area -A and thickness -h is weighed after taking it out from storage of distilled water and then carefully removing the superficial water with filter paper. The wet membrane is dried in a vacuum oven at 75 ^{o}C for 24 h before measuring the weight in dry state. From the weights of the membrane sample in wet (W_0) and dry (W_1) states, the porosity (ø) of membrane is calculated using Eq. 14 as:

$$\phi(\%) = \frac{W_0 - W_1}{\rho_w A h} \times 100 \tag{14}$$

Where, ρ_w is density of pure water at room temperature. In order to minimize the experimental error, measurements are carried out in duplicates and then calculated the average.

Pure water flux measurement of the base membrane with effective membrane area of 14.4 cm^2 is conducted under a cross-flow filtration mode operated at 1 bar transmembrane pressure. The steady-state pure water flux (PWF, L.m^{-2}day^{-1} or LMD) is determined by direct measurement of the permeate flow *i.e.*, volume (V, in L) collected during a time period (T, in day) through a membrane area (A, in m^2) at certain pressure. Prior to the UF test experiment, membrane is initially subjected to undergo hydraulic compaction for 1 hr in water at standard UF test conditions, to achieve stabilized performance of the membrane.

Utilizing the porosity of the membrane, mean pore size (r_m in nm) is determined by employing the Guerout–Elford–Ferry equation [30] as:

$$r_m = \sqrt{\frac{(2.9 - 1.75\phi) \times 8\eta h v}{\phi \times A \times \Delta P}} \tag{15}$$

where, ø (%) and h (m) denote the porosity and thickness of the membrane. The viscosity of water (8.9×10^{-4} Pa s) is represented as η. The volume of water permeated per unit time (v in m^3.s^{-1}) is considered to pass through an effective membrane area of A (m^2), under 1 bar transmembrane pressure (ΔP).

For measurement of MWCO of the base membrane, analysis of solute rejection behavior is carried out using neutral organic solutes such as PEG with average Mw of 12k, 20k, 35k Da and PEO with average Mw of 100k Da. The test solutions are prepared by dissolving pre-weighed amounts of PEG or PEO in ultra-pure water at a concentration of 200 ppm. The solute rejection studies are carried out at a transmembrane pressure of 1 bar at room temperature. The concentration of PEG or PEO in both feed and product were measured by analysing the total organic carbon (TOC) content of the samples using TOC analyzer (ANATOC-II, SGE analytical science, Australia). The MWCO is determined from a plot of solute rejection *vs* molecular weight, generated in order to construct a MWCO curve, which implies a molecular weight of the organic solute that is 90% retained by the Psf base membrane.

Measurement of mechanical stability of the base membranes are carried out with a universal tensile testing machine (Hemetek Techno Instrument, model LRX Plus, India), at 25 °C with a relative humidity of 40-50%. A constant deformation rate of 100 mm/min is controlled during the analysis. For analysis, dumb-bell shaped specimens of the membrane samples with length of 4 cm and width of 0.6 cm are employed. Tensile strength (TS) and percent elongation at break (EB) are calculated for the membranes in duplicates, using the NEXYGEN plus software.

1.6.5.2. Nanofiltration performance evaluation of charged membranes

The evaluation of transport properties of the membranes has been conducted using a cross-flow test cell (Fig. 1. 12), at 10 – 15 bar of transmembrane pressure. Circular membrane samples, with an effective membrane area of 14.4 cm^2 are properly washed in de-ionized water and then placed in the test cell with the membranes' active skin layers facing the incoming feed solution. To maintain a steady feed concentration, the experiments are carried out in recycle mode *i.e.*, both the concentrate and the permeate streams are recirculated into the feed tank. Iso-osmotic feed solutions comprising of varying combination of mono- and bi-valent cations and anions, such as 0.03M NaCl, 0.02M Na_2SO_4, 0.02M $CaCl_2$ or $MgCl_2$ and 0.03M $MgSO_4$ are employed for performance evaluation of membranes. The feed solution temperature is maintained at 25-30 ^oC. Prior to the start of data accumulation, steady-state conditions are achieved for all the NF test experiments when the membranes are allowed to get stabilized by operating for long-run. The solute concentrations in the feed and permeate solutions are obtained through the measurement of conductivities of the respective solutions using a digital conductivity meter (TESTRONIX 15, Microlab, Mumbai, India). All membrane samples are prepared and tested in duplicate for NF performances, results of which have been averaged. The steady-state readings of all the cases are recorded and reported.

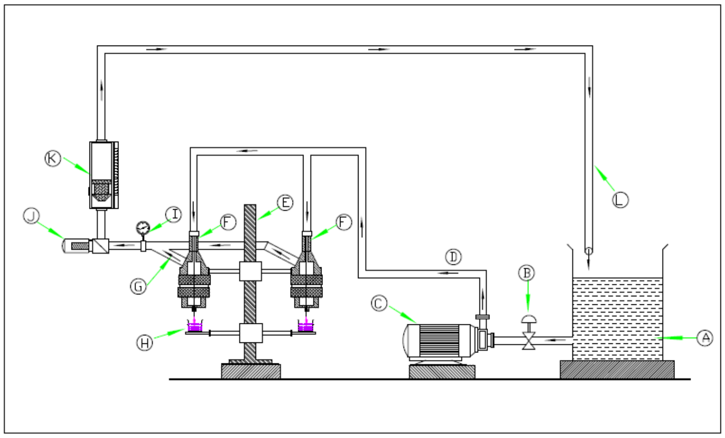

Fig. 1. 12 Schematic description of NF performance testing equipment.

(A) Feed tank, (B) Valve, (C) diaphragm pump, (D) Feed line, (E) Stand with clamps, (F) Test cell, (G) Permeate line, (H) Permeate collector, (I) Pressure gauge, (J) Pressure relief valve, (K) Rota meter and (L) Reject line.

The percentage of solute rejection (SR) is determined by conductivity measurement of the respective solutions and calculated as:

$$SR(\%) = \frac{C_F - C_P}{C_F} \times 100 \tag{16}$$

Where C_P and C_F are the solute concentrations in permeate and feed solutions, respectively.

The steady-state solvent flux (J_W), expressed in terms of L.m^{-2}day^{-1} (LMD) is determined by direct measurement of the permeate flow *i.e.*, volume (V, in L) collected during a time period, (T, in day) through a membrane area, (A, in m^2) at certain pressure using the following Eq. 17 as

$$J_W = \frac{V}{AT} \tag{17}$$

CHAPTER – 2

Structure - topography - morphology - performance relationship of non-crosslinked and crosslinked co-polyamide based negatively charged TFC NF membranes

CHAPTER – 2

2. 1. Introduction

Despite the ever rising demands of NF membranes, the predominant types of these membranes are polymeric in nature because of their easy tunability, wide ranging options available as membrane materials and possibility of easy scale up. Reasonably, developments of charged polymeric membranes for nanofiltration applications have become one of the major areas for research work nowadays. The NF membranes with fixed charged groups exhibit advantages towards applications related to fractional separations of mixed solutes [1]. Unlike the neutral NF membranes which, in general, allow the passage of smaller monovalent ions and retain the larger multivalent ones, the charged NF membranes, comprising either positive or negative charge bearing groups, influence the separation behaviors of the membranes by preferentially rejecting certain components and passing some other depending on the interactions between charges of the membranes and charges of the solutes under considerations. The inclusion of charges in the membranes have been carried out by adopting various methods, where some of the common routes include, grafting of polymers to introduce charge and making membranes using them by phase separation technique [4], modification of preformed membranes by radiation grafting [5], coating of charged polymer layer over another substrate [6], applying multilayer polyelectrolytes (alternative layers of oppositely charged polyelectrolytes) over an existing substrate membrane [7], coating or filling of charged gels in the porous structure of the membrane [8] etc. The TFC class of membranes with very thin active layers, being capable of discriminating varying ionic constituents with concurrent high solute rejections and high fluxes as well, is thus more preferable as charged membranes for nanofiltration applications. Some of the challenges involved in preparation of such class of membranes include the successful introduction of charge in the membranes during the *in situ* polymerization process of manufacture, thereby eliminating any post fabrication modification step, easy tunability of membrane properties, etc. For this, several interlinking factors influencing the membranes' formation and performances need to be understood in depth for their optimizations during membrane fabrication processes. In a typical fabrication process of TFC membrane, factors like monomeric combinations and compositions, reaction conditions during *in situ* interfacial polymerization, curing conditions like the curing process, its' extent and duration etc. are considerably important parameters, since each of these parameters tune the physicochemical features of the membranes significantly. An in depth understanding of their effects, thus leads to the development of membranes with optimum performances.

In the present study, we descript an investigative correlation between the structural aspects of two different classes of co-polyamides with non-crosslinked and crosslinked molecular architectures, functioning as selective barriers of the negatively charged TFC NF membranes and the changes in membranes' skin layer morphologies as well as surface topographies with variation in curing conditions during optimization of the membrane preparative conditions. Their resultant effects on the nanofiltration performances have also been analyzed to correlate the variations in physicochemical characteristics on the separation features of the membranes.

2. 2. Experimental

2.2.1. Materials and methods

High purity (> 99%) monomers *i.e.*, piperazine (PIP), 2, 4 - diamino benzene sulfonic acid (DABSA), trimesoyl chloride (TMC) and terephthaloyl chloride (TPC) were procured from Sigma-Aldrich. The monomer, TPC was purified by double recrystallization using n-hexane as a solvent, followed by drying at 60 ^{o}C under vacuum. Other monomers were used without further purification. Polysulfone (Psf; M_W: 30k Da) from Solvay Speciality Polymers (India), N-methyl-2-pyrrolidone (NMP; purity: ≥ 99 %) from Sigma-Aldrich and polyvinyl pyrrolidone (PVP, K-30; M_W: 40k Da) from SRL (India) were employed to prepare Psf base membrane. The nonwoven porous polyester fabric used as a support material for preparation of the base membrane had a density of 75 g/m^2 and a thickness of 110 μm with an air permeability of 70 dm^3/m^2 at 2 mbar. Analytical grade n-hexane, NaCl, Na_2SO_4, $CaCl_2$ and $MgSO_4$ were procured from different companies in India. The conductivity of mili-Q ultra-pure water used in the experiments was below 2μS/cm.

2.2.2. Fabrication of thin film composite negatively charged nanofiltration membranes

2.2.2.1. Preparation of Psf base membrane by nonsolvent induced phase inversion method

Asymmetric flat sheet type porous Psf base membrane was prepared by nonsolvent induced phase inversion method following few consecutive steps. A casting solution comprising of 30 (w/v)% Psf in NMP and PVP (40 w/w% of Psf) as pore-forming additive, was prepared in a hermetically sealed glass-bottle through vigorous agitation for several hours accomplishing complete dissolution of Psf and PVP in the solvent. The resultant viscous solution was kept overnight in an environmentally controlled atmosphere maintaining the temperature and relative humidity at 25 ^oC and 35-40%, respectively and then undergone vacuum degassing to eliminate the trapped air bubbles from the solution. The resultant homogeneous polymer solution was cast on a nonwoven polyester support fabric maintaining a uniform thickness of 100 µm, using an automated casting machine. The cast film was immediately immersed in a precipitation bath containing ultra-pure water as nonsolvent. To ensure complete removal of the additive as well as solvent from the membrane matrix, through exchange between solvent and nonsolvent, the resulting membrane was taken out of water bath and adequately rinsed in fresh water several times. The entire process of casting was carried out in a controlled atmospheric condition by maintaining the temperature of the surrounding atmosphere at 24(±1) ^{o}C with a relative humidity of 30–35%.

2.2.2.2. Preparation of TFC NF membranes by in situ interfacial polymerization technique

The TFC type negatively charged NF membranes were prepared by *in situ* interfacial polymerization technique, under varying conditions. The Psf base membranes were soaked in an aqueous amine solution of 5 (w/v)%, comprising of mixture of monomeric diamines *i.e.*, DABSA and PIP (1:4) ratio for 4 min. They were then removed from the aqueous amine bath and the excess solutions sticking to its surface was gently wiped off by keeping it sandwiched between two polyethylene sheets and then passing through a pair of rubber rollers. The amine soaked Psf base membranes were then dipped in the reaction bath containing certain concentration of the reactive acyl chloride monomers *i.e.*, either di-functional acid chloride (TPC, 0.5 (w/v)%) or tri-functional acid chloride (TMC, 0.1(w/v)%) in n-hexane medium, for varying periods, allowing the polycondensation reactions to take place at the interface of two immiscible liquids with subsequent formations of nascent thin films on the surfaces of the Psf base membranes. The nascent thin film-coated base membranes were further subjected to undergo heat curing at varying elevated temperatures and durations, in a temperature controlled oven having accuracy of ±0.2 ^{o}C, to tune its stabilities, physicochemical properties and performances. The as treated membranes were then taken out of the oven, allowed to stand at ambient temperature and then stored in de-mineralized water for all unreacted materials to leach out.

For the structural characterization through solid state ^{13}C NMR, pure polymers were also synthesized by the technique of interfacial polymerization at room temperature using the following procedure. To a 50 ml solution of the aqueous amine taken in a beaker, n-hexane based acid chloride solutions were slowly poured and then gently stirred. The polymers were formed instantly, in the interfacial regions of the two immiscible liquids *i.e.*, water and n-hexane. The polymers were then filtered and washed with n-hexane, methanol and water to remove the solvents and unreacted monomers and finally dried under vacuum at 100 ^{o}C for 6 h.

2.2.3. Physicochemical characterizations of the membranes

2.2.3.1. Spectral features of skin layers of TFC-NF membranes

The Bruker Vertex 70 FTIR spectrometer equipped with an ATR (Attenuated Total Reflectance) accessory (ZnSe crystal, 45^{o} angle of incidence and refractive index of 2.4) was employed for ATR-FTIR analysis of skin layers of the two different classes of membranes to investigate the presence of functional groups on their skin surfaces. The membranes' skin surfaces were kept faced down onto the ATR crystal element and a light pressure was applied using a MIRacle high pressure clamp with torque-limited press. The radiation penetration depth was 2 µm. All infrared spectra were recorded in absorbance mode over a wave number range 600-4000 cm^{-1} at 25 ^{o}C. For evaluation, 200 scans were taken with a spectral resolution of 2 cm^{-1}.

Solid state ^{13}C NMR analyses of the pure polymers were performed at ambient temperature using a Bruker av 500 FT-NMR spectrometer at 500MHz. The NMR spectra were obtained using the technique of Cross Polarization (CP) with Magic Angle Spinning (MAS) and Dipolar Decoupling (DD).

2.2.3.2. Investigation of skin layers' morphology of TFC NF membranes by SEM

For evaluation of the variations in skin layers' morphology of the TFC NF membranes with change of curing duration, cross-sectional as well as skin surface SEI images of the membranes were acquired using a SEM instrument (CamScan MAKE – CS3200LV, UK). For cross-sectional imaging purposes, the membranes (without support fabric) were fractured in liquid nitrogen before coating with the conducting layers. For both the cases, in the course of making the membranes electrically conductive, all the membrane samples were cut into 2 mm × 2 mm strips and then fixed with carbon tape on brass holders. A conducting layer of Au/Pd (60:40) alloy was coated on each of the skin surfaces and cross-sectional layers of the membranes using a sputter coater, Quorum (Q150R ES) under optimized coating conditions (sputtering time: 60 s, sputter current: 30 mA and tooling factor: 2.3). The cross-sectional SEI images of the membranes were recorded under high vacuum at 10 kV and 15 kV of operating voltages, with 700X and 6000X magnifications, respectively. The SEI images for skin surfaces of the two different classes of the membranes were taken at 5000X and 8000X magnifications, under operating voltage of 15 kV.

2.2.3.3. Analysis of skin surface topography of TFC NF membranes by AFM

The variations in skin surface topographies of the membranes with change in curing temperatures were assessed by an AFM instrument (NT-MDT SOLVER next, Russia). A small piece of each of the membranes was fixed on to a metallic platform and 20μm × 20μm area of the surface of the membrane was scanned at a rate of 0.1 Hz in semi contact mode to get the required analysis done. The scanned regions were flattened using a second order polynomial to remove any curvatures and slopes from the images and then the resulting best fits were subtracted from the images. For image acquisition and evaluation of surface roughness parameters (average roughness, R_a and root mean square roughness, R_q) of the membranes NOVA-P9 software was used. For comparing the surface roughness parameters of different membrane samples, the same scan size range was used since the roughness is dependent on the spatial wavelength of the scan area *i.e.*, both lower and higher frequencies of the scan area.

2.2.4. Nanofiltration performance evaluation of TFC NF membranes

The evaluation of transport properties of the investigating TFC NF membranes was conducted using a cross-flow test cell, at 15 bar of transmembrane pressure. Circular membrane samples, with an effective membrane area of 14.4 cm^2 were properly washed in de-ionized water and then placed in the test cell with the membranes' active skin layers facing the incoming feed solution. To maintain a steady feed concentration, the experiments were carried out in recycle mode *i.e.*, both the concentrate and the permeate streams were recirculated into the feed tank. Iso-osmotic feed solutions comprising of varying combination of mono- and bi-valent cations and anions, such as 0.03M NaCl, 0.02M Na_2SO_4, 0.02M $CaCl_2$ and 0.03M $MgSO_4$ were employed for performance evaluation of the membranes. The feed solution temperature was maintained at 25-30 ^oC. Prior to the start of data accumulation, steady-state conditions were achieved for all the NF test experiments when the membranes were allowed to get stabilized by operating for long-run. The solute concentrations in the feed and permeate solutions were obtained through the measurement of conductivities of the respective solutions using a digital conductivity meter (TESTRONIX 15, Microlab, Mumbai, India). All membrane samples were prepared and tested in duplicate for NF performances, results of which have been averaged. The steady-state readings of all the cases were recorded and reported.

The percentage of solute rejection (SR) was determined by conductivity measurement of the respective solutions. The steady-state solvent flux (J_W), expressed in terms of $L.m^{-2}day^{-1}$ (LMD) was determined by direct measurement of the permeate flow *i.e.*, volume (V, in L) collected during a time period, (T, in day) through a membrane area, (A, in m^2) at certain pressure.

2. 3. Results and discussions

2.3.1. Structural characterizations of non-crosslinked and crosslinked co-polyamide based TFC NF membranes

The characteristic IR bands of skin layers of the TFC NF membranes, comprising of non-crosslinked and crosslinked polymeric networks, one derived employing di-functional acid chloride and another using tri-functional acid chloride as a constituent monomer, are presented in the ATR-FTIR spectra of Figs. 2. 1a and 1b, respectively. This substantiates the successful deposition of charge bearing polymers as the selective skin layers. In case of the membranes with non-crosslinked and crosslinked polymeric structures, the bands appearing at 1156, 1169 cm^{-1} and 1426, 1442 cm^{-1} are attributed to the $–SO_2$ symmetric stretching and $–SO_2$ asymmetric stretching, respectively [33]. Their origin is accredited to the tethering of $–SO_3^- H^+$ groups in the skin layers of the respective membranes, through the reactive participation of DABSA as co-monomer of the ternary monomeric compositions. The bands appearing at 1509 and 1487 cm^{-1} are attributed to the combined contribution of both N–H in-plane bending and the C–N stretching vibrations of the –C(=O)–NH– as well as –C(=O)–N– groups of the constituent tertiary and secondary amide segments for the non-crosslinked and crosslinked polymeric structures, respectively [34]. The bands appearing at 1254 and 1247 cm^{-1} are attributed to the C–N stretch and –C(=O)–NH– as well as –C(=O)–N–bend (in opposite phase) for the constituent tertiary and secondary amide segments of the non-crosslinked and crosslinked polymeric structures, respectively [35]. The successive formations of the secondary and tertiary amide segments corroborate to the occurrences of interfacial co-polycondensation reactions, involving the $–NH_2$ groups of DABSA and the –NH groups of PIP with the –COCl groups of the acid chlorides. For the co-polyamide based skin layers of the membranes with non-crosslinked and crosslinked polymeric structures, the characteristic C=O stretching (amide-I), further substantiate the formations of both secondary as well as tertiary amide segments through their overlapping appearances at 1619 and 1630 cm^{-1}, respectively [36]. The characteristic bands appearing at 3432 and 3436 cm^{-1} occur due to hydrogen bonded –NH stretching (amide-A, between –CO and –NH sites) of the secondary amides [36]. The structural orientation as well as organization of the resultant non-crosslinked and crosslinked polyamide structures likely induces extensive interactions but at varying extent within the chain segments, in the course of secondary noncovalent interactions like intra-molecular H-bondings within adjacent amide-I and amide-A regions, which get observed by the alterations in intensity of the corresponding peaks. Such interactions include van der Waals interactions and dipole-dipole interactions or n→π* interactions happening through delocalization of a lone pair (n) of the donor carbonyl groups of amide segments into the antibonding (π*) orbital of the acceptor carbonyl groups (C=O·····C=O or C–N·····C=O) of the adjacent polymer chains [37].

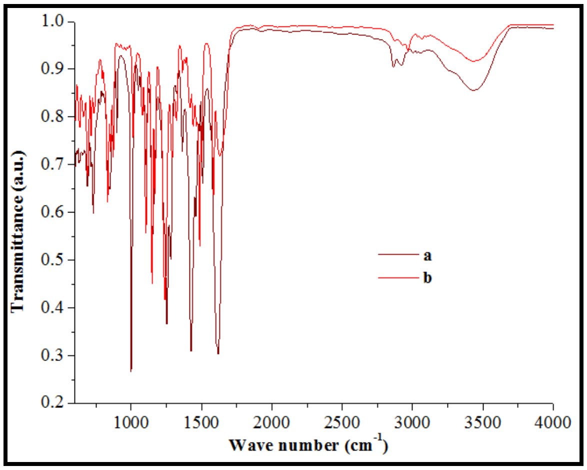

Fig. 2. 1 ATR-FTIR spectra of the skin layers of a) non-crosslinked and b) crosslinked co-polyamide based TFC NF membranes.

The solid state ^{13}C NMR spectra of the non-crosslinked and crosslinked co-polyamide polymers, as representative of skin layers of the TFC NF membranes, namely Polymer I and Polymer II are given in Figs. 2. 2a and 2b, respectively. Due to the amorphous nature of the synthesized polymers the resolutions of their resonance signals are not enough sharp.

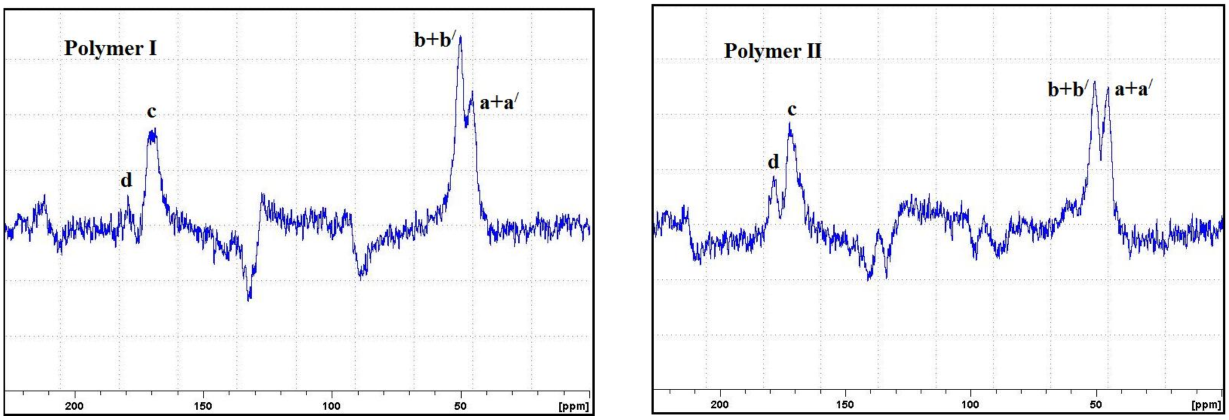

Fig. 2. 2 Solid state ^{13}C NMR spectrum of a) non-cross linked co-polyamide (Polymer I) and b) crosslinked co-polyamide (Polymer II).

The strong ^{13}C signals at δ of 168.57 ppm in Polymer I and 172.09 ppm in Polymer II, are attributed to the carbonyl carbon (c), corresponding to the tertiary amide (–CON) segment in the co-polyamides (Fig. 2. 3a). The formations of secondary amide (–CONH) segment of the co-polyamides, have also been substantiated by the presence of low intensity ^{13}C signals (Fig. 2.2) for the secondary carbonyl carbon (d), corresponding to the structure of Fig. 2. 3b, at δ of 179.17 and 178.45 ppm in Polymer I and II, respectively. The signal of carbonyl carbon of secondary amide shifts downfield compared to that of carbonyl carbon of tertiary amide. In DABSA unit of the co-polyamide, the lone pair of electrons of N atom prefers extended conjugation with the adjacent benzene ring system rather than towards the carbonyl group, leaving the carbonyl carbon (d) comparatively deshielded as shown in Fig. 2. 3b. Additionally, intra-molecular H-bonding between –NH and the non-bonding electron of carbonyl oxygen makes the carbonyl carbon more deshielded. These factors resultantly lead to downfield shift of secondary carbonyl carbon signal (d), as reflected in Figs. 2. 2a and 2b.

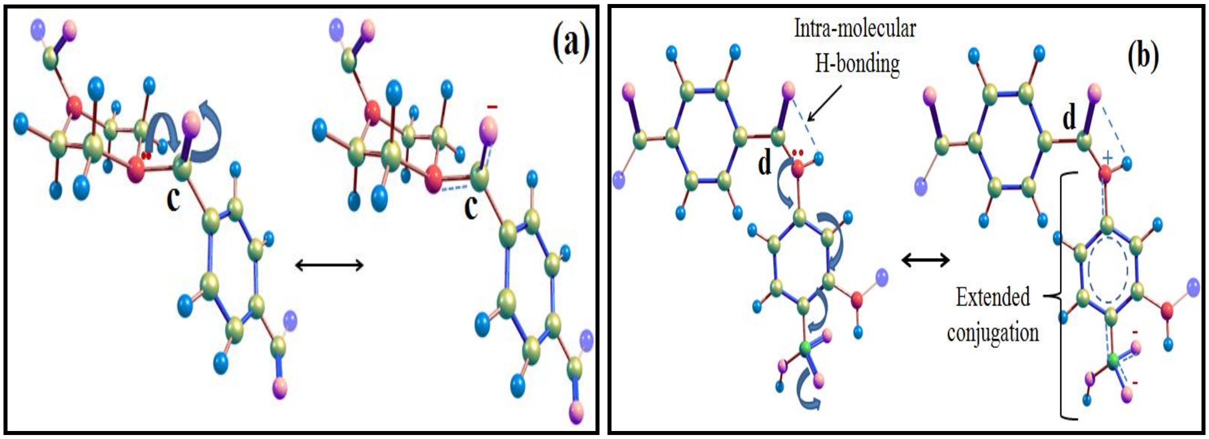

Fig. 2. 3 Responses of NMR signals on structural variations in the co-polyamide a) shielding effect on carbonyl carbon of tertiary amide and b) de-shielding effect on carbonyl carbon of secondary amide.

In contrast, due to the electron donating effect of the N of cyclo-aliphatic PIP ring, attached to the carbonyl carbon of tertiary amide (Fig. 2. 3a), the carbonyl carbon experiences an enhanced shielding effect. This effect drives the signal of the tertiary carbonyl carbon to shift upfield. The signal of carbonyl carbons of tertiary amide groups in Polymer I occurs upfield (168.57 ppm) as compared to that of Polymer II (172.09 ppm). This is explained as below. In a six membered heterocyclic ring like PIP, of the tertiary amide segment of the co-polyamide, two types of hindered rotations (*i.e.*, rotation around the C–N linkage of the tertiary amide group having partial double bond character and ring inversion through chair-chair interconversion of the PIP ring in its most stable chair conformations) may lead to the formation of rotational isomers, cis and trans [38]. Each isomer is having two different conformations *i.e.*, cis- equatorial-axial (e-a), cis- axial-equatorial (a-e), and trans- equatorial-equatorial (e-e), trans- axial-axial (a-a). Both, bond rotation and/or ring inversion may result in dynamic equilibrium between the possible conformers of N substituted PIP in the polymer, which preferentially keeps the spatially oriented substituents in axial and equatorial positions of the PIP ring depending on the energy order of different conformations *i.e.*, trans-1,4 – (e-e) < cis-1,4 – (e-a / a-e) < trans-1,4 – (a-a).

Reasonably, most stable trans-1,4 – (e-e) conformation will be the most favored one, hence predominant content in the dynamic equilibrium. Since any substituent in equatorial position is less sterically interacted with its surroundings as compared to that in axial position, the substituent oriented equatorially is less shielded than that oriented axially [39]. Thus, the downfield shift of ^{13}C signal for tertiary carbonyl carbon of Polymer II as compared to that of Polymer I, indicates the occurrence of higher population of the most stable conformation *i.e.*, trans-1,4 – (e-e) in the former polymer than in the later. The possibility of low population of other conformers, in the dynamic equilibrium of Polymer II is attributed to the rigid crosslinked polymer network which restricts the freedom of interconversion during conformational changes. Similarly, a lower δ value for tertiary carbonyl carbon of Polymer I implies presence of the other conformers in significant amounts in addition to the most stable one *i.e.*, trans-1,4 – (e-e) in the polymer. This is due to superior freedom of interconversion in this non-crosslinked polymer between trans-1,4 – (e-e) and cis- 1,4 – (e-a) through C–N bond rotation and/or trans-1,4 – (e-e) and trans- 1,4 – (a-a) through rapid ring inversion (Fig. 2. 4). Among them, the conformers cis-1,4 – (e-a / a-e) and trans- 1,4 – (a-a) experience more shielding because of steric crowding with a resultant overall shifting of the signal upfield in this polymer (Fig. 2. 2a).

In these rotational isomers, two asymmetric, magnetically non-equivalent methylene ($–CH_2$) carbons dwell as pair in a chemical environment, where they remain flanked between the tertiary N atoms of the PIP in tertiary amide segment. They are assigned as syn (a,a') and anti (b,b') with respect to the orientation of carbonyl group in axial and equatorial positions of PIP in tertiary amide segment [40].

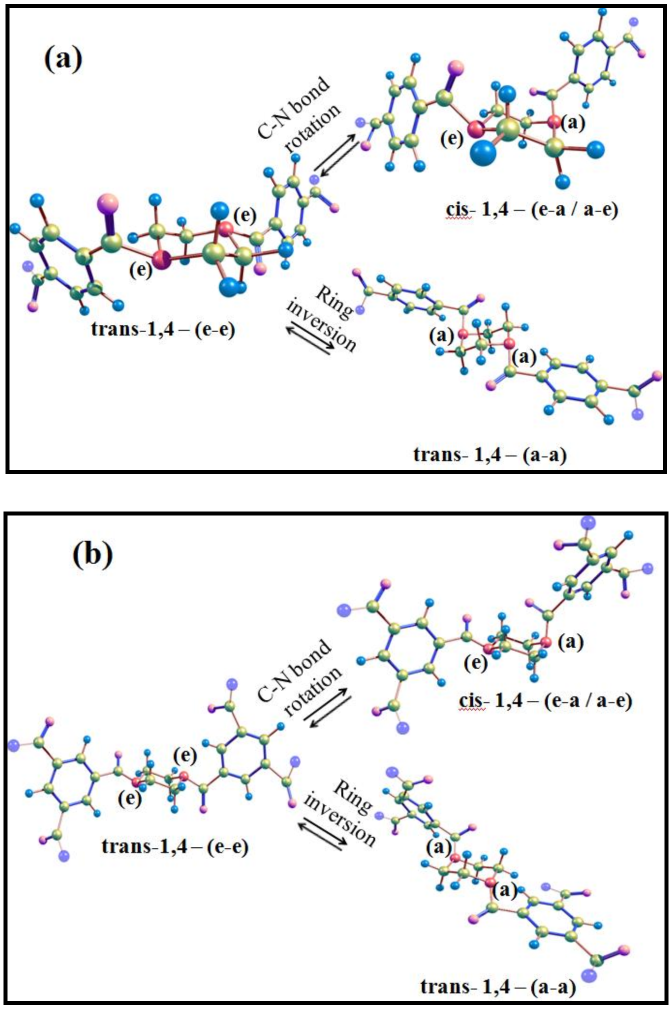

Fig. 2. 4 Predicted dynamic conformational equilibrium for cis-trans isomers of PIP in tertiary amide segment of a) non-cross linked co-polyamide (Polymer I) and b) crosslinked co-polyamide (Polymer II).

Steric compressions, mostly arising from the close approach of carbonyl group to the methylene group of PIP lead to shielding of the methylene carbon atoms from the magnetic field. This implies that shielding is more for the syn ones as compared to the anti ones and hence the ^{13}C signals for anti carbons shift downfield and that for syn carbons shift upfield. They appear at δ 45.31, 49.88 ppm for Polymer I and at δ 45.19, 50.37 ppm for Polymer II. The syn-anti differential shielding (Δsa) is more for the Polymer II (5.18 ppm) with rigid crosslinked molecular architecture than Polymer I (4.57 ppm) comprising of non-crosslinked molecular architecture. The ^{13}C signal intensities of the methylene carbons *i.e.*, syn (a,a') and anti (b,b') in the Polymer II is symmetrical in nature, however asymmetric in case of polymer I. This type of distribution pattern may be attributed to the occurrences of composite steric and resonance effects, based on the differential population of cis-trans isomers and their conformers present in the dynamic equilibrium in the two types of polymers as explained above.

2.3.2. Morphological characterizations of the non-crosslinked and crosslinked TFC NF membranes by SEM analysis

The cross sectional SEM images (at 700X magnifications) of the non-crosslinked co-polyamide based TFC NF membranes (without fabric support), cured at 100 ^{o}C for different durations, presented in Fig. 2. 5a, 5b (curing period: 30 min) and Fig. 2. 5a$^{/}$, 5b$^{/}$ (curing period: 60 min), exhibit the two distinct layers of polymers where the lowest layers of Psf consist of finger like structures resulted during their formations through wet phase inversion stage and the top most dense skin layer of the negatively charged polymer, deposited through *in situ* interfacial polymerization process, constituting the TFC NF membrane. Similar features have also been observed in case of the crosslinked co-polyamide based TFC NF membranes of Figs. 2. 6a, 6b (curing period: 30 min) and Figs. 2. 6a$^{/}$, 6b$^{/}$ (curing period: 60 min) which are cured at 90 ^{o}C.

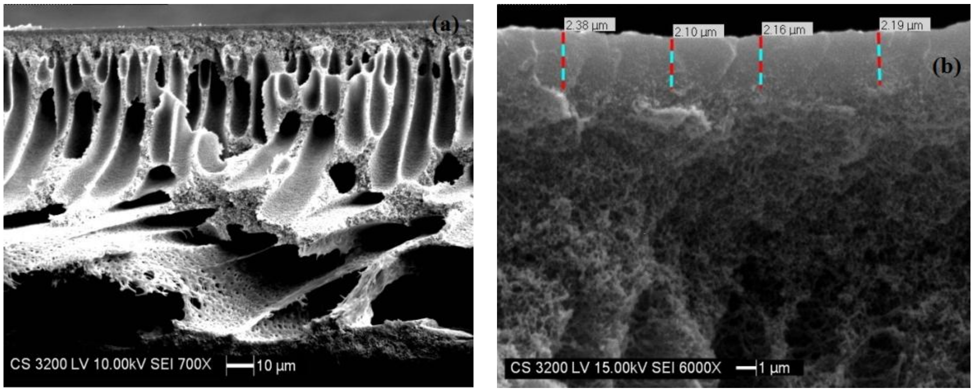

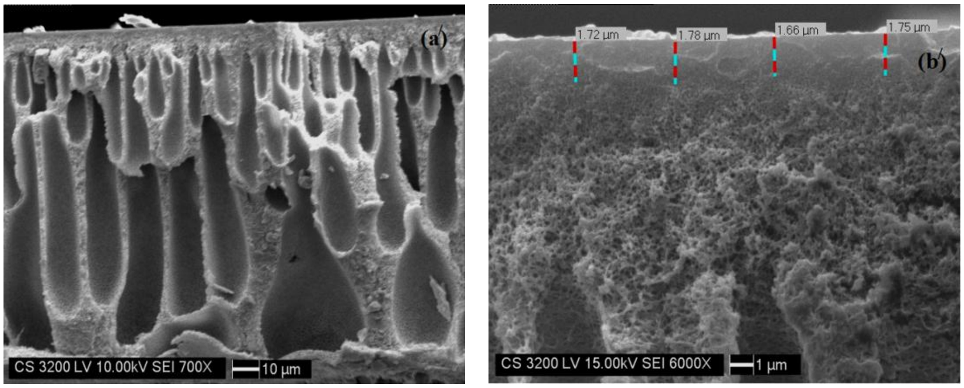

Fig. 2. 5 Cross sectional SEM images of non-crosslinked co-polyamide based TFC NF membranes – a) 700X and b) 6000X (skin region) magnifications with curing condition: 100 ^{o}C for 30 min; $a^{/}$) 700X and $b^{/}$) 6000X (skin region) magnifications with curing condition: 100 ^{o}C for 60 min.

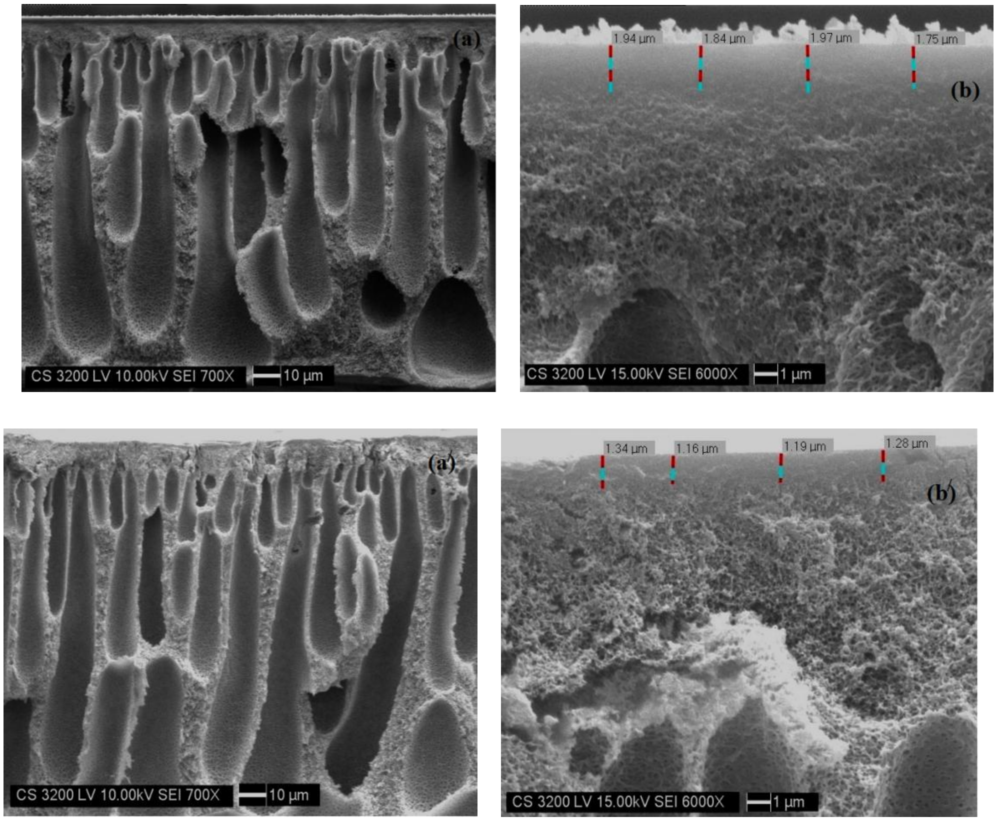

Fig. 2. 6 Cross sectional SEM images of crosslinked co-polyamide based TFC NF membranes – a) 700X and b) 6000X (skin region) magnifications with curing condition: 90 ^{o}C for 30 min; $a^{/}$) 700X and $b^{/}$) 6000X (skin region) magnifications with curing condition: 90 ^{o}C for 60 min.

At the mildest curing conditions of 100 ^{o}C for 30 min, for the non-crosslinked and 90 ^{o}C for 30 min, for the crosslinked co-polyamide based membranes the magnified views (Figs. 2. 5b and 6b, respectively) show that the skin region of the former membrane is thicker (2.10 - 2.38 µm; average 2.21 µm approximately) and more dense than that of the later membrane (1.75 - 1.94 µm; average 1.88 µm approximately). When the curing condition becomes still harsher, with enhanced duration of heating *i.e.*, 100 ^{o}C for 60 min, for the non-crosslinked and 90 ^{o}C for 60 min, for the crosslinked co-polyamide based TFC NF membranes (Figs. 2. 5b$^{/}$ and 6b$^{/}$, respectively), the skin regions seem to be getting further compacted, the corresponding values being 1.66 - 1.78 µm (average 1.73 µm approximately) for the former and 1.19 - 1.34 µm (average 1.24 µm approximately) for the latter class of membranes.

The elevated compaction for skin layer of the TFC NF membrane with crosslinked molecular architecture over that of the TFC NF membrane with non-crosslinked molecular architecture may sound unusual as one would expect that the polymeric network with three dimensional, crosslinked structures bear more resistivity towards any compaction more than the open, non-crosslinked polymeric structure. Moreover, the former membrane has been cured at a lower temperature, 90 ^{o}C than the later one. However, this seemingly anomalous behavior can be explained if one compares the ^{13}C NMR spectra of the respective polymers, (Figs. 2. 2a and 2b) where it has been established that the non-crosslinked polymer structure (Polymer I) acquires more freedom of rotation whereas, in case of the crosslinked polymer structure (Polymer II) the rotations are not favored due to the structural rigidity residing in the networked architecture. Such alteration in the freedom of rotation of the polymers is assumed to be responsible for the extent of compaction of the skin layers in their respective membranes. Due to the higher degree of freedom for rotation in the non-crosslinked polymer, it resists the cause of compaction (heating) more than the crosslinked polymer, which is much less free for any such rotation. Consequently a lot of energy is also utilized in rotation of the isomers in non-crosslinked polymer, leaving less energy available for compaction, which is not the case with the crosslinked polymer. This explains the higher compaction behavior of the TFC NF membrane with crosslinked co-polyamide than the TFC NF membrane with the non-crosslinked one, even when the former is cured at lower temperature.

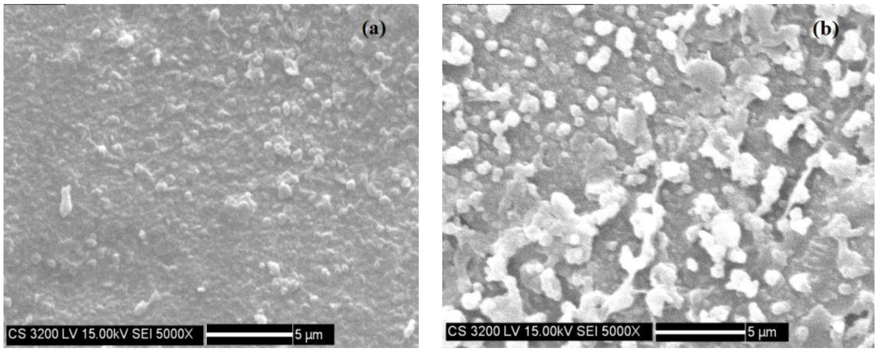

Fig. 2. 7 Skin surface SEM images of non-crosslinked co-polyamide based TFC NF membrane – a) curing condition: 30 min at 100 ^{o}C and b) curing condition: 60 min at 100 ^{o}C.

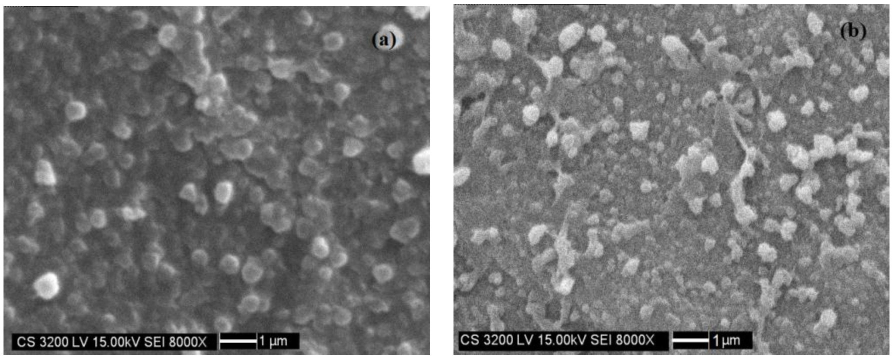

Fig. 2. 8 Skin surface SEM images of crosslinked co-polyamide based TFC NF membrane – a) curing condition: 30 min at 90 ^{o}C and b) curing condition: 60 min at 90 ^{o}C.

The corresponding skin surface SEM images of these membranes, given in Figs. 2. 7a - 7b and Figs. 2. 8a - 8b, respectively show the changes happening on the top skin layers of the membranes and the impact of curing conditions on membrane morphology. In both the types of membranes, as duration of cure increases there seems to the merger of smaller clusters of polymer resulting out formation of bigger sized polymeric agglomerates, which leads to densification.

2.3.3. Topographical characterization of the non-crosslinked and crosslinked TFC NF membranes by AFM analysis

The 2D AFM images of non-crosslinked (Fig. 2. 9) and crosslinked (Fig. 2. 10) co-polyamide based TFC NF membranes show that the entire membrane surfaces are strewn with globular polymer clusters [41, 42] whose dimensions seem to change with change in curing temperatures. When the curing temperature increases from 75 (Fig. 2. 9a) to 100 ^{o}C (Fig. 2. 9b), in case of the membranes comprising of non-crosslinked polymeric network structure or from 75 to 90 ^{o}C, for the membranes comprising of crosslinked polymeric network structure (Figs. 2. 10a and 10b), the dimensions of these polymer clusters seem to become smaller. In the corresponding 3D images (Figs. 2. 9a$^{/}$ vs 9b$^{/}$ and Figs. 2. 10a$^{/}$ vs 10b$^{/}$), the surface features seem to be getting sharper and more uniformly distributed. However, while the curing temperature increases to even higher temperature, both the 2D and 3D images (Figs. 2. 9c, 9c$^{/}$ and Figs. 2. 10c, 10c$^{/}$) show some irregularities in their features.

It may be noted that the non-crosslinked and crosslinked polymeric structure based TFC NF membranes could not be prepared under identical membrane preparative conditions since the tri-functional acid chloride monomer exerts higher reactivity than the di-functional acid chloride monomer and hence the former acquired less time to form the membrane. Further, identical curing temperature could also not be maintained since the temperature at which crosslinked co-polyamide yielded proper skin layer with an utilizable features as TFC NF membranes the non-crosslinked co-polyamide based TFC NF membranes could not yield one such. So the reaction time, curing time and also the duration of curing for crosslinked network structure based membranes are lower than the membranes with non-crosslinked co-polyamide structure, in these studies.

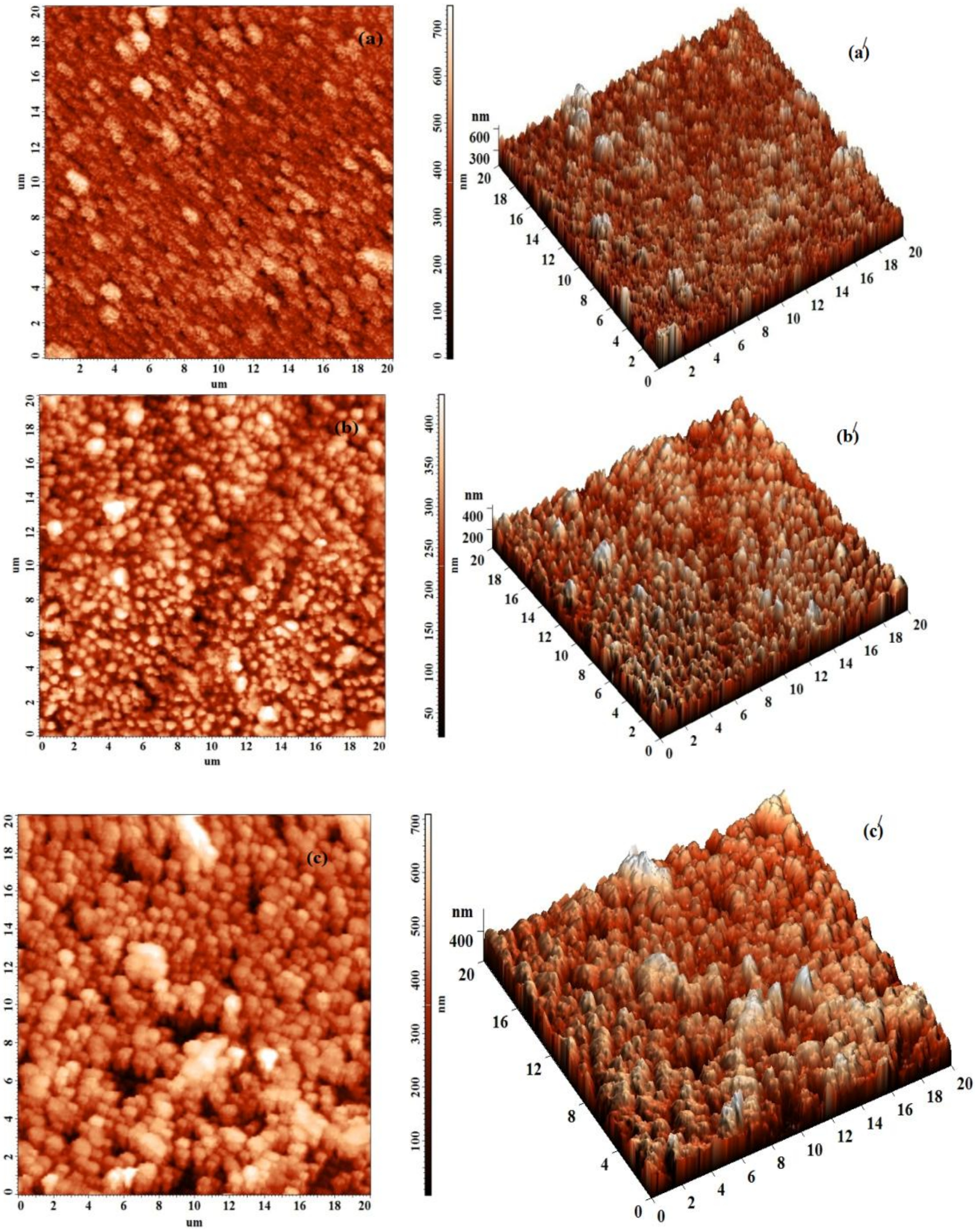

Fig. 2. 9 2D and 3D AFM images of non-crosslinked co-polyamide based TFC NF membrane, cured at – a, a$^{/}$) 75 ^{o}C; b, b$^{/}$) 100 ^{o}C and c, c$^{/}$) 150 ^{o}C for 30 min.

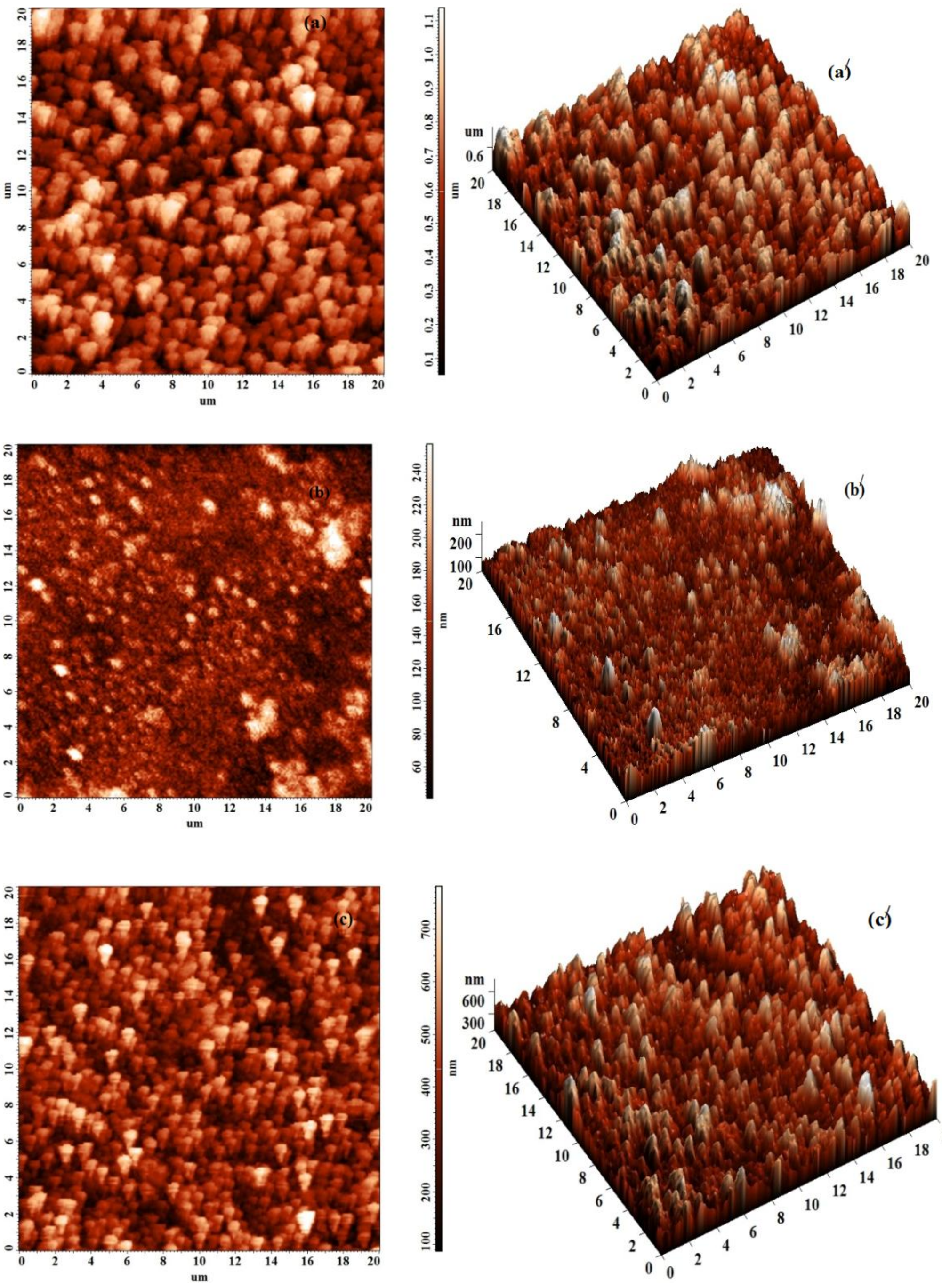

Fig. 2. 10 2D and 3D AFM images of crosslinked co-polyamide based TFC NF membrane, cured at – a, $a^{/}$) 75 ^{o}C; b, $b^{/}$) 90 ^{o}C and c, $c^{/}$) 100 ^{o}C for 30 min.

The average roughness (R_a) of the TFC NF membrane with non-crosslinked co-polyamide skin layer (Fig. 2. 11a), derived at 75 ^{o}C curing temperature is 71.41 nm. The R_a value decreases to 53.88 nm when the curing temperature is increased to 100 ^{o}C. The R_a value gives a measure of smoothness of the membrane surface, where the lower value of R_a implies a smoother surface. The formation of a smoother surface as evidenced by the decrease in R_a value, with increasing curing temperature is assumed to happen due to the densification or reorganization of the skin layer co-polyamides which, in turn, may lead to formation of smaller pore sizes. Such occurrence may account to the fact that at elevated temperatures the mobility of the polymer chains, at the just deposited skin layer increases and they tend to rearrange and redistribute themselves, forming new polymeric clusters which are smaller in sizes and more in numbers. This, combined with densification of the polymer layers, may be responsible for more orderly surface features, which is reflected in the lower value of R_a. This may also account to the fact of formation of smaller pore sizes in terms of aggregate pores as well as network pores, and, consequently, more number of pores in the membranes' skin layer. A pictorial depiction (Fig. 2. 12) reflects the effect of rearrangement and redistribution of polymer chains to form smaller polymer clusters leading to formation of smaller aggregate and network pores as the membrane is cured at high temperatures.

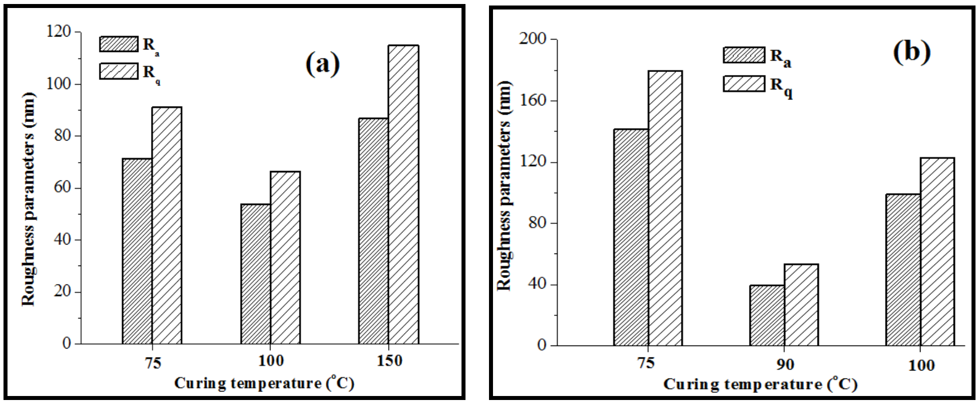

Fig. 2. 11 Variation in surface roughness parameters of the TFC NF membranes comprising a) non-crosslinked and b) crosslinked co-polyamides as skin layer polymers.

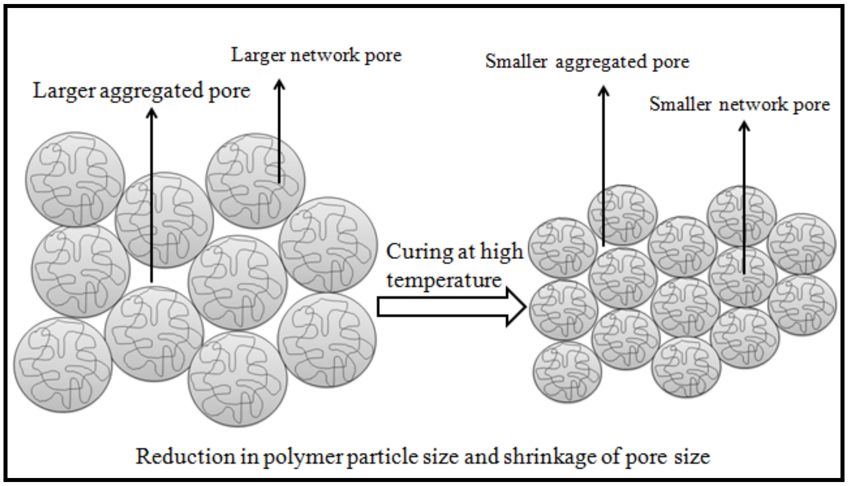

Fig. 2. 12 Conceptual representation of rearrangement and redistribution of polymer networks at high temperatures.

The R_a value of the membrane, however, increases to 86.73 nm when the membrane is cured at still higher temperature, 150 ^oC (Fig. 2. 9c and 9c$^/$). This is because, during the curing step, due to so high temperature, the trapped solvents and unreacted chemicals left in the nascent membrane after the *in situ* polymerization, rapidly comes out of the top layer and membrane subsurface, leaving behind an irregular surface feature. This leads to the increase in roughness of the membrane at higher curing temperature [42]. Visually also, in the 2D image (Fig. 2. 9c), there appears a lot of irregular features which could be attributed to this cause. The root mean square roughness (R_q) of the of the corresponding membranes follow the same trend, the values being 91.16, 66.53 and 114.90 nm for membranes cured at 75, 100 and 150 ^oC, respectively.

For the membranes comprising of crosslinked co-polyamide skin layers, where the membranes for AFM studies have been cured at 75, 90 and 100 ^oC, the images are presented in Figs. 2. 10a, 10b, 10c for 2D and Figs. 2. 10a$^/$,10b$^/$ and 10c$^/$ for 3D, respectively. Here as well, like the earlier categories of investigating membranes, the 2D images reveal decrease in size of the polymeric clusters, as the temperature of curing increases from 75 to 90 ^oC, presumably for the same reason of redistribution and rearrangement of polymer chains, due to their increased mobility at higher temperature, to form polymeric clusters of smaller dimensions. The R_a and R_q values derived from the 3D images show that the smoothness improves when the curing temperature increases from 75 to 90 ^oC, the corresponding values of R_a being 141.32 and 39.21 nm and for R_q, 179.47 and 53.28 nm, respectively. When the curing temperature increases further to 100 ^oC (Figs. 2. 10c and 10c$^/$) there is an increase in R_a (99.08 nm) and R_q (122.56 nm) values. The increase in R_a values for this membrane (Fig. 2. 10c) may not be due to the same reason as the increase of R_a values in case of earlier categories (Fig. 2. 9c), since there is variation of curing temperature. The reason may rather be attributed to the fact that any unreacted –COCl groups (or –COOH groups on hydrolysis) in the tri-functional acid chloride monomer, left in the membrane may be undergoing further reaction, at this elevated temperature, with residual amine monomers left in the membrane matrix, leading to more crosslinking of the polymer. This may lead to more irregular features in the membrane surface due to the three dimensional crosslinked nature of the polymer which is reflected in an increased R_a value of this membrane.

2.3.4. Nanofiltration performance of membranes with single solute feed systems

2.3.4.1. Effect of variation of polymerization time on membrane performance

The polymerization time, leading to TFC NF membrane formation by *in situ* interfacial polymerization process, was varied to study the effect of the polymerization time on membranes' performances. The set of polymerization times studied in case of the non-crosslinked and the crosslinked co-polyamide based TFC NF membranes were different since variable reactivities of the acid chloride monomers (TPC and TMC), playing the roles of reactant cum crosslinking agent yielded usable membranes at different reaction times for the two monomers. The duration of polymerization period given for preparation of the former membranes was 15 to 120 s (curing at 90 ^oC for 30 min) and that for the later class of membranes was 5 to 30 s (curing at 100 ^oC for 30 min). The percent solute rejections and solvent fluxes, as presented in Figs. 2. 13a and 13b vary with change of the polymerization time for the non-crosslinked and crosslinked types of membranes, respectively.

Out of the four solutes employed for characterization of the membranes' performance behaviors towards different ionic environments, the solute rejection of Na_2SO_4 becomes the highest, which reaches more than 90% for the highest rejecting membranes, closely followed by that of $MgSO_4$. The rejection of NaCl is the lowest of all the four solutes, whereas, the rejection of $CaCl_2$ by the membranes is intermediate. The high solute rejections of the sulfate containing solutes are attributed to the strong Donnan exclusion experienced by the bivalent SO_4^{2-} ions at the membrane surface due to the surface negative charge of the membranes, resulted by the presence of $–SO_3^-H^+$ groups. However, in case of $CaCl_2$ and NaCl, the higher solute rejection in the former solute containing bivalent cations, by a negatively charged membrane indicates that steric exclusion takes precedence over Donnan exclusion, in which, the hydrated Ca^{+2} ions with higher hydrated radii are rejected more than the Na^+ ions with lower hydrated radii. This pattern of solute rejection has been observed by other researchers as well with negatively charged membrane [43-45].

In both types of membranes there is an initial increase in solute rejection values when the polymerization time increases from 15 to 30 s for the non-crosslinked and 5 to 10 s for the crosslinked co-polyamide based TFC NF membranes. This is because the formation of the skin layer is improper and more prone to local defects at the lowest polymerization time. With increasing polymerization time, formation of a thicker top layer results in better solute rejections. With further increase of polymerization time, there is a slow increase in solute rejections of the membranes, which somewhat plateaus off, indicating that proper membrane formation does not need much long polymerization time and after the formation of the proper membrane further deposition of polymer does not significantly improve the solute rejection [46, 47]. The results also show that TMC with three reactive –COCl groups take much less time for polymerization than TPC having two reactive –COCl groups to form a proper membrane.

There is an incessant drop of solvent fluxes of the non-crosslinked class of membranes with increasing polymerization time, which indicates that more and more polymers are deposited making the skin layer thicker. However, for the crosslinked membranes the solvent fluxes initially decrease followed by slight increase at higher polymerization time. The initial decrease in flux is accredited to an increased deposition of polymer layer on the membrane. With increasing polymerization time, when a layer is deposited on the top membrane, the diffusion of the amine monomer may be hindered leading to availability of less amine for reaction with TMC in the organic phase side. This leads to a partial transformation of the reactive –COCl groups of TMC into the resultant amide linkages, which further implicates that the remnant –COCl groups of the TMC monomers get later hydrolyzed to form pendent –COOH groups, making the skin layer more hydrophilic and subsequently increasing the fluxes of the membranes [48, 49]. Though, a similar decrease in diffusion of amine may be happening in non-crosslinked co-polyamide based membranes, but, since there is no scope of hydrolysis in TPC as both –COCl groups have already taken part in polymerization, so no corresponding increase in solvent fluxes of these membranes happens at higher polymerization time.

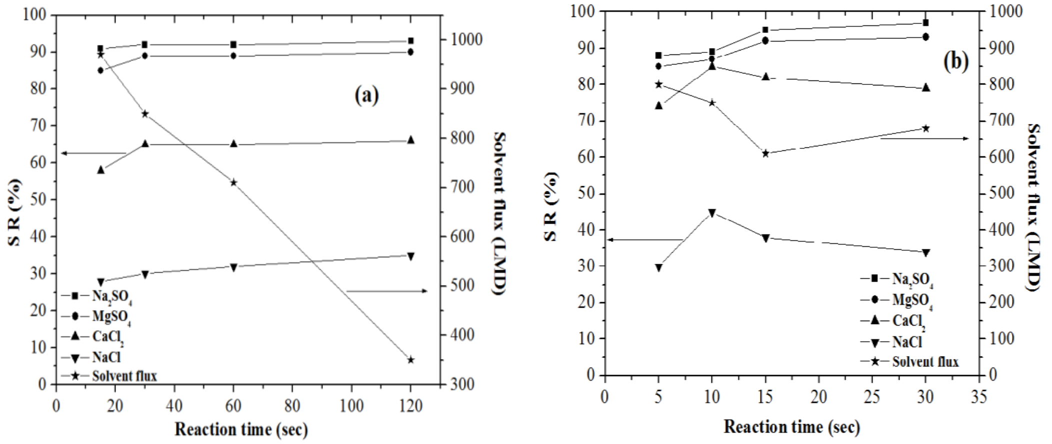

Fig. 2. 13 Solute rejections and solvent fluxes of a) non-crosslinked co-polyamide based TFC NF membranes (curing: 100 °C, 30 min) and b) crosslinked co-polyamide based TFC NF membranes (curing: 90 °C, 30 min), made at different polymerization times.

2.3.4.2. Effect of variation of curing temperature on membranes' performances

The effects of curing temperature on the skin surfaces' topographic properties of non-crosslinked and crosslinked co-polyamide based TFC-NF membranes were studied to optimize the membrane preparative conditions. The variations in solute rejection and solvent flux of these membranes, as presented in Figs. 2. 14a and 14b are subjected to be dependent on the variations of the temperatures employed for curing.

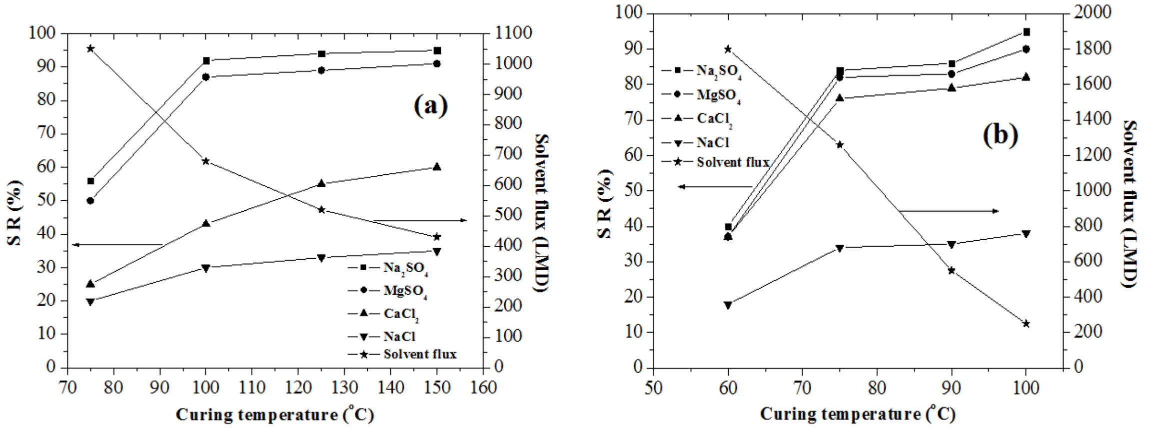

Fig. 2. 14 Solute rejections and solvent fluxes of a) non-crosslinked and b) crosslinked co-polyamides based TFC NF membranes, made at different curing temperatures with duration of cure: 30 min.

For both the membranes, solute rejections of all the four solutes increase steadily with increasing curing temperature; accompanied with a concurrent decline of solvent flux (solvent flux with respect to the NaCl solution is only given in the figures for brevity). The enhanced rejection is noticeably rapid during the initial stages of curing *i.e.*, when curing temperature increases from 75 to 100 ^{o}C in non-crosslinked polymeric structure based TFC NF membranes and from 60 to 75 ^{o}C in crosslinked polymeric structure based TFC NF membranes. Such variation is attributed to the densification of the TFC skin layer during curing, an effect discussed in the AFM section (Fig. 2. 11), where there is prediction of formation of smaller pore sizes and more number of pores through rearrangement and redistribution of the polymer chains, due to their increased mobility at high temperatures. In spite of the possible formation of more number of pores, the fact that the membranes still give lower flux indicates the dominance of densification effect over the possible increase in number of pores. At still higher temperatures of curing, the enhancement in rejection reaches saturation which is obvious from the slower rate of increment of the rejection values. But, the solvent fluxes of the membranes decrease steadily over the entire range of curing, approaching very low values at high curing temperatures. The solvent fluxes of crosslinked membranes decrease more steeply, than those of the non-crosslinked membranes, indicating higher densification of the membranes' skin layer at elevated temperatures which is believed to be due to some additional crosslinking reaction of unreacted functional groups, an effect described in the AFM analysis of the corresponding membranes.

2.3.4.3. Effect of variation of curing duration on membranes' performances

The effect of duration of cure, at temperatures of 100 ^{o}C for non-crosslinked and 90 ^{o}C for crosslinked co-polyamides based TFC NF membranes, on the performances of the membranes, presented in Figs. 2.15a and 2.15b, respectively show that solute rejections increase with enhancement in the duration of curing. Though a decline in solvent flux is observed under these conditions, it is not as rapid as with the case of increased curing temperature. That seems obvious since it is expected that the mobility of polymer chains, which is suspected to be one of the reasons for densification of membranes' skin layers leading to flux decline, will be more pronounced with increase in temperatures rather than with increased duration at a particular temperature. The decline in solvent fluxes, for the TFC NF membranes with non-crosslinked co-polyamide based skin layers are more pronounced than the TFC NF membranes with crosslinked co-polyamide based skin layers, when duration of cure changes from 30 to 60 min. This particular observation seems anomalous, since the SEM of the corresponding membranes, when cured for 30 and 60 min, have shown that the skin layers of the former membrane undergoes compaction from an average thickness of 2.21 to 1.73 µm and those of the later membrane to compact from 1.88 to 1.24 µm. The more gradual decline in solvent fluxes of the later class of membranes, in spite of a higher compaction of the skin layers, may be due to the lesser overall thickness of the skin layer of this membrane as compared to the non-crosslinked membrane.

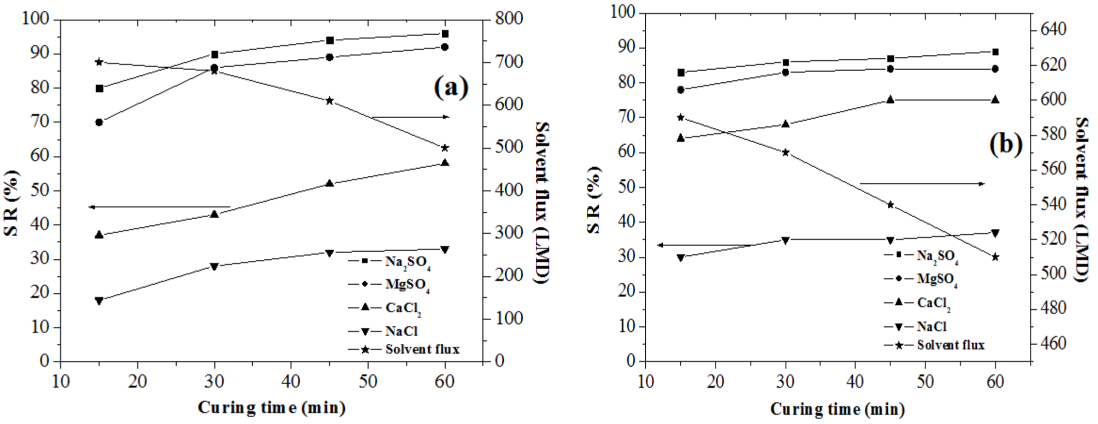

Fig. 2. 15 Solute rejections and solvent fluxes of a) non-crosslinked and b) crosslinked co-polyamide based TFC NF membranes, made at different curing durations; Curing temperature: 100 °C.

2. 4. Conclusions

The investigations on variation in structural, morphological and topographical features of the two different classes of negatively charged TFC NF membranes, derived from co-polyamides containing $-SO_3^-H^+$ moieties in their backbones, depict some interesting insights into these properties which varied for the non-crosslinked and crosslinked molecular architectures of the polymers.

The ATR FTIR spectroscopic studies of the membranes substantiate the presence of $–SO_3^-H^+$ groups as the negative charge bearing functionalities for the skin layers of the TFC NF membranes. Solid state ^{13}C NMR reveal the structural variations as well as local molecular motions of the co-polyamides in terms of distribution of the rotational isomers of the polymer chain. The topographical features of both non-crosslinked and crosslinked co-polyamide based TFC NF membranes exhibits that the surface roughnesses of the membranes change as a function of curing temperature, where elevated temperature for the curing resulted in the rearrangement and redistribution of polymer chains of the thin film skin layers due to their increased mobilities, affecting their surface roughness. The morphological insights of the membranes' skin surfaces for both the membranes show that the merger of smaller polymer aggregates leading to formation of bigger agglomerates resulting in densification when they are subjected to undergo prolonged curing conditions. Cross sectional SEM images of both types of membranes further reveal that the compaction of skin layers are more prone at higher duration of curing. These observations suggest that curing is an important process, which, if not properly controlled, could lead to an excessive densification of the skin layer and decrease the solvent fluxes of the membranes. The membranes' performances also vary with change in polymerization time as well as curing conditions such as curing temperature and its' duration. The membranes provide solute rejection in the order of $Na_2SO_4 > MgSO_4 > CaCl_2 > NaCl$, which is typical of negatively charged TFC NF membranes. Further, this study gives an idea about the sensitivity of the membranes' performances towards the variation of preparation parameters like polymerization time and curing conditions, which can be used to prepare membranes of desired performances.

CHAPTER – 3

Development and characterization of negatively charged TFC NF membranes, derived employing diaryl diamines with multiple sulfonic acid groups

3. 1. Introduction

The earlier research efforts on development of various negatively charged NF membranes reveal that the most commonly used processes for generation of such charged membranes with various polymeric constitutions include interfacial polymerization [3], grafting of polymers to introduce charge and making membranes using them by phase separation technique [4], modification of preformed membranes by radiation grafting [5], coating of charged polymer layer over another substrate [6], applying multilayer polyelectrolytes (alternative layers of oppositely charged polyelectrolytes) over an existing substrate membrane [7], coating or filling of charged gels in the porous structure of the membrane [8] etc.

The TFC type NF membranes, bearing negative surface charges are prepared following the conventional route of *in situ* interfacial polymerization, employing reactive diamine monomers and polyfunctional acid chlorides, on ultrafiltration type base membranes. The negative charges residing on the membranes' active skin surfaces are usually either in the form of residual ionogenic functionalities, mostly generated during the membrane fabrication stages or ionogenic functionalities incorporated during modification stages of subsequent membrane preparation processes. Thus, there remains the requirement of a simple process in bolstering the charge properties of such negatively charged TFC NF membranes which not only provides easy processability and superior performances, but additionally contribute in prevailing over the various drawbacks associated with the existing membranes and their fabrication processes.

The present study extensively deals with the development of a series of negatively charged TFC NF membrane (TFC-NCNF) with polyamide and co-polyamide type skin layers, bearing high density of negative charges, developed by *in situ* interfacial polymerization technique employing novel chemical compositions. The negative charges are contributed by presence of ionogenic functionalities, in the form of sulfonic acid moieties, on the surface of the TFC membranes. The research work pertains to the use of unique combinations as well as compositions of monomers *i.e.*, binary and ternary monomeric compositions to develop these membranes. Thus, the membranes have been derived using a set of reactive monomers, comprising of diaryl diamines with multiple sulfonic acid groups per molecule such as 4, $4^{/}$-diamino stilbene-2, $2^{/}$-disulfonic acid (DASDSA) and 2, $2^{/}$-benzidene disulfonic acid (BDSA) and polyfunctional acid chloride such as trimesoyl chloride (TMC). Membranes have also been derived by employing a cyclo-aliphatic diamine, piperazine (PIP), as a co-monomer along with the charge bearing diaryl diamine monomer. Extensive physicochemical characterizations have been done to analyze various surface features of the membranes. The negatively charged TFC NF membranes exhibited high degree of selectivity towards solutes having ionic constituents of varying valences, by showing different differential rejection patterns. Their potentials in removal of ionic constituents with concurrent fractionation of mono and multivalent ionic species from different mixed feed systems have also been evaluated.

3. 2. Experimental

3.2.1. Materials and methods

Polysulfone (Psf; M_W: 30k Da) from Solvay Speciality Polymers (India), N-methyl-2-pyrrolidone (NMP; purity: ≥ 99 %) from Sigma-Aldrich and polyvinyl pyrrolidone (PVP, K-30;

M_W: 40k Da) from SRL (India) were employed to prepare Psf base membrane. The nonwoven porous polyester fabric used as a support material for preparation of the base membrane had a density of 75 g/m^2 and a thickness of 110 μm with an air permeability of 70 dm^3/m^2 at 2 mbar. For evaluation of molecular weight cut off (MWCO) of the Psf base membrane through determination of rejection behaviors towards organic solutes, poly(ethylene glycol) (PEG) of varying molecular weights *i.e.*, 12k, 20k and 35k Da and poly(ethylene oxide) (PEO) of molecular weight 100k Da were procured from Fluka (Germany) and Sigma-Aldrich, respectively. The diaryl diamine monomers *i.e.*, 4, 4$^/$-diamino stilbene-2, 2$^/$-disulfonic acid (DASDSA, purity: 85%) and 2, 2$^/$-benzidene disulfonic acid (BDSA, purity: >70%) were procured from Aldrich and TCI (Japan), respectively. The cyclo-aliphatic diamine monomer, piperazine (PIP; purity: 99%) was procured from Sigma-Aldrich. The crosslinking monomer: trimesoyl chloride (TMC; purity: >99%) was purchased from Sigma-Aldrich. Analytical grade n-hexane, magnesium chloride heptahydrate ($MgCl_2.7H_2O$), magnesium sulphate hexahydrate ($MgSO_4.6H_2O$), anhydrous sodium sulphate (Na_2SO_4), sodium chloride (NaCl), sodium nitrate ($NaNO_3$) and potassium chloride (KCl) were procured from different companies in India. The conductivity of mili-Q ultra-pure water used in the experiments was below 2μS/cm.

3.2.2. Fabrication of thin film composite negatively charged nanofiltration membranes

3.2.2.1. Preparation of Psf base membrane by nonsolvent induced phase inversion method

Asymmetric flat sheet type porous Psf base membrane was prepared by nonsolvent induced phase inversion method following few consecutive steps. A casting solution comprising of 30 (w/v)% Psf in NMP and PVP (40 w/w% of Psf) as pore-forming additive, was prepared in a hermetically sealed glass-bottle through vigorous agitation for several hours accomplishing complete dissolution of Psf and PVP in the solvent. The resultant viscous solution was kept overnight in an environmentally controlled atmosphere maintaining the temperature and relative humidity at 25 ^{o}C and 35-40%, respectively and then undergone vacuum degassing to eliminate the trapped air bubbles from the solution. The resultant homogeneous polymer solution was cast on a nonwoven polyester support fabric maintaining a uniform thickness of 100 µm, using an automated casting machine. The cast film was immediately immersed in a precipitation bath containing ultra-pure water as nonsolvent. To ensure complete removal of the additive as well as solvent from the membrane matrix, through exchange between solvent and nonsolvent, the resulting membrane was taken out of water bath and adequately rinsed in fresh water several times. The entire process of casting was carried out in a controlled atmospheric condition by maintaining the temperature of the surrounding atmosphere at 24(±1) ^{o}C with a relative humidity of 30–35%.

3.2.2.2. Preparation of TFC-NCNF membranes by in situ interfacial polymerization technique

The TFC NF membranes of the present study were prepared through *in situ* interfacial polymerization of reactive monomers on the Psf base membrane. The diaryl diamine monomers having two sulfonic acid groups per molecule (either DASDSA or BDSA), dissolved in polar protic solvents (water) were employed to react through interfacial polycondensation technique with TMC, dissolved in nonpolar organic solvent (n-hexane), forming an ultra-thin polyamide layer at the liquid-liquid interface, which deposited as a semi-permeable membrane barrier on the base membrane. Additionally, a binary combination of diamines or the ternary monomeric compositions, comprising of PIP and either of the above two diamines (DASDSA or BDSA) were also utilized for the purpose of developing the negatively charged TFC NF membranes.

In a detailed description, the procedures for development of the TFC NF membranes have been described below:

A sheet of Psf base membrane was first dipped in the 4 (w/v %) aqueous amine solution comprising of either DASDSA or BDSA with NaOH or triethylamine (TEA) as acid acceptor cum solubilizer, for certain period of time. It was then removed from the aqueous amine bath and the excess solution sticking to its surface was gently wiped off by keeping it sandwiched between two polyethylene sheets and then passing through a pair of rubber rollers. The amine soaked Psf base membrane was then dipped in the reaction bath containing 0.1 – 0.3 (w/v)% of TMC solution for a predetermined period, allowing the polycondensation reaction to take place at the interface of two immiscible liquids, *i.e.*, the amine of the aqueous phase and the acid chloride of the non aqueous n-hexane phase, allowing a nascent thin film to get deposited on the surface of the Psf base membrane. During the course of soaking stage and the polycondensation reaction, the temperature of the aqueous amine solution as well as n-hexane solution containing TMC were maintained at 10 – 15 ^{o}C, facilitating the exothermic type polycondensation reaction to carry on at low temperature, favorably. The membranes with the nascent skin surfaces were further subjected to an elevated temperature curing, to tune its stabilities, physicochemical properties and performances.

The schematics of reactions (Figs. 3. 1 to 3. 4) for formation of the probable crosslinked polyamide or co-polyamide type structures as skin layer polymeric materials of the negatively charged TFC-NCNF membranes, using the varying monomeric compositions are listed in Tables 3. 1 to 3. 4, respectively.

Table 3. 1

Binary composition of monomers and experimental conditions for development of DASDSA based TFC-NCNF membranes.

Sr No.	Membrane Code	Amine monomer (w/v)% (aqueous)		Acid acceptor/ Solubilizer	Acid Chloride Monomer (w/v)% (organic; n-hexane)
		DASDSA	PIP		TMC
1	NCNF-I	4	–	NaOH 25(w/w_{DASDSA})%	0.1
2	NCNF-II	4	–	NaOH 25 (w/w_{DASDSA})%	0.2

- Soaking time:4 min; Polymerization time:1 min; Curing time:30 min; Curing temperature:100(±1) °C

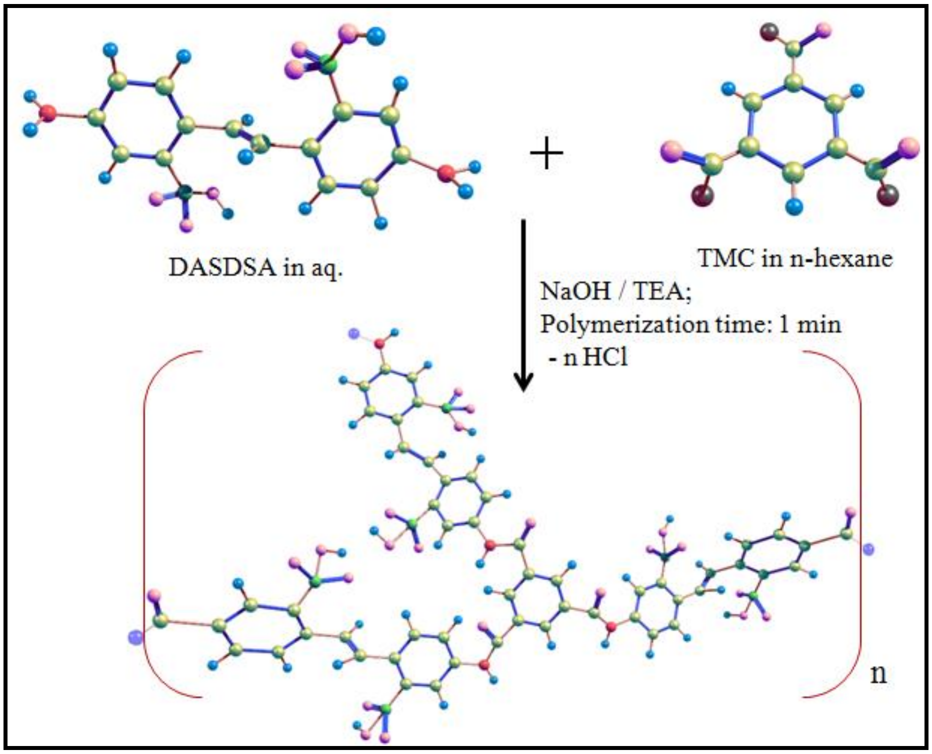

Fig. 3. 1 Reaction scheme for the DASDSA-TMC based crosslinked polyamide, as formed during development of TFC-NCNF membranes [Membrane code: NCNF-I & NCNF-II].

Table 3. 2

Ternary composition of monomers and experimental conditions for development of DASDSA & PIP based TFC-NCNF membranes.

Sr No.	Membrane Code	Amine Monomer (w/v)% (aqueous)		Acid acceptor/ solubiliser	Acid Chloride Monomer (w/v)% (organic;n-hexane)
		DASDSA	PIP		TMC
1	NCNF-III	3	1	NaOH 13.3 (w/w$_{DASDSA}$) %	0.1
2	NCNF-IV	3	1	NaOH 13.3 (w/w$_{DASDSA}$) %	0.2

- Soaking time:4 min; Polymerization time:1 min; Curing time:30 min; Curing temperature:100(±1) °C

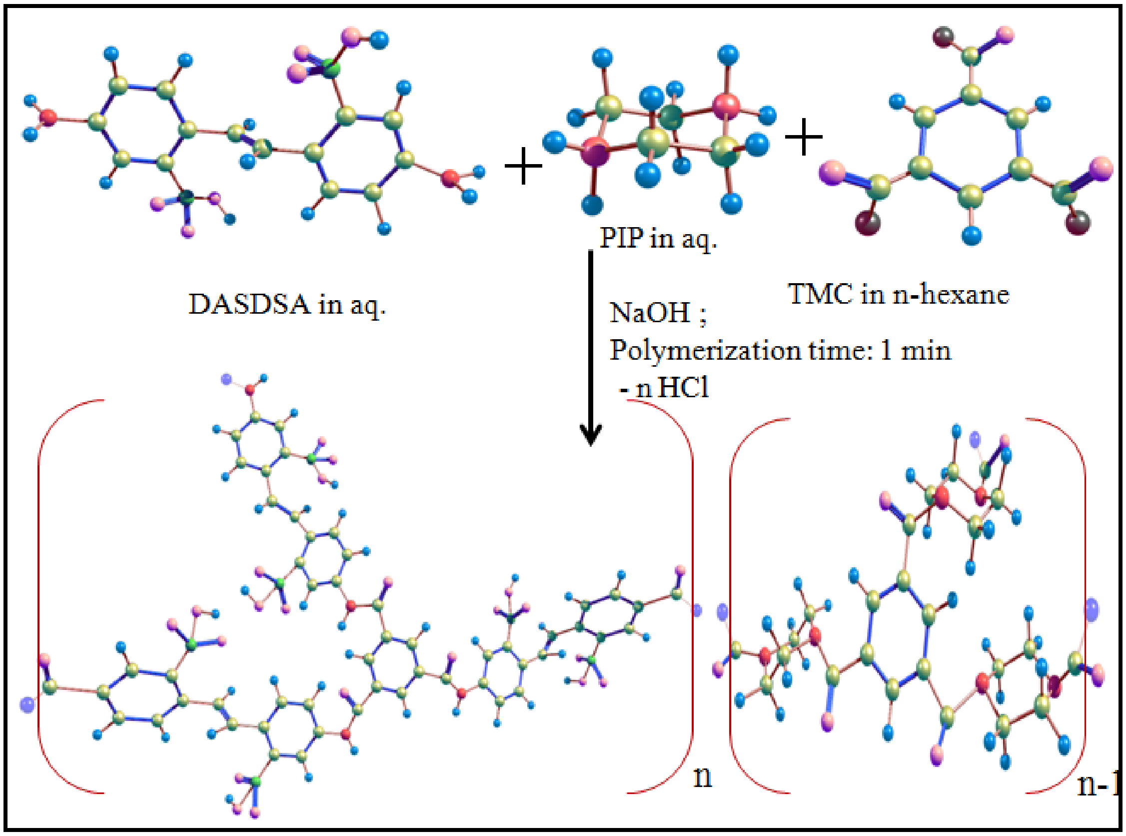

Fig. 3. 2 Reaction scheme for the DASDSA-PIP-TMC based crosslinked co-polyamide, as formed during development of TFC-NCNF membranes [Membrane code: NCNF-III & NCNF-IV].

Table 3. 3

Binary composition of monomers and experimental conditions for development of BDSA based TFC-NCNF membranes.

Sr No.	Membrane Code	Amine Monomer (w/v)% (Aqueous)		Acid Aceceptor/ Solubiliser	Acid Chloride Monomer (w/v)% (organic; n-hexane)
		BDSA	PIP		TMC
1	NCNF-V	4	–	NaOH 25 (w/w_{BDSA})%	0.2
2	NCNF-VI	4	–	NaOH 25 (w/w_{BDSA})%	0.3

- Soaking time: 4 min; Polymerization time: 2 min; Curing time: 30 min; Curing temperature:100(±1) °C

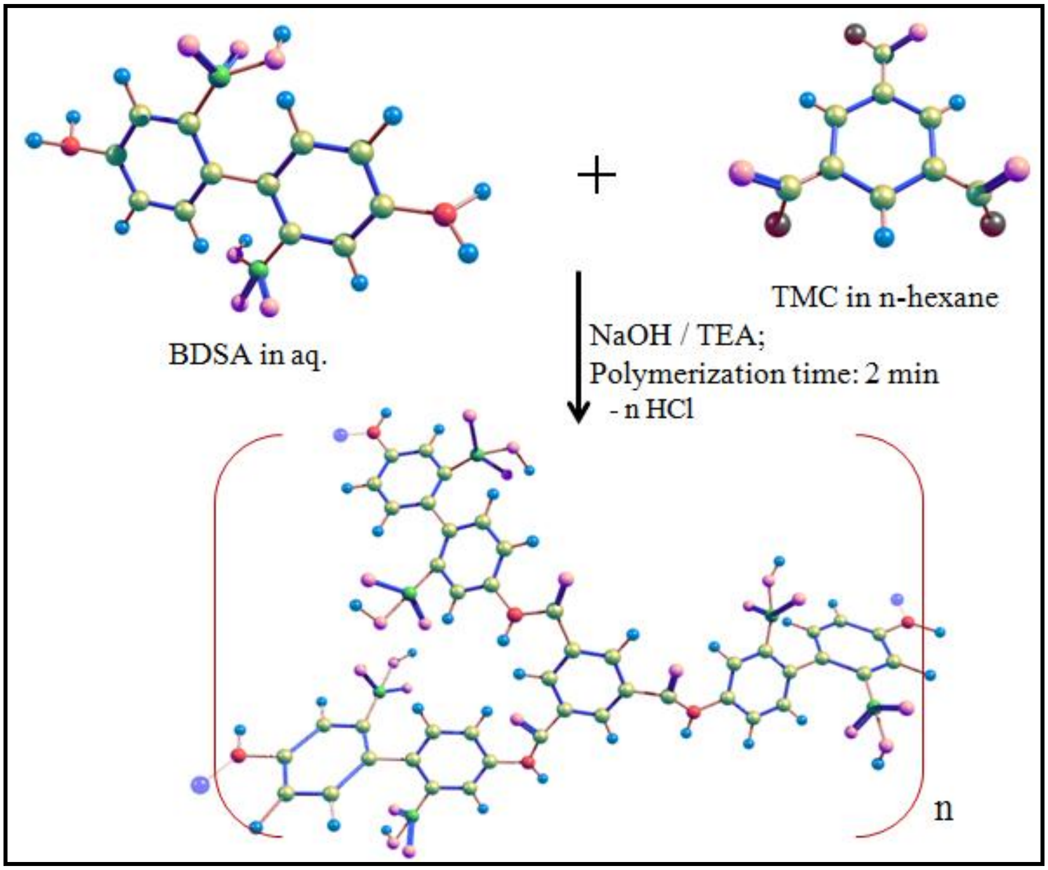

Fig. 3. 3 Reaction scheme for the BDSA-TMC based crosslinked polyamide, as formed during development of TFC-NCNF membranes [Membrane codes: NCNF-V & NCNF-VI].

Table 3. 4

Ternary composition of monomers and experimental conditions for development of BDSA & PIP based TFC-NCNF membranes.

Sr No.	Membrane Code	Amine Monomer (w/v)% (Aqueous)		Acid Aceceptor/ Solubiliser	Acid Chloride Monomer (w/v)% (organic; n-hexane)
		BDSA	PIP		TMC
1	NCNF-VII	3	1	NaOH 10 (w/w$_{BDSA}$)%	0.2
2	NCNF-VIII	3	1	NaOH 10 (w/w$_{BDSA}$)%	0.3

- Soaking time: 4 min; Polymerization time: 2 min; Curing time: 30 min; Curing temperature:100(±1) °C

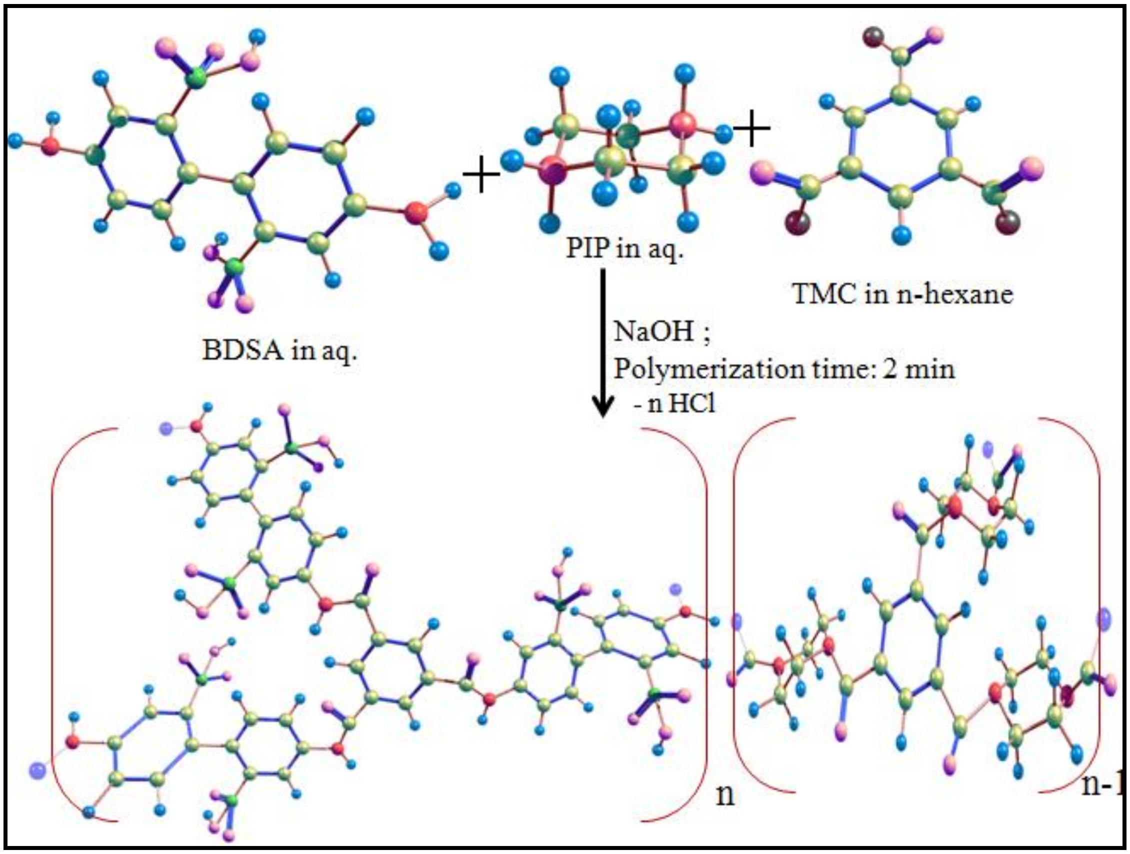

Fig. 3. 4 Reaction scheme for the BDSA-PIP-TMC based crosslinked co-polyamide, as formed during development of TFC-NCNF membranes [Membrane code: NCNF-VII & NCNF-VIII].

3.2.3. Physicochemical characterizations of the TFC-NCNF membranes

3.2.3.1. Spectral features of skin layers of TFC-NCNF membranes

The Bruker Vertex 70 FTIR spectrometer equipped with an ATR (Attenuated Total Reflectance) accessory (ZnSe crystal, 45^{o} angle of incidence and refractive index of 2.4) was employed for ATR-FTIR analysis of the skin layers of the membranes to investigate the presence of functional groups on their skin surfaces. The membranes' skin surfaces were kept faced down onto the ATR crystal element and a light pressure was applied using a MIRacle high pressure clamp with torque-limited press. The radiation penetration depth was 2 µm. All infrared spectra were recorded in absorbance mode over a wave number range 600-4000 cm^{-1} at 25 ^{o}C. For evaluation, 200 scans were taken with a spectral resolution of 2 cm^{-1}.

3.2.3.2. Investigation of skin surface morphology of TFC-NCNF membranes by SEM

Surface-morphology analysis of the membranes was carried out using CamScan MAKE – CS3200LV, UK to investigate morphological characteristics of the skin layers with variation in membranes functional nature. In order to make membranes electrically conductive, all the membrane samples, as dried in room atmosphere were cut into 2 mm × 2 mm strips and then fixed with carbon tape on brass holders. A conducting layer of Au/Pd (60:40) alloy was coated on the skin surfaces of the membranes using a sputter coater, Quorum (Q150R ES) under optimized coating conditions (sputtering time: 60 s, sputter current: 30 mA and tooling factor: 2.3). The skin layer images were taken at an acceleration voltage of 20 keV and 1000X & 4000X of magnifications when operated in secondary electron mode.

3.2.3.3. Skin surface topography study of TFC-NCNF membranes by AFM

Membranes' skin surface topographies were analyzed by recording the two dimensional and three-dimensional topographies, using an AFM instrument (NT-MDT SOLVER next, Russia) adopting the semi-contact mode. Small squares of the membranes (approximately 1 cm^2) were cut and glued on to a metal substrate. The rectangular cantilever NSG 10 (NT-MDT, Russia) was made out of Si_3N_4 with a spring constant of 11.8 N/m, having 240 kHz resonance frequency and a nominal tip apex radius of 10 nm with a high aspect ratio. The scanning was done on a 5 µm×5 µm areas of the membranes in air, at room temperature (25 ^{o}C), with a scanning frequency of 0.1Hz. The scanned region was flattened using a second order polynomial to remove curvature and slope from the image and then the resulting best fit was subtracted from the image. For image acquisition and evaluation of surface roughness parameters of the membranes NOVA-P9 software was used. For comparing the surface roughness parameters of different membrane samples, the same scan size range is used since the roughness is dependent on the spatial wavelength of the scan area i.e. both lower and higher frequencies of the scan area. Variation of the membranes' skin surface textures and roughness were evaluated by three dimensional surface-topographic measurements which provide specific 3D roughness parameters namely field parameters comprise of amplitude parameters, spatial parameters, functional parameters and hybrid parameters.

3.2.3.4. Evaluation of hydrophilicity of TFC-NCNF membranes by contact angle analysis

Static contact angle measurement with water at ambient temperature was performed using sessile drop method with contact angle measuring instrument (DSA 100 of KRUSS Gmbh, Germany) to assess the hydrophilicity for the active skin layers of the membranes. The sessile drop was slowly and steadily formed on the membrane surface by depositing 3 µl of the selected liquids with a microsyringe for a residence time of 60 sec. At least eight measurements of contact angles were performed at membrane/water/air interface on different locations of each membrane surface and then averaged to yield the contact angle with their standard deviations.

3.2.3.5. Electrokinetic studies of TFC-NCNF membranes by streaming potential analysis

The electrokinetic features of the membranes were evaluated by employing ZetaCAD electrokinetic analyzer (CAD Inst., France). The streaming potential analyzer consisted of a quartz-cell configuration which was capable of holding two flat sheet membranes in such a way that the membranes remained separated by spacers and the skin layers faced each other creating a slit channel for tangential flow of electrolytic solution across the membranes. The electrical potential difference, generated due to the bidirectional flow of electrolyte solution (10^{-2}, 10^{-3} and 10^{-4} M KCl) under pressure gradient across the membrane was measured by Ag/AgCl electrodes, equipped with the cell. Zeta potentials of the membranes were evaluated utilizing the streaming potential values and the relationship between the measurable streaming potential (V_{st}) and the zeta potential (ζ), following the Helmholtz-Smoluchowski equation. An average value of ζ from three replicates was reported and the measurement error was found to be ± 0.5 mV. The values of ζ were further employed to calculate electrokinetic surface charge densities (σ_s) at the shear planes of the membranes as a function of the respective pH environments.

3.2.3.6. Determination of ion exchange capacities of the TFC-NCNF membranes

The ion exchange capacities (IEC) of negatively charged membrane was determined by placing the membranes in 0.1N HCl for 24 hrs to convert all the negatively charged sites in H^+ form, and then after several wash with water to remove the traces of HCl from the membrane's surface. Thereafter, the membranes were cut in small pieces, placed in 500 ml flask having 200 ml of 0.1N NaOH solution. The samples were left in the solution for another 24 hrs. After that 5 ml of the aliquot was pipetted and titrated against standard HCl (0.1N).

$$\text{Memb.}^{-}\,\text{Na}^{+} + \text{H}^{+} \rightarrow \text{Memb.}^{-}\,\text{H}^{+} + \text{Na}^{+}$$

$$\text{Memb.}^{-}\,\text{H}^{+} + \text{Na}^{+}\,\text{OH}^{-} \rightarrow \text{Memb.}^{-}\,\text{Na}^{+} + \text{H}_2\text{O}$$

The ion exchange capacity was estimated from Eq. 5

$$\text{IEC} = (N_{NaOH}\,.\,V_{NaOH}) - (40.\,N_{HCl}.\,V_{HCl}) / m_{dry} \qquad (5)$$

Where, V_{NaOH} & N_{NaOH} are the volume & normality of NaOH taken initially for exchange with the membrane; N_{HCl} & V_{HCl} are the volume & normality of HCl consumed by the aliquot NaOH after the exchange process. m_{dry} is the mass of the dry membrane.

3.2.4. Performance evaluation of membranes

3.2.4.1. Evaluation of characteristic features of Psf base membrane

For measurement of porosity of the Psf base membrane, gravimetric method was applied. There, a circular piece of the Psf membrane with an area -A and thickness -h was weighed after taking it out from storage of distilled water and then carefully removing the superficial water with filter paper. The wet membrane was dried in a vacuum oven at 75 °C for 24 h before measuring the weight in dry state. From the weights of the membrane sample in wet (W_0) and dry (W_1) states, the porosity (ø) of membrane was calculated using Eq. 14. In order to minimize the experimental error, measurements were carried out in duplicates and then calculated the average.

Pure water flux measurement of the Psf base membrane with effective membrane area of 14.4 cm^2 was conducted under a cross-flow filtration mode operated at 1 bar of transmembrane pressure. The steady-state pure water flux (PWF, $L.m^{-2}day^{-1}$ or LMD) was determined by direct measurement of the permeate flow *i.e.*, volume (V, in L) collected during a time period (T, in day) through a membrane area (A, in m^2) at certain pressure. Prior to the UF test experiment, membrane was initially subjected to undergo hydraulic compaction for 1 h in water at standard UF test conditions, to achieve stabilized performance of the membrane.

The porosity of the membrane and mean pore radius (r_m in nm) was determined by employing the Guerout–Elford–Ferry equation. For measurement of MWCO of the Psf base membrane, analysis of solute rejection behavior was carried out using neutral organic solutes such as PEG with average Mw of 12k, 20k, 35k Da and PEO with average Mw of 100k Da. The test solutions were prepared by dissolving pre-weighed amounts of PEG or PEO in ultra-pure water at a concentration of 200 ppm. The solute rejection studies were carried out at a transmembrane pressure of 1 bar at room temperature. The concentration of PEG or PEO in both feed and product were measured by analysing the total organic carbon (TOC) content of the samples using TOC analyzer (ANATOC-II, SGE analytical science, Australia). The MWCO was determined from a plot of solute rejection *vs* molecular weight, generated in order to construct a MWCO curve, which implies a molecular weight of the organic solute that is 90% retained by the Psf base membrane.

Measurement of mechanical stability of the base membranes were carried out with a universal tensile testing machine (Hemetek Techno Instrument, model LRX Plus, India), at 25°C with a relative humidity of 40-50%. A constant deformation rate of 100 mm/min was controlled during the analysis. For analysis, dumb-bell shaped specimens of the membrane samples with length of 4 cm and width of 0.6 cm were employed. Tensile strength (TS) and percent elongation at break (EB) were calculated for the membranes in duplicates, using the NEXYGEN plus software.

3.2.4.2. Nanofiltration performance evaluation of TFC-NCNF membranes

The evaluation of transport properties of the TFC-NCNF membranes was conducted using a cross-flow test cell, at 15 bar trans-membrane pressure. Circular membrane samples, with an effective membrane area of 14.4 cm^2 were properly washed in de-ionized water and then placed in the test cell with the membranes' active skin layers facing the incoming feed solution. To maintain a steady feed concentration, the experiments were carried out in recycle mode *i.e.*, both the concentrate and the permeate streams were recirculated into the feed tank. Iso-osmotic feed solutions comprising of varying combination of mono- and bi-valent cations and anions, such as 0.03M NaCl, 0.02M Na_2SO_4, 0.02M $MgCl_2$ and 0.03M $MgSO_4$ were employed for performance evaluation of membranes. The feed solution temperature was maintained at 25-30 ^oC. Prior to the start of data accumulation, steady-state conditions were achieved for all the NF test experiments when the membranes were allowed to get stabilized by operating for long-run. The solute concentrations in the feed and permeate solutions were obtained through the measurement of conductivities of the respective solutions using a digital conductivity meter (TESTRONIX 15, Microlab, Mumbai, India). All membrane samples were prepared and tested in duplicate for NF performances, results of which have been averaged. The steady-state readings of all the cases were recorded and reported. The percentage of solute rejection (SR) was determined by conductivity measurement of the respective solutions. The steady-state solvent flux (J_w), expressed in terms of L.m^{-2}day^{-1} (LMD) was determined by direct measurement of the permeate flow *i.e.*, volume (V, in L) collected during a time period, (T, in day) through a membrane area, (A, in m^2) at certain pressure.

For evaluation of the membranes' performances in mixed salt streams comprising of NaCl - Na_2SO_4 and $NaNO_3$ - Na_2SO_4, representative membranes, one each from binary and ternary monomeric compositions, namely NCNF-II and NCNF-IV, respectively have been used for the separation of salt streams. The mixtures of salt stream containing 1000 ppm each of the mentioned salts were treated with the membranes at 10 bar applied pressure.

3. 3. Results and Discussion

3.3.1. Physicochemical characterization of TFC-NCNF membranes

3.3.1.1. Spectral analysis of skin surfaces of the TFC-NCNF membranes by ATR-FTIR

The FTIR spectra of skin surfaces of the TFC-NCNF membranes, as derived using the monomeric compositions listed in Tables 3. 1a, 2a, 3a and 4a are presented in Figs. 3. 5a, 5b, 5c and 5d, respectively. The formations of polyamide type skin layers for the membranes: NCNF-I & NCNF-II and the membranes: NCNF-V & NCNF-VI, prepared using the binary monomeric compositions, through *in situ* interfacial polymerization process, have been substantiated by the characteristic IR spectral information (Table 3. 5) for secondary amide linkages. The incorporation of sulfonic acid groups in the membrane is also evidenced by the presence of its' related IR signals *i.e.*, –SO_2 symmetric stretching and –SO_2 asymmetric stretching signals in the spectra. The absence of any characteristic peak for the –COOH indicates that all the reactive sites of TMC (–COCl groups) have participated in the reaction leading to formation of crosslinked polyamide structures as skin surface polymer materials of the respective TFC-NCNF membranes.

Similarly, in case of ternary monomeric compositions, the formations of the co-polyamide type skin layers of the membranes: NCNF-III & NCNF-IV and the membranes: NCNF-VII & NCNF-VIII, through *in situ* interfacial polymerization process have been evidenced by the presence of characteristic IR signals (Table 3. 5) of secondary and tertiary amide linkages. Here also, the incorporation of the sulfonic acid functional groups is manifested through the presence of –SO_2 symmetric stretching and –SO_2 asymmetric stretching signals of the spectra. Furthermore, the absence of any characteristic peaks for the –COOH groups indicates about the participation of the entire –COCl groups of TMC in the polycondensation reaction, leading to the formations of crosslinked co-polyamide structures as skin surface polymer materials of the respective TFC-NCNF membranes.

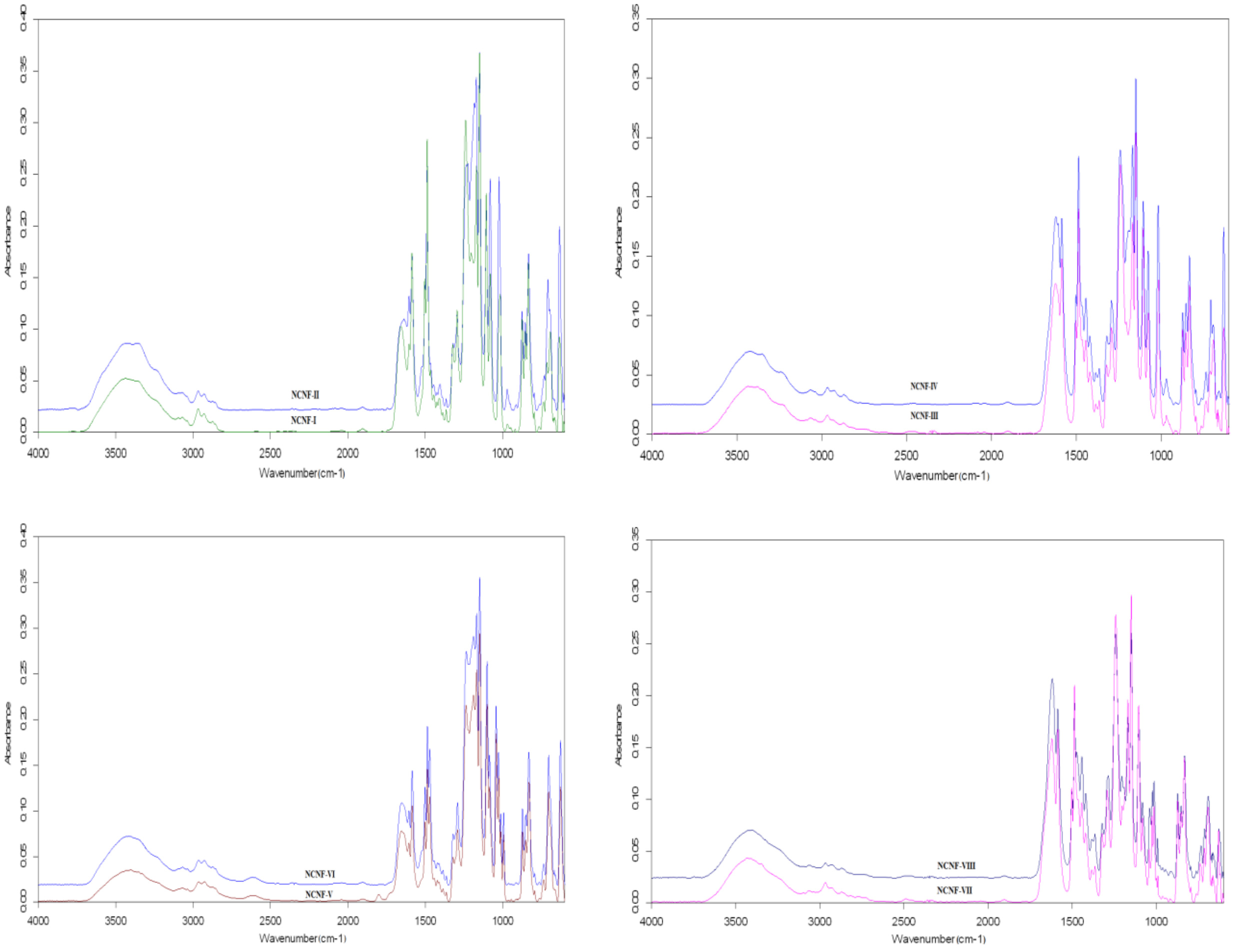

Fig. 3. 5a-5d. FTIR spectra of the skin surfaces of the TFC NF membranes: NCNF-I & NCNF-II, NCNF-III & NCNF-IV, NCNF-V & NCNF-VI and NCNF-VII & NCNF-VIII.

Table 3. 5

Characteristic IR signals of the skin surfaces of TFC NF membranes having polyamide and co-polyamide structures tethered with sulfonic acid groups.

FT IR assignment	**Characteristic Wave numbers (cm^{-1})**			
	NCNF-I & II	NCNF-III & IV	NCNF-V & VI	NCNF-VII & VIII
Amide A H bonded N-H stretching	~3448	~3429	~3434	~3433
Amide B Overtone of amide II	~3068	~3064	~3057	~3057
Amide I C=O stretching	~1658	~1621	~1619	~1619
Amide II C-N stretch + C(=O)-N-H bend	~1487	~1487	~1487	~1487
Amide III C-N stretch + C(=O)-N-H bend (in opposite phase)	~1239	~1242	~1242	~1243
Amide IV In plane C=O bend	~971	~969	~993	~993
Amide V Out of plane N-H bend	~707	~707	~703	~703
SO_2 symm. stretching	~1149	~1149	~1149	~1149
SO_2 asymm. stretching	~1322	~1320	~1322	~1322
CH_2 asymm. stretch	~2928	~2928	~2928	~2928
CH_2 symm. stretch	~2872	~2869	~2866	~2854

3.3.1.2. Skin surface morphological analysis of TFC-NCNF membranes by SEM

Skin surface SEM images of the TFC-NCNF membranes, made with binary monomeric compositions, *i.e.*, NCNF-II and NCNF-VI, presented in Figs. 3. 6a and 8a (with 1000x magnification) and Figs. 3. 6b and 8b (with 4000x magnification) respectively, reveal that the thin skin layers' polymer is interspersed with nodular formations distributed on its entire surface. The higher magnification further shows that the nodular polymeric formations are of random sizes and shapes. However, the skin surface SEM images of the membranes, made using ternary monomeric compositions, *i.e.*, NCNF-IV and NCNF-VIII, where the additional co-monomer is PIP, presented in Figs. 3. 7a and 9a (with 1000X magnification) and Figs. 3. 7b and 9b (with 4000X magnification), respectively, show more frequent occurrences of these nodular polymeric formations which are larger in size and more exposed on the surface of the skin layer than those of former membranes. This indicates that PIP plays a significant role in influencing the nature of the deposited skin layer of the TFC membranes.

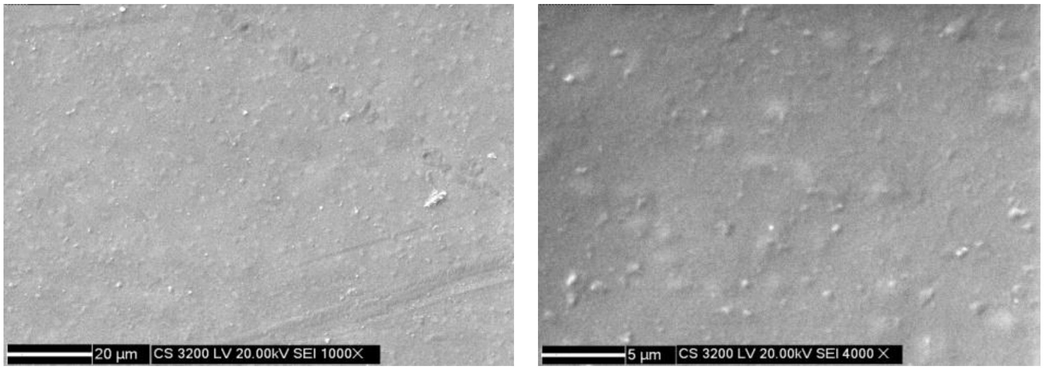

Figs. 3. 6a & 6b SEM images of the skin surface of TFC-NCNF membrane (NCNF–II); Mag.:1000X and 4000X.

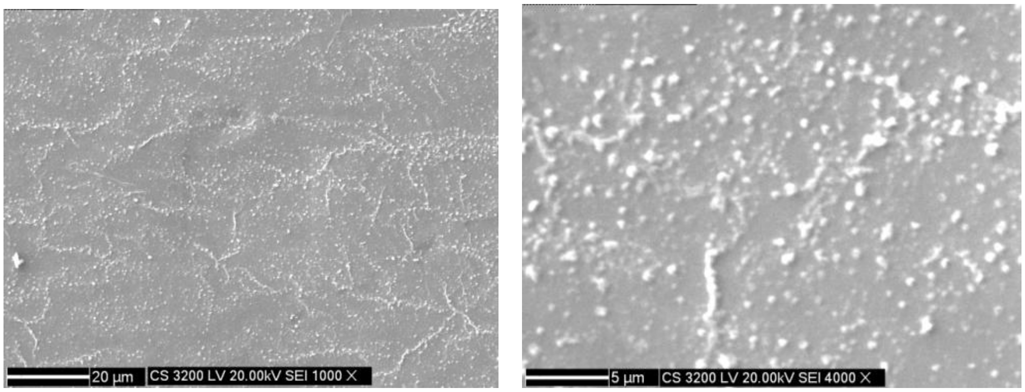

Figs. 3. 7a & 7b SEM images of the skin surface of TFC-NCNF membrane (NCNF–IV); Mag.:1000X and 4000X.

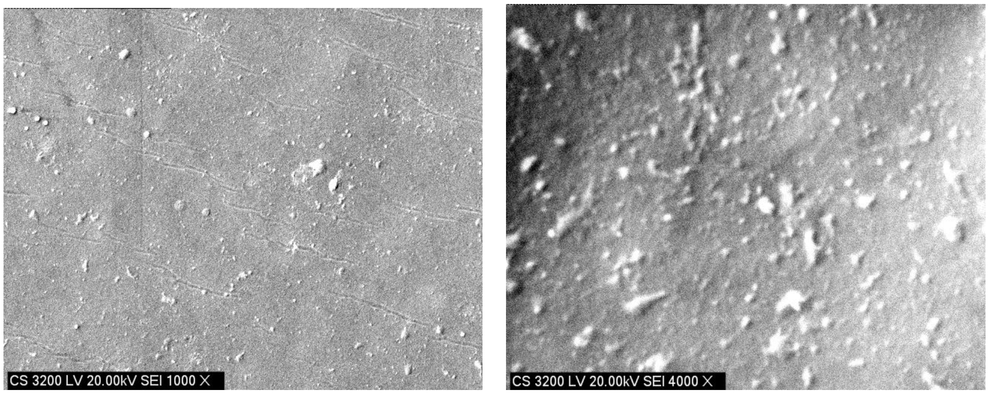

Figs. 3. 8a & 8b SEM images of the skin surface of TFC-NCNF membrane (NCNF–VI); Mag.:1000X and 4000X.

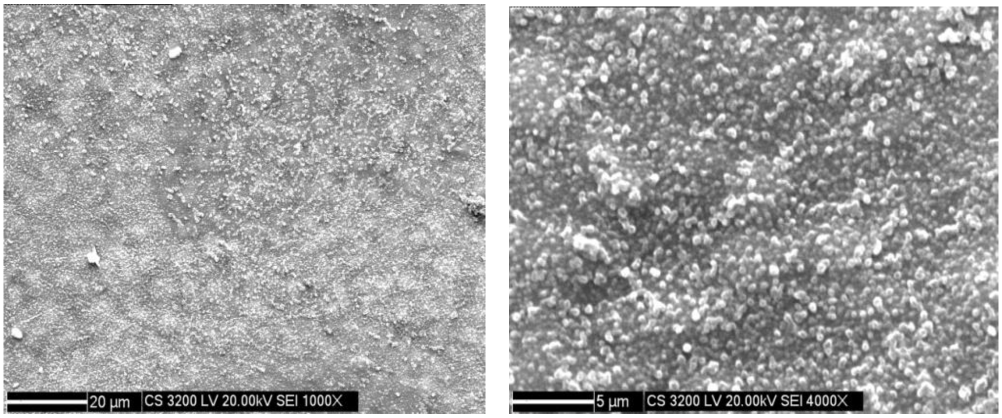

Figs. 3. 9a & 9b SEM images of the skin surface of TFC-NCNF membrane (NCNF–VIII); Mag.:1000X and 4000X.

3.3.1.3. Skin surface topographical study of TFC-NCNF membranes by AFM

The 2D and 3D AFM images of NCNF–II made using binary monomeric composition (*i.e.*, DASDSA and TMC) are presented in Fig. 3. 10a and 10b, respectively and those of the NCNF–IV made using ternary monomeric composition (*i.e.*, DASDSA, PIP and TMC) are listed in Figs. 3. 11a and 11b. Careful observations of the both 2D and 3D images show that the surface features of the NCNF–II are much smoother than those of NCNF–IV. In the 2D images there are distinct occurrences of granular polymeric formations over the entire surface of the NCNF–IV; these features in NCNF–II are much less developed giving making it a surface with less roughness. The corresponding 3D images confirm that the surface roughness is less in NCNF–II than in NCNF–IV. The average surface roughness (R_a) and root mean square roughness (R_q) values listed in Table 6 justify the observations, where both the values are less for NCNF–II (R_a: 5.02 nm and R_q: 6.52 nm) than NCNF–IV (R_a: 27.97 nm and R_q: 45.72 nm).

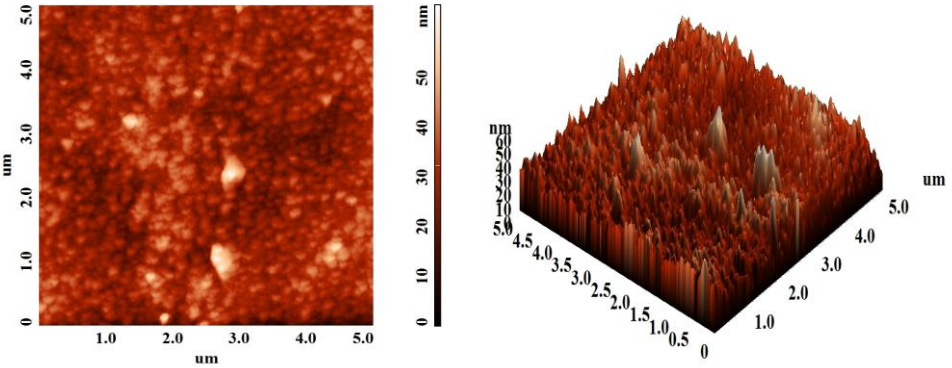

Figs. 3. 10a & 10b 2D and 3D AFM image of the skin surface of TFC-NCNF membrane (NCNF–II).

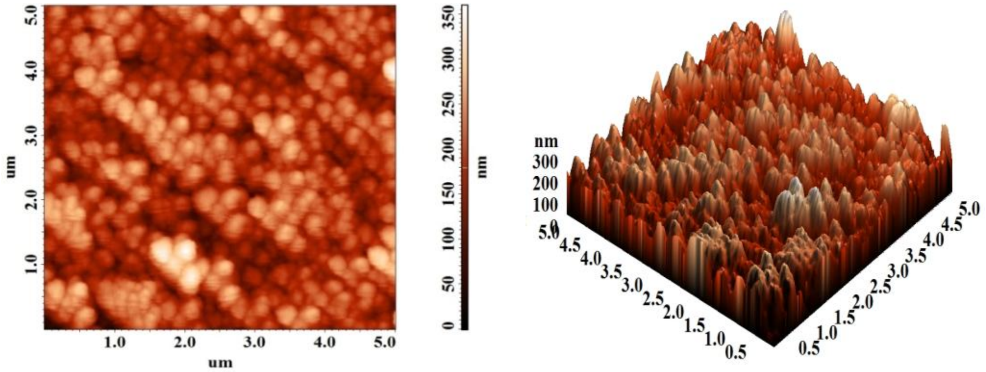

Figs. 3. 11a & 11b 2D and 3D AFM image of the skin surface of TFC-NCNF membrane (NCNF–IV).

Table 3. 6
Surface roughness parameters for TFC-NF membranes: NCNF–II & NCNF–IV.

Membrane code	Amplitude Parameters					
	R_a (nm)	R_q (nm)	R_z (nm)	R_{Sk}	R_{Ku} (%)	R_{dr} (%)
NCNF–II	5.02	6.52	24.71	0.54	4.64	1.21
NCNF–IV	27.97	45.72	16.07	0.09	2.96	25.68

In the same way, careful observation of the 2D and 3D AFM images of the TFC-NCNF membrane, NCNF–VI made using binary monomeric composition (*i.e.*, BDSA and TMC), presented in Figs. 3. 12a and 12b, respectively and those of the TFC-NCNF membrane, NCNF–VIII made using ternary monomeric composition (*i.e.*, BDSA, PIP and TMC), presented in Figs. 3. 13a and 13b, respectively show that the surface features of the NCNF–VI are much smoother than those of NCNF–VIII. The 2D images reveal the distinct occurrences of the granular polymeric formations over the entire surface of the NCNF–VIII; these features in NCNF–VI are much less developed giving making it a surface with less roughness. The corresponding 3D images confirm that the surface roughness is less in NCNF–VI than in NCNF–VIII. The average surface roughness (R_a) and root mean square roughness (R_q) values listed in Table 3. 7 justify these observations, where both the values are less for NCNF–VI (R_a: 21.24 nm and R_q: 36.74 nm) than NCNF–VIII (R_a: 90.36 nm and R_q: 110.62 nm).

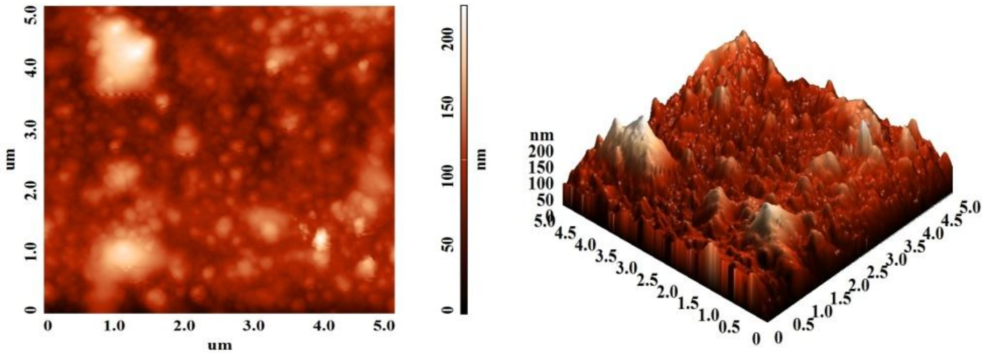

Figs. 3. 12a & 12b 2D and 3D AFM image of the skin surface of TFC-NCNF membrane (NCNF–VI).

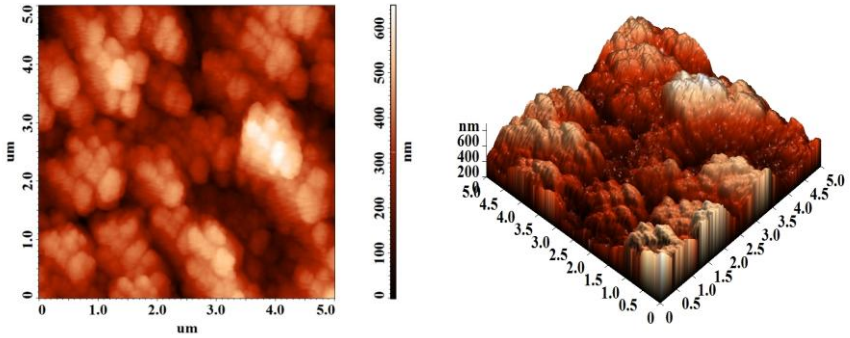

Figs. 3. 13a & 13b 2D and 3D AFM image of the skin surface of TFC-NCNF membrane (NCNF–VIII).

Table 3. 7
Surface roughness parameters for TFC-NCNF membranes: NCNF–VI & NCNF–VIII.

Membrane code	Amplitude Parameters					
	R_a (nm)	R_q (nm)	R_z (nm)	R_{Sk}	R_{Ku}	R_{dr} (%)
NCNF–VI	21.24	36.74	58.91	0.89	4.56	3.78
NCNF–VIII	90.36	110.62	43.68	0.07	2.66	36.86

PIP, used in the ternary composition as a co-monomer of DASDSA and BDSA, is known to have a higher reactivity than the bulkier aromatic diamine monomers, resulting in the formation of a skin layer with thicker and denser polymer network for the TFC-NCNF membranes comprising of co-polyamide type skin layer polymeric material. Further, diffusivity of PIP being higher than that of the bulkier aromatic diamines, there is a faster mass transport of this amine co-monomer through the interfacial barrier layer that might have already formed during the *in situ* interfacial polymerization process, leading to more reaction with the acid chloride and a thicker deposit of the skin layer polymer. These dual effects significantly contribute to the morphological variations like increased surface roughness, and the related parameters of the respective membranes. The lower reactivity as well as lower diffusivity of the lone diaryl diamine monomers *i.e.*, DASDSA and BDSA of NCNF-II and NCNF-VI, respectively do not alter the interfacial property to that extent, as in NCNF-IV and NCNF-VIII, resulting in smoother skin surfaces for the formers. Thus, it is strongly believed that the presence of PIP is largely responsible for all the topographical variations which are observed in the two different types of membranes studied.

The section analysis of height profiles of TFC-NCNF membranes, NCNF–II, NCNF-IV, NCNF-VI and NCNF–VIII, along a particular line in X- (Blue line) and Y- axes (Red line) are presented in Figs. 3. 14a, 14b, 14c and 14d, respectively. They show the variation in distribution of peaks and valleys on the surfaces of the membranes along the selected lateral zones. The height profiles along these lines show that in case of the skin surface of the membrane, NCNF–II the average heights of the peaks (Z-axis) are populated between 15 to 30 nm. Similarly, in case of the membrane, NCNF-VI the average heights of the peaks (Z-axis) are populated between 20 to 50 nm with some occasional peaks rising up to 80 nm. Whereas in case of the membrane, NCNF–IV the average heights of the peaks are populated between 50 to 140 nm, in a more uniformly distributed manner and for the membrane, NCNF-VIII the average heights of the peaks are populated between 50 to 250 nm.

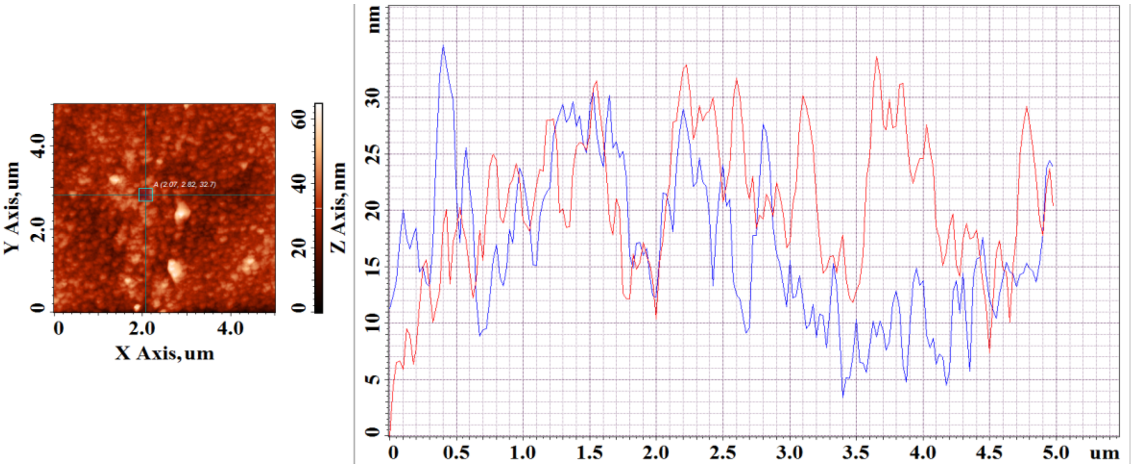

Figs. 3. 14a Section analysis of the scanned skin surface region of TFC-NCNF membrane (NCNF–II).

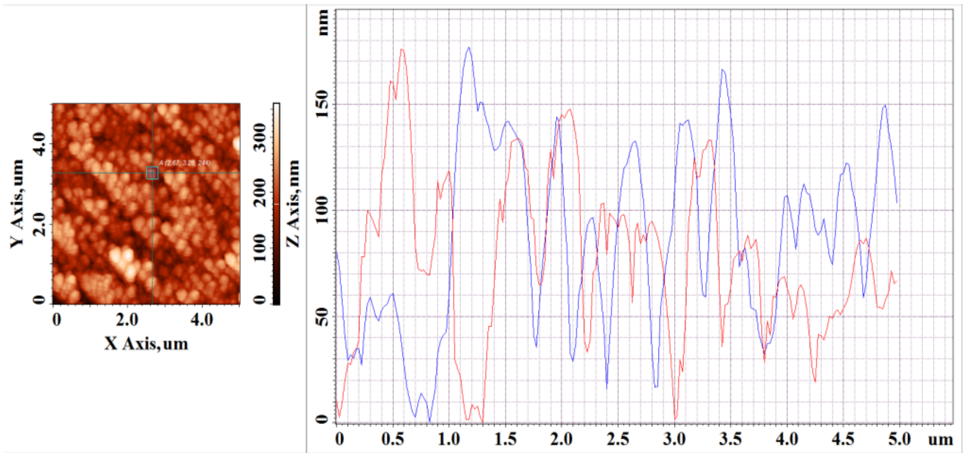

Figs. 3. 14b Section analysis of the scanned skin surface region of TFC-NCNF membrane (NCNF–IV).

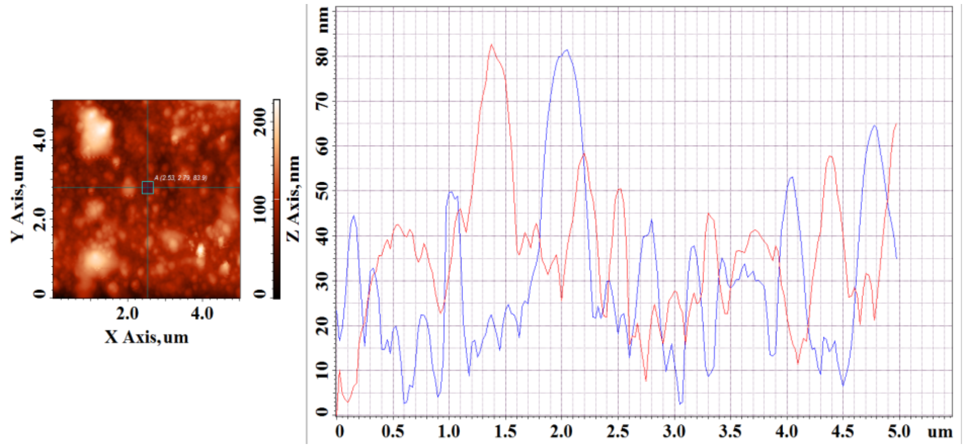

Figs. 3. 14c Section analysis of the scanned skin surface region of TFC-NCNF membrane (NCNF–VI).

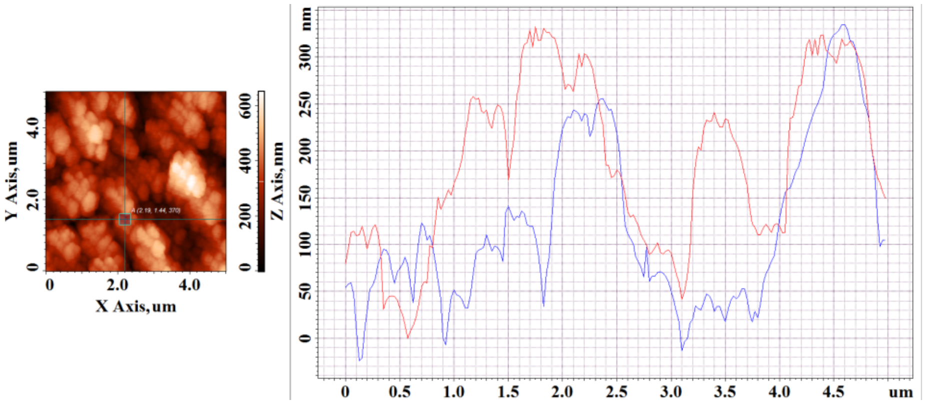

Figs. 3. 14d *Section analysis of the scanned skin surface region of TFC-NCNF membrane (*NCNF–VIII*).*

The height histograms of the TFC-NCNF membranes, NCNF–II and NCNF–VI presented in Figs. 3. 15a and 15c, respectively reveal a narrow Gaussian distribution of peak heights indicating that majority of the peaks are of more or less uniform heights, whereas that of membranes, NCNF–IV (Fig. 3. 15b) and NCNF–VIII (Fig. 3. 15d) provide a Gaussian curve which may be characterized by the occurrence of peaks with a broader distribution of heights. However, there is a significant tailing effect between 150 to 250 nm, though with less population, making the curve of membrane, NCNF–II slightly non symmetrical as compared to the curve of the membrane, NCNF–IV which is near symmetrical in nature. In the former membrane the peak heights range between 20 to 40 nm with majority population having their heights between 25 to 35 nm. In the later membrane the peak heights have a wider range, between 100 to 280 nm with majority population crowded between 120 to 270 nm. In case of membrane, NCNF-VI the peak heights range between 60 to 140 nm with majority population having their heights between 70 to 120 nm. Whereas, the height histogram of the membrane, NCNF-VIII shows the peak heights range, between 100 to 500 nm with majority population having their heights between 150 to 450 nm. These facts can very well be understood from the 3D pictures (Figs. 3. 10b, 11b, 12b and 13b) of the membranes corresponding to these curves.

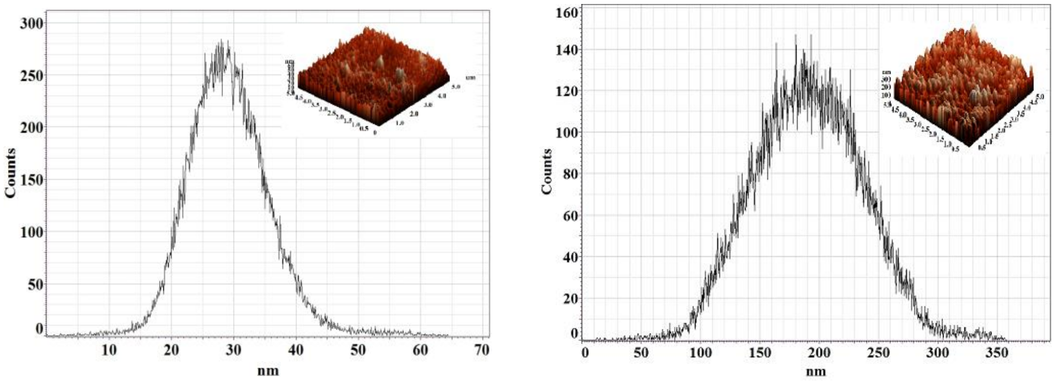

Figs. 3. 15a & 15b Height histograms of NCNF–II and NCNF–IV.

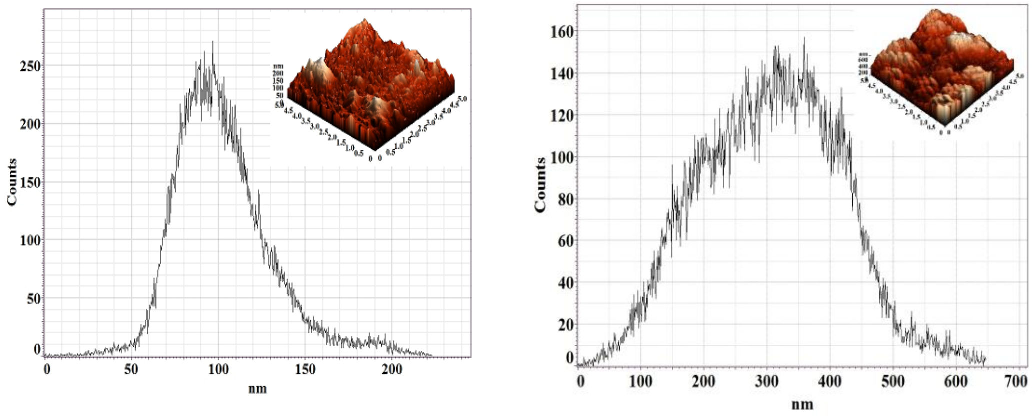

Figs. 3. 15c & 15d Height histograms of NCNF–VI and NCNF-VIII.

In spite of having lower average and rms surface roughnesses, the ten point height, $R_{z,}$ has a higher value for the NCNF–II (24.71 nm) and NCNF–VI (58.91 nm), than that of NCNF–IV (16.07 nm) and NCNF–VIII (43.68 nm). Ten point height, by definition, denotes the contrast between the heights and depths of extreme peaks and valleys that may be occasionally present on the surface of the membrane. The higher values in NCNF–II and NCNF–VI indicate the presence of greater heterogeneity among the surface peaks and valleys than those of NCNF–IV and NCNF–VIII, which is clearly observable in the respective 3D images. The lower R_z values of NCNF–IV and NCNF–VIII result from a surface having peaks and valleys of less contrast in heights and depths. The observations of these surface features in terms of the R_z values are quite indicative of the role of PIP in controlling the morphological features like peaks and valleys on the surface of the ultra thin barrier layer of the resulting TFC-NCNF membrane.

The positive values of the membrane skewness, R_{Sk}, result from the presence of filled in valleys and high peaks in the membrane surfaces. The values presented in Tables 3. 6 and 3. 7 show that the skewness of the membranes, NCNF–II and NCNF–VI are more than that of the membranes, NCNF–IV and NCNF–VIII which is due to the presence of occasional high peaks in NCNF–II and NCNF–VI leading to an unsymmetrical height distribution. The very low skewness values of NCNF–IV and NCNF–VIII, close to zero, are indicative of the fact that the membrane surfaces have near symmetrical distribution of heights *i.e.*, peaks and depths *i.e.*, valleys and with much less irregular occurrences. Thus PIP helps in influencing the skewness properties of the membranes leading to the formation of much orderly features.

The higher positive Kurtosis coefficients, R_{Ku} *i.e.*, 4.64% and 4.56% for the membranes, NCNF-II and NCNF-VI indicate a dominantly peaked distribution on the surfaces of the membranes. A higher R_{Ku} value for the membranes NCNF-II and NCNF-VI make it leptokurtic that is sharper than a normal distribution, with values concentrated around the mean and thicker tails and probability for extreme values. Such distribution curve implies extremities and sharpness of the peaks over the normal distribution. Whereas, a lower R_{Ku} value of 2.96% and 2.46% for the membranes, NCNF-IV and NCNF-VIII makes them platykurtic having characteristics of a wider distribution of peaks around the mean value and associated with less extremity of peaks. The value however approaches mesokurtic distribution (R_{Ku} =3). The height histograms of these membranes are also indicative of these features.

The surface area ratio, S_{dr}, is higher for the TFC-NCNF membranes, NCNF-IV and NCNF-VIII (25.68 and 36.86%, respectively) due to its higher surface roughness than for the TFC-NCNF membranes, NCNF-II and NCNF-VI (1.21 and 3.78%, respectively). Such higher surface area ratio can provide better wettability to the membrane surfaces of the former membranes as compared to the later membranes. The change in morphological and topographical features of the TFC-NCNF membrane's skin surface show their dependency on the ordering of the polymer chains constituting them, since they get affected by the kinetics of formation of the polymer during the *in situ* interfacial polymerization process as it is controlled by the rate of mass transfer through the interfacial layer.

3.3.1.4. Evaluation of hydrophilicity of TFC-NCNF membranes by contact angle analysis

The hydrophilic nature of any polymer is in major part a function of the chemistry of its' constituent monomers and its' polymeric linkages. Quantitative estimation of hydrophilic/hydrophobic nature of the membranes by contact angle measurements (Table 3. 8) show that skin surfaces of the membranes derived from ternary monomeric compositions (DASDSA+PIP+TMC: NCNF-IV & BDSA+PIP+TMC: NCNF-VIII) are more hydrophilic as compared to the skin surfaces of the membranes derived from respective binary monomeric compositions (DASDSA+TMC: NCNF-II & BDSA+TMC: NCNF-VI) under similar membrane preparative conditions. The trend implies that the extents of presence of hydrophilic sites (>C=O, N–H and $-SO_3H$) in the skin layer-air or skin layer-solvent interface get affected by the variant molecular architectures of the co-polyamide in comparison to the polyamide.

Table 3. 8

Contact angle results of the TFC-NCNF membranes.

Membrane Code	θ_w, (°)
NCNF-II	61.2 ± 0.6
NCNF-IV	55.9 ± 2.7
NCNF-VI	39.1 ± 2.0
NCNF-VIIII	29.5 ± 2.7

The reason of such behavior is due to the higher reactivity of PIP monomer as compared to the DASDSA or BDSA monomer, towards the crosslinking monomer TMC, which results in more H-bonding interactions between the water molecules and the amide linkages of the co-polyamide chains, enhancing the hydrophilicity of the surfaces. The more hydrophilic nature of the polyamide and co-polyamide type of membranes comprising BDSA as compared to the polyamide and co-polyamide type of membranes comprising DASDSA is reasonably due to the use of higher concentration of the cross-linking agent, TMC as well as prolonged polymerization time for formation of the former.

3.3.1.5. Analysis of surface charge properties of the TFC-NCNF membranes

Electrokinetic behaviors of charged surfaces of the TFC-NCNF membranes, determined by tangential streaming potential measurements with respect to 10^{-3}M KCl solution are represented in Table 3. 9. The surfaces of the membranes acquire stationary layer of negative charges due to the presence of tethered sulfonic acid groups bearing anionic charges. Thus, determination of ζ for the negatively charged TFC-NCNF membranes provides an understanding on the electrostatic interactions between the membranes' surface charges and the mobile ionized species of the ionic solutes. Both types of the TFC-NCNF membranes, NCNF-IV and NCNF-VIII, comprising of co-polyamides as the skin layer polymers show more negative ζ values, indicating the presence of higher surface negative charges. Whereas, the TFC-NCNF membranes, NCNF-II and NCNF-VI, comprising of polyamides as the skin layer polymers exhibit comparatively lower negative ζ values, indicating the presence of less surface negative charges. The electrokinetic features of the membranes further substantiate that the presence of

PIP eventually promotes the inclusion of more number of negative charge bearing sites in the co-polyamide structure based skin layers of the membranes as compared to the membranes derived from the binary monomeric compositions.

Table 3. 9

Electrokinetic features and ion exchange capacities of the negatively charged TFC-NCNF membranes.

Membrane Code	**V_{st} (mV/mBar)**	**ζ (mV)**	**σ_s (C/m^2)**	**IEC (meq./g)**
NCNF-II	-5.08×10^{-2}	- 12.52	$- 0.91\times10^{-3}$	0.78
NCNF-IV	-5.21×10^{-2}	- 19.73	$- 1.43\times10^{-3}$	0.89
NCNF-VI	-6.55×10^{-2}	- 18.84	$- 1.37\times10^{-3}$	1.35
NCNF-VIII	-4.76×10^{-2}	- 23.07	$- 1.68\times10^{-3}$	1.41

The IEC determinations of the negatively charged TFC-NCNF membranes, presented in Table 3. 9 provide the information about the presence of total amount of exchangeable acidic ($-SO_3H$) groups in the membranes' skin surfaces or total fixed surface charges of the membranes. The IEC values of the DASDSA containing membranes are 0.78 meq/g dry for NCNF-II, 0.89 meq/g dry for NCNF-IV and those for the BDSA series of membranes are 1.35 meq/g dry for NCNF-VI and 1.41 meq/g dry for NCNF-VIII. The magnitude of the IEC values for the four categories of TFC-NCNF membranes also account to the facts illustrated earlier, discussing the role of PIP monomer in enhancing the extent of inclusion of the charge bearing monomer into the resultant polymeric structures.

3.3.2. Analysis of cross-flow permeation studies of TFC-NCNF membranes

Analysis of basic features of the Psf membrane, prepared by phase inversion method reveals that the membrane achieves a MWCO of 38k Da and also exhibits PWF of 1900(±10) LMD at 1 bar transmembrane pressure. The mean porosity and mean pore radius of the base membrane are estimated as 59.77% and 24.95 nm, respectively. These values of porosity, mean pore size, MWCO and PWF indicate that the Psf membrane, contributing as a base for growth of the thin skin layers of TFC-PCNF membranes falls in the ultrafiltration range. The mechanical properties of the Psf base membrane reveals that the tensile strength, Young's modulus and % elongation at break are 5.15 MPa, 169.91 MPa and 30.29%, respectively.

3.3.2.1. Study of solute rejection and solvent flux behaviors in single feed systems

The solute rejection behaviors and solvent flux results of the negatively charged TFC-NCNF membranes, NCNF-I and NCNF-II, derived using the monomer DASDSA and TMC are represented in Figs. 3. 16a and 16b, respectively. The membranes, NCNF-I and NCNF-II give 91-92% solute rejection for the bivalent anion containing solute like Na_2SO_4 and 82-87% solute rejection for $MgSO_4$. Such high solute rejections of the sulfate containing solutes are attributed to the strong electrostatic repulsion *i.e.*, Donnan exclusion between the negatively charged skin surfaces resulted by the presence of $-SO_3^-H^+$ groups and the bivalent SO_4^{-2} ions with high charge density approaching at the membrane surface. The membranes, NCNF-I and NCNF-II show 54-62% solute rejection for NaCl and 47-50% solute rejection for $MgCl_2$, respectively. This indicates that solute like $MgCl_2$, having bivalent cation Mg^{2+} exhibits higher affinity towards the negatively charged membrane surface, whereas, solute like NaCl with a combination of monovalent cation and anion show better retention by the membrane because of less attractive interaction with the negatively charged membrane skin surface. The solvent fluxes of the membranes vary from 1020 to 1180 LMD at 10 bar of transmembrane pressure under standard nanofiltration test conditions.

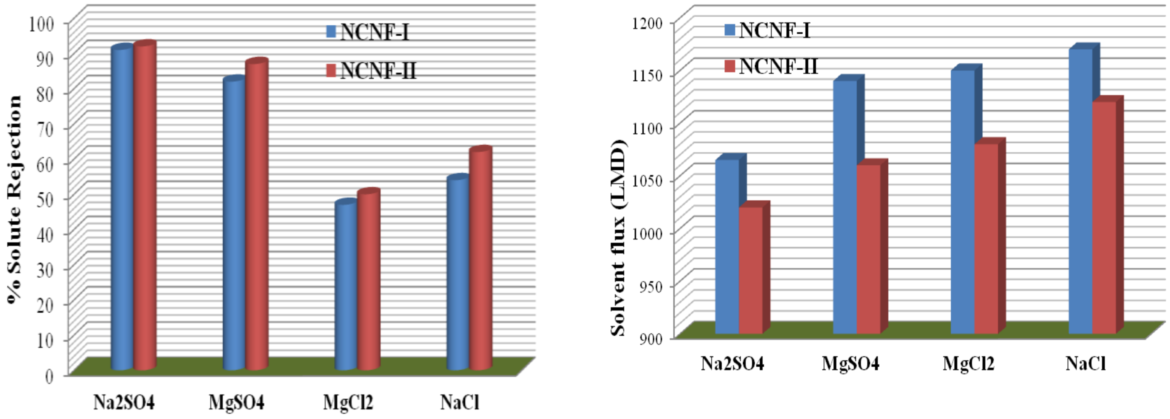

Figs. 3. 16a & 16b Variation of % SR and solvent fluxes for the TFC-NCNF membranes, NCNF-I & NCNF-II.

The solute rejection behaviors and solvent flux results of the negatively charged TFC NF membranes, NCNF-III and NCNF-IV, derived using the monomer DASDSA, PIP and TMC are presented in Figs. 3. 17a and 17b, respectively. Both the membranes provide high solute rejection behaviors towards solutes like Na_2SO_4 and $MgSO_4$. The results show that the % SR for Na_2SO_4 and $MgSO_4$ resides in the range of 90-92% and 88-76%, respectively. This trend is because of the presence of higher density of $-SO_3^-H^+$ groups within the membranes' skin surfaces. However, analyzing the solute rejection behaviors of the membranes, NCNF-III and NCNF-IV, between the solutes $MgCl_2$ and NaCl, it is noticed that there is a higher solute rejection of the former (51-42%) as compared to the later (39-33%), indicating the occurrence of steric exclusion, taking precedence over the Donnan effect. This is because of the hindered spatial interaction of the Mg^{2+} ions with high hydrated radius (0.428 nm) than the Na^+ ions with smaller hydrated radius (0.358 nm), exhibiting the role of the co-monomer PIP in formation of the skin layers' pore structure by the crosslinked architectures of the co-polyamides and consequent hindrance towards transport of larger sized hydrated Mg^{2+} ions as compared to the smaller sized hydrated Na^{+} ions. The solvent fluxes of the membranes (represented in Fig. 17b) reside in 1150 to 1750 LMD at 10 bar of transmembrane pressure under standard nanofiltration test conditions. The enhanced solvent flux behaviors of the negatively charged TFC-NCNF membranes, NCNF-III and NCNF-IV as compared to the membranes, NCNF-I and NCNF-II are corroborated by the physicochemical differences of the two membranes *i.e.*, higher surface roughnesses with higher surface areas, more hydrophilic nature and greater extent of negative surface charges of the formers than the later ones.

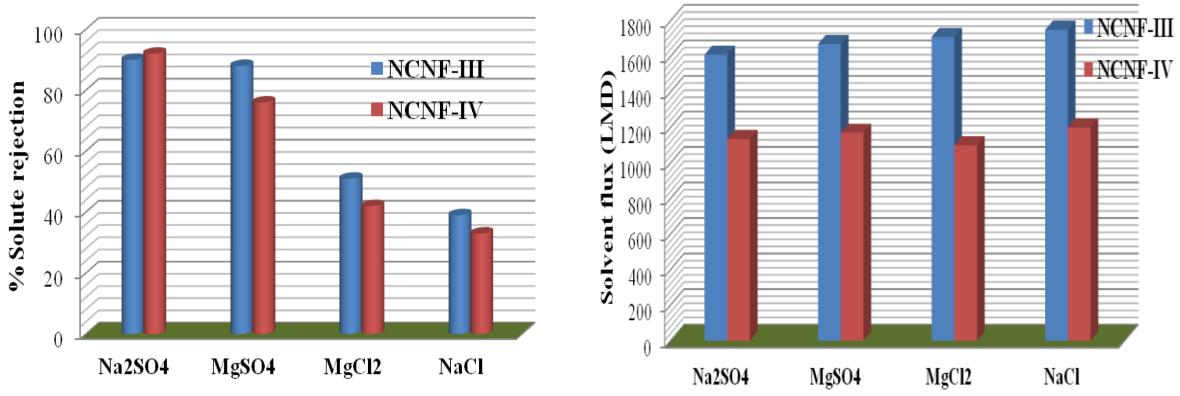

Figs. 3. 17a & 17b Variation of % SR and solvent fluxes for the TFC-NCNF membranes, NCNF-III & NCNF-IV.

For the other types of TFC-NCNF membranes, NCNF-V and NCNF-VI, derived using the monomer BDSA and TMC, the % SR behavior and solvent flux results, as represented in Figs. 3. 18a and 18b, respectively reveal that the membranes provide 89-94% and 74-87% of rejections towards the bivalent anion containing solutes like Na_2SO_4 and $MgSO_4$. This kind of high solute rejections for the sulfate containing solutes are attributed to the strong electrostatic repulsion *i.e.*, Donnan exclusion between the negatively charged skin surfaces of the membranes, resulted by the presence of $-SO_3^-H^+$ groups and the SO_4^{-2} ions. The membranes, NCNF-V and NCNF-VI show 45-49% of rejection for NaCl and 37-41% of rejection for $MgCl_2$. This yet again indicates the fact of preferential passage of $MgCl_2$ over NaCl, implying the higher affinity of the Mg^{2+} and on the contrary, less attractive interaction of Na^+ towards the negatively charged membrane skin surface. The solvent fluxes of the membranes are about 1560 to 1770 LMD at 10 bar of transmembrane pressure under standard nanofiltration test conditions.

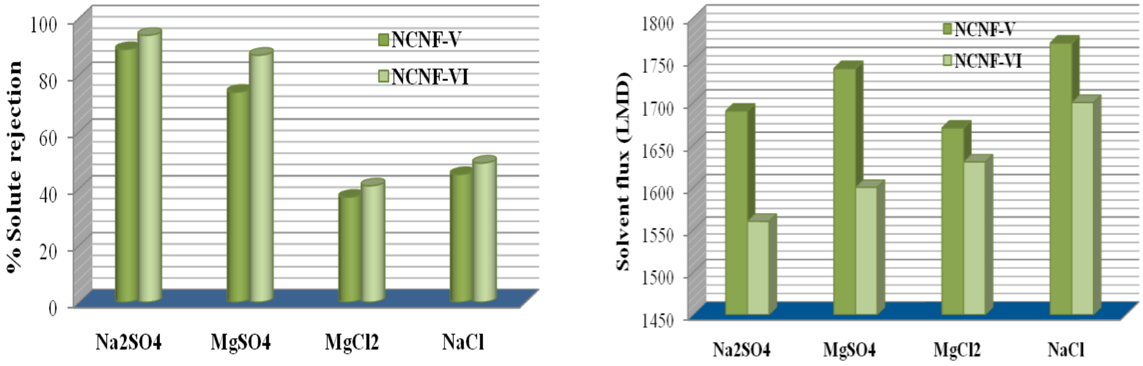

Figs. 3. 18a & 18b Variation of % SR and solvent fluxes for the TFC-NCNF membranes, NCNF-V & NCNF-VI.

The TFC-NCNF membranes, NCNF-VII and NCNF-VIII, derived using the monomer BDSA, PIP and TMC, exhibit different pattern of % SR in comparison to the earlier category of membranes, as presented in Fig. 3. 19a. Both the membranes provide high % SR towards the solutes, Na_2SO_4 and $MgSO_4$ *i.e.*, 95-92% for Na_2SO_4 and 90-91% for $MgSO_4$, substantiating the surface charge characteristics of the respective membranes. The % SR of the membranes, NCNF-VII and NCNF-VIII towards the solutes $MgCl_2$ and NaCl reveal the converse trend of higher rejection of the former (47-45%) as compared to the later (40-27%), indicating the overcompensating role of steric exclusion over the Donnan exclusion, as specifically discussed during illustration of the performances of NCNF-III and NCNF-IV. This further demonstrates that introduction of PIP as co-monomer alters the morphological features of the crosslinked architectures of resultant co-polyamides, tuning pore structures of the membranes as well.

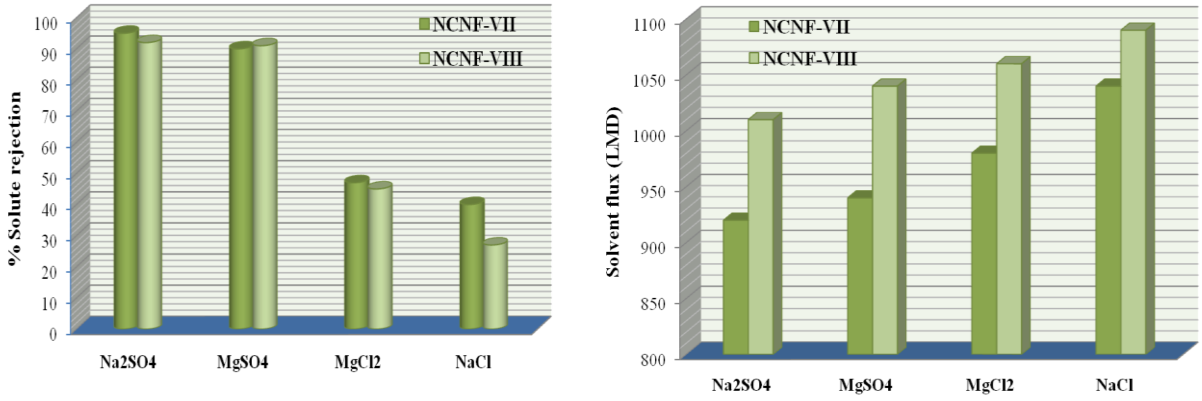

Figs. 3. 19a & 19b Variation of % SR and solvent fluxes for the TFC-NCNF membranes, NCNF-VII & NCNF-VIII.

The solvent flux behaviors of the membranes (Fig. 3. 19b) vary from 920 to 1090 LMD at 10 bar of transmembrane pressure under standard nanofiltration test conditions. Even though the membranes, NCNF-VII and NCNF-VIII have higher surface roughness with higher surface area, more hydrophilic nature and better negative surface charges than the membranes, NCNF-V and NCNF-VI, the reduced solvent flux of the formers is assumed to happen due to the deposition of a thicker and denser crosslinked co-polyamide layers. Such effect of inclusion of PIP along with BDSA in the co-polyamide matrix of the thin skin layer of membranes, NCNF-VII and NCNF-VIII shows a contrast with the membranes, NCNF-III and NCNF-IV with co-polyamide skin layers derived by the use of DASDSA and PIP.

3.3.2.2. Study of solute rejection and solvent flux behaviors TFC-NCNF membranes in mixed salt streams

Representative membranes, one each from binary and ternary monomeric compositions, namely NCNF-II and NCNF-IV have been employed to evaluate the transport behaviors of the membranes in mixed solute streams comprising of NaCl - Na_2SO_4 and $NaNO_3$ - Na_2SO_4.

Table 3. 10

Transport features of NCNF-II and NCNF-IV towards mixed salt streams comprising of NaCl and Na_2SO_4.

Membrane Code	NaCl / Na_2SO_4		
	Ionic rejection (%)		J (LMD)
	Cl^-	SO_4^{2-}	
NCNF-II	42	90	1180
NCNF-IV	45	91	1210

The results, presented in Table 3. 10 indicate about the potentiality of the membranes in fractionally separating a mixture into two streams, one lean in the solute component (NaCl) containing the univalent anion (Cl^-) with a high concentration of the solute component (Na_2SO_4) containing the bivalent anion (SO_4^{2-}) and one lean in the solute component (Na_2SO_4) containing the bivalent anion (SO_4^{2-}) with a high concentration of the solute (NaCl) component containing the monovalent anion (Cl^-).

Table 3. 11

Transport features of NCNF-II and NCNF-IV towards mixed salt streams comprising of $NaNO_3$ and Na_2SO_4.

Membrane Code	$NaNO_3$ / Na_2SO_4		
	Ionic rejection (%)		J (LMD)
	NO_3^-	SO_4^{2-}	
NCNF-II	31	91	1190
NCNF-VII	14	94	1230

Another study on mixed solute streams comprising of $NaNO_3$ and Na_2SO_4, presented in Table 3. 11 exhibits the membranes' ability to fractionally separate the mixture into two streams, one lean in the salt component ($NaNO_3$) containing the univalent anion (NO_3^-) with a high concentration of the solute component (Na_2SO_4) containing the bivalent anion (SO_4^{2-}) and one lean in the solute component (Na_2SO_4) containing the bivalent anion (SO_4^{2-}) with a high concentration of the solute component ($NaNO_3$) containing the monovalent anion (NO_3^-).

3. 4. Conclusions

The present study towards development of a novel class of negatively charged polyamide and co-polyamide based TFC NF membranes, by employing two different kinds of diaryl diamine monomers containing multiple sulfonic acid groups (*i.e.*, DASDSA and BDSA), either lonely or along with a cyclo-aliphatic diamine monomer (*i.e.*, PIP) provide membranes with better selectivity and improved productivity. In particular, the membranes give very high solute rejection for bivalent anion containing solutes like Na_2SO_4 and $MgSO_4$ and low solute rejection for solutes with monovalent ions like NaCl. The differential rejection patterns of the membranes are attributed to the presence of high negative charges on the membranes' skin surfaces due to the presence of sulfonic acid groups to a higher extent. The high solute rejection of the bivalent anions and low solute rejection of the monovalent anions make this membrane a potential candidate for use in brackish water conditions to produce potable water. This can be achieved by removing hardness causing components to a large extent and a partial removal of other monovalent ions like NaCl from brackish water/ground water making it suitable for drinking and other applications.

CHAPTER – 4

Variation in physicochemical features and separation characteristics of positively charged TFC NF membranes with change in molecular architectures of quaternized poly(ethyleneimine amide)s

4. 1. Introduction

With advancement in the expansive area of positively charged NF membrane based separation processes for extensive industrial applications as well as progressive findings of polymeric materials for production of such potential NF membranes; membranologists find opportunity to enlarge the area of research on this kind of membrane system. Prior efforts by the researchers towards development of positively charged NF membranes following different ways provided various polymeric constitutions with modified structural and physicochemical features. The different ways towards tuning of macroscopical features of such NF membranes included bromination followed by *in situ* amine crosslinking method [9], interfacial polymerization through crosslinking process [10], phase inversion [11], phase inversion followed by *in situ* amination [12], *in situ* amination followed by phase inversion [13-15], sol-gel process [16], UV-induced graft polymerization [17], UV-induced graft polymerization followed by quaternization though crosslinking process [18] and method of glutaraldehyde crosslinking [19] etc. In recent years, the highly branched dendritic architectures of hyperbranched polymers associated with unique chemical and physical properties [20] have gained the attention of the membranologists for development of novel classes of membrane matrices [14]. A group of researchers like Y.-C. Chiang *et al*. [21], S. P. Sun *et al*. [50], X.-Z. Wei *et al*. [22] and S.-J. Park *et al*. [51] reported the development of various nanofiltration membranes from a hyperbranched polymer like poly(ethyleneimine), employing the advantageous availability of plenty terminal functional groups in it. Among various categories of NF membranes, thin film composite (TFC) type, comprising of ultra-thin polymeric skin layer with positively charged functionalities, fabricated on a chemically different thicker polymeric asymmetric porous layer as support substrate has drawn much attention due to their superior surface features and transport mechanisms. In an attempt, made by T. K. Dey *et al*. [23], TFC type positively charged NF membranes were successfully developed by *in situ* interfacial polymerization process, employing glycidyltrimethyl ammonium chloride (GTACl) functionalized branched poly(ethyleneimine) having quaternized amine sites, as amine monomer and terephthaloyl chloride (TPC), as acid chloride monomer. An extensive illustration was made there on the variation in performances of the charged NF membranes with respect to the effect of functionalization as well as degree of functionalization of the branched poly(ethyleneimine) and membrane preparative conditions like curing temperature, duration of curing and reactant concentration. The surface features of TFC type NF membranes vary with the process parameters like monomeric nature, composition and concentration; membrane preparative conditions like polymerization time, reaction temperature, curing type, curing duration and its' extent; and also with the consequent effect of polymeric crosslinking density, porosity, segmental orientation and their distribution over the surfaces. Therefore, knowledge of structural, morphological, topographical as well as hydrophilic-electrokinetic features of a membrane through an in depth investigation of the process parameters and subsequent optimization of the physicochemical properties become immensely significant since they exclusively supervise the macroscopical behaviors of the membranes, such as high rejection capability towards specific solutes and better throughput towards the solvent.

In this study, we report the details of our attempt to develop and characterize another potential TFC type NF membranes having tethered positive surface charges, made by employing GTACl functionalized branched amine-rich polycationic polymer, BPEI of varying molecular weights and TMC as the crosslinking acid chloride monomer. The different as-synthesized functionalized branched poly(ethyleneimine), BPEI precursors were comprehensively characterized by ^{1}H-

NMR and FTIR spectroscopic techniques. The membranes were fabricated on a polysulfone base membrane by *in situ* interfacial polymerization of the amine and acid chloride monomers. The skin surfaces of the membranes were investigated by FTIR and XPS techniques for structural diagnosis of the polyamide material, developed as selective polymeric layer. Drop shape analysis was employed for determination of hydrophilic behaviors of the membranes. Streaming potential measurement was done to analyze the surface charge variation of the membranes under varying pH environments. The positively charged TFC NF membranes were undergone cross-flow permeation experiments with respect to varying solutes having different permutation of mono- and bi-valent ionic constituents under standard operating conditions. The study focus on analyzing the effect of variation in structural features of the resultant polyamide matrices of the membranes on quaternization of the amine monomers of varying molecular weights, more particularly assessing the variation in hydrophilic - electrokinetic features of the membranes' skin surfaces as well as the concurrent collective effect of them on membranes' performances.

4. 2. Experimental

4.2.1. Materials and methods

Polysulfone (Psf; M_W: 30k Da) from Solvay Speciality Polymers (India), N-methyl-2-pyrrolidone (NMP; purity: ≥ 99 %) from Sigma-Aldrich and polyvinyl pyrrolidone (PVP, K-30; M_W: 40k Da) from SRL (India) were employed to prepare Psf base membrane. The nonwoven porous polyester fabric used as a support material for preparation of the base membrane had a density of 75 g/m^2 and a thickness of 110 μm with an air permeability of 70 dm^3/m^2 at 2 mbar. For evaluation of molecular weight cut off (MWCO) of the Psf base membrane through determination of rejection behaviors towards organic solutes, poly(ethylene glycol) (PEG) of varying molecular weights *i.e.*, 12k, 20k and 35k Da and poly(ethylene oxide) (PEO) of molecular weight 100k Da were procured from Fluka (Germany) and Sigma-Aldrich, respectively. A solution of branched poly(ethyleneimine), BPEI (viscosity: 13k-18k mPa.s at 50 ^{o}C and density: 1.03 g/ml at 25 ^{o}C) with number-average molecular weight, M_n: 10k Da was purchased from Aldrich. An aqueous solution of 30% BPEI (density: 1.07 g/ml at 20 ^{o}C) with M_n: 50k-100k Da was obtained from Alfa Aesar. The BPEI with higher M_n of 600k-1000k Da (50% aqueous solution) was procured from Fluka. The functionalizing agent, glycidyltrimethyl ammonium chloride (GTACl, assay: ≥ 90%) was obtained from Aldrich. The crosslinking monomer: trimesoyl chloride (TMC; purity: >99%) was purchased from Sigma-Aldrich. Analytical grade n-hexane, magnesium chloride heptahydrate ($MgCl_2.7H_2O$), magnesium sulphate hexahydrate ($MgSO_4.6H_2O$), anhydrous sodium sulphate (Na_2SO_4), sodium chloride (NaCl) and potassium chloride (KCl) were procured from different companies in India. For contact angle measurements, the solvents were used as received: ethylene glycol (Qualigen, assay: 98%) and diiodomethane (Spectrochem, assay: 98%). The conductivity of mili-Q ultra-pure water used in the experiments was below 2μS/cm.

4.2.2. Fabrication of thin film composite positively charged nanofiltration membranes

4.2.2.1. Preparation of Psf base membrane by nonsolvent induced phase inversion method

Asymmetric flat sheet type porous Psf base membrane was prepared by nonsolvent induced phase inversion method following few consecutive steps. A casting solution comprising of 25 (w/v)% Psf in NMP and PVP (40 w/w% of Psf) as pore-forming additive, was prepared in a hermetically sealed glass-bottle through vigorous agitation for several hours accomplishing complete dissolution of Psf and PVP in the solvent. The resultant viscous solution was kept overnight in an environmentally controlled atmosphere maintaining the temperature and relative humidity at 25 ^{o}C and 35-40%, respectively and then undergone vacuum degassing to eliminate the trapped air bubbles from the solution. The resultant homogeneous polymer solution was cast on a nonwoven polyester support fabric maintaining a uniform thickness of 100 µm, using an automated casting machine. The cast film was immediately immersed in a precipitation bath containing ultra-pure water as nonsolvent. To ensure complete removal of the additive as well as solvent from the membrane matrix, through exchange between solvent and nonsolvent, the resulting membrane was taken out of water bath and adequately rinsed in fresh water several times. The entire process of casting was carried out in a controlled atmospheric condition by maintaining the temperature of the surrounding atmosphere at 24(±1) ^{o}C with a relative humidity of 30–35%.

4.2.2.2. Functionalization of BPEIs with GTACl

The functionalizing agent, GTACl was employed for quaternization of the multifunctional amine monomer, BPEI of all the three different molecular weights (M.W.) *i.e.*, 10k, 50k-100k and 600k-1000k Da, following a typical synthetic method reported by T. K. Dey *et al* [23]. An aqueous solution of 4 (w/v)% BPEI of each molecular weight was allowed to react with 30 (w/w$_{BPEI}$)% of GTACl for a vigorous agitation period of 6 h at an ambient temperature. Facile termolecular-complex mediated *in situ* autocatalysed quaternization was resulted for inclusion of the trimethylammonium groups as positively charged terminal functional-moieties in the branches of polymer backbone.

4.2.2.3. Preparation of TFC-PCNF membranes by in situ interfacial polymerization technique

Positively charged TFC type NF membranes (TFC-PCNF) were prepared adopting *in situ* interfacial polymerization process involving functionalized BPEI and TMC. Pieces of porous Psf base membranes were immersed in the amine-baths containing the respective functionalized BPEI solutions for 3 min. These functionalized amine saturated base membranes were taken out of the amine-baths and squeezed through a pair of rubber rollers to remove the excess solution, making a homogeneous distribution of it over the skin surfaces of the base membranes. The as-treated membranes were then immersed in reaction baths comprising of n-hexane containing 0.1 (w/v)% of TMC, for 30 s, to facilitate the formation of crosslinked thin poly(ethyleneimine amide) films over the surfaces of the Psf base membranes following diffusion limited film growth by *in situ* interfacial polymerization. The base membranes with nascent poly(ethyleneimine amide) thin films were then subjected to undergo heat curing in an air-circulated oven at 90(±1) ^{o}C for 20 min. The resulting membranes having polyamide type of skin layers with fixed charged-moieties were categorized as TFC-PCNF$_{I}$, TFC-PCNF$_{II}$ and TFC-PCNF$_{III}$ based on the M.W. of the BPEIs used *i.e.*, 10k, 50k-100k and 600k-1000k Da, respectively.

4.2.3. Characterization of quaternized BPEI amine monomers

The three different precursor monomeric amines, quaternized BPEIs were characterized by ^{1}H-NMR and FTIR spectroscopy, for establishing the successful derivatisation of BPEIs by GTACl. The ^{1}H-NMR spectra were recorded on a Bruker Avance II-300 (300 MHz for ^{1}H) nuclear magnetic resonance spectrometer (Germany) with a 2.726 s acquisition time, 6 kHz spectral width, 1 s relaxation delay and 40 number of scans. The samples were dissolved in D_2O before carrying out the NMR measurements. FTIR spectra of the functionalized BPEIs were acquired with a Bruker Vertex 70 FTIR spectrometer with 100 scans over the wave-number range of 400-4000 cm^{-1} and a spectral resolution of 4 cm^{-1}.

4.2.4. Characterization of TFC-PCNF membranes

4.2.4.1. Spectral features of skin layers of TFC-PCNF membranes

The Bruker Vertex 70 FTIR spectrometer equipped with an ATR (Attenuated Total Reflectance) accessory (ZnSe crystal, 45^o angle of incidence and refractive index of 2.4) was employed for ATR-FTIR analysis of the skin layers of the membranes to investigate the presence of functional groups on their skin surfaces. The membranes' skin surfaces were kept faced down onto the ATR crystal element and a light pressure was applied using a MIRacle high pressure clamp with torque-limited press. The radiation penetration depth was 2 µm. All infrared spectra were recorded in absorbance mode over a wave number range 600-4000 cm^{-1} at 25 ^{o}C. For evaluation, 200 scans were taken with a spectral resolution of 2 cm^{-1}.

4.2.4.2. Chemical characterization of skin layers of TFC-PCNF membranes

The surface chemical characterization of the TFC-PCNF membranes was carried out using a XPS instrument, DLD-150 electron analyzer (SPECS, Germany) equipped with non-monochomatized Mg-Kα X-ray (300 W, 1253.6 eV) as excitation source. The spectrometer binding energy (BE) scale was calibrated with $Cu_{2p\text{-}3/2}$, $Ag_{3d\text{-}5/2}$, and $Au_{4f\text{-}7/2}$ photoelectron lines at 932.7, 368.3 and 83.95 eV, respectively. The spectral regions were scanned several sweeps until a good signal-to-noise ratio was obtained, and then the survey scans were recorded in the range of 0–1400 eV at 187.85 eV of pass energy. The CasaXPS programme (Casa Software, UK) was used for acquisition and data analysis. A Shirley-type background was accurately subtracted from the signals. The binding energies were calculated with respect to the C-(C,H) component of the C_{1s} peak of adventitious carbon fixed at 284.5 eV. Atomic concentration percentages of characteristic elements (C, N and O) were determined from the recorded XPS spectra, plotted as the intensity (number of counts per second) versus binding energy (BE). The recorded high resolution XPS spectrum for the core level of C_{1s} was undergone curve fitting using Gaussian functions to determine the BE values with their respective full width at half maximum (FWHM).

4.2.4.3. Characterization of hydrophilic properties of the TFC-PCNF membranes

Static contact angle measurement was conducted using sessile drop method at ambient temperature. A contact angle measuring instrument (DSA 100 of KRUSS Gmbh, Germany) with DSA 1 v 1.92 software was employed to assess the hydrophilicity and surface free energy (SFE) with its polar and dispersive components of the active skin layers of the membranes. For this purpose, three different solvents (water, ethylene glycol and diiodomethane) with known surface tension values were employed. The sessile drop was slowly and steadily formed on the membrane surface by depositing 3 µl of the given solvent with a microsyringe and the measurement at the membrane-solvent-air interface was completed with a residence time of 60 s. At least eight such measurements were done at different locations of each membrane skin surface and then averaged out to calculate the contact angle with their standard deviations. Fowkes method was applied to calculate the SFE along with the polar and dispersive components of the membranes' surfaces from the surface tension values of the probe solvents and contact angle values of the membranes with respect to those solvents. Wetting envelopes were also constructed for the membranes' surfaces by reversing the method applied to determine the polar and dispersive part of SFE. The closed contour or envelope, with coordinate system made from polar and dispersive part of the SFE defines the line where the condition of contact angle 0^{o} ($\cos\theta = 1$) is satisfied.

4.2.4.4. Determination of surface charge properties of the TFC-PCNF membranes

The electrokinetic features of the membranes were evaluated by employing ZetaCAD electrokinetic analyzer (CAD Inst., France). The streaming potential analyzer consisted of a quartz-cell configuration which was capable of holding two flat sheet membranes in such a way that the membranes remained separated by spacers and the skin layers faced each other creating a slit channel for tangential flow of electrolytic solution across the membranes. The electrical potential difference, generated due to the bidirectional flow of electrolyte solution (10^{-3}M KCl) under pressure gradient across the membrane was measured by Ag/AgCl electrodes, equipped with the cell. Zeta potentials of the membranes under varying pH environments, ranging from pH 3 to 11 were evaluated utilizing the streaming potential values and the relationship between the measurable streaming potential (V_{st}) and the zeta potential (ζ), following the Helmholtz-Smoluchowski equation. An average value of zeta potential from three replicates was reported and the measurement error was found to be ± 0.5 mV.

The values of ζ of the membranes as determined with respect to the variation of pH were further employed to calculate electrokinetic surface charge densities (σ_s) at the shear planes of the membranes as a function of the respective pH environments. For electrokinetic measurements under varying pH environments, HCl and NaOH were used to adjust the pH values which led to presence of excess of similar counter-ions (Cl^-) at acidic pH and additional dissimilar counter-ion (OH^-) at alkaline pH, respectively.

4.2.5. Performance evaluation of membranes

4.2.5.1. Evaluation of characteristic features of Psf base membrane

For measurement of porosity of the Psf base membrane, gravimetric method was applied. There, a circular piece of the Psf membrane with an area -A and thickness -h was weighed after taking it out from storage of distilled water and then carefully removing the superficial water with filter paper. The wet membrane was dried in a vacuum oven at 75 ^{o}C for 24 h before measuring the weight in dry state. From the weights of the membrane sample in wet (W_0) and dry (W_1) states, the porosity (ø) of membrane was calculated using Eq. 15. In order to minimize the experimental error, measurements were carried out in duplicates and then calculated the average.

Pure water flux measurement of the Psf base membrane with effective membrane area of 14.4 cm^2 was conducted under a cross-flow filtration mode operated at 1 bar of transmembrane pressure. The steady-state pure water flux (PWF, L.m^{-2}day^{-1} or LMD) was determined by direct measurement of the permeate flow *i.e.*, volume (V, in L) collected during a time period (T, in day) through a membrane area (A, in m^2) at certain pressure. Prior to the UF test experiment, membrane was initially subjected to undergo hydraulic compaction for 1 h in water at standard UF test conditions, to achieve stabilized performance of the membrane. Utilizing the porosity of the membrane, mean pore radius (r_m in nm) was determined by employing the Guerout–Elford–Ferry equation.

For measurement of MWCO of the Psf base membrane, analysis of solute rejection behavior was carried out using neutral organic solutes such as PEG with average Mw of 12k, 20k, 35k Da and PEO with average Mw of 100k Da. The test solutions were prepared by dissolving pre-weighed amounts of PEG or PEO in ultra-pure water at a concentration of 200 ppm. The solute rejection studies were carried out at a transmembrane pressure of 1 bar at room temperature. The concentration of PEG or PEO in both feed and product were measured by analysing the total organic carbon (TOC) content of the samples using TOC analyzer (ANATOC-II, SGE analytical science, Australia). MWCO was determined from a plot of solute rejection *vs* molecular weight, generated in order to construct a MWCO curve, which implies a molecular weight of the organic solute that is 90% retained by the Psf base membrane.

Measurement of mechanical stability of the base membranes were carried out with a universal tensile testing machine (Hemetek Techno Instrument, model LRX Plus, India), at 25 °C with a relative humidity of 40-50%. A constant deformation rate of 100 mm/min was controlled during the analysis. For analysis, dumb-bell shaped specimens of the membrane samples with length of 4 cm and width of 0.6 cm were employed. Tensile strength (TS) and percent elongation at break (EB) were calculated for the membranes in duplicates, using the NEXYGEN plus software.

4.2.5.2. Nanofiltration performance evaluation of TFC-PCNF membranes

The evaluation of transport properties of the TFC-PCNF membranes was conducted using a cross-flow test cell, at 10 bar of transmembrane pressure. Circular membrane samples, with an effective membrane area of 14.4 cm^2 were properly washed in de-ionized water and then placed in the test cell with the membranes' active skin layers facing the incoming feed solution. To maintain a steady feed concentration, the experiments were carried out in recycle mode *i.e.*, both the concentrate and the permeate streams were recirculated into the feed tank. Iso-osmotic feed solutions comprising of varying combination of mono- and bi-valent cations and anions, such as 0.03M NaCl, 0.02M Na_2SO_4, 0.02M $MgCl_2$ and 0.03M $MgSO_4$ were employed for performance evaluation of membranes. The feed solution temperature was maintained at 25-30 ^{o}C. Prior to the start of data accumulation, steady-state conditions were achieved for all the NF test experiments when the membranes were allowed to get stabilized by operating for long-run. The solute concentrations in the feed and permeate solutions were obtained through the measurement of conductivities of the respective solutions using a digital conductivity meter (TESTRONIX 15, Microlab, Mumbai, India). All membrane samples were prepared and tested in duplicate for NF performances, results of which have been averaged. The steady-state readings of all the cases were recorded and reported. The percentage of solute rejection (SR) was determined by conductivity measurement of the respective solutions. The steady-state solvent flux (J_W), expressed in terms of L.m^{-2}day^{-1} (LMD) was determined by direct measurement of the permeate flow *i.e.*, volume (V, in L) collected during a time period, (T, in day) through a membrane area, (A, in m^2) at certain pressure.

4. 3. Results and discussion

4.3.1. Structural diagnosis of functionalized branched poly(ethyleneimine)

4.3.1.1. Structural investigation by ^{1}H-NMR spectroscopy

An asymmetry resides in reactivity of the different amine sites of precursor amine monomers (BPEI) due to presence of primary, secondary and tertiary amine functionalities in α–β nitrogen configurations under different conformations as well as proportions. The methylene groups of the BPEIs dwell as pair, in a chemical environment where they remain flanked between the α–β nitrogens *i.e.*, 1°($-NH_2$)-2°($-NH$), 1°($-NH_2$)-3°($-N$), 2°($-NH$)-3°($-N$) and 3°($-N$)-3°($-N$). The ^{1}H-NMR spectra (Fig. 4. 1) of the three different functionalized BPEIs (M.W.: 10k, a; 50k-100k, b and 600k-1000k Da, c), employed as monomeric amines, exhibit broad upfield signals for ^{1}H of $-CH_2-$ units of the BPEI chains which are ranged within δ 2.59-2.72, 2.61-2.84 and 2.59-2.73 ppm, respectively [52].

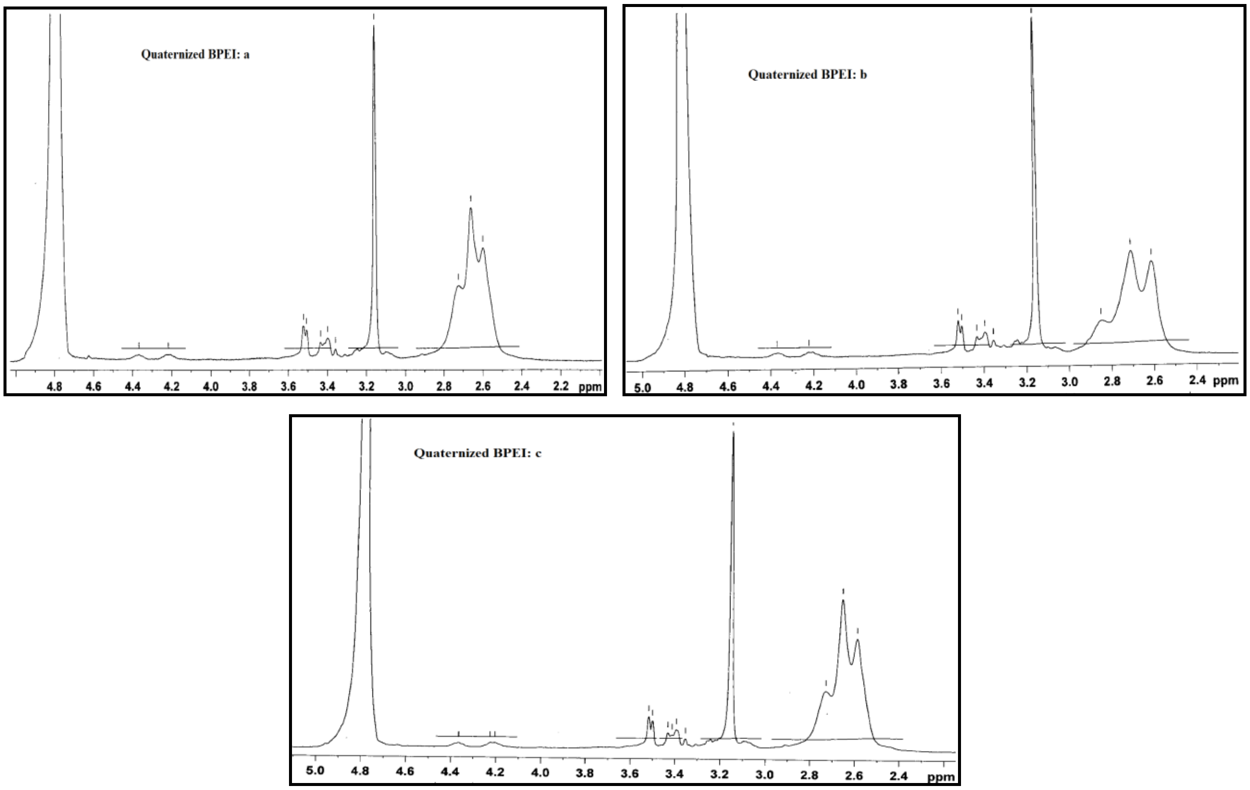

Fig. 4. 1 ^{1}H-NMR spectra of the three different functionalized BPEIs (M.W.: 10k, a; 50k-100k, b and 600k-1000k Da, c).

Presence of a strong downfield signal at δ 3.15 ppm in each of the functionalized monomer, assigned to the sterically hindered and chemically equivalent methyl protons of the hydroxypropyl trimethylammonium groups ($–NH–CH_2–CH(OH)CH_2–N^+(\mathbf{C\underline{H}_3})_3$) substantiates that there is certain presence of covalent chemical interaction between the amine sites of BPEIs, preferentially between the primary amines and the quaternizing agent GTACl with concurrent inclusion of quaternized amine sites in the backbone of BPEIs [53]. Such preferential transformation of primary amine sites into hydroxypropyl trimethylammonium groups *i.e.*, ($–\mathbf{\underline{NH}}–CH_2–CH(OH)CH_2–N^+(CH_3)_3$) and an apparent concomitant reaction of the secondary amine with the epoxide to form a tertiary amine *i.e.*, $–\mathbf{\underline{N}}(CH_2–CH(OH)CH_2–N^+(CH_3)_3)_2$ are the probable chemical reactions that may occur during the functionalization process [54].

The process of functionalization of BPEIs by GTACl is believed to follow a bimolecular nucleophilic substitution type reaction, occurred through the ring opening of the three-membered strained oxirane ring by nucleophilic addition of primary amine sites of BPEIs to the less sterically hindered site of the oxirane ring. It is proposed by earlier research efforts [55-56] that such kinds of functionalization processes consist of consecutive non-catalytic and catalytic steps, where, at an earlier stage of the reaction, there happens formation of either inter-molecular H-bonding between the amine sites and the oxirane ring (Fig. 4. 2, pathway-a) or inter-molecular H-bonding between the amine sites of contiguous chain segments (Fig. 4. 2, pathway-b), in a non-catalytic manner which is followed by formation of the amine-oxirane adduct (*i.e.*, BPEI-GTACl adduct through reaction of BPEI and GTACl, as in case of our processes in the current study). However, the hydroxyl groups as formed in our products during decomposition of the BPEI-GTACl adduct presumably exert autocatalytic behavior and concurrently induce formation of termolecular-complex (Fig. 4. 2) comprising amine sites of the BPEI, oxirane ring of GTACl and the hydroxyl group [57].

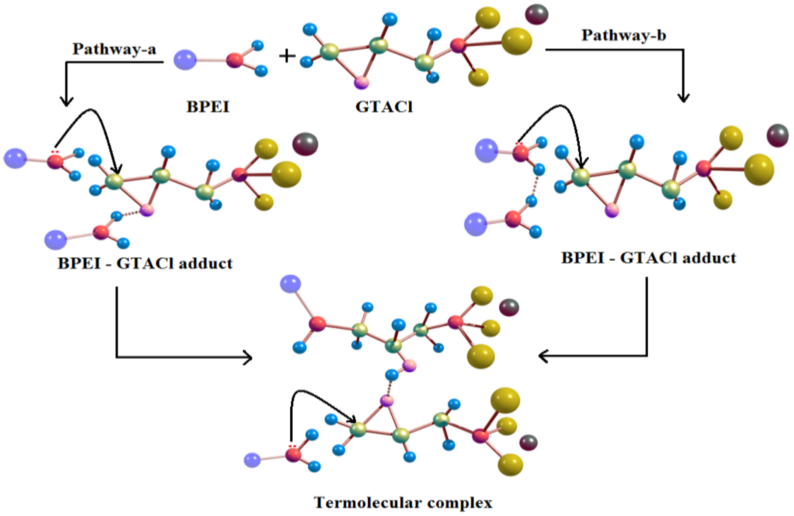

Fig. 4. 2 A 3-D schematic representation of the consecutive steps involved in functionalization of BPEI by GTACl following non-catalytic intermediate pathways-a/b in formation of BPEI-GTACl adduct and autocatalytic pathways in formation of termolecular complex as intermediate prior to decomposition of the intermediate into the product, quaternized BPEI.

Thus, formation of the termolecular-complex is attributed as the rate determining step of the reaction which is followed by the decomposition of the intermediate complex through ring opening of the oxirane ring.

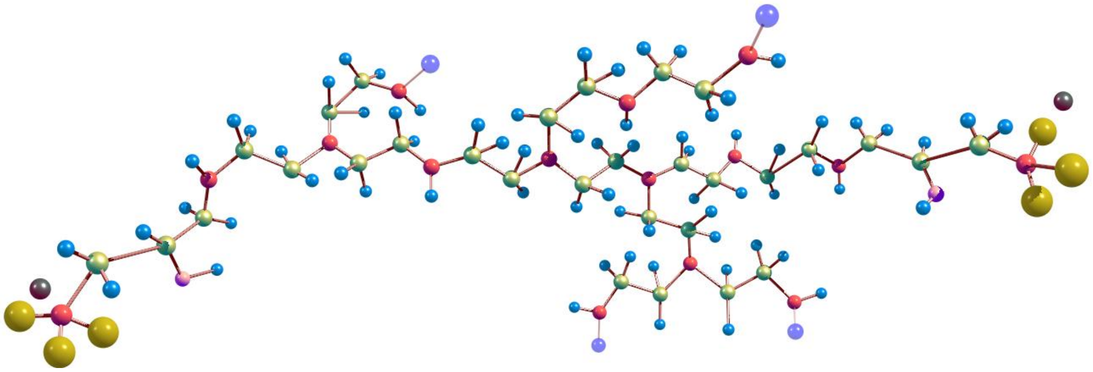

Fig. 4. 3 A 3-D representation of the probable chemical structure of synthesized quaternized BPEI.

Characteristic downfield peaks at δ 3.50 and 3.52 ppm (broad, m, 2H, diastereotopic for $–NH–CH_2–CH(OH)\mathbf{C}\underline{\mathbf{H}}_{\mathbf{2}}–N^+(CH_3)_3$), δ 4.22 and 4.36 ppm (broad, m, 1H, chiral for $–NH–CH_2–\mathbf{C}\underline{\mathbf{H}}(OH)\mathbf{C}H_{\mathbf{2}}–N^+(CH_3)_3$) and δ 3.39 and 3.43 ppm (broad, m, 1H, diastereotopic for $–NH–C\underline{\mathbf{H}}_2–\mathbf{C}H(OH)\mathbf{C}H_{\mathbf{2}}–N^+(CH_3)_3$) further substantiate the formations of the termolecular-complex as intermediate and resultant functionalized BPEIs (Fig. 4. 3) as the three precursor amines.

4.3.1.2. Analysis of structural features by FTIR spectroscopy

The results of FTIR spectroscopic analysis, employed to corroborate the incorporation of quaternary trimethylammonium groups as quaternized terminal functional-moieties in the network of BPEIs through chemical transformations of the primary amine sites of BPEIs, is presented in Fig. 4. 4.

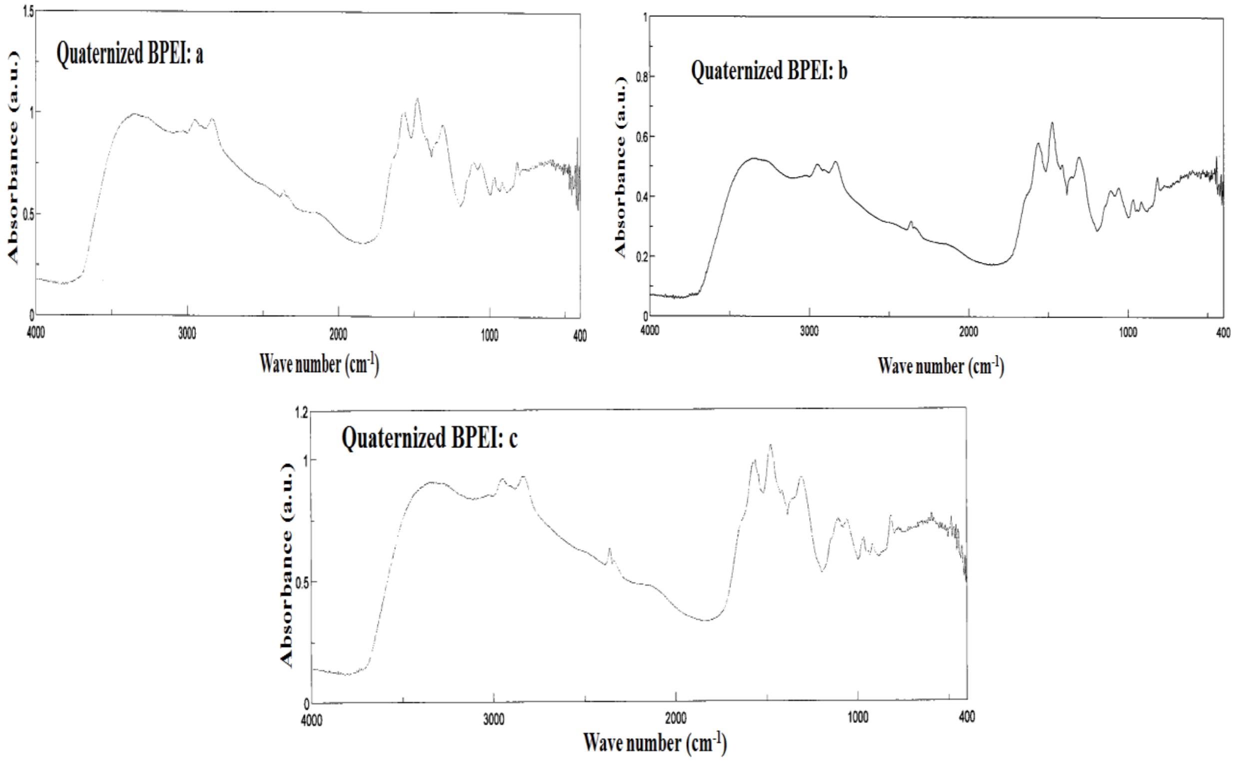

Fig. 4.4 FTIR spectra of the three different functionalized BPEIs (M.W.: 10k, a; 50k-100k, b and 600k-1000k Da, c).

The FTIR spectra of functionalized BPEIs, presented in Fig. 4.4 show the presence of characteristic bands at ~ 967 cm^{-1}, which is attributed to the quaternary nitrogen of the tethered quaternary trimethylammonium chloride moieties [58]. This refers to the involvement of N–H wagging mode of primary amine sites of the BPEI backbone in the process of GTACl induced quaternization. The bands appearing at 1307-1311, 1475 and 1559-1568 cm^{-1} are attributed to C–N stretching, C–H and N–H bending, respectively. The absorption bands appearing at 2947-2951 and 2834-2838 cm^{-1} are assigned to the symmetrical and asymmetrical stretching vibrations of C–H of BPEIs, respectively. The broad absorption bands at 3333-3344 cm^{-1} refer to the overlapping of symmetric and asymmetric N–H stretching of the residual primary and secondary amines as well as the O–H stretching of the hydroxypropyl trimethylammonium groups of three different functionalized BPEIs (M.W.: 10k, [a]; 50k-100k, [b] and 600k-1000k Da, [c]). The intense broad absorption bands at ~ 3343 cm^{-1}, associated with hydroxyl groups further reveal the presence of hydroxyl bonds formed as a result of opening of the oxirane ring. The FTIR study conclusively suggests the transformation of the amine functionalities, which preferentially occurs at the primary amine sites, into quaternary trimethylammonium chloride groups that would form the basis of the charge in the TFC membranes later [59,60].

4.3.2. Physicochemical characterizations of TFC-PCNF membranes

4.3.2.1. Investigation on spectral features of skin layers of TFC-PCNF membranes

The ATR-FTIR spectra (Fig. 4. 5) of skin layers of the TFC-PCNF membranes, namely TFC-PCNF$_{I}$, TFC-PCNF$_{II}$ and TFC-PCNF$_{III}$, exhibiting the presence of characteristic absorption bands for amide regions substantially imply the formation of diagnostic quaternized poly(ethyleneimine amide)s through *in situ* interfacial polymerization of the quaternized amine monomer, BPEI with the acid chloride monomer, TMC.

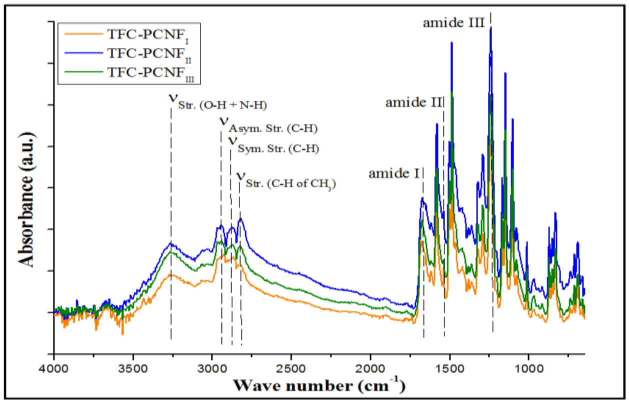

Fig. 4. 5 ATR-FTIR spectra of skin layers of the membranes: TFC-PCNF$_{I}$, TFC-PCNF$_{II}$ and TFC-PCNF$_{III}$.

The absorption bands varying in the vibrational frequency region of 1674-1676 cm^{-1} are ascribed as amide-I mode in secondary amide groups of the polymer chains, which consists of contributions from the C=O stretching (maximum contribution), C–N stretching and C–C–N deformation vibration. The bands with lower intensity appearing as shoulders in the region of 1537-1540 cm^{-1} are designated as characteristic amide-II mode which arises due to a combined contribution of both N–H in-plane bending and the C–N stretching vibrations of the –C(=O)–NH– group of the polyamide structure. The absorption bands in the region of 1240 cm^{-1} are assigned to amide-III vibrational modes which are contributed by the C–N stretch and –C(=O)–NH– bend (in opposite phase) [61,62]. The presence of bands at 2821-2826 cm^{-1} is referred to the C–H stretching vibrations of the methyl groups attached to N atom of quaternary ammonium moieties. This establishes the existence of trimethylammonium moieties as the tethered cationic quaternized amine sites in the structures of poly(ethyleneimine amide) as well. The weak bands appearing in the region of 2866-2876 and 2932-2946 cm$^{−1}$ are referred to the symmetric and asymmetric CH_2 stretching vibrations, respectively, which correspond to the collective contribution of flanked methylene groups of chain segments of the BPEIs as well as the methylene units of the hydroxypropyl groups associated with trimethylammonium moieties of the quaternized poly(ethyleneimine amide)s. The membranes exhibit broad bands at 3256-3266 cm^{-1}which can be assigned as overlapping of stretching vibrations of both H-bonded N–H of the amide segments (amide-A) and O–H of the tethered functionalities, the latter resulting out from the ring opening reaction of the oxirane ring of GTACl [63]. The structural orientation as well as organization of the resultant crosslinked-quaternized poly(ethyleneimine amide) likely induce extensive interactions within the chain segments in the course of secondary noncovalent interactions like intra-molecular H-bondings within adjacent amide-I and amide-A regions, van der Waals interactions and dipole-dipole interactions or n→π* interactions happening through delocalization of a lone pair (n) of the donor carbonyl groups of amide segments or amine groups of the BPEI chains into the antibonding (π*) orbital of the acceptor carbonyl groups

(C=O·····C=O or C–N·····C=O) of the adjacent polymer chains [37]. It thus seems obvious that such interactions get affected by the variation in M.W. of BPEIs as well as presence of the bulky terminal quaternized functional moieties *i.e.*, hydroxypropyl trimethylammonium groups in the polymer chains. Consequently, it can be cogitated that factors like M.W. variation of BPEIs, subsequent change in branching density, extent of quaternization and simultaneous effect of them on the conformations of the chain segments play a synergistic role in configuring the molecular architectures of the crosslinked-quaternized poly(ethyleneimine amide)s as skin layer polymers of the TFC-PCNF membranes.

4.3.2.2. Investigation of skin layers of TFC-PCNF membranes by XPS

Analyses of XPS spectra of the skin layers of TFC-PCNF membranes provide quantitative estimations on enrichment of the elements like N and O in poly(ethyleneimine amide)s, within the XPS probe depth (5-10 nm), which may be linked to the presence of quaternary trimethylammonium chloride groups in the membrane surface. The relative elemental compositions of skin surfaces of TFC-PCNF membranes (Table 4. 1) have been determined based on the intensity of the C_{1s}, N_{1s} and O_{1s} peaks (presented in the XPS survey scan spectra, Fig. 4. 6) centered at 284, 399 and 531 eV, respectively. Variations in the enrichment of O and N are observed through a descending trend of O to C elemental ratios (O/C) accompanying with an enhancement of the N to C elemental ratios (N/C), on moving from TFC-PCNF$_{I}$ to TFC-PCNF$_{III}$ through TFC-PCNF$_{II}$ *i.e.*, with increase in the M.W. of BPEI. Further, a marked increase in values of the N to O elemental ratios (N/O) is also noticed in membranes derived employing progressively higher M.W. of BPEI. Such features substantiate that the exterior region of the probed skin layer of TFC-PCNF$_{I}$ are populated with greater number of terminal oxygenated polar sites (contributed by C=O of the amide segments and O–H of the quaternized functionalities *i.e.*, hydroxypropyl trimethylammonium moieties) leaving the chain segments, mostly the nonpolar C–C linkages, inside whereas the exterior regions of skin layers of TFC-$PCNF_{II}$ and TFC-$PCNF_{III}$ remain populated more with the chain segments of the quaternized poly(ethyleneimine amide)s [64, 65].

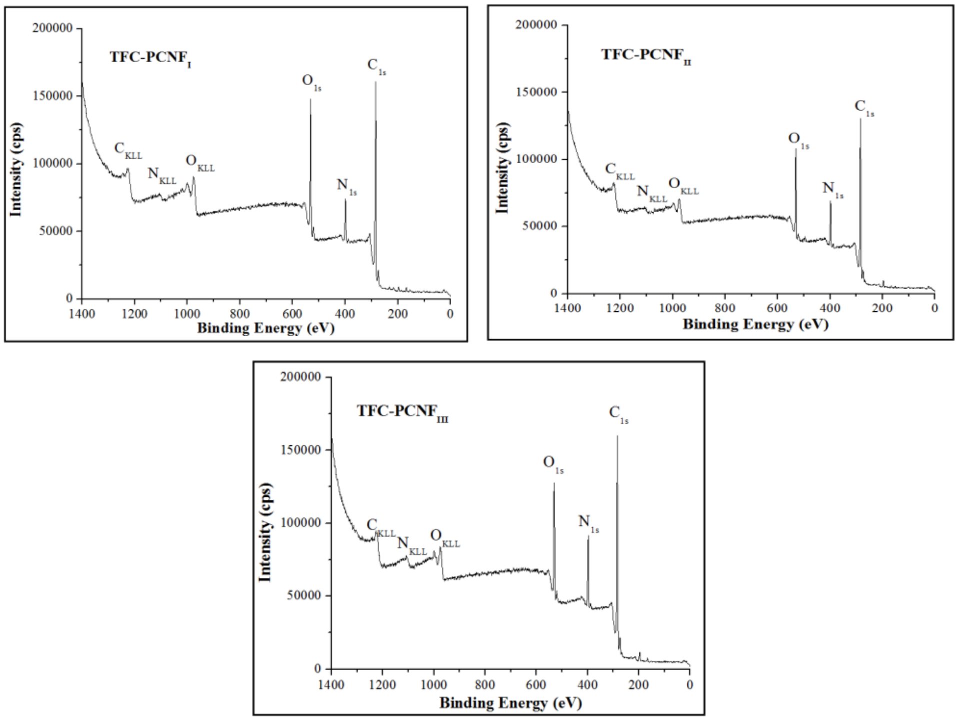

Fig. 4. 6 XPS survey scan spectra of skin layers of the membranes: TFC-$PCNF_I$, TFC-$PCNF_{II}$ and TFC-$PCNF_{III}$.

Table 4. 1
Elemental compositions of skin surfaces of the TFC-PCNF membranes, evaluated by XPS analysis.

Membrane Code	Percentage elemental analysis based on C_{1s}, N_{1s} and O_{1s} peaks			Elemental ratios		
	% C	% N	% O	O/C	N/C	N/O
TFC-$PCNF_I$	73.46	8.39	18.14	0.25	0.11	0.46
TFC-$PCNF_{II}$	74.76	11.10	14.13	0.19	0.15	0.79
TFC-$PCNF_{III}$	73.14	12.60	14.24	0.19	0.17	0.88

Further in depth informations about the chemical environments of various carbon atoms were obtained from the deconvoluted high resolution XPS spectra for C_{1s} (Fig. 4. 7). Asymmetric nature of the core-level C_{1s} spectra implies that the C species present in the polyamide skin layers exist in different states of chemical bonding. The constituent peaks of the deconvoluted asymmetric spectra of C_{1s} depict that the high intensity peak at lower BE of 284.24 (FWHM: 2.15 eV), 284.35 (FWHM: 2.31 eV) and 284.65 eV (FWHM: 2.23 eV) for TFC-PCNF$_{I}$, TFC-PCNF$_{II}$ and TFC-PCNF$_{III}$, respectively (Table 4. 2) correspond to the carbons in aliphatic/ aromatic C–C or C–H bonds of the poly(ethyleneimine amide), more particularly the carbons nonadjacent to electron rich sites of the chain segments of polymer chains [66].

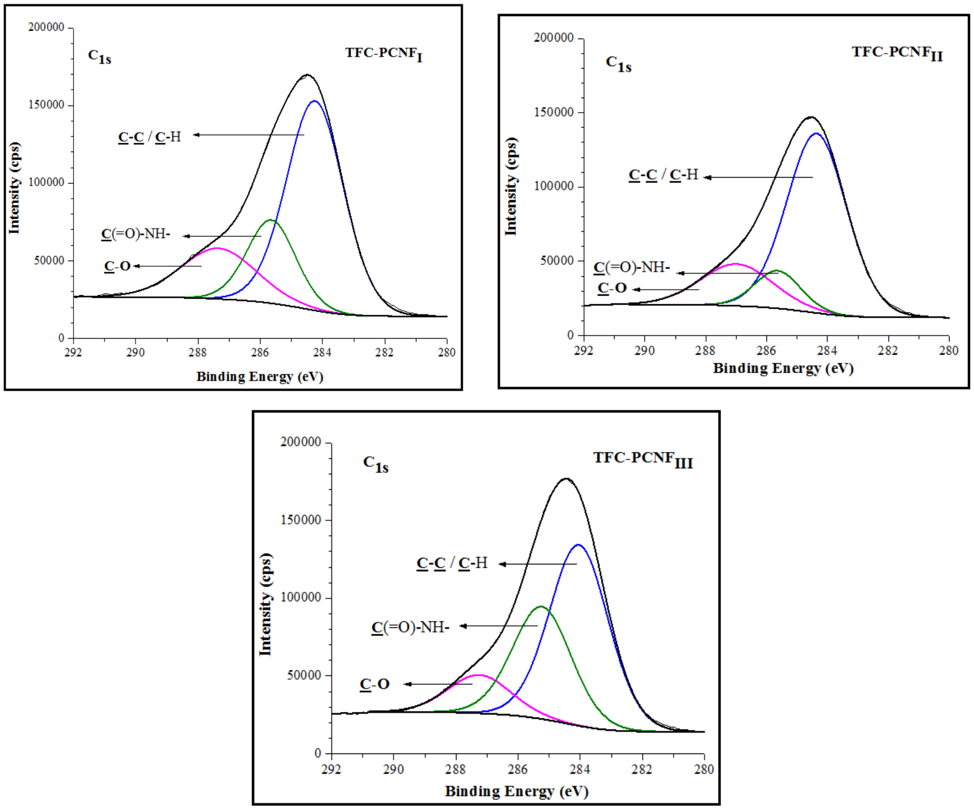

Fig. 4.7 High resolution C_{1s} XPS spectra obtained from skin layers of the membranes: TFC-PCNF$_{I}$, TFC-PCNF$_{II}$ and TFC-PCNF$_{III}$.

Table 4. 2
Curve fitting summary of C_{1s} peak for the TFC-PCNF membranes' skin surfaces.

Membrane Code	C_{1s}		
	BE (eV)	FWHM (eV)	Peak area (%)
$\text{TFC-PCNF}_{\text{I}}$	284.24	2.15	60.41
	285.64	2.84	19.17
	287.34	1.83	20.42
$\text{TFC-PCNF}_{\text{II}}$	284.35	2.31	60.78
	285.64	2.79	19.49
	286.98	1.76	19.73
$\text{TFC-PCNF}_{\text{III}}$	284.65	2.23	80.61
	285.23	2.23	9.94
	287.24	2.37	9.45

The enhanced peak area for this peak region in $\text{TFC-PCNF}_{\text{III}}$ (peak area: 80.61%) as compared to $\text{TFC-PCNF}_{\text{I}}$ (peak area: 60.41%) and $\text{TFC-PCNF}_{\text{II}}$ (peak area: 60.78%) reflects that the presence of such sites is more pronounced in the skin regions of the former membrane. Such enhancement in the relative area of the peak appearing at 284.65 eV subsequently compensates the areas of the shoulder peaks. The intermediate peaks at higher BE of 285.64 (FWHM: 2.84 eV), 285.64 (FWHM: 2.79 eV) and 285.23 eV (FWHM: 2.23 eV) for $\text{TFC-PCNF}_{\text{I}}$, $\text{TFC-PCNF}_{\text{II}}$ and $\text{TFC-PCNF}_{\text{III}}$, respectively are assigned to the carbons of –C(=O)–NH– groups in the structures of poly(ethyleneimine amide)s, more specifically the carbons adjacent to secondary and tertiary nitrogen atoms of amides and amine sites of polymer backbone as well as nitrogen atoms of amines and amides which are involved in intermolecular H-bondings through inter-chain interactions [66].

The deconvoluted spectra also reveal the presence of carbons in a weak electron withdrawing environment (such as carbons in C–O bonds) as the low intensity peaks appear at higher BE of 287.34 (FWHM: 1.83 eV), 286.98 (FWHM: 1.76 eV) and 287.24 eV (FWHM: 2.37 eV) for $\text{TFC-PCNF}_{\text{I}}$, $\text{TFC-PCNF}_{\text{II}}$ and $\text{TFC-PCNF}_{\text{III}}$, respectively, indicating the contributing presence of the tethered hydroxypropyl trimethylammonium moieties in the skin surfaces [66]. These observations further corroborate the illustrations as mentioned earlier regarding the variant presence of the poly(ethyleneimine amide)s, concerning the difference in their structural orientations and crosslinking densities.

4.3.2.3. Determination of hydrophilic features of TFC-PCNF membranes

Contact angle analyses, performed by using the three different probe solvents *i.e.*, water, ethylene glycol and diiodomethane, on the skin surfaces of the membranes show that the contact angle values (Fig. 4. 8) with respect to the polar solvent, water (θ_w) increase from 61.4(±0.9)^o to 67.9(±1.3)^o and further to 71.5(±1.4)^o, whereas with respect to the non-polar solvent, diiodomethane (θ_{DIM}) decrease from 46.5(±1.5)^o to 31.7(±1.1)^o through 37.5(±2.7)^o, as M.W. of the quaternized BPEI increases.

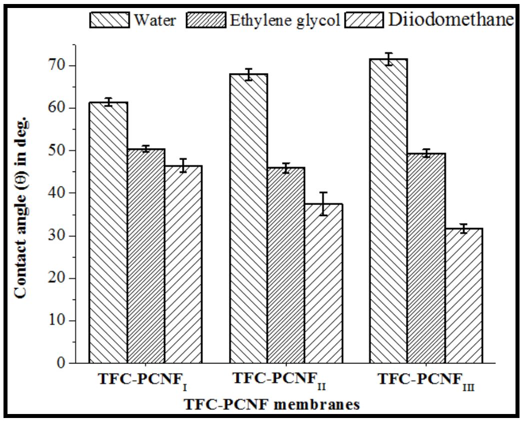

Fig. 4. 8 Variation in contact angles of the membranes with change in M.W. of BPEIs, with respect to water, ethylene glycol and diiodomethane.

This substantiates a declining trend of hydrophilicity for the TFC-PCNF membranes having poly(ethyleneimine amide) skin layers, as derived employing progressively higher M.W. of BPEI. The trend implies that the extent of presence of quaternized terminal functional-moieties as well as the hydrophilic amine and amide sites in the skin layer-air or skin layer-solvent interface gets affected by the variant molecular architectures of the quaternized BPEIs, which might have played a governing role in determining the hydrophilic features of the membranes' surfaces. The increase in constrained mobility or decrease in configurational entropy of the chain segments due to increase in branching density, with enhanced M.W. of BPEI [67,68] reduces the approach of interior primary amine sites towards periphery of the globular shaped BPEI during functionalization by GTACl. On the contrary, availability of more primary amine sites in BPEI with lower M.W. turns them more susceptible towards quaternization through reaction with GTACl, leading to formation of more sites of charge carriers [69]. Thus, it is justifiable to presume that such effects also get propagated in the respective formed structures and subsequent structural orientations as well as organizations of the resultant poly(ethyleneimine amide)s as the skin layer polymers of TFC-PCNF membranes. Moreover, the structural aspects of the bulky hydroxypropyl trimethylammonium moieties introduce more polarity in the resultant poly(ethyleneimine amide) as well, making the skin layer more susceptible for favorable interaction with the polar solvent. Thus, the observed hydrophilic features of the TFC-PCNF membranes relevantly attribute to the consequent effects of functionalization of BPEIs of varying M.W.

Quantification of surface free energies of the TFC-PCNF membranes (Fig. 4. 9) was carried out using Fowkes theory and employed to calculate the corresponding dispersive and polar components of the investigated membranes' surfaces. The trend for membranes' total surface free energy ($\gamma_{\text{Total SFE}}$) follows an order - TFC-PCNF$_{\text{I}}$ < TFC-PCNF$_{\text{II}}$ < TFC-PCNF$_{\text{III}}$. With increase in M.W. of BPEI, the polar parts (γ_{Polar}) of the poly(ethyleneimine amide) layer of the membranes decrease from 14.91(±0.74) to 4.63(±0.51) through 9.08(±0.87) mN/m, whereas the dispersive parts ($\gamma_{\text{Dispersive}}$) increase from 25.05(±0.80) to 39.01(±0.64) via 31.95(±1.36) mN/m.

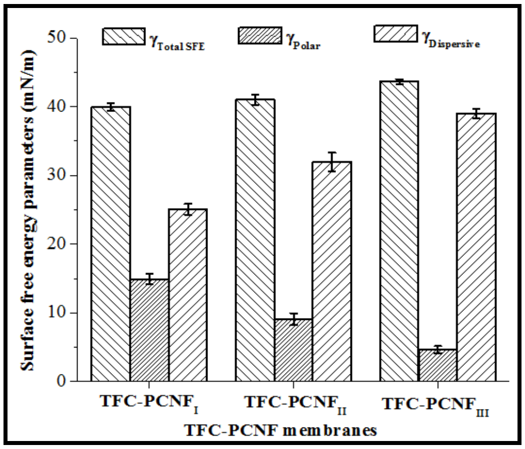

Fig. 4. 9 Variation in surface free energy parameters of the membranes with change in M.W. of BPEIs.

This pattern of γ_{Polar} and $\gamma_{Dispersive}$ may be attributed to the spatial distribution of lesser extent of polar and higher extent of dispersive segments of the poly(ethyleneimine amide) chains at the skin surfaces of the membranes when higher M.W. of quaternized BPEI are engaged in forming the polymers. In contact with a hydrophobic medium, the high energy quaternary functional-moieties, covalently tethered at the terminal of low energy segments of polymer chains of the charged polymeric surface tend to orient more into the bulk phase of the skin layer moving away from the polymer/hydrophobic medium interface in order to reduce the SFE. However, in contact with hydrophilic medium, such polar terminal functional-moieties may exhibit a propensity to reorient and migrate preferentially more into the polymer/hydrophilic medium interface over the non-polar segments of the polymer chains, in minimizing the interfacial energy [70]. Thus, our elucidation corroborates that the skin layer derived from higher M.W. of quaternized BPEI bears lower mobility of the chain segments due to the rigid crosslinked polymeric structure and as a consequence, the migration of polar terminal functional-moieties from the interior to the periphery of the polymer may get prevented. This illustration about the impact of mobility of chain segments in a branched structure like BPEI on molecular architecture is comparable to a previous work by J. A. Orlicki *et al.* [71], where the surface energy of branched polyetherimides show their strong dependency on the molecular architecture and end-group functionalities due to variation in mobility of chain segments. The surface property results of our investigation can also be elucidated with the aid of speculation that quaternization on BPEI of higher M.W. with greater branching density may increase stiffness of the resultant poly(ethyleneimine amide) and reduce the polymer free volume to a greater extent in comparison to its' lower M.W. counterpart. The studies carried out by Y. Hu *et al*. [72] and G. H. Pehlert *et al*. [73] provide a knowledge on effect of functional group spacing and steric crowding on the extent of intermolecular H-bondings in polymeric systems, where enhanced spacing between functional groups leads to greater intermolecular H-bondings, however an enhanced steric crowding imposes limiting accessibility to the functional groups for participation in forming intermolecular H-bondings. Thus, the variations in spacing of bulky functional-moieties in structures of crosslinked-quaternized poly(ethyleneimine amide)s, derived from BPEIs of varying M.W. predictably influence the packing patterns of the polymeric chains as well as the extent of inter- and intra-molecular H-bondings, due to differential hindrance in segmental orientations of the polymer chains, in spite of the fact that more number of chain-ends in a branched polymer leads to increase in free volume [74].

Further, extrapolation of the assessment of polar and dispersive components of SFE of the TFC-PCNF membranes' surfaces configures closed contours or more specifically the wetting envelopes, by plotting the polar fraction against the dispersive fraction of SFE. The importance of knowledge on wetting envelopes of the membrane surfaces lies in the fact that the formation of envelope provides more precise and wide idea about the ability as well as extent of interaction of a solvent with the membrane surface since a solvent can wet the surface if the components of its' surface tension (γ_s^p and γ_s^d) fall below the wetting envelope. The wetting envelopes (Fig. 4.

10) demonstrate that the wetting behaviors of the membranes vary significantly with change of the M.W. of BPEIs.

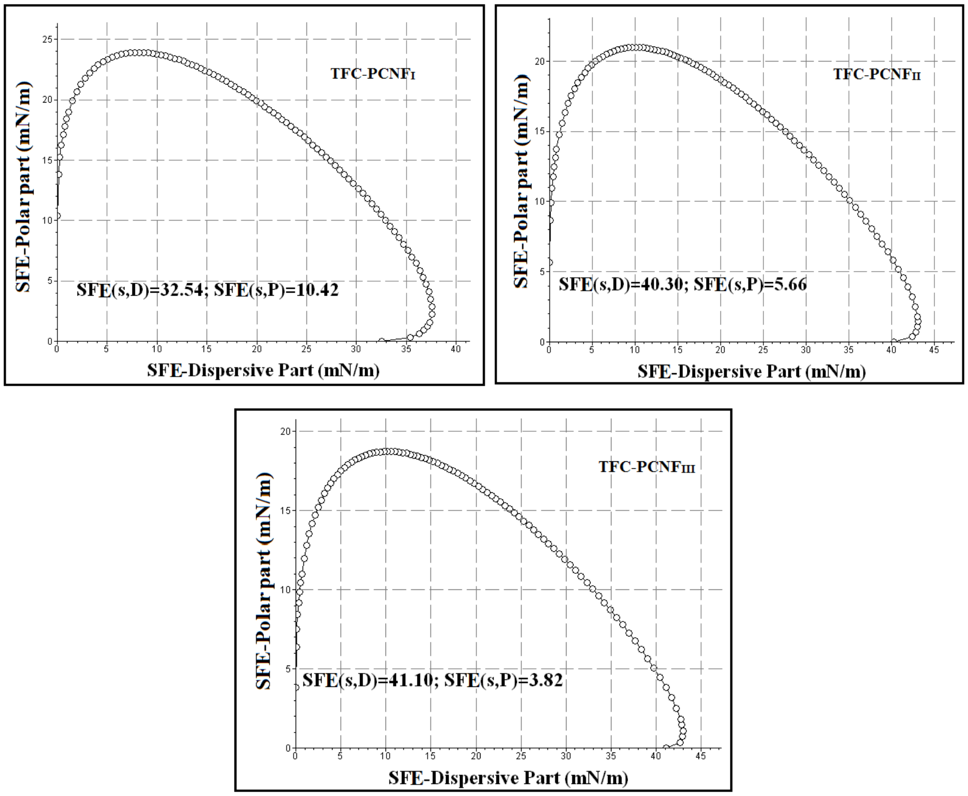

Fig. 4. 10 Wetting envelopes for skin surfaces of the TFC-PCNF membranes.

The values of dispersive component of SFE *i.e.*, 32.54, 40.30 and 41.10 mN/m, and polar component of SFE *i.e.*, 10.42, 5.66 and 3.82 mN/m for TFC-PCNF$_{I}$, TFC-PCNF$_{II}$, and TFC-PCNF$_{III}$, respectively substantiate such variant behavior. This is attributed to the fact that the skin surface of the membrane derived using higher M.W. of BPEI *i.e.*, TFC-PCNF$_{III}$ having greater number of dispersive segments of the polymeric chains, exposed more towards the membrane/solvent interface behaves to be more prone in interaction with relevant solvents having higher γ_s^d. However, exposure of more number of polar segments of the polymeric chains towards the membrane/solvent interface leads to a wetting envelope which is widened towards solvents having higher γ_s^p, for the membrane made employing lower M.W. of BPEI *i.e.*, TFC-PCNF$_I$.

4.3.2.4. Evaluation of electrokinetic behaviors of TFC-PCNF membranes

Electrokinetic behaviors of charged surfaces of the TFC-PCNF membranes, determined by tangential streaming potential measurements with respect to 10^{-3}M KCl solution at varying pH conditions are represented in Fig. 4. 11. The surfaces of the membranes acquire stationary layer of positive charges due to the presence of tethered quaternary trimethylammonium groups bearing cationic charges, in addition to the different accessible protonated amine sites in the polyamide network of the skin layer polymers.

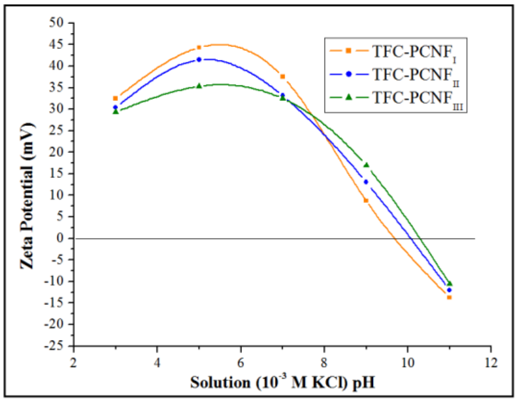

Fig. 4.11 Variation of zeta potential with pH, for TFC-PCNF$_I$, TFC-PCNF$_{II}$ and TFC-PCNF$_{III}$ membranes, with respect to 10^{-3} M KCl solution.

In all the membranes, it is noticed that the extent of positive charge increases with decreasing values of pH *i.e.*, from pH 7 to 5 as absolute values of ζ increase from 37.54 to 44.31 mV for TFC-PCNF$_I$, 33.13 to 41.46 mV for TFC-PCNF$_{II}$ and 32.50 to 35.31 mV for TFC-PCNF$_{III}$. This observation signifies the fact that with initial enhancement in acidity of the KCl solution and during the period of equilibration of the membranes in that medium, the secondary, tertiary and also the residual primary amine sites of the poly(ethyleneimine amide) layer at the skin surfaces of the membranes get protonated, enhancing the density of overall positively charged sites. However, at pH 3, the absolute values of ζ fall to 32.49 mV for TFC-PCNF$_{I}$, 30.39 mV for TFC-PCNF$_{II}$ and 29.36 mV for TFC-PCNF$_{III}$. Such reductions in absolute ζ values at higher acidic environment of pH 3 happen regardless of extensive protonation of the amine sites as well as with subsequent enhancement in the skin layer conductivity of the membranes to a large extent. This occurrence is believed to happen due to dragging of the tangentially driven counter-ions (during streaming potential measurements), from the hydrodynamic slipping plane or plane of shear to the bulk of the membranes stationary positively charged layer through the hydrodynamically stagnant layer of counter-ions (Fig. 4. 12, Schematic a).

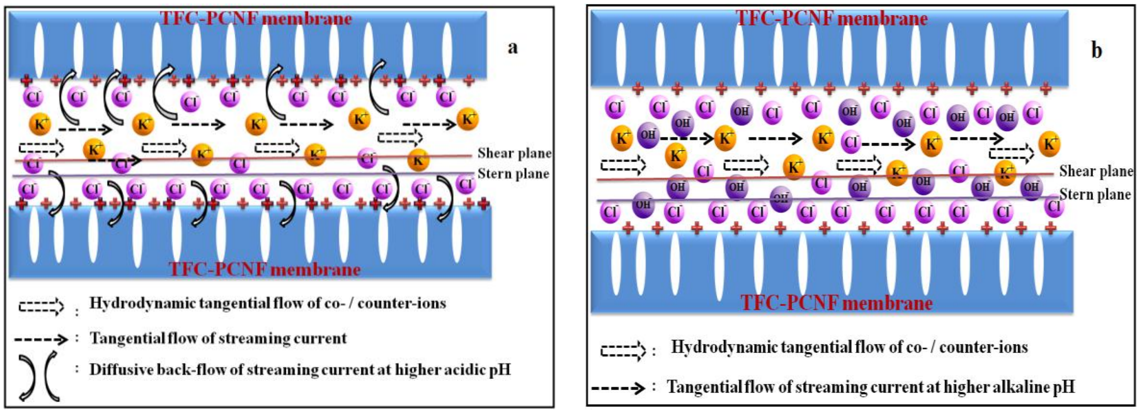

Fig. 4. 12 Schematic representations of the electrokinetic incidences - (a): diffusive back-flow of streaming current at higher acidic pH environment and (b): non-specific adsorption of the excess counter-ions with concurrent screening of the membranes' surface positive charges at higher alkaline pH environment, during streaming potential measurements.

Thus, the effective streaming current gets reasonably reduced to some extent due to such diffusive back flow of the streaming current; the effect of which is substantially manifested in the resultant ζ of the respective membranes. Further, the enhancement in absolute values of ζ with respect to decrease in M.W. of the BPEI, at neutral pH condition is attributed to the effect of more accessibility of primary amine sites for the BPEI of lower M.W. and in turn, the resultant degree of quaternization of the BPEI by GTACl.

However, a pronounced decline in absolute values of ζ (8.73 mV for TFC-PCNF$_{\mathrm{I}}$, 13.05 mV for TFC-PCNF$_{\mathrm{II}}$ and 16.92 mV for TFC-PCNF$_{\mathrm{III}}$) during streaming potential measurements in alkaline environment of pH 9 implies that there happens neutralization of positive surface charges of the membranes. Such change in surface charge behavior of the membranes with increasing pH can be attributed to the more accessibility of the additional counter-ions (OH^-) for extensive interactions with the protonated amine sites of the polyamide type of network, successively resulting in protolysis of the charged amine sites for TFC-PCNF$_{\mathrm{I}}$ than TFC-PCNF$_{\mathrm{II}}$ and then TFC-PCNF$_{\mathrm{III}}$. Furthermore, there occurs non-specific adsorption of the excess counter-ions (OH^-) at the skin surfaces of the membranes during measurement at even higher alkaline pH condition like pH 11. The study correlating the surface charge behaviors of nanofiltration membranes with varying degree of ionic concentration, by M. D. Afonso *et al*. [75] substantially reflect our inference that enhanced pH may also cause concentration build up of the counter-ions with concurrent effect of compression in the electrical double layer thickness as well as decrease in Debye length, leading to a severe reduction in the positive absolute ζ values of the TFC-PCNF membranes. Eventually, inversion of charge is observed to happen beyond isoelectric points *i.e.*, 9.67 mV for TFC-PCNF$_{\mathrm{I}}$, 9.96 mV for TFC-PCNF$_{\mathrm{II}}$ and 10.19 mV for TFC-PCNF$_{\mathrm{III}}$. The trend in shifting of isoelectric points implies that the membrane, TFC-PCNF$_{\mathrm{III}}$ remains more positively charged than TFC-PCNF$_{\mathrm{II}}$ and TFC-PCNF$_{\mathrm{I}}$. This can be ascribed to the screening effect (Fig. 4. 12, Schematic b) on the stationary layer of positively charged sites, since, at such ionic environment, the excess of OH^- ions beyond the plane of shear engage in overcompensation of the positive surface charges [76, 77]. Thus, variation of pH affects the net surface charge density of the membranes through change in protonation/de-protonation equilibria as occurred at the different charged amine sites of the polyamide skin surfaces of the membranes. Concomitantly, concentration of counter-ions (Cl^- and/ OH^-) affects the degree of shielding of the surface charge and thus, effective ζ of the membranes. Indeed, such behaviors further indicate that extent of penetration of the counter-ions to the charged sites of skin layers of the membranes gets influenced by the variation in molecular architectures of the poly(ethyleneimine amide)s.

The determination of electrokinetic surface charge densities, σ_s (Table 4. 3) at the shear planes of the TFC-PCNF membranes, with respect to varying pH environments provides a glimpse about the charge-atmosphere of skin surfaces of the membranes at respective pH conditions.

Table 4. 3
Results of electrokinetic surface charge density variation of the TFC-PCNF membranes at different pH environments.

Membrane Code	Electrokinetic surface charge density, σ_s (C/m^2)				
	pH 3	pH 5	pH 7	pH 9	pH 11
TFC-PCNF$_I$	2.33×10^{-3}	3.20×10^{-3}	2.71×10^{-3}	0.06×10^{-3}	-0.99×10^{-3}
TFC-PCNF$_{II}$	2.18×10^{-3}	2.99×10^{-3}	2.39×10^{-3}	0.94×10^{-3}	-0.87×10^{-3}
TFC-PCNF$_{III}$	2.11×10^{-3}	2.55×10^{-3}	2.34×10^{-3}	1.22×10^{-3}	-0.76×10^{-3}

This brings a significant importance since the σ_s predominantly influences the transport of ionic constituents through these membranes by tuning the membrane potentials and in turn the electrostatic interactions between the charged sites of skin layers of the membranes and ionic species of the feed solutions. It is observed from the assessed results that the values of σ_s rise with change of pH *i.e.*, from pH 7 to 5 and then fall down to some extent at pH 3 for all the investigated membranes, following the illustrations as mentioned earlier. This signifies the fact that all the membranes' surfaces carry maximum positive charge-atmosphere at pH 5, and the extent of such is more in TFC-PCNF$_I$ as compared to TFC-PCNF$_{II}$ and TFC-PCNF$_{III}$. However, the extent of positive charge-atmosphere gets reduced at enhanced pH condition where the membrane, TFC-PCNF$_{III}$ shows signs of carrying more positively charged sites in comparison to TFC-PCNF$_{II}$ and then TFC-PCNF$_I$, reflecting the pronounced occurrence of screening of surface positive charges in the latter two membranes due to their skin layers' unconstrained molecular architectures.

4.3.3. Analysis of cross-flow permeation studies of TFC-PCNF membranes

Analysis of basic features of the Psf membrane, prepared by phase inversion method reveals that the membrane achieves a MWCO of 45k Da and also exhibits PWF of 2200(±15) LMD at 1 bar transmembrane pressure. The mean porosity and mean pore radius of the base membrane are estimated as 80.8% and 21.78 nm, respectively. These values of porosity, mean pore size, MWCO and PWF indicate that the Psf membrane, contributing as a base for growth of the thin skin layers of TFC-PCNF membranes falls in the ultrafiltration range. The cross-flow permeation study, performed for all the positively charged TFC-PCNF membranes at a similar transmembrane pressure of 10 bar reveals that the membranes bearing high extent of positive surface charges follow a rejection trend of $MgCl_2 > MgSO_4 > Na_2SO_4 > NaCl$, under iso-osmotic environment of solutes (Fig. 4. 13). The higher rejection efficiency for solutes like $MgCl_2$ - 97.1(±0.2)% for TFC-PCNF$_I$, 97.6(±0.1)% for TFC-PCNF$_{II}$ and 98.9(±0.3)% for TFC-PCNF$_{III}$; and $MgSO_4$ - 86.1(±0.3)% for TFC-PCNF$_I$, 85.2(±0.2)% for TFC-PCNF$_{II}$ and 78.2(±0.5)% for TFC-PCNF$_{III}$ are governed predominantly by the influence of strong electrostatic repulsive potential.

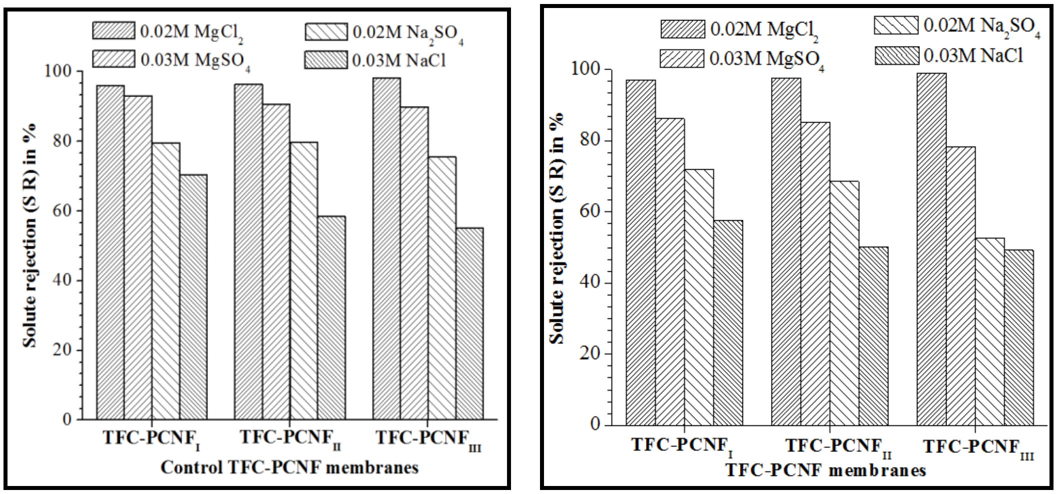

Fig. 4. 13 Variation of solute rejection behaviors of the Control TFC-PCNF and TFC-PCNF membranes, with change in M.W. of BPEI and inclusion of quaternized charged moieties in the membranes' skin layers.

Such electrostatic effect is exerted by the stationary layer of positively charged sites of the membranes to the ionic constituent with higher positive charge density *i.e.*, bi-valent co-ion (Mg^{2+}), leading to Donnan exclusion. Further, B. Tansel *et al.* [78] reveal that the co-ion, Mg^{2+} with small crystal radius (0.065 nm) and high hydrated radius (0.428 nm) [79], can firmly hold its hydration shell during nanofiltration process. This further affirms the fact of higher rejection efficiency for solutes having such ion during their cross-flow permeation. However, there also exists electrostatic attractive potential between the membranes and the anionic constituents of the solutes. Thus, in spite of having higher hydrated radius of the bi-valent counter-ion (SO_4^{2-}, 0.379 nm) as compared to the mono-valent counter-ion (Cl^-, 0.332 nm), the contrast in their negative charge densities plays a dominant role in deciding the superior rejection for $MgCl_2$ over $MgSO_4$. The lower efficiency in rejection of solutes like Na_2SO_4 - 71.9(±0.3)% for TFC-PCNF$_I$, 68.5(±0.5)% for TFC-PCNF$_{II}$ and 52.6(±0.2)% for TFC-PCNF$_{III}$; and NaCl - 57.6(±0.2)% for TFC-PCNF$_I$, 50.1(±0.4)% for TFC-PCNF$_{II}$ and 49.2(±0.1)% for TFC-PCNF$_{III}$ can be attributed to the weaker effect of Donnan exclusion by the membrane. The co-ion, Na^+, with lower positive charge density and smaller hydrated radius (0.358 nm) exhibits weaker binding to its hydration shell and consequently leads to such rejection behavior for the solutes. However, it is expected that the presence of bi-valent counter-ion in Na_2SO_4 may facilitate its transport through the membrane over NaCl, due to the greater electrostatic attraction between the positively charged sites of the membranes and the former. But, in our present study, the higher rejection trend for Na_2SO_4 over NaCl signifies that solute with the anionic constituent having even more negative charge density experiences higher degree of rejection than the solute with anionic constituent having lesser negative charge density. Such contrast in interaction behavior and concurrent rejection trend may thus be attributed to the additional and overcompensating contribution of size exclusion phenomena, exhibiting the role of skin layers' pore structure formed by the crosslinked architecture of the poly(ethyleneimine amide) in restricting the transport of larger sized hydrated SO_4^{2-} ions as compared to the smaller sized hydrated Cl^- ions [80].

A further investigation on cross-flow permeation study of the membranes (Fig. 4. 13) reveals that there exists feasible variation in rejection behaviors between the control TFC-PCNF membranes comprising of poly(ethyleneimine amide)s as skin layers and the TFC-PCNF membranes with quaternized poly(ethyleneimine amide)s as skin layers. The unique advantageous feature of the latter class of membranes resides in their efficiency towards enhanced differential rejection for solutes comprising of bi- and mono-valent cations, which is ensured by comparing the variation in solute rejection ratios ($MgCl_2$/NaCl) of the control TFC-PCNF and TFC-PCNF membranes. The solute rejection ratio enhances from 1.36 to 1.69, 1.65 to 1.95 and 1.78 to 2.01 for TFC-$PCNF_I$, TFC-$PCNF_{II}$ and TFC-$PCNF_{III}$ from the respective control TFC-PCNF membranes, respectively. This further indicates that the membrane made from higher M.W. of BPEI provides more pronounced differential rejection efficiency and accordingly transmits the potential to exhibit superior fractionation ability towards any mixed solute streams comprising of different cationic constituents as well. However, the better differential rejection efficiency of the TFC-PCNF membrane derived employing higher M.W. of BPEI as compared to the membranes made by the use of lower M.W. of BPEI seems to be anomalous since such behavior shows a contrast to the trend in variation of surface positive charges of the membranes, as discussed during analysis of their electrokinetic features. The established feature *i.e.*, enhancement in the extent of charged sites in polymer chains of the quaternized poly(ethyleneimine amide) on moving from TFC-PCNF$_{III}$ to TFC-PCNF$_{I}$ through TFC-PCNF$_{II}$, evidenced by the analyzed hydrophilic and electrokinetic features of the membranes implies that there may occur a probable steady increase in electrostatic repulsion between the bulky polar terminal functional-moieties and monomeric units within the polymer chains. This concurrently changes the spacing of bulky functional-moieties as well as conformations of the polymer chains within the crosslinked structure of quaternized poly(ethyleneimine amide) type skin layer, further affecting the membranes' pore structure. The investigation carried out by Y.-C. Chiang *et al*. [21], correlating the effect of charge on transport characteristics of PEI/TMC based nanofiltration membranes, with variation of pH substantiates the role of charges in changing the membranes' pore structure. Further, C. Sun *et al*. [81] proposed that enhanced branching as well as protonation in PEI results in an enhanced radius of gyration (the average squared distance of every atom from the center of mass of the polymer chain) and end-to-end distances (the root mean square distance of the two ends of the polymer chain) of the polymer chains. In depicting the role of molecular architecture of polyimide based membranes, Y. Xiao *et al*. [82] explained that enhanced polarity and bulkiness of the pendant groups increase the interchain spacing and concurrently reduce the packing efficiency of the polymer chains. Thus, the resultant compactness or packing efficiency of the polymer chain segments, affecting the crosslinking density of the poly(ethylene amide) through concomitant formation of an elongated polymer structure in membrane with more charge bearing sites may be attributed to the fact of increase in inter-chain spacing and polymer chain mobility. However, the solvent fluxes of the membranes (Fig. 4. 14) decrease from TFC-PCNF$_{I}$ to TFC-PCNF$_{III}$ through TFC-PCNF$_{II}$, with increase in M.W. of BPEIs.

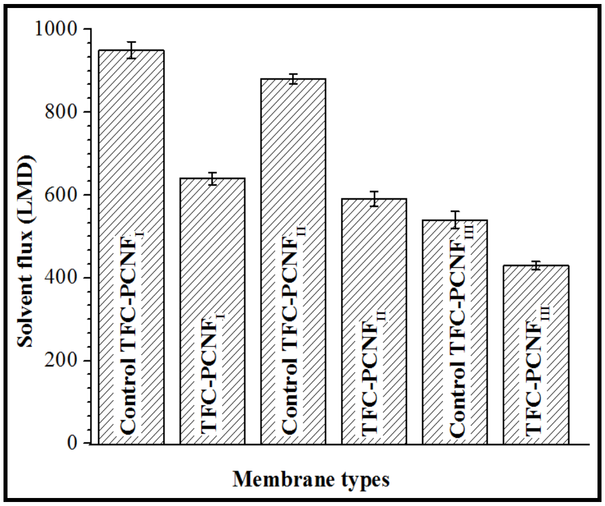

Fig. 4.14 Variation of solvent flux behaviors of the TFC-PCNF membranes, with change in M.W. of BPEI and inclusion of quaternized charged moieties in the membranes' skin layers.

This variant behavior as well as the noticeable trade-off between the differential rejection efficiency and the solvent flux are in accordance with the trend of decrease in polymer free volume due to quaternization on BPEI of varying M.W. with different branching density, as mentioned during the discussion on change in hydrophilic and surface charge features of the membranes in earlier sections. Therefore, the proposed explanations on variation in physicochemical features based on the trends in obtained solute rejections and solvent fluxes of the investigated membranes signify that factors like incorporation of charges in polymeric structure, extent of charged sites and their impact on the conformations (pore structure) as well as compactness (crosslinking density) of the skin layer polymer collectively play prevailing role in determining the macroscopic behaviors of the membranes.

Furthermore, the investigation on variation in solvent flux behaviors between the TFC-PCNF and control TFC-PCNF membranes explicates that the membranes comprising of quaternized poly(ethyleneimine amide) as skin layers exhibit less solvent fluxes as compared to the membranes having non-quaternized poly(ethyleneimine amide) as skin layers, derived employing similar M.W. of BPEI. Such kinds of variations occur in spite of inclusions of charged moieties in the membranes' skin layer and show a contrast to the proposed correlations made during analysis of the physicochemical and macroscopic behaviors of the TFC-PCNF membranes. The observed trend substantiates the fact that, albeit there are incorporation of charges in the polymer network of TFC-PCNF membranes, factor like dynamics of solvent transport through the nano-sized channels of the polyamide networks (having hydrophilic N/O-sites and comparatively hydrophobic polymer backbone), depending on the interaction behavior between the solvent and the solvation regions of the polymer structure may intermittently play dominating role over other physicochemical factors. This kind of variations have also been observed in the earlier study carried out by T. K. Dey *et al*. [23], where solvent fluxes of the membranes (prepared under identical conditions of curing) decrease with progressively higher degree of functionalization of the amine monomer *i.e.*, with more inclusion of the trimethylammonium groups as positively charged terminal functional-moieties in the branches of the polymer backbone of membranes' skin layer. In the present investigation, the variant transport characteristics are found to be in accordance with the possibility of a decrease in polymer free volume due to quaternization on BPEI of increasingly higher M.W., as highlighted during the discussion on change in hydrophilic and surface charge features of the membranes in earlier sections.The anisotrpy in dynamics of solvent molecules during their transport through the nano-sized channels of the crosslinked-quaternized poly(ethyleneimine amide) and crosslinked poly(ethyleneimine amide) networks may further be ascribed to the varying interaction between the solvent and the solvation regions of the polymer structure comprising of hydrophilic N/O-sites and the hydrophobic polymer backbone. The observed trend of solvent fluxes substantiates the fact that, albeit there are incorporation of charges in the polymer network of TFC-PCNF membranes, the variant spatial distribution of the strewn quaternized sites may intermittently play decisive role towards reorientation dynamics of the solvent over other physicochemical factors.

4. 4. Conclusions

Structural investigations by ^{1}H-NMR and FTIR establishes that facile quaternization of BPEIs of varying M.W. by GTACl involves formation of termolecular-oxirane/amine/hydroxyl complex following *in situ* autocatalytic approach during the consecutive non-catalytic and catalytic steps, where inclusion of the hydroxypropyl trimethylammonium groups as quaternized functional-moieties happens in the amine sites of the BPEIs' backbone.

The formations of crosslinked-quaternized poly(ethyleneimine amide)s as the synthesized thin skin layers of the TFC-PCNF membranes, following *in situ* interfacial polymerization process are substantiated by FTIR and XPS studies.

An extensive investigation of the variations in hydrophilic features of TFC-PCNF membranes implies that the structural orientation as well as organization of the resultant rigid crosslinked poly(ethyleneimine amide) get affected by the enhancement of M.W. of BPEI, since increase in branching density of polymeric backbone of the quaternized BPEI induces constrained mobility in the chain segments and thus, consequently restricts the migration of polar terminal functional-moieties from the interior to the periphery of the skin layer polymer. The study also signifies the effect of inclusion of the quaternized functional-moieties on packing patterns of the polymer chains in structures of crosslinked poly(ethyleneimine amide)s, where the extent of differential hindrance in segmental orientations depend on the resultant variation in spacing of the moieties. Electrokinetic features of the TFC-PCNF membranes, analyzed with variation of pH reveal that absolute Z.P. values get enhanced with lowering of pH followed by decline at even higher acidic environment. This signifies that the effective streaming current is reasonably reduced by the diffusive back flow of the streaming current due to dragging of the tangentially driven counter-ions from the hydrodynamic slipping plane to the bulk of the membranes stationary positively charged layer. However, progressively enhanced pH condition results in non-specific adsorption of the excess counter-ions as well as concentration build up of the counter-ions with subsequent compression in the electrical double layer thickness, leading to screening of the surface positive charges with resultant severe reduction in the positive absolute Z.P. values of the membranes.

Cross-flow permeation study, performed for all the positively charged TFC-PCNF membranes reveals that the membranes bearing high extent of positive surface charges follow a rejection trend of $MgCl_2$ > $MgSO_4$ > Na_2SO_4 > NaCl, under iso-osmotic environment of solutes. The higher rejection trend towards $MgCl_2$ and $MgSO_4$ profoundly indicates the effect of Donnan exclusion, governed by the stationary layer of positively charged sites of the membranes. However, the higher rejection efficiency for Na_2SO_4 over NaCl signifies the additional and overcompensating contribution of size exclusion phenomena, exhibiting the role of skin layer pore structure formed by the crosslinked architecture of the poly(ethyleneimine amide) in restricting the transport of larger sized hydrated anionic constituents as compared to the smaller sized ones. Based on the trends in obtained solute rejections and solvent fluxes of the investigated membranes, it is proposed through extensive illustrations that factors like incorporation of charges in polymeric structure, extent of charged sites and their impact on the conformations (pore structure) as well as compactness (crosslinking density) of the skin layer polymer collectively play dominant role in tuning the physicochemical features as well as macroscopic behaviors of the membranes.

CHAPTER – 5

Nano-ZnO impregnated thin film nanocomposite NF membranes: An investigation of variation in structure, morphology and transport properties

5. 1. Introduction

For almost a decade, when it seemed that the performance of the membranes in tems of solute rejection and especially the solvent flux, had reached the limits, the advent of nanotechnology provided a new dimension to the membranologists by changing the scenario [85]. They explored promising ways to prevail over some of the limitations associated with the synthetic polymeric membranes by developing new types of organic-inorganic hybrid nanocomposite materials [86-88]. Extensive research works on various metals, metal oxides as well as ceramic and zeolite nanoparticles have been conducted to impart improved physicochemical properties in the membranes. Production of membranes by incorporation of nanomaterials tendered better chemical, mechanical and thermal resistance and also prevented adhesion as well as adsorption of the undesired fouling materials on their surfaces, thereby maintaining the membrane permeability and selectivity as well as minimizing the load on pretreatment and chemical cleaning. It has been observed that microstructural features of the membranes are affected by site specific interaction between the metal oxide nanoparticle and the host polymer matrix, altering the skin layer morphology, pore size, pore size distribution, surface roughness, etc. which eventually influence their performance. Different metal oxide nanoparticles like silica (SiO_2) [89,90], alumina (Al_2O_3) [91,92], titania (TiO_2) [93-95], ferric oxide (Fe_2O_3) [96], zinc oxide (ZnO) [97, 98], zeolites [99,100], etc. have been employed as nanofillers in nanocomposite membranes’ polymeric host matrix leading to promising improvements like better chemical and thermomechanical properties.

In recent times, ZnO nanoparticles has drawn much attention of the membranologists as a suitable nontoxic, bio-safe and bio-compatible material with strong inhibitory and antibacterial effect, over a broad spectrum, of both G^+ and G^- bacteria [101-103]. Adams et al. [104], Brayner et al. [105] and Jeng and Swanson [106] have reported that ZnO is more efficient in controlling the growth of micro-organisms than other metal oxides such as SiO_2, MgO, TiO_2 and CaO by significantly inhibiting the growth of a wide range of pathogenic bacteria under visible light conditions. The commonly proposed antimicrobial mechanisms for nano-ZnO are i) generation of reactive oxygen species like hydrogen peroxide (H_2O_2), hydroxyl radical ($^{\cdot}OH$) and singlet oxygen ($^1O_2$) from the surface of zinc oxide, penetrating the cell membrane and inhibiting the growth of the cells and ii) rupture of cell membrane and leakage of cytoplasmic content because of binding between the bacterial cell and ZnO nanoparticles due to electrostatic forces [107-109].

The present study emphasizes on investigations of structural and physicochemical features of the inorganic-polymer hybrid thin film nanocomposite nanofiltration (TFN-NF) membranes, prepared by impregnation of as synthesized nano-ZnO into the polymer skin layer during the *in situ* interfacial polycondensation of branched polyethyleneimine (PEI) and trimesoyl chloride (TMC). The synthesized nano-ZnO have been characterized by X-ray powder diffraction (XRD) analysis, Fourier Transform Infra-red (FTIR) spectroscopy, Raman spectroscopy and X-ray photoelectron spectroscopy (XPS). For membranes, XPS as well as ATR FTIR analysis of skin layers investigated the influence of nano-ZnO, with variation in the ways of incorporation, on the electronic and molecular level interactions happening within the nanocomposite polyamide matrices of the TFN-NF membranes. Changes in skin surface morphologies of the skin layer of nanocomposite membranes have been investigated by scanning electron microscopy (SEM). Quantitative surface roughness analysis by atomic force microscopy (AFM) has been applied to probe the role of the nanomaterials in influencing the membrane topographies. Energy dispersive

X-ray (EDX) analysis has been employed to determine the elemental composition of skin layer of the TFN-NF membranes. Hydrophilic and electrokinetic features of the membranes have been evaluated by contact angle measurements and zeta potetial studies, respectively. Cross-flow permeation experiments have been performed to correlate the variation in physicochemical features of the membranes with their transport parameters like solute rejection and solvent flux behaviors.

5. 2. Experimental

5.2.1. Materials and methods

Polysulfone (Psf; M_W: 30k Da), procured from Solvay Speciality Polymers (India), N-methyl-2-pyrrolidone (NMP; purity: ≥ 99 %), procured from Sigma-Aldrich and polyvinyl pyrrolidone (PVP, K-30; M_W: 40k Da), procured from SRL (India), were used for preparation of the polysulfone (Psf) base membrane. The nonwoven porous polyester fabric used as a reinforcement material for making the base membrane had a density of 75 g/m^2 and a thickness of 110 μm with an air permeability of 70 dm^3/m^2 at 2 mbar. Aqueous solution (50 w/v %) of branched poly(ethyleneimine) (PEI; M_W: 600k-1000k Da; d_4^{20}: 1.08), typically constituting about 25 % primary, 50 % secondary and 25 % tertiary amine groups and trimesoyl chloride (TMC) with 98 % purity, procured from Sigma-Aldrich were used without any further purification. The organic solvent, extrapure (99 %) AR grade n-hexane was procured from SRL, India. Various electrolytes of AR grade, like magnesium chloride heptahydrate ($MgCl_2.7H_2O$), anhydrous sodium sulphate (Na_2SO_4), sodium chloride (NaCl) and potassium chloride (KCl) were obtained from different companies in India. For contact angle measurements, the solvents were used as received: ethylene glycol (Qualigen, assay: 98%) and diiodomethane (Spectrochem, assay: 98%). The conductivity of ultra pure water used for preparation of monomer solutions, membrane preparation as well as nanofiltration experiments was below 2μS/cm. Zinc(II) acetylacetonate hydrate (99.995 % purity) [$Zn(acac)_2.H_2O$] was obtained from Sigma-Aldrich.

5.2.2. Synthesis of ZnO nanocrystals

ZnO nanocrystals (nano-ZnO) were synthesized by thermal decomposition of anhydrous $Zn(acetylacetonate)_2$ in n-octylamine at temperature as low as 110 ^{o}C. The precursor anhydrous $Zn(acetylacetonate)_2$ was prepared following the method of Rudolph and Henry [110]. In a typical preparation, 0.5 g (1.89 mmol) of anhydrous $Zn(acetylacetonate)_2$ was taken in a 50 mL three-neck flask with 10 mL (~60.5 mmol) of n-octylamine. The reaction flask was evacuated to a vacuum level of 2 mbar for 30 minutes at 40 ^{o}C. The reaction system was then heated (~10 ^{o}C min^{-1}) to 110 ^{o}C under argon flow and maintained at this temperature for 2 hours. A white suspension was obtained which was cooled to 60 ^{o}C and 5 mL of methanol was added to the reaction flask. The nanocrystals of ZnO were recovered by centrifugation, dispersed in toluene, and precipitated by addition of methanol. The redispersion and precipitation steps were repeated twice to remove any unreacted precursors and excess solvent.

5.2.3. Fabrication of thin film nanocomposite nanofiltration membranes

5.2.3.1. Preparation of Psf base membrane by nonsolvent induced phase inversion method

The flat-sheet microporous Psf base membrane was prepared following nonsolvent induced phase inversion method, where a homogeneous casting solution, comprising of 30 (w/v) % Psf in NMP, along with the pore forming additive - PVP (40 % wt. of Psf), was cast on a nonwoven polyester substrate to a thickness of 100 μm using an automated casting machine. The membrane was immediately dipped in a water bath, maintained at room temperature, for immersion precipitation. The water of the bath was changed several times to ensure a complete removal of the solvent (NMP) and additive (PVP) from the membrane matrix by leaching. The entire casting machine was kept in an environmentally controlled atmosphere where temperature and relative humidity were maintained at 25 ^{o}C and 35-40 %, respectively. This Psf membrane was subsequently used as a base material for preparation of the thin film nanocomposite nanofiltration (TFN-NF) membranes.

5.2.3.2. Preparation of Control-NF and inorganic-polymer hybrid TFN-NF membranes

A control, thin film composite nanofiltration membrane, (Control-NF), devoid of any nanomaterial, was prepared by *in situ* interfacial polycondensation reaction (Fig. 5. 1, Scheme of synthesis) between PEI (in aqueous medium) and TMC (in organic, n-hexane medium).

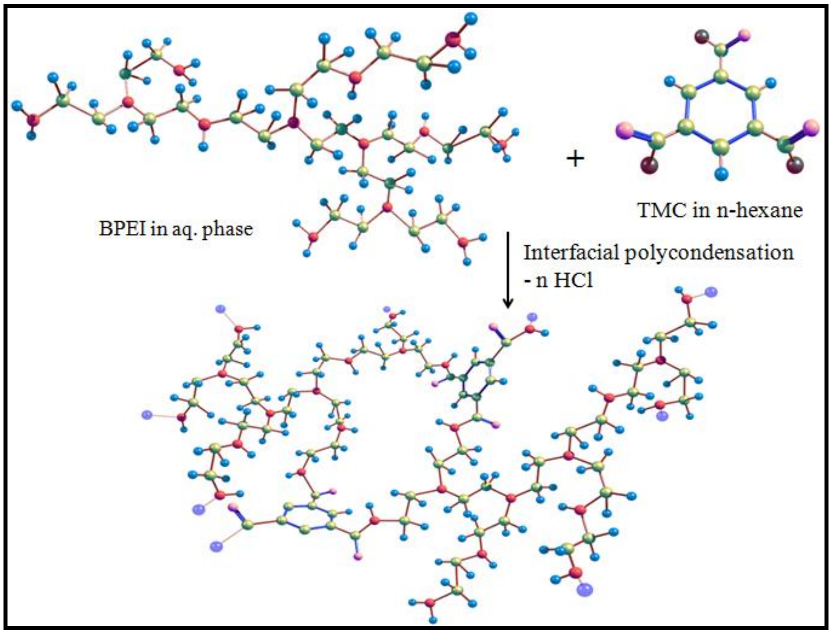

Fig. 5.1 Schematic of synthesis of polyamide from PEI and TMC, following *in situ* interfacial polycondensation process.

A piece of microporous Psf base membrane was treated with 4 (w/v) % aqueous solution of PEI for 4 minutes. After removing the amine soaked base membrane from the aqueous medium and eliminating the excess solution by gently squeezing it between two rubber rollers the membrane was dipped in a 0.1 (w/v) % TMC solution for 30 seconds. The nascent TFC membrane, comprising of a freshly deposited ultrathin polyamide film over the surface of the Psf base membrane was further heat cured at 90 ^{o}C in a hot air circulated oven for 30 minutes.

For development of the inorganic-polymer hybrid TFN-NF membranes, the nano-ZnO was introduced in either aqueous or organic phase. The nano-ZnO was dispersed in aqueous or n-hexane medium by applying ultrasonication for 15 min prior to the start of membrane making process. When prepared by incorporation of the nano-ZnO through the aqueous phase, 4 (w/v) % aqueous solutions of PEI containing well dispersed nano-ZnO of varying concentrations of 0.05, 0.1 and 0.2 (w/v) % were used. The membranes were prepared using the same procedure as the Control-NF, by performing *in situ* interfacial polycondensation reaction with 0.1 (w/v) % TMC solution (Schematics in Fig. 5. 2a), followed by curing at 90 ^{o}C for 30 min. These membranes were named as Aq-ZnO:TFN-NF-1, Aq-ZnO:TFN-NF-2 and Aq-ZnO:TFN-NF-3, respectively. Similarly, in another set of experiments, nano-ZnO of various concentrations of 0.05, 0.1 and 0.2 (w/v) % were ultrasonically dispersed in n-hexane, containing 0.1 (w/v) % TMC monomer. The *in situ* interfacial polycondensation was conducted adopting the same approach as the Control-NF, with 4 (w/v) % aqueous PEI solution (Schematics in Fig. 5. 2b), followed by curing at 90 ^{o}C for 30 min.

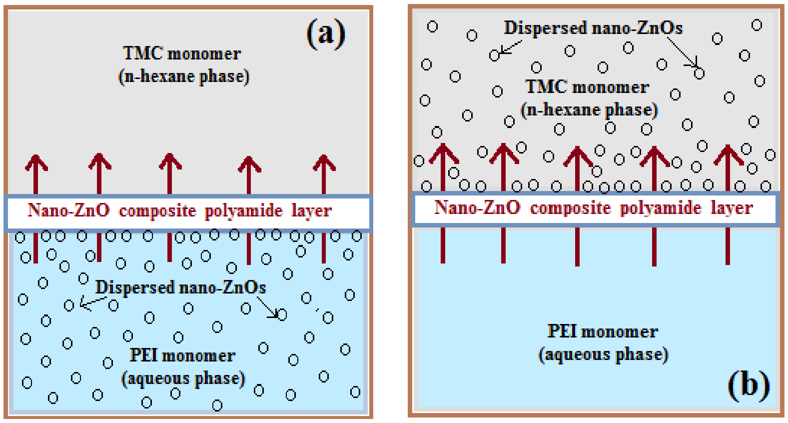

Fig. 5. 2 Schematics of two different pathways: (a) through aqueous phase of PEI and (b) through n-hexane phase of TMC, for nano-ZnO incorporation in the thin skin layer of TFN-NF membranes by *in situ* interfacial polycondensation process; (The arrows ↑ indicate the direction of diffusion of PEI monomer across the interfacially formed polymeric barrier layer to react with TMC at the organic phase side).

These membranes were named as Org-ZnO:TFN-NF-1, Org-ZnO:TFN-NF-2 and Org-ZnO:TFN-NF-3, respectively. They were washed with de-ionized water to remove the leachable chemicals before conducting performance evaluation tests.

5.2.4. Textural and structural characterizations of as synthesized nano-ZnO

Phase purity and structure of the ZnO nanocrystals were determined by X-ray powder diffraction (XRD) data, which were collected on a Philips X'Pert pro X-ray diffractometer using Cu-Kα radiation (λ = 1.5418 Å) at 40 kV and 30 mA. FTIR spectrum of the ZnO nanocrystals was recorded in attenuated total reflectance (ATR) mode using a Bruker Vertex 70 FTIR spectrometer, in the range of 500–1500 cm^{-1}. Micro-Raman spectra of the nanocrystals were obtained on a LABRAM-I, ISA make spectrometer using an Ar^+ ion laser (488 nm) equipped with a Peltier-cooled CCD detector. For XPS characterization of the ZnO nanocrystals, a DESA-150 electron analyzer (Staib Instruments, Germany) equipped with Mg-Kα X-ray source (1253.6 eV) was employed. The spectrometer’s binding energy scale was calibrated with Au-$4f_{7/2}$ photopeak at a binding energy (BE) of 83.95 eV. Curve fitting of intensity versus binding energy

(BE) plots comprising the multiplex photo peaks was performed using Gaussian functions (XPSPEAK 41 software) and then peak area as well as full width at half maximum (FWHM) were also determined.

5.2.5. Characterization of TFN-NF membranes

5.2.5.1. Characterization of skin layers of TFN-NF membranes by XPS

The technique of XPS was employed for quantitative evaluation of chemical interactions, in the skin layer polymer matrices of the TFN-NF membranes. The skin layer was characterized and compared in terms of change in core level binding energies of Zn, N and O for Control-NF, Aq-ZnO:TFN-NF and Org-ZnO:TFN-NF class of membranes.

5.2.5.2. Spectral characterization of skin layers of TFN-NF membranes by FTIR

Bruker Vertex 70 FTIR spectrometer, equipped with an ATR attachment (ZnSe crystal, 45^{o} angle of incidence and refractive index 2.4), was employed for ATR-FTIR analysis of membranes. The membrane’s skin surface was kept faced down onto the ATR crystal element and a light pressure was applied using a MIRacle high pressure clamp with torque-limited press. The radiation penetration depth was 2 µm. All infrared spectra were recorded in transmittance mode, in the range of 600-4000 cm^{-1}, at 25 ^{o}C. Evaluation of each spectra was done by acquiring 100 scans at a spectral resolution of 2 cm^{-1}.

5.2.5.3. Investigation of skin surface morphology of TFN-NF membranes by SEM

The morphological analyses, through SEM, of ultrathin skin surfaces of the TFN-NF membranes were carried out using CamScan–CS3200LV, UK. In order to make the membranes electrically conducting, 2 mm × 2 mm strips of the dry membrane samples were sputter coated on the skin surface with gold-palladium alloy for 60 s employing a current of 30 mA. The skin layer images were recorded at an acceleration voltage of 15 kV and 4000X magnification when operated in secondary electron mode. For acquiring the cross-sectional images of the TFN-NF membranes, the membrane samples (without support polyester fabric) were fractured in liquid nitrogen into smaller sized strips and sputter coated on the cross-sectional layer with gold-palladium alloy for 100 s at a current of 15 mA. The image acquisition was done in secondary electron mode at an acceleration voltage of 20 kV and 1000X magnification.

5.2.5.4. Topographical characterization of skin surfaces of TFN-NF membranes by AFM

Topographical charaterization of membrane skin surfaces was done by extracting quantitative informations from the three-dimensional (3D) topographies acquired in the semi-contact mode by using an AFM instrument (NT-MDT SOLVER next, Russia). Small squares of approximately 1 cm^2 of the membrane were cut and glued onto a metal substrate. The rectangular cantilever NSG 10 (NT-MDT, Russia) was made out of Si_3N_4 with a spring constant of 11.8 N/m, having a typical resonance frequency of 240 kHz and a nominal tip apex radius of 10 nm with high aspect ratio. The scanning was done on a 10 µm × 10 µm area of the membrane, in air, at room temperature, with a scanning frequency of 0.1 Hz. The scanned regions were flattened using a second order polynomial to remove the curvatures and slopes from the image and then the resulting best fit was subtracted from it. NOVA-P9 software was used for the purpose of image acquisition and evaluation of surface roughness parameters of the membranes. Surface roughness parameters of the membranes were calculated from the height profiles of the image in terms of average roughness (R_a), root mean square roughness (R_q) and ten point height (R_{10Z}).

5.2.5.5. Elemental analysis and mapping of skin surfaces of TFN-NF membranes

Quantitative surface elemental analysis and mapping were performed by an energy dispersive X-ray spectrometer (EDX) coupled to the SEM and a micro analysis system (INCA Oxford

Instruments, UK), employing an accelerating voltage of 20 kV and a magnification of 4000X. It was equipped with an ultrathin beryllium window and 20 mm^2 Si detector. The spectra were acquired for 2 h to map the elements of interests like N, Zn and O in each membrane. The elemental analysis of N, Zn and O, were carried out over 170 points in a grid spectrum where each point was allowed to undergo 60 s of detection period.

5.2.5.6. Characterization of hydrophilic properties of the TFC-PCNF membranes

Static contact angle measurement was conducted using sessile drop method at ambient temperature. A contact angle measuring instrument (DSA 100 of KRUSS Gmbh, Germany) with DSA 1 v 1.92 software was employed to assess the hydrophilicity and surface free energy (SFE) with its polar and dispersive components of the active skin layers of the membranes. For this purpose, three different solvents (water, ethylene glycol and diiodomethane) with known surface tension values were employed. The sessile drop was slowly and steadily formed on the membrane surface by depositing 3 µl of the given solvent with a microsyringe and the measurement at the membrane-solvent-air interface was completed with a residence time of 60 s. At least eight such measurements were done at different locations of each membrane skin surface and then averaged out to calculate the contact angle with their standard deviations. Fowkes method was applied to calculate the SFE along with the polar and dispersive components of the membranes' surfaces from the surface tension values of the probe solvents and contact angle values of the membranes with respect to those solvents. Wetting envelopes were also constructed for the membranes' surfaces by reversing the method applied to determine the polar and dispersive part of SFE. The closed contour or envelope, with coordinate system made from polar and dispersive part of the SFE defines the line where the condition of contact angle 0^o ($\cos \theta = 1$) is satisfied.

5.2.5.7. Determination of surface charge properties of the TFC-PCNF membranes

The electrokinetic features of the membranes were evaluated by employing ZetaCAD electrokinetic analyzer (CAD Inst., France). The streaming potential analyzer consisted of a quartz-cell configuration which was capable of holding two flat sheet membranes in such a way that the membranes remained separated by spacers and the skin layers faced each other creating a slit channel for tangential flow of electrolytic solution across the membranes. The electrical potential difference, generated due to the bidirectional flow of electrolyte solution (10^{-3}M KCl) under pressure gradient across the membrane was measured by Ag/AgCl electrodes, equipped with the cell. Zeta potentials of the membranes were evaluated utilizing the streaming potential values and the relationship between the measurable streaming potential (V_{st}) and the zeta potential (ζ), following the Helmholtz-Smoluchowski equation. An average value of zeta potential from three replicates was reported and the measurement error was found to be ± 0.5 mV.

The values of ζ of the membranes as determined were further employed to calculate electrokinetic surface charge densities (σ_s) at the shear planes of the membranes as a function of the respective pH environments.

5.2.6. Nanofiltration performance evaluation through cross-flow permeation experiments of TFN-NF membranes

Transport experiments of the Control-NF, Aq-ZnO:TFN-NF and Org-ZnO:TFN-NF class of membranes were conducted in cross-flow test cells, using single feed solutions of three different solutes consisting of varying combination of monovalent and bivalent cations and anions. Solutions of NaCl, $MgCl_2$ and Na_2SO_4, having concentrations iso-osmotic with 0.03 M NaCl were used as feeds. The experiments were conducted at 10 bar of transmembrane pressure using a pump with 10 liter per minute feed flow rate. Temperature of the feed solution was maintained at 25 ^{o}C. Circular membrane samples having an effective membrane area of 15.1 cm^{2} were properly washed in deionized water and placed in the test cell with their selective skin layers facing the incoming feed. All the membranes were given sufficient time for stabilization before evaluating of their performances. The percentage of solute rejection (SR) was determined by conductivity measurement of the respective solutions. The steady-state solvent flux (J_W), expressed in terms of L.m^{-2}day^{-1} (LMD) was determined by direct measurement of the permeate flow *i.e.*, volume (V, in L) collected during a time period, (T, in day) through a membrane area, (A, in m^{2}) at certain pressure.

5. 3. Results and discussion

5.3.1. Analysis of textural and structural features of nano-ZnO

The X-ray diffraction patterns of nano-ZnO, obtained by thermal decomposition of the acetylacetonate in n-octylamine at 110 ^{o}C, are shown in Fig. 5. 3. The patterns can be indexed to hexagonal wurtzite lattice structure of the nano-ZnO. The indexing to X-ray patterns is attributed to (100), (002), (101), (102), (110), (103), (200), (112), (201), (004) and (202) peaks of hexagonal crystalline phase of nano-ZnO. The average crystallite sizes as determined using Scherrer's formula ($t = K\lambda/B \cos\theta$, where t = average crystallite size in Å, K = Scherrer constant usually taken as 0.9 Å, λ = X-ray wavelength, θ is the Bragg angle, and B = integral breadth of a reflection located at 2θ) range from 22 ± 2 nm. The lattice structure of the nanocrystals of ZnO can be depicted as a number of alternating planes arranged in tetrahedral and/or octahedral fashion through coordination of O^{2-} and Zn^{2+} ions, stacked alternately along the *c*-axis.

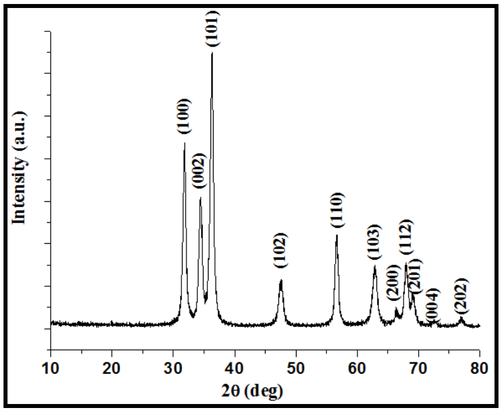

Fig. 5. 3 XRD pattern of as-synthesized nano-ZnO.

The FTIR spectrum of the as synthesized ZnO nanocrystals, acquired in the atmospheric conditions, is shown in Fig. 5. 4. The most prominent band at 510 cm^{-1} and a weak band at 660 cm^{-1} are assigned to the stretching vibrations of Zn–O bonds, in the tetrahedral and octahedral coordinations, respectively [111].

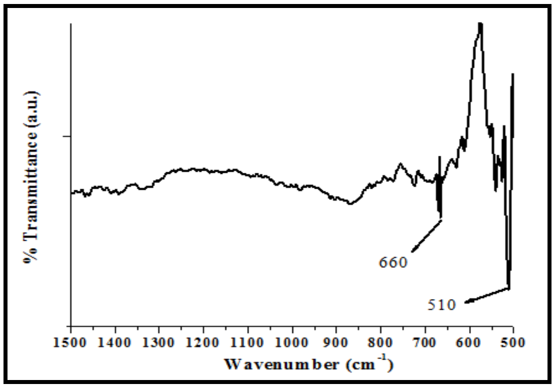

Fig. 5. 4 FTIR spectra for nano-ZnO.

A Raman spectrum of the ZnO nanocrystals, acquired at room temperature, is shown in Fig. 5. 5. Hexagonal wurtzite structure of ZnO belongs to the space group C_{6v}^4 with two formulae units per primitive cell, where all atoms occupy C_{3v} sites. The Raman active zone-centre optical phonons predicted by group theory is $A_1+2E_2+E_1$. Of these, the phonons of A_1 and E_1 symmetry are polar and both Raman and IR active. Hence, they show different frequencies for the transverse optical (TO) and longitudinal optical (LO) phonons. A weak band at 407 cm^{-1} is assigned to E_1TO phonon mode. The nonpolar optical phonon modes with symmetry E_2, being Raman active only, exhibit dual frequencies where E_2 (Low frequency) at 99 cm^{-1} is associated with oxygen atoms and E_2 (High frequency) at 437 cm^{-1} is associated with the sublattice of Zn, which are characteristic of the wurtzite hexagonal phase of ZnO [112-113].

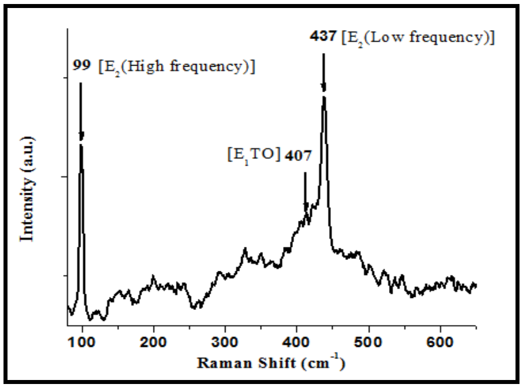

Fig. 5. 5 Room-temperature Raman spectrum for nano-ZnO.

The XRD, FTIR and Raman scattering measurements confirm the formation of ZnO nanocrystals in hexagonal wurtzite structure.

XPS analysis of the ZnO nanocrystals exhibits presence of a strong peak (Fig. 5. 6a) at 1020.5 eV with FWHM of 2.20 eV, attributed to Zn-2$p_{3/2}$ and a weaker peak at 1043.8 eV with FWHM of 2.21 eV, attributed to Zn-2$p_{1/2}$ [114]. In Fig. 5. 6b, the component peaks of the deconvoluted O-1s photoelectron spectrum show the presence of a dominant O-1s peak with lowest binding energy, centered at 529.8 eV with FWHM of 1.79 eV, which can be indexed to the surface and near-surface region lattice oxygen of the hexagonal lattices of nano-ZnO. A distinct higher binding energy of O-1s peak at 531.3 eV, with FWHM of 1.63 eV, can be ascribed to the strongly anchored hydroxyl groups (Zn-OH) at different intrinsic or extrinsic defect sites or oxygen vacancies (O_v) of nano-ZnO [115]. However, the weakest but relatively broadened shoulder peak at 532.5 eV with FWHM of 2.04 eV is due to chemisorbed oxygen contributed by surface hydroxyl groups [116].

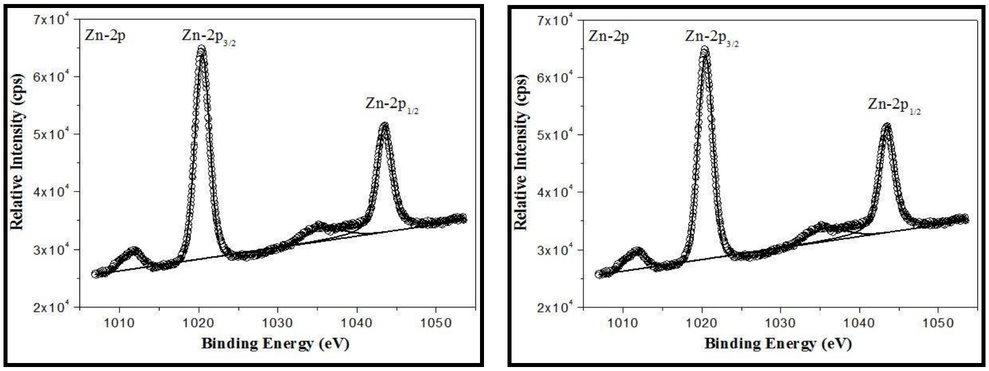

Fig. 5. 6a High resolution Zn-2$p_{3/2}$ and Zn-2$p_{1/2}$ photoelectron spectra obtained from nano-ZnO (line with bullets: experimental data; solid line: curve fit of the experimental data; Zn-2$p_{3/2}$: 1020.5 eV peak contribution and Zn-2$p_{1/2}$: 1043.8 eV peak contribution).

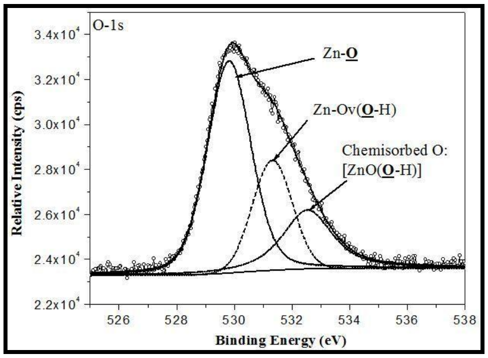

Fig. 5. 6b High resolution O-1s photoelectron spectra obtained from nano-ZnO (line with bullets: experimental data; solid line: curve fit of the experimental data; Zn-O: 529.8 eV peak contribution; Zn-Ov(O-H): 531.3 eV peak contribution and ZnO(O-H): 532.5 eV peak contribution).

5.3.2. Characterization of skin layers of TFN-NF membranes by XPS

Representative TFN-NF membranes, one each from the series made by introducing nano-ZnO through aqueous phase as well as organic phase, (*i.e.*, Aq-ZnO:TFN-NF-2 and Org-ZnO:TFN-NF-2) were employed for XPS analysis to investigate the electronic and molecular level interactions of the nanocomposite polyamide skin layers, within the XPS probe depth (5-10 nm). Further, comparisons of XPS analysis of skin layers of these two membranes with that of the Control-NF were made, with respect to the variation in core level binding energies and respective peak areas, to study the effect of nano-ZnO impregnation in polyamide matrices.

The Zn-2p photoelectron spectra of nano-ZnO impregnated polyamide skin layer of Aq-ZnO:TFN-NF-2 and Org-ZnO:TFN-NF-2 are presented in Fig. 5. 7b and 7c, respectively.

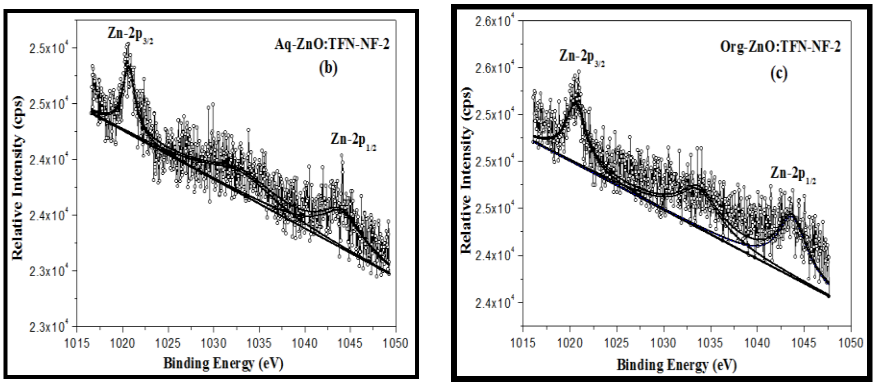

Fig. 5. 7 High resolution Zn-2p photoelectron spectra obtained from nano-ZnO impregnated (b) Aq-ZnO:TFN-NF-2 and (c) Org-ZnO:TFN-NF-2.

In case of Aq-ZnO:TFN-NF-2, the high intensity peak at low BE of 1020.7 eV (FWHM: 1.87 eV) corresponds to Zn-2$p_{3/2}$ and the peak at higher BE with lower intensity, attributed to Zn-2$p_{1/2}$, appears at 1044 eV (FWHM: 3.64 eV), (Table 5. 1). Similarly, for the Zn-2p photoelectron spectrum of Org-ZnO:TFN-NF-2, the peak corresponding to Zn-2$p_{3/2}$ appears at 1020.6 eV (FWHM: 2.75 eV) and a weaker peak, corresponding to Zn-2$p_{1/2}$, appears at 1043.7 eV (FWHM: 3.94 eV). No significant deviations in BE values for Zn-2$p_{3/2}$ as well as Zn-2$p_{1/2}$ of both Aq-ZnO:TFN-NF-2 and Org-ZnO:TFN-NF-2, from the corresponding BE values of the pure nano-ZnO, indicate that there is no redistribution of charge density in Zn-O framework and hence, there is no occurence of inter-atomic charge transfer between the nano-ZnO and the host polymeric material. In other words, ZnO does not form any chemical bonds with the host polymer matrix during the nanocomposite polymer formation. Thus, it is assumed that only the peripheral hydroxyl groups of nano-ZnO play a role in forming noncovalent type secondary chemical interactions with the polyamide network. However, a decrease in BE accompanied by broadening of peaks for Zn-2$p_{3/2}$ by 0.88 eV and Zn-2$p_{1/2}$ by 0.30 eV, from Aq-ZnO:TFN-NF-2 to Org-ZnO:TFN-NF-2 are attributed to the presence of clusters of nano-ZnO with a broad size distribution in the skin surface of the later membrane, as compared to the former, where the size distribution is much more uniform [117].

Table 5. 1

Curve fitting summary of different XPS peaks for skin layers of Control-NF, Aq-ZnO:TFN-NF-2 and Org-ZnO:TFN-NF-2 membranes.

	Zn-2p3/2 & Zn-2p1/2			O-1s			N-1s		
Membrane Code	BE (eV)	FWHM (eV)	Peak area (%)	BE (eV)	FWHM (eV)	Peak area (%)	BE (eV)	FWHM (eV)	Peak area (%)
Control-NF				530.4	1.99	71.18	398.9	2.04	82.26
		-		531.9	2.28	28.82	400.6	2.15	17.74
Aq-ZnO:TFN-NF-2	1020.7	1.87	42.29	530.9	2.37	80.88	399.0	2.01	68.24
	1044.0	3.64	57.71	532.8	2.09	19.12	400.0	2.31	31.76
Org-ZnO:TFN-NF-2	1020.6	2.75	40.88	530.9	2.36	86.02	399.2	2.09	84.82
	1043.7	3.94	59.12	532.7	1.99	13.98	400.7	2.40	15.18

Figs. 5. 8a, 8b and 8c show the O-1s core level photoelectron spectra of skin layer polymers for Control-NF, Aq-ZnO:TFN-NF-2 and Org-ZnO:TFN-NF-2, respectively. The curve fitting and deconvolution of each O-1s XPS spectrum yield two constituent spectra which indicate the presence of oxygen in two different chemical states.

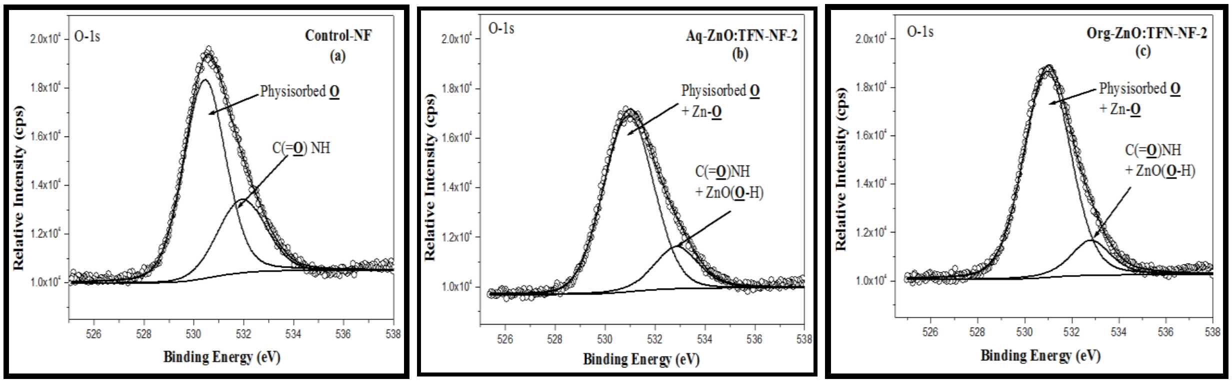

Fig. 5. 8 High resolution O-1s photoelectron spectra obtained from nano-ZnO impregnated (a) Control-NF, (b) Aq-ZnO:TFN-NF-2 and (c) Org-ZnO:TFN-NF-2.

The intense peak with low BE value of 530.4 eV (FWHM: 1.99 eV) for Control-NF is assigned to physisorbed oxygen (Table 5. 1). The shifting of values to higher BE of 530.9 eV, with concurrent broadening of peaks for both Aq-ZnO:TFN-NF-2 (FWHM: 2.37 eV) and Org-ZnO:TFN-NF-2 (FWHM: 2.36 eV), refer to the collective contribution of physisorbed oxygen as well as the surface and near-surface region lattice oxygen of the impregnated nano-ZnO. The less intense component shoulder peak of the deconvoluted O-1s spectra with higher BE value of 531.9 eV for Control-NF is assigned to oxygen in the structure of C=O of amide linkages of polyamide network [118] and those of Aq-ZnO:TFN-NF-2 (BE: 532.8 eV) and Org-ZnO:TFN-NF-2 (BE: 532.7 eV) are contributions from oxygen in the structure of C=O of amide linkages of polyamide network and surface hydroxyl groups of nano-ZnO. The chemical shifts of 0.9 and 0.8 eV for Aq-ZnO:TFN-NF-2 and Org-ZnO:TFN-NF-2 as compared to Control-NF are ascribed to the chemisorbed surface hydroxyl groups of nano-ZnO. Presence of nano-ZnO leads to an increase in areas for the major peaks by 9.7 and 14.84 % for the Aq-ZnO:TFN-NF-2 and Org-ZnO:TFN-NF-2, respectively over the Control-NF. The relative area is subsequently compensated in the shoulder peak, which is contribution of amide oxygen and chemisorbed surface hydroxyl groups of the impregnated nano-ZnO.

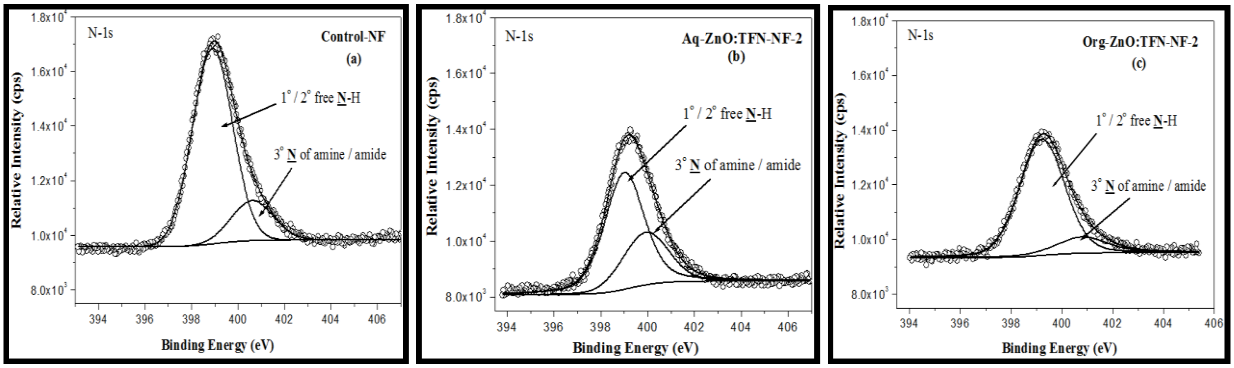

Fig. 5. 9 High resolution N-1s photoelectron spectra obtained from nano-ZnO impregnated (a) Control-NF, (b) Aq-ZnO:TFN-NF-2 and (c) Org-ZnO:TFN-NF-2.

The component peaks of N-1s spectra (Fig. 5. 9a, 9b and 9c*)* with the high intensity, at lower BE of 398.9, 399.0 and 399.2 eV, for Control-NF, Aq-ZnO:TFN-NF-2 and Org-ZnO:TFN-NF-2, respectively (Table 1), correspond to the 2^o nitrogen atoms of free N-H of polyamides and free 1^o as well as 2^o amines of the polymer backbone. The peaks with lower intensity at higher BE of 400.6 eV for Control-NF, 400.0 eV for Aq-ZnO:TFN-NF-2 and 400.7 eV for Org-ZnO:TFN-NF-2 are due to 3^o nitrogen atoms of amides and amines of the polymer backbone as well as nitrogen atoms of amines and amides which are involved in intermolecular hydrogen bonding either through inter-chain interaction or through the surface hydroxyl groups of nano-ZnO. The peak positions are concordant with the reported data in literature [119]. A chemical shift of the N-1s signal to higher BE values in case of Control-NF as well as Org-ZnO:TFN-NF-2, as compared to Aq-ZnO:TFN-NF-2, are attributed to enhanced protonation of amine sites, during the course of polycondensation reaction, of the former two membranes. This may result in an increase in the positive charge densities on N sites of these membranes. Peak area referring to free N–H sites in the polyamide, corresponding to the Control-NF, decreases by 14.02 % as nano-ZnO of 0.1 % is incorporated in the skin surface of Aq-ZnO:TFN-NF-2. This is ascribed to the extensive association of the nano-ZnO with N–H of polyamides and 1^o as well as 2^o amines of polymer backbone, reducing the number of free amine sites. However, the peak area assigned to such N–H sites corresponding to the Org-ZnO:TFN-NF-2 increases only by 2.56 % as compared to the Control-NF indicating that there are less extensive H bondings and existence of more free N–H sites. These changes in the areas of the major peaks for Aq-ZnO:TFN-NF-2 and Org-ZnO:TFN-NF-2 are compensated in the areas of the shoulder peaks at higher BE. The peak areas of N and O are sensitive to the presence and variation of nano-ZnO in the polyamide skin layer, and hence may not be considered as absolute.

5.3.3. Spectral characterization of TFN-NF membranes by FTIR

ATR FT IR spectrum of Control-NF and those of the TFN-NF membranes, made by introducing nano-ZnO either through aqueous or organic phase, are presented in Fig. 5. 10a and 10b, respectively. They show that introduction of progressively increasing amounts of nano-ZnO through either medium leads to significant physicochemical changes in the skin layer polymers of the resulting nanocomposite membranes.

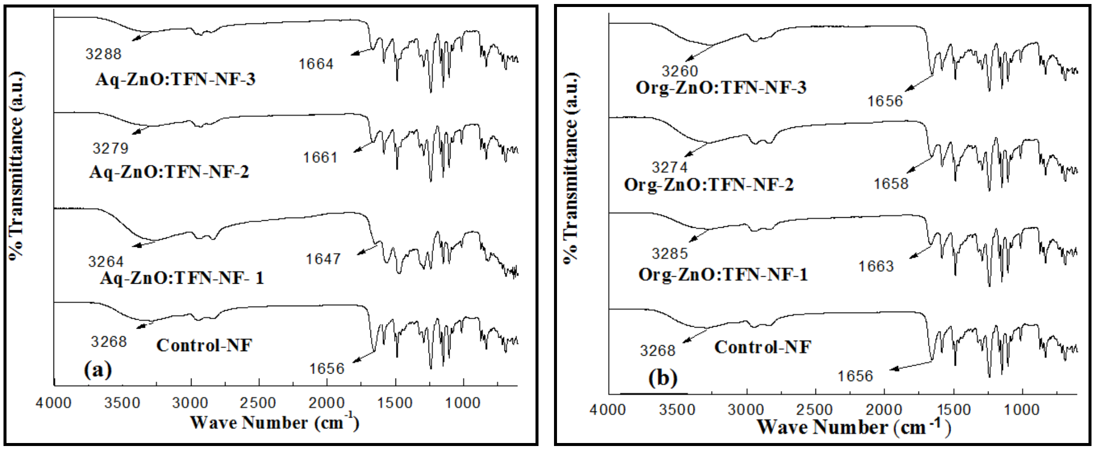

Fig. 5. 10 ATR FT IR spectra of skin layers of TFN-NF membranes: (a) Aq-ZnO:TFN-NF and (b) Org-ZnO:TFN-NF.

The ZnO nanoparticles, produced by synthesis in n-octylamine as in the present case, is known to have a tendency to chemisorb water molecules on its surface making it predominantly hydrophilic [120,121] and assuming a structure where the core material is enveloped in a sheath of hydroxyl groups. When this nano-ZnO, at varying concentration of 0.05, 0.1 and 0.2 (w/v) %, is taken in the aqueous monomeric solution containing PEI, due to the alkaline nature of the solution, it remains in the form of nano-$ZnO(OH)_n$, where ‘n’ represents the number of surface anchored hydroxyl groups depending on pH of the medium [122]. In this phase extensive noncovalent type secondary chemical interactions occur, mostly in the form of H-bondings, between surface hydroxyl groups of nano-ZnO and the amine groups of the branched PEI monomer. These H-bondings preferentially engage the primary amine sites of PEI, because, in addition to being more electropositive than the H of the secondary amines, the former sites are known to be oriented more towards outside in a somewhat spherically coiled structure of the polymer [123]. When PEI, in the form of this molecular association, participates in interfacial polycondensation reaction with TMC, the resulting crosslinked polyamide is assumed to form similar H-bondings involving peripheral –OH of nano-ZnO and N–H as well as >C=O of amide groups of the polyamide. Thus, when nano-ZnO accommodates in the interstices of the nanocomposite polymer it promotes more H-bondings in the polyamide network structure of Aq-ZnO:TFN-NF-1 than that of the Control-NF. The ATR FT IR spectra of the nanocomposite membranes, presented in Fig. 10a, corroborate these facts where deviations are seen in both amide-I region *i.e.*, in carbonyl stretching frequency, $\nu_{C=O}$ and amide-A region *i.e.*, N–H stretching frequency, $\nu_{N–H}$ of the Aq-ZnO:TFN-NF-1 from those of the Control-NF. Thus, with incorporation of 0.05 % nano-ZnO in Aq-ZnO:TFN-NF-1, the $\nu_{C=O}$ value show a red shift from 1656 to 1647 cm^{-1} and $\nu_{N–H}$ from 3268 to 3264 cm^{-1}. However, a reverse trend is noticed, showing a blue shift for $\nu_{C=O}$ from 1647 to 1661 cm^{-1} and then to 1664 cm^{-1} as well as for $\nu_{N–H}$, from 3264 to 3279 cm^{-1} and further to 3288 cm^{-1}, with incremental addition of 0.1 and 0.2 % nano-ZnO in making the respective membranes. This reversal of trend is assumed to happen because, at this higher concentration the nanomaterials find much less space to accommodate in the resulting polymer network, forcing a reorganization of the polymer chains and subsequent disruption of the intermolecular H-bondings. The blue shift in $\nu_{C=O}$ values may further reflect the fact that with enhanced nanoparticle density in the nanocomposite polymer matrix there is a decline of dipole-dipole interaction or n→π* interaction happening though delocalization of a lone pair (n) of the donor carbonyl groups of amide segments or amine groups of the PEI chains into the antibonding (π^*) orbital of the acceptor carbonyl groups (C=O·····C=O or C–N·····C=O) of the adjacent polymer chains. This also supports the above mentioned occurrence of reorganization of the polymer chains, affecting the conformationally sensitive amide-I region of amide segments [124-125].

In contrast to the aqueous phase, introduction of nano-ZnO in the polyamide matrix through the organic phase results in an initial blue shift in the $\nu_{C=O}$ from 1656 to 1663 cm^{-1} and ν_{N-H} from 3268 to 3285 cm^{-1}, for Org-ZnO:TFN-NF-1 as compared to the Control-NF (Fig. 5. 10b). It is well known that there are extensive intermolecular H-bondings between the amide-I and amide-A regions as well as strong dipole-dipole interaction or n→π^* interaction among the adjacent chains of polyamides of Control-NF. More number of conformationally free >C=O groups in Org-ZnO:TFN-NF-1, evident from its higher $\nu_{C=O}$ value, than the Control-NF, implies that there is less extensive H-bondings in the nanocomposite polymer matrix. This is possible if the polymer chains of the former membrane are further away from each other, with less number of >C=O groups present within the range of H-bonding distance with the adjacent H atom of either N–H of the amide group or peripheral –OH of ZnO, to experience extensive noncovalent interactions. The pathway of nonpolar organic medium, employed for introduction of nano-ZnO, may be responsible for this type of network structure of the nanocomposite polyamide, resulting in lesser extent of H-bondings for Org-ZnO:TFN-NF-1. This is in contrast with the counterpart of aqueous phase *i.e.*, Aq-ZnO:TFN-NF-1. However, with increase in nanoparticle density in the organic phase from 0.05 to 0.1 and then to 0.2 (w/v) %, a distinctive red shift occurs from 1663 to 1656 cm^{-1} via 1658 cm^{-1} for $\nu_{C=O}$ and 3285 to 3260 cm^{-1} through 3274 cm^{-1} for ν_{N-H}. The former change can be ascribed to an increase in secondary chemical interactions within the nanocomposite polyamide matrix which is assumed to happen because of distribution of more nano-ZnO in the open interstices of the polyamide network promoting more H-bondings between the surface –OH of the nano-ZnO and the nearby >C=O groups of the polyamide. However, the later change, in ν_{N-H}, may result mostly due to the involvement of more N–H sites in forming association with the liberated HCl during the course of reaction which can further lead to progressive increase in positive charge densities of the membranes. The ATR FT IR results of both classes of membranes show that the medium of incorporating nanomaterial into TFN-NF membranes has significant influence over the nature of interaction within the polymer network and physicochemical features of the inorganic-polymer hybrid material.

5.3.4. Analysis of skin surface morphology of TFN-NF membranes by SEM

The compatibility of nano-ZnO as a constituent of the monomeric aqueous amine phase is evident from a clear homogenous nano-ZnO/PEI/water solution (Fig. 5. 11b). In contrast, the turbid suspensions of nano-ZnO/water solution (Fig. 5. 11a) and of nano-ZnO/TMC/n-hexane solution (Fig. 5. 11c) indicate the physicochemical incompatibility of the nanomaterials in the medium. Electrodynamic interactions between the nano-ZnO and the two respective dispersion media, water and n-hexane, play significant roles in determining the interparticle interactions.

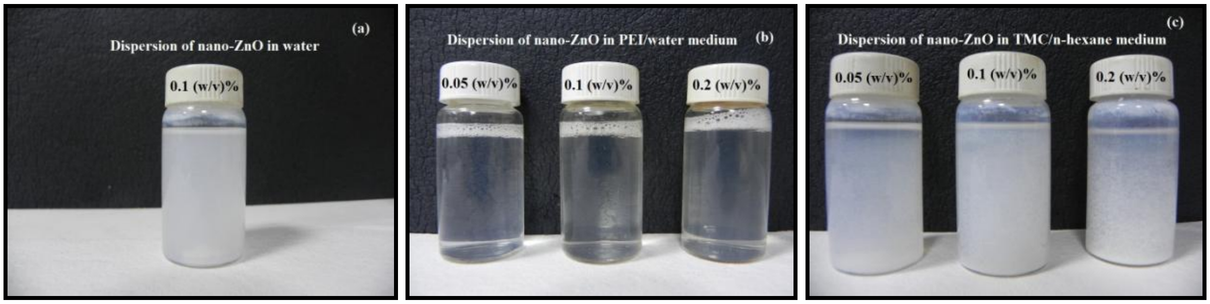

Fig. 5. 11 Photographs of nano-ZnO dispersion (a) in water (without PEI); (b) aqueous phase monomeric-PEI solutions and (c) organic phase monomeric-TMC solutions containing different concentrations of nano-ZnO.

Thus, van der Waals pair interaction energy which is proportionally dependent on a material dependent property, Hamaker Constant that varies with the contrast between the dielectric constants of nanoparticles and the dispersion medium, and inversely dependent on the separation distance between the particles that differs with the concentration and surrounding chemical environment of the particle, becomes a measure of stability for such dispersions. Higher value of Hamaker constant for nano-ZnO in water (26×10^{-21} J) as compared to that in n-hexane (19×10^{-21} J) reflects the higher degree of incompatibility of nano-ZnO in water than in n-hexane since a higher value of the parameter implies greater interparticle attractive force and, hence, more prone is the system to come closer and induce flocculation [126]. However, in the PEI environment of the aqueous monomeric solution the flocculation of nano-ZnO gets restricted due to a reduction in the attractive van der Waals inter-particle potential through accumulation of PEI chains on their surfaces. The steric repulsion between the chains of branched PEI molecules on the exterior of sheathed nano-ZnO also helps in stabilization of the solution, emphasizing the role of the former in enhancing the physicochemical compatibility of the later in the solution [127].

Scanning electron micrographs of skin layer as well as cross-sections of the Aq-ZnO:TFN-NF class of membranes are presented in Figs. 5. 12a, 12b and 12c. Skin layer images show that the particles of nano-ZnO are well accommodated and evenly distributed inside the nanocomposite polyamide matrix of the membrane, formed through interfacial polycondensation process.

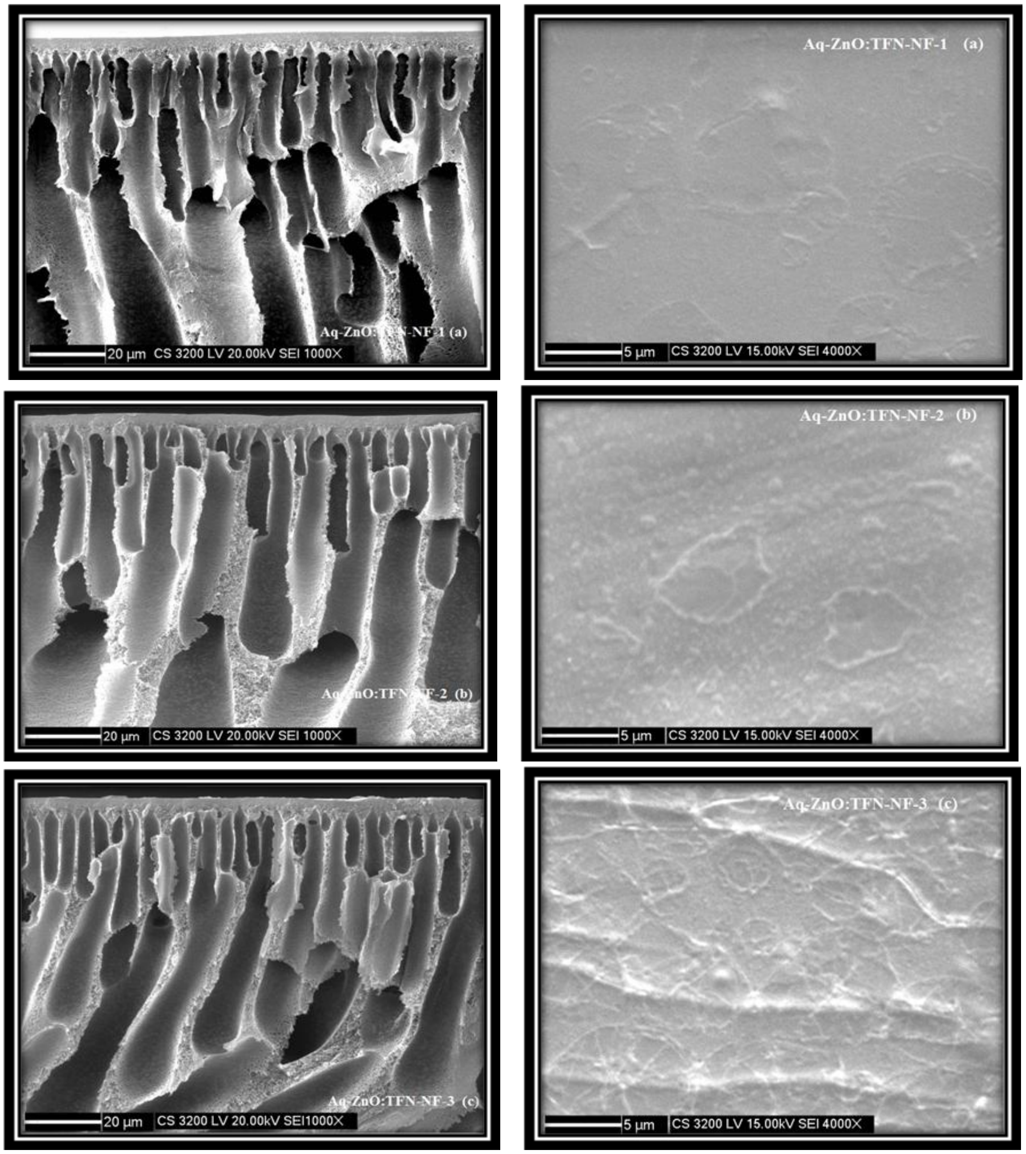

Fig. 5. 12 Cross-sectional and skin surface SEM images of Aq-ZnO:TFN-NF class of membranes made by introducing the nano-ZnO at different concentrations: (a) 0.05 %, (b) 0.1 % and (c) 0.2 % , through aqueous phase containing PEI.

With increase in concentration of the nano-ZnO from 0.05 to 0.2 %, their density on the skin layer of the membranes is seen to increase, which is supposed to perturb the polymeric chains through stretching and induce deformation in the network structure. As the nano-ZnO domains grow with increase of concentration, they are seen to arrange themselves forming some long range ordering and patterns indicating that there is a cohesive interaction between the nanomaterials themselves as well as between the nanomaterials and the polymer chains. This pattern formation presumably occurs through multiple-point secondary chemical interactions between the nano-ZnO and the polyamide network which leads to a significant loss of translational entropy for the particles as well as conformational entropy for the polymeric chains. At higher nano-ZnO density of 0.2 %, therefore, there is formation of more number of smaller coils of the nanomaterials in the polymer matrix to compensate the entropy loss [128].

In contrast to the aqueous amine medium, the nano-ZnO is chemically incompatible in solution of n-hexane containing TMC and results in the formation of an unstable dispersion (Fig. 5. 11c). The skin surface as well as cross-sectional SEM images of the Org-ZnO:TFN-NF class of membranes, prepared by introduction of nano-ZnO via organic phase, presented in Figs. 13a, 13b and 13c. Skin layer images show that the nanomaterials are not evenly distributed in the polymer matrix but rather present in the form of discrete clusters whose number and size increase with increasing concentration of the nanomaterials in the organic phase. This indicates that the nanomaterials are unable to cohesively accommodate themselves within the polymer matrix when they are introduced through the organic phase. The orders and patterns found in the membranes of the Aq-ZnO:TFN-NF series are significantly missing. Since, formation of the thin skin layer of the TFN-NF membrane, takes place through crossing over of the PEI monomers from the aqueous phase to the organic side, across the polymer barrier (Fig. 5. 2b), in a diffusion controlled manner by *in situ* interfacial polycondensation route [129], the nanomaterials do not get enough chance of encountering a compatible polar environment to get evenly distributed, before being embedded in the polyamide matrix. This results in an uneven distribution of the nano-ZnO in the form of uneven clusters in the resultant polyamide network.

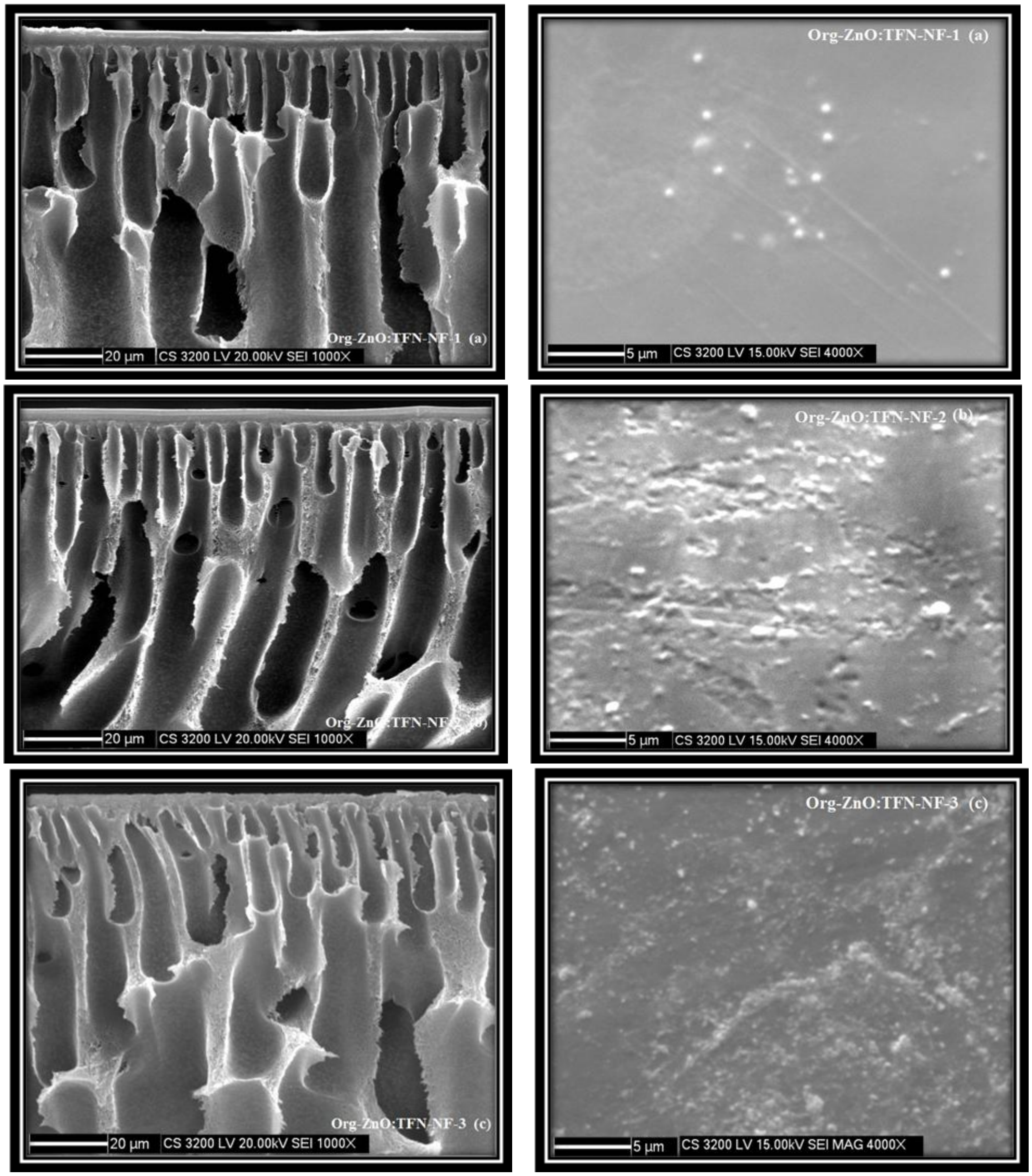

Fig. 5. 13 Cross-sectional and skin surface SEM images of the Org-ZnO:TFN-NF class of membranes made by introducing the nano-ZnO at different concentrations: (a) 0.05 %, (b) 0.1 % and (c) 0.2 % , through organic phase containing TMC.

These observations through SEM studies emphasize the fact that the dynamics of skin layer formation through interfacial polycondensation process, distribution of the nanomaterials within the skin layer and the resultant skin layer morphology of the nano-ZnO impregnated TFN-NF membranes are influenced by the type of precursor media employed for dispersion of the nano-ZnO to a great extent.

5.3.5. Evaluation of skin surface topographies of the TFN-NF membranes by AFM

The 3D AFM images as well as the respective height histograms of TFN-NF membranes, prepared by introducing nano-ZnO through aqueous phase are presented in Fig. 5. 14. They show that the surface topographies of the membranes change significantly, from a relatively smooth profile for the membrane Aq-ZnO:TFN-NF-1 to progressively rougher surfaces for membranes made with impregnation of more and more nanomaterials. Further, formations of patterns on the surfaces of membranes, a feature observed in the respective SEM images as well, justify the occurrence of long range association of the nanomaterials in the polymer matrix. The 3D AFM images of Aq-ZnO:TFN-NF class of membranes, read along with the corresponding height histograms, show that the peaks are more or less uniform in height, having a very narrow distribution between 18 to 28 nm for Aq-ZnO:TFN-NF-1, however, in case of Aq-ZnO:TFN-NF-2, the surface is seen to be populated with a larger number of peaks, whose heights are significantly more than those of Aq-ZnO:TFN-NF-1, most of them occurring between 20 to 130 nm, contributing to a much broader distribution pattern. The higher area of the height histogram of Aq-ZnO:TFN-NF-2 also indicates a higher peakedness of this membrane compared to Aq-ZnO:TFN-NF-1 and consequently, an increased membrane surface area of the former membrane than the latter. With a still higher concentration of the nanomaterial, in Aq-ZnO:TFN-NF-3, the peak heights of the membrane are far from uniform, their distribution is much wider and range between 10 to 270 nm. A significant tail in the height histogram suggests the presence of a few isolated high peaks with heights between 150 to 270 nm. As compared to Aq-ZnO:TFN-NF-2, where a number of narrow peaks are distributed over the entire surface of the membrane, the presence of higher concentration of nano-ZnO makes some of the isolated high peaks in Aq-ZnO:TFN-NF-3 quite broad.

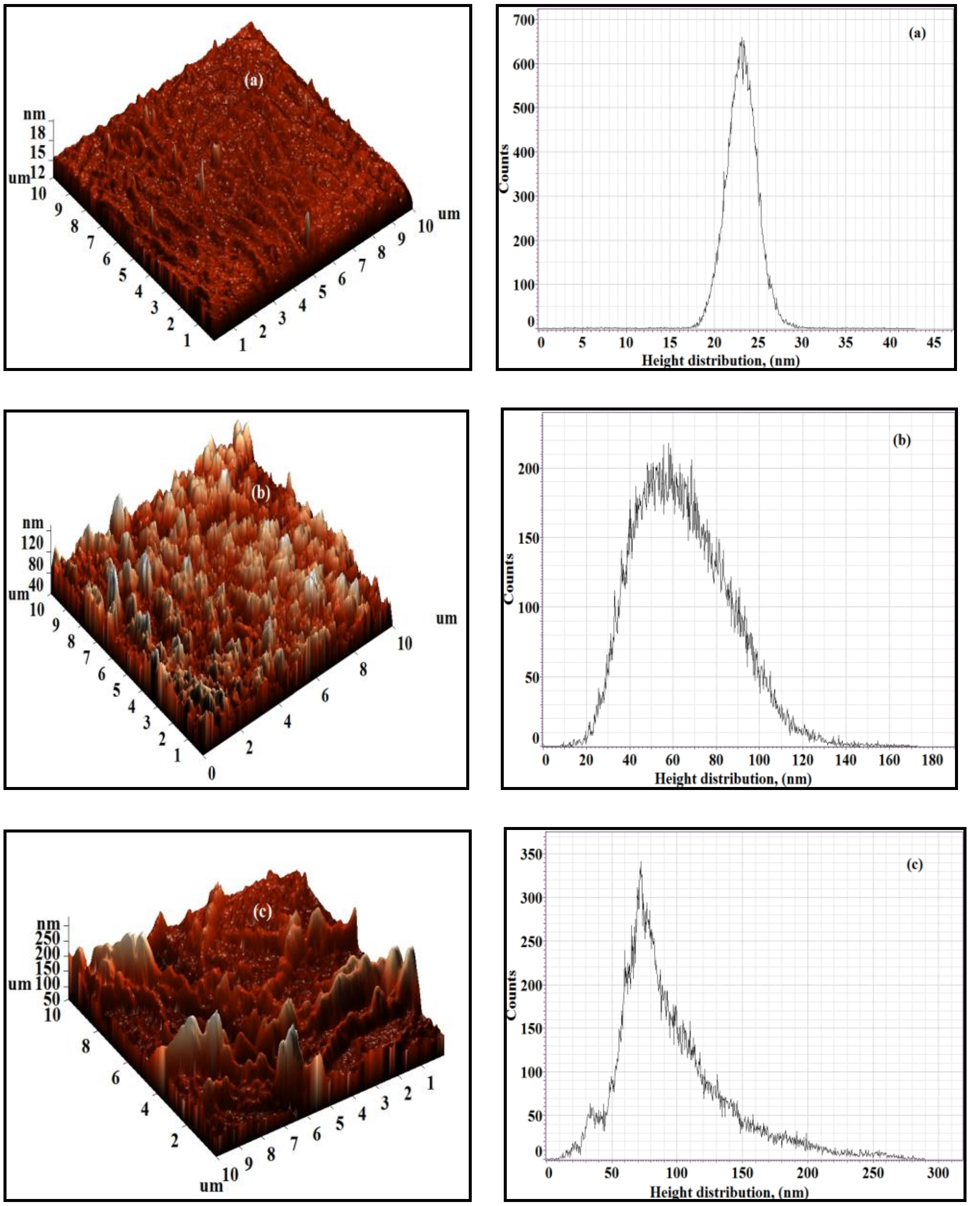

Fig. 5. 14 3D AFM images and height histograms of Aq-ZnO:TFN-NF class of membranes: (a) Aq-ZnO:TFN-NF-1, (b) Aq-ZnO:TFN-NF-2 and (c) Aq-ZnO:TFN-NF-3.

The computed amplitude parameters of the nanocomposite membranes, presented in Table 5. 2, shows that the average roughness (R_a) of the membranes increase from 1.48 to 17.59 nm and further to 31.69 nm as concentration of nanomaterials in the aqueous monomer solution are increased. The corresponding root mean square roughness (R_q) of the membrane increases from 2.09 to 21.96 nm and finally to 41.96 nm. This is in accordance with the topographical features discussed in response to their 3D images. R_{10z}, which is the difference in heights between the average of the five highest peaks and the five lowest valleys relative to the mean plane, denotes the contrast between the heights and depths of extreme peaks and valleys that may be occasionally present on the surface of the membrane. The lowest R_{10z} value of 9.96 nm for Aq-ZnO:TFN-NF-1 results from a surface having peaks and valleys of less contrast in heights and depths. However, impregnation of still higher amount of nanomaterials lead to higher values of R_{10z} for Aq-ZnO:TFN-NF-2 (39.89 nm) and Aq-ZnO:TFN-NF-3 (101.57 nm) which indicate the occurrence of more contrast in heights and depths due to the onset of formation of isolated high peaks and low valleys on the membrane surface.

Table 5. 2

Computed amplitude parameters for Aq-ZnO:TFN-NF and Org-ZnO:TFN-NF class of membranes by AFM.

Membrane Code	Amplitude Parameters		
	R_a (nm)	R_q (nm)	R_{10z} (nm)
Aq-ZnO:TFN-NF-1	1.48	2.09	9.96
Aq-ZnO:TFN-NF-2	17.59	21.96	39.89
Aq-ZnO:TFN-NF-3	31.69	41.96	101.57
Org-ZnO:TFN-NF-1	4.07	5.27	2.58
Org-ZnO:TFN-NF-2	5.58	7.16	9.78
Org-ZnO:TFN-NF-3	49.09	72.23	178.21

The 3D AFM images and height histograms of the Org-ZnO:TFN-NF class of membranes, prepared by introduction of nano-ZnO through organic phase, presented in Fig. 5. 15, show different type of surface topographies than the membranes prepared by introduction of the nanomaterials through the aqueous phase.

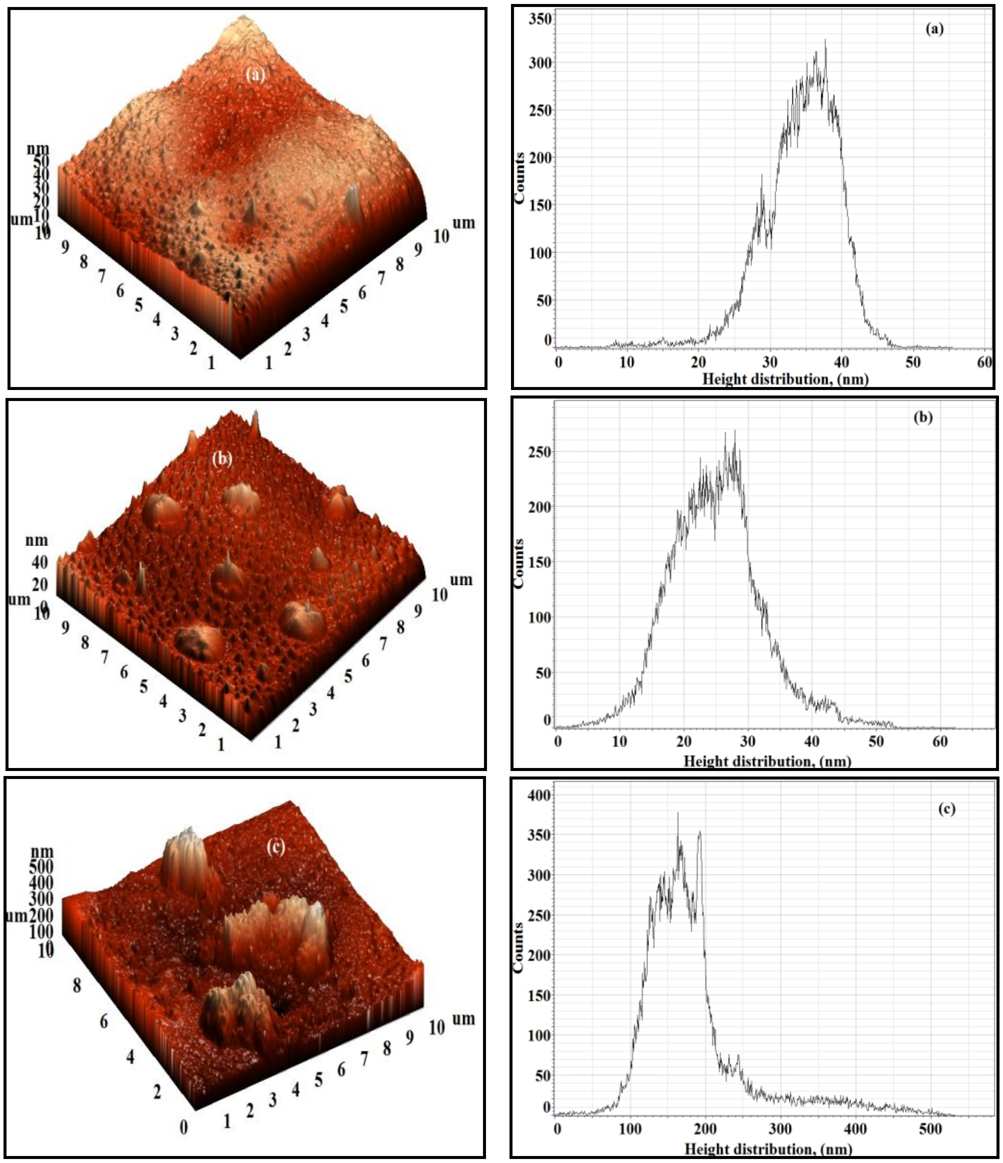

Fig. 5. 15 3D AFM images and height histograms of Org-ZnO:TFN-NF class of membranes: (a) Org-ZnO:TFN-NF-1, (b) Org-ZnO:TFN-NF-2 and (c) Org-ZnO:TFN-NF-3.

The occurrence of long range patterns due to distribution of nano-ZnO in the polymer nanocomposite, a characteristic of the latter class of membranes, are significantly absent. The nanomaterials, though found present throughout the skin surface of the membranes in the form of discrete clusters, are not evenly distributed. The 3D images and the respective height histograms for Org-ZnO:TFN-NF-1 and Org-ZnO:TFN-NF-2 show that the number of peaks are fewer and their heights are much smaller than the respective membranes of aqueous phase. For the Org-ZnO:TFN-NF-1, the peak heights on the membrane surface are between 20 to 45 nm and, for Org-ZnO:TFN-NF-2, they are between 10 to 45 nm. However, for Org-ZnO:TFN-NF-3, the peak heights range between 100 to 500 nm which is due to the presence of occasional high peaks on the surface of the membrane caused by entrapment of larger sized clusters of nano-ZnO in the polyamide network.

The R_a values of the membranes, listed in Table 5. 2, show that they are 4.07 and 5.58 nm when 0.05 and 0.1% of the nano-ZnO were used. This nominal increase in the roughness values is due to the absence of any significant number of peaks on the membrane surface, unlike their counterparts of the aqueous phase membranes. However, the R_a value increases to 49.09 nm in the membrane, Org-ZnO:TFN-NF-3 which is believed to be due to the uneven distribution of the entrapped clusters of nanomaterials in the polymer matrix of the membrane. The variation in surface topography, due to the effect of impregnation of nano-ZnO at progressively higher concentrations is also manifested through the change of R_q and R_{10z} values.

The AFM studies bring out the fact that surface roughness features such as formation, distribution as well as variation of peaks and valleys are highly influenced by the nature of the medium through which nanomaterials are impregnated into the skin layer of TFN-NF membranes.

5.3.6. Elemental analysis and mapping of TFN-NF membranes by EDX

The skin layer elemental mappings of both Aq-ZnO:TFN-NF and Org-ZnO:TFN-NF class of membranes presented in Figs. 5. 16 and 17, respectively, show a differential distribution of the elements (N, Zn and O) within the bulk of skin layer, with increasing amount of nanomaterial impregnation.

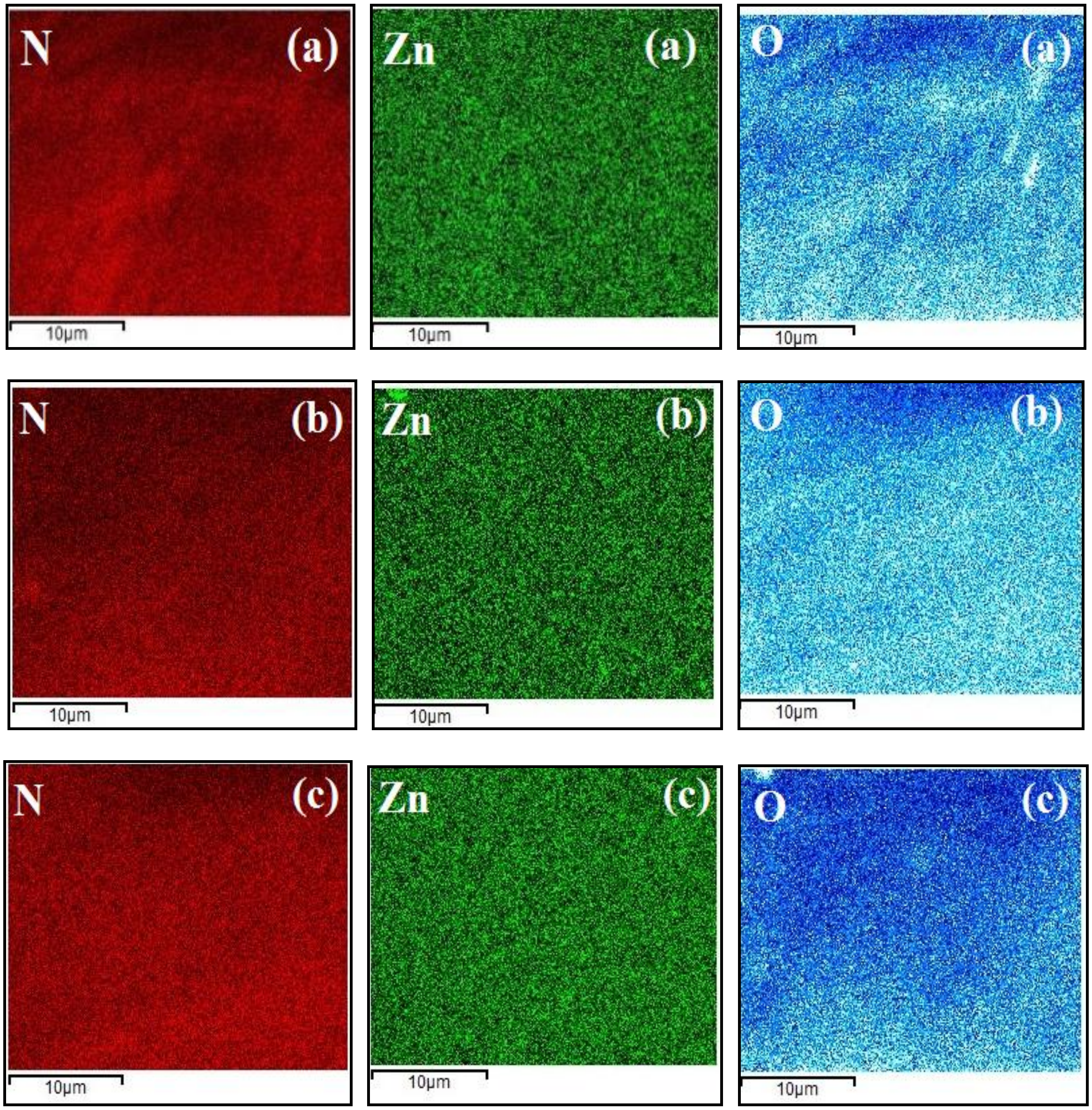

Fig. 5. 16 Elemental mapping of the nanocomposite polyamide skin layers of the Aq-ZnO:TFN-NF class of membranes: (a) Aq-ZnO:TFN-NF-1, (b) Aq-ZnO:TFN-NF-2 and (c) Aq-ZnO:TFN-NF-3.

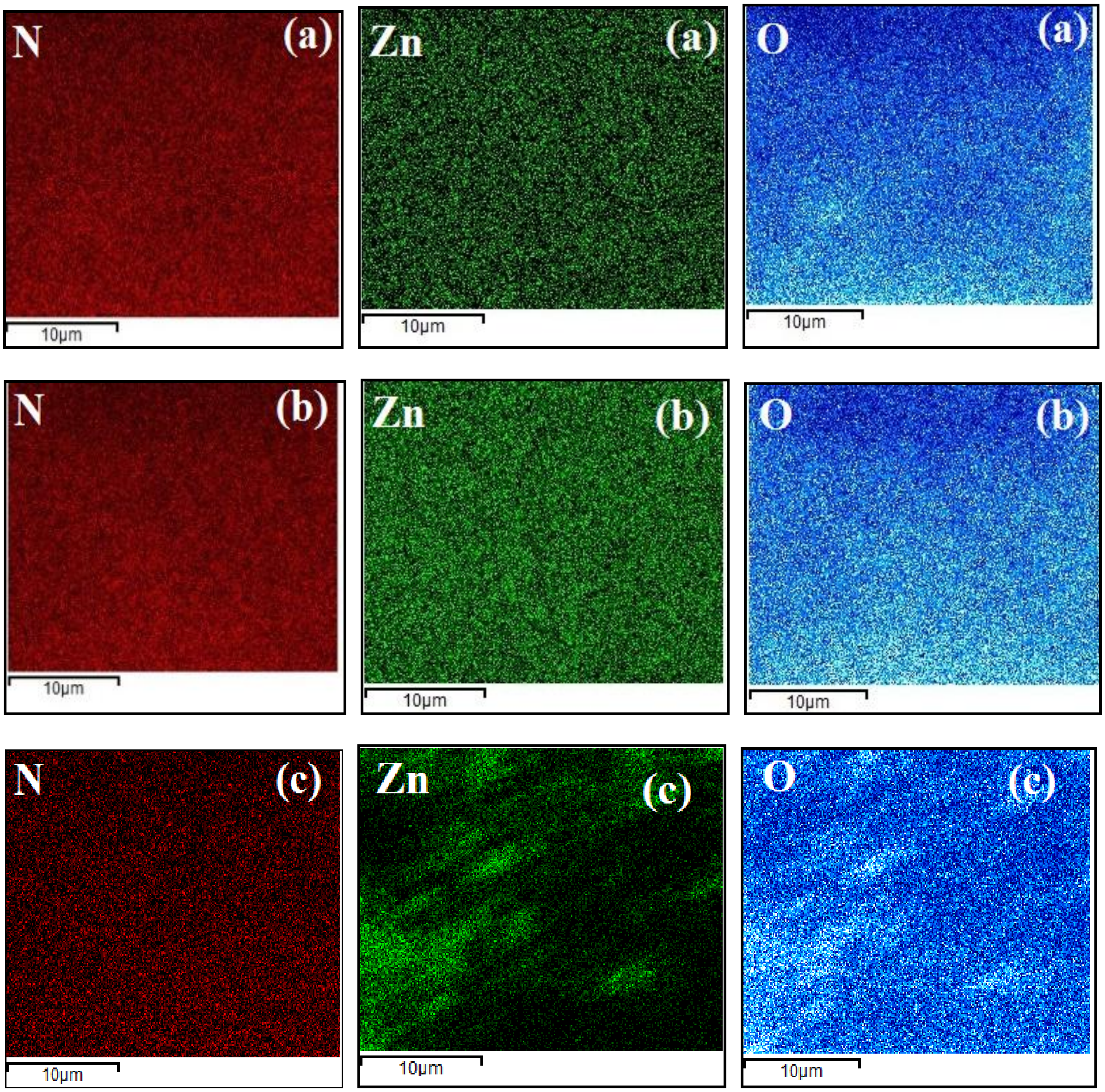

Fig. 5. 17 Elemental mapping of the nanocomposite polyamide skin layers of the Org-ZnO:TFN-NF class of membranes: (a) Org-ZnO:TFN-NF-1, (b) Org-ZnO:TFN-NF-2 and (c) Org-ZnO:TFN-NF-3.

Elemental analysis of the Aq-ZnO:TFN-NF class of membranes by EDX, presented in Table 5. 3 reveals that when the nano-ZnO concentration is increased from 0.05 to 0.1 % and then to 0.2 %, the relative nanoparticle density in the skin layer polyamide matrix increases from 2.48 ± 0.12 weight % (*i.e.*, 0.64 atomic %) to 7.33 ± 0.13 weight % (*i.e.*, 1.83 atomic %) and finally to 10.02

± 0.29 weight % (*i.e.*, 3.65 atomic %). The corresponding values of relative atomic ratios of the unique elements Zn and N (*i.e.*, Zn:N) in the skin layers of these membranes show an increasing trend from 1:44.02 to 1:7.24 through 1:15.04.

Table 5. 3

Skin layer elemental analysis of the Aq-ZnO:TFN-NF & Org-ZnO:TFN-NF class of membranes by EDX.

Membrane Code	Elemental (N) quantification		Elemental (O) quantification		Elemental (Zn) quantification		Relative atomic ratio (Zn/N)
	Wt (%)	Atomic (%)	Wt (%)	Atomic (%)	Wt (%)	Atomic (%)	
Aq-ZnO:TFN-NF-1	25.01 ± 0.16	28.17	72.51 ± 0.14	71.19	2.48 ± 0.12	0.64	1:44.02
Aq-ZnO:TFN-NF-2	23.57 ± 0.17	27.52	69.10 ± 0.19	70.65	7.33 ± 0.13	1.83	1:15.04
Aq-ZnO:TFN-NF-3	22.73 ± 0.42	26.42	67.25 ± 0.25	69.93	10.02 ± 0.29	3.65	1:7.24
Org-ZnO:TFN-NF-1	24.87 ± 0.68	28.05	72.08 ± 0.80	71.13	3.05 ± 0.59	0.82	1:34.21
Org-ZnO:TFN-NF-2	22.98 ± 0.28	27.24	67.86 ± 0.32	70.43	9.16 ± 0.20	2.33	1:11.69
Org-ZnO:TFN-NF-3	20.52 ± 0.51	26.07	62.91 ± 0.33	69.53	16.57 ± 0.29	4.40	1:5.93

However, increase in the respective values of the Org-ZnO:TFN-NF class of membranes are much higher. The nano-ZnO density increases from 3.05 ± 0.59 weight % (*i.e.*, 0.82 atomic %) to 9.16 ± 0.20 weight % (*i.e.*, 2.33 atomic %) and then to as high as 16.57 ± 0.29 weight % (*i.e.*, 4.40 atomic %) with introduction of 0.05, 0.1 and 0.2% of nano-ZnO, respectively. Similarly, the relative atomic ratios of the unique elements Zn and N of these membranes increase from 1:34.21 to 1:11.69 and finally to 1:5.93 indicating incorporation of progressively more amount of nano-ZnO in the nanocomposite polyamide skin layer.

Impregnations of higher amount of nano-ZnO in skin layer of the latter class of the membranes have also been observed during their respective SEM and AFM analyses. This happens so because, during the progress of heterogeneous type interfacial polycondensation reaction and successive formation of nascent polymer layer, the migrating reactant PEI meets the reactant of the organic phase *i.e.*, TMC (with or without nano-ZnO, as the case may be), in the organic phase

(Fig. 5. 2) close to the boundary between the mutually immiscible solvents. In this situation, when the nanomaterials are present in the organic phase, there is a possibility of more nano-ZnO being present in the reaction zone during the process of polycondensation reaction. The unstable dispersion of the nanomaterial in the organic medium may further be responsible for some deposition and subsequent entrapment of the nano-ZnO in the skin layer of the membrane. But, when the nano-ZnO becomes a constituent of the aqueous amine phase, the monomer along with nano-ZnO has to cross the barrier of the nascent polyamide film and approach the reactants of the organic phase to undergo further polymerization. The transport of nano-ZnO in the reaction zone may not be facilitated since, the rate of diffusion across the nascent polymeric barrier, for the bulky sized nano-ZnO associated constituent PEI of the aqueous amine phase, becomes comparatively slow. This may be responsible for presence of less amount of nano-ZnO in the skin layer polyamide of Aq-ZnO:TFN class of membranes.

5.3.7. Determination of hydrophilic features of TFN-NF membranes

Contact angle analyses, performed by using the three different probe solvents *i.e.*, water, ethylene glycol and diiodomethane, on skin surfaces of the Aq-ZnO:TFN-NF membranes show that there is a declining trend of hydrophilicity as the contact angle values (Fig. 5. 18a) with respect to the polar solvent, water (θ_w) increase from 77.9(±0.5)^o to 79.6(±0.3)^o and further to 81.2(±0.6)^o, whereas with respect to the non-polar solvent, diiodomethane (θ_{DIM}) decrease from 52.8(±0.5)^o to 44.3(±0.9)^o through 49.7(±0.6)^o, as the concentration of nano-ZnO increases progressively for Aq-ZnO:TFN-NF-1 to Aq-ZnO:TFN-NF-3, through Aq-ZnO:TFN-NF-2. However, the variations observed for contact angles of the probe solvents on skin surfaces of the Org-ZnO:TFN-NF membranes (Fig. 5. 18b) show a contrast to the trends in hydrophilicity as observed for Aq-ZnO:TFN-NF membranes. The θ_w decreases from 76.4(±0.8)^o to 73.7(±1.1)^o and further to 65.1(±1.7)^o, whereas the θ_{DIM} increases from 41.1(±0.9)^o to 46.8(±0.5)^o, through 44.5(±0.3)^o as the concentration of nano-ZnO increases progressively for Org-ZnO:TFN-NF-1 to Org-ZnO:TFN-NF-3, through Org-ZnO:TFN-NF-2. The trends imply that the extents of presence of the nano-ZnO as well as the hydrophilic amine and amide sites in the skin layer-air or skin layer-solvent interface get also affected by the variant impregnation route of the nanoparticles.

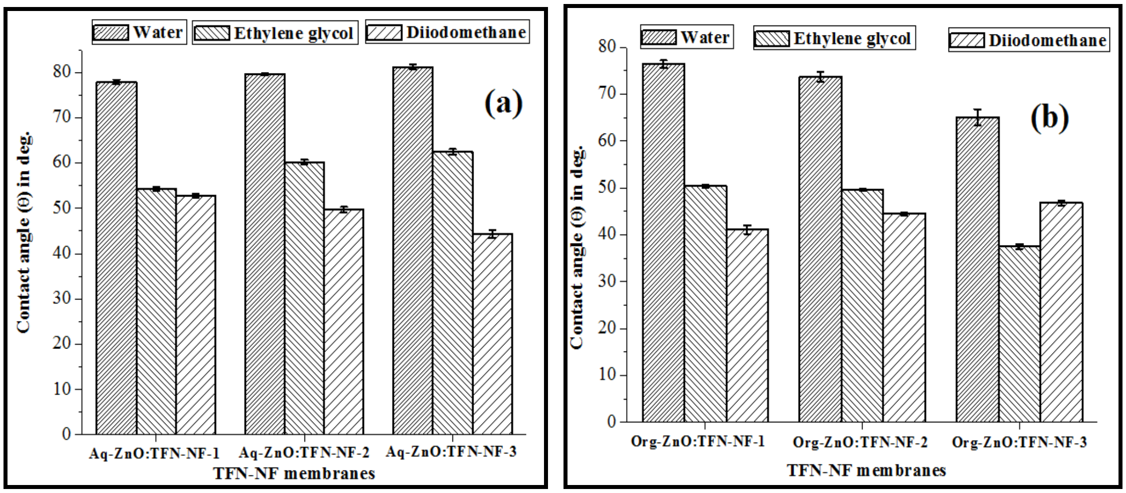

Fig. 5. 18 Variation in contact angles of the membranes a) Aq-ZnO:TFN-NF and b) Org-ZnO:TFN-NF, with respect to water, ethylene glycol and diiodomethane.

The observed trend in the former stands justifiable as the secondary chemical interactions between the nano-ZnO and the polyamide network lead to a significant loss of translational entropy for the particles as well as conformational entropy for the polymeric chain segments, further affecting the structural orientations as well as organizations of the resultant nanocomposite polyamide network as the skin layer polymers of Aq-ZnO:TFN-NF. Conversely, the enhanced presence of nano-ZnO in the skin layers' nanocomposite polyamide matrices, through entrapment or distribution of clusters of the nano-ZnO turns the surfaces of Org-ZnO:TFN-NF more hydrophilic. Thus, the observed hydrophilic features of the membranes, Aq-

ZnO:TFN-NF and Org-ZnO:TFN-NF relevantly attribute to the consequent effects of the route specific introduction of nano-ZnO into the skin layer polymer matrix through either aqueous or organic phase route, during *in situ* interfacial polymerization of reactive monomers.

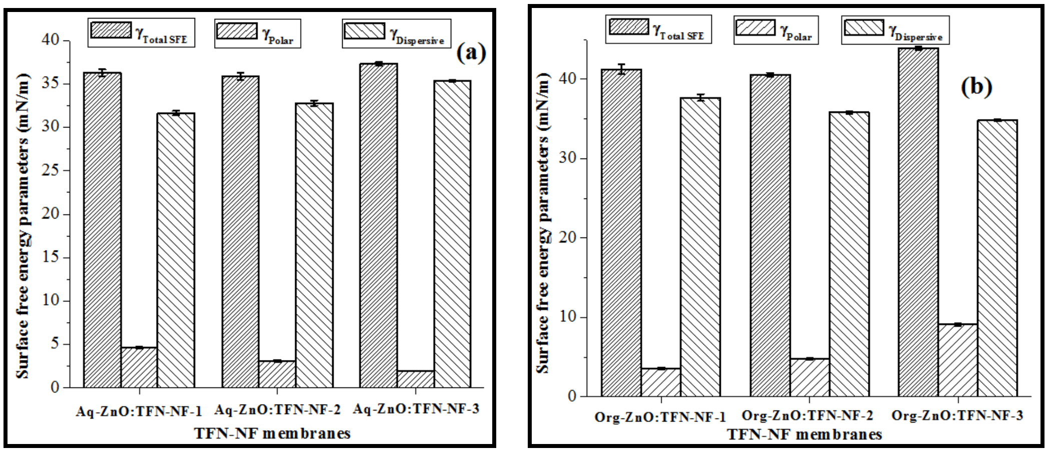

Fig. 5. 19 Variation in surface free energy parameters of the membranes a) Aq-ZnO:TFN-NF and b) Org-ZnO:TFN-NF.

Quantification of surface free energies of the membranes, Aq-ZnO:TFN-NF and Org-ZnO:TFN-NF (Figs. 5. 19a and 19b, respectively), carried out using Fowkes theory reveals further intrinsic details of the investigated membranes' surfaces through resolution of the total surface free energy ($\gamma_{\text{Total SFE}}$) into the dispersive and polar components. With increase in concentration of nano-ZnO, the polar parts (γ_{Polar}) of the nanocomposite polyamide layers of the Aq-ZnO:TFN-NF class of membranes decrease from 4.65(±0.11) to 1.95(±0.04) through 3.12(±0.13) mN/m, whereas that for the Org-ZnO:TFN-NF class of membranes increase from increase from 3.57(±0.14) to 9.11(±0.15) via 4.78(±0.07) mN/m. The dispersive parts ($\gamma_{\text{Dispersive}}$) subsequently increase from 31.63(±0.25) to 35.35(±0.14) through 32.76(±0.31) mN/m for the former and decrease from 37.67(±0.43) to 34.79(±0.11) through 35.80(±0.16) mN/m for the later class of membranes. The skin surfaces of the Aq-ZnO:TFN-NF class of membranes thus have lower surface energy as compared to the skin surfaces of the Org-ZnO:TFN-NF class of membranes.

The polar and dispersive components of SFE of the membranes' surfaces further configure closed contours or more specifically the wetting envelopes (Figs. 5. 20a and 20b), by plotting the polar fraction against the dispersive fraction of SFE. The formations of such wetting envelopes provide more precise and wide idea about the ability as well as extent of interaction of a solvent with the membranes' skin surfaces as derived from the nanocomposite polyamides. The skin surfaces of Aq-ZnO:TFN-NF class of membranes, having greater number of dispersive segments of the polymeric chains, exposed more towards the membrane/solvent interface behave to be more prone in interaction with relevant solvents having higher γ_s^d . However, exposure of more number of polar sites of the nanocomposite polymeric matrices towards the membrane/solvent interface leads to a wetting envelope which is widened towards solvents having higher γ_s^p , for the Org-ZnO:TFN-NF class of membranes.

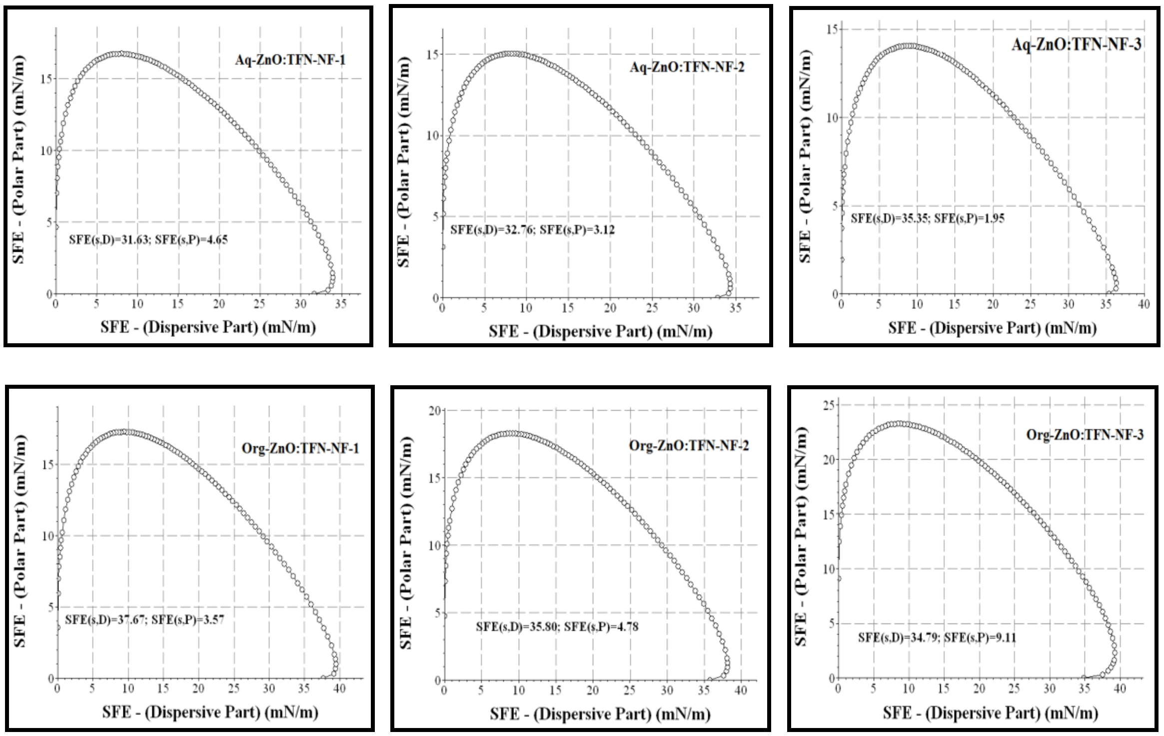

Fig. 5. 20 Wetting envelopes for skin surfaces of the membranes, a) Aq-ZnO:TFN-NF and b) Org-ZnO:TFN-NF.

5.3.8. Evaluation of electrokinetic behaviors of TFN-NF membranes

Electrokinetic behaviors of skin surfaces of the Aq-ZnO:TFN-NF and Org-ZnO:TFN-NF class of membranes, determined by tangential streaming potential measurements with respect to 10^{-3}M KCl solution, are represented in Table 5. 4. This reveals that the surfaces of both the classes of membranes acquire cationic charges but at varying extents, depending on the route of introduction of nano-ZnO into the skin layers' polymer matrices.

Table 5. 4

Variation of electrokinetic surface charge density in Aq-ZnO:TFN-NF and Org-ZnO:TFN-NF, with change of concentration of nano-ZnO.

Membrane Code	ζ (mV)	σ_S (C/m^2)
Aq-ZnO:TFN-NF-1	15.36	1.12×10^{-3}
Aq-ZnO:TFN-NF-2	14.29	1.03×10^{-3}
Aq-ZnO:TFN-NF-3	13.30	0.97×10^{-3}
Org-ZnO:TFN-NF-1	8.52	0.62×10^{-3}
Org-ZnO:TFN-NF-2	8.96	0.65×10^{-3}
Org-ZnO:TFN-NF-3	9.51	0.69×10^{-3}

In case of the membranes of Aq-ZnO:TFN-NF class, it is noticed that the extent of positive charge decreases with enhancement in the concentration of nano-ZnO as the absolute values of ζ decrease from 15.36 to 13.30 mV, through 14.29 mV. Evaluation of σ_S for the Aq-ZnO:TFN-NF class of membranes (Table 5. 4) exhibits the subsequent variations in charge-atmospheres of skin surfaces of the membranes. This observation signifies the fact that increase in concentration of nano-ZnO reduces the density of overall positively charged sites in the skin layer polyamides of the Aq-ZnO:TFN-NF class of membranes. However, the absolute values of ζ increases from 8.52 to 8.96 mV and then further to 9.51 mV for Org-ZnO:TFN-NF-1, Org-ZnO:TFN-NF-2 and

Org-ZnO:TFN-NF-3, respectively. Such enhancement in the absolute values of ζ and corresponding changes in the σ_S imply enrichment of the skin layers' conductivity of the membranes on progressive incorporation of nano-ZnO.

It is also observed that the Aq-ZnO:TFN-NF class of membranes reside with higher positive surface charges than the Org-ZnO:TFN-NF class of membranes. Such behavior shows a contrast to the inferences drawn based on the earlier XPS as well as FTIR investigations, which reflected that the Org-ZnO:TFN-NF class of membranes comprises higher density of protonated amine sites as compared to the Aq-ZnO:TFN-NF class of membranes, resulting an increase in the positive charge densities of the former membranes. However, the apparent drop in the value of ζ or respective σ_S than the predicted extent of charges for the Org-ZnO:TFN-NF class of membranes signifies that the high surface electrical conductivity of the nano-ZnO, because of their excess of electrical charges at the solid/liquid interface and very high surface to volume ratio influences the zeta potential of the membranes [130]. Thus, these facts corroborate to the predominant influence of the variant presence of nano-ZnO in the nanocomposite polyamide matrices of the membranes of both classes due to the approach of impregnating nano-ZnO through two different routes *i.e.*, either aqueous or organic phase route, during *in situ* interfacial polymerization of the reactive monomers.

5.3.9. Evaluation of transport characteristics of TFN-NF membranes

The solute rejection behaviors of the Aq-ZnO:TFN-NF class of membranes as well as that of the Control-NF, presented in Fig. 5. 21a, show that the TFN-NF membranes give much higher rejections for $MgCl_2$ than for NaCl and Na_2SO_4, which follows a general trend $MgCl_2 > NaCl \geq$

Na_2SO_4. This implies that the membranes are inherently positively charged which is characteristic of membranes derived using PEI. It is observed that with increase in concentration of nano-ZnO in the skin layers of the membranes there is a decline in the differential rejection between these three solutes, more specifically between $MgCl_2$ and Na_2SO_4. Their solute rejection ratios of 92.3:51.3, 87.6:50.2 and 84.2:48.4 indicate the possibility of decrease in the surface positive charge of the membranes with enhanced incorporation of nano-ZnO in the nanocomposite matrix. However, this may not be the sole factor for this trend since morphological factors, especially the possibility of formation of a more open polymer matrix further influences the porous nature of the nanocomposite membranes, consequently contributing to an overall decline of SR values for all the solutes. In these positively charged membranes, the maximum solute rejection for $MgCl_2$ is predominantly governed by Donnan exclusion, where, due to presence of the multivalent cation (Mg^{2+}) with higher positive charge density, the solute experiences maximum electrostatic repulsion by the charged membranes [23, 49]. A lower solute rejection of NaCl is due to a poorer Donnan exclusion of the monovalent Na^+ ions by the membrane. However, the presence of bivalent anion in Na_2SO_4 facilitates its transport through the membrane further lowering the respective solute rejection.

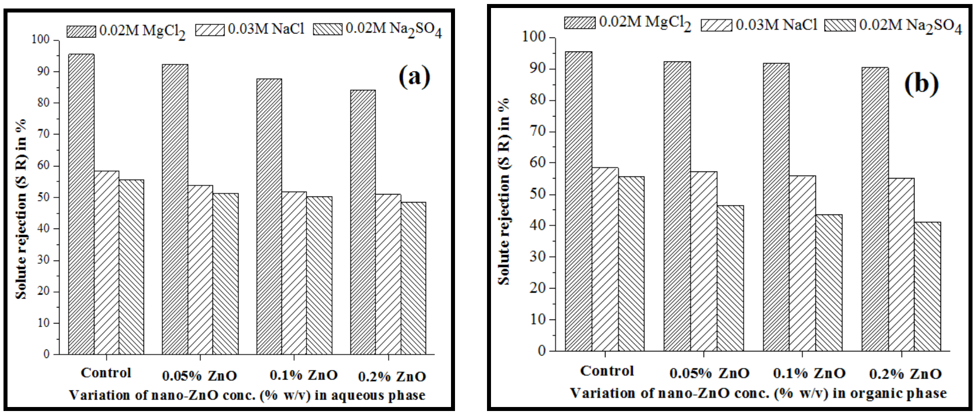

Fig. 5. 21 Effect of variation of nano-ZnO concentration on solute rejection behaviors of (a) Aq-ZnO:TFN-NF and (b) Org-ZnO:TFN-NF class of membranes.

A similar order of solute rejection pattern, $MgCl_2 > NaCl \geq Na_2SO_4$, for Org-ZnO:TFN-NF class of membranes, however comes with a superior differential rejection ability between $MgCl_2$ and Na_2SO_4, as compared to the Aq-ZnO:TFN-NF class of membranes (Fig. 5. 21b). This signifies a higher positive charge of the Org-ZnO:TFN-NF class of membranes, the origin of which has been discussed during characterization of the skin layers of the membranes by FTIR as well as XPS. Consequently, the solute rejection ratios for $MgCl_2$ and Na_2SO_4 of the Org-ZnO:TFN-NF-1, Org-ZnO:TFN-NF-2 and Org-ZnO:TFN-NF-3 show an increasing trend i.e. 92.3:46.4, 91.6:43.6 and 90.3:41.2, respectively. However, decline in the solute rejections of Org-ZnO:TFN-NF class of membranes, with increase in concentration of nano-ZnO beyond 0.05 %, is not as pronounced as the Aq-ZnO:TFN-NF class of membranes.

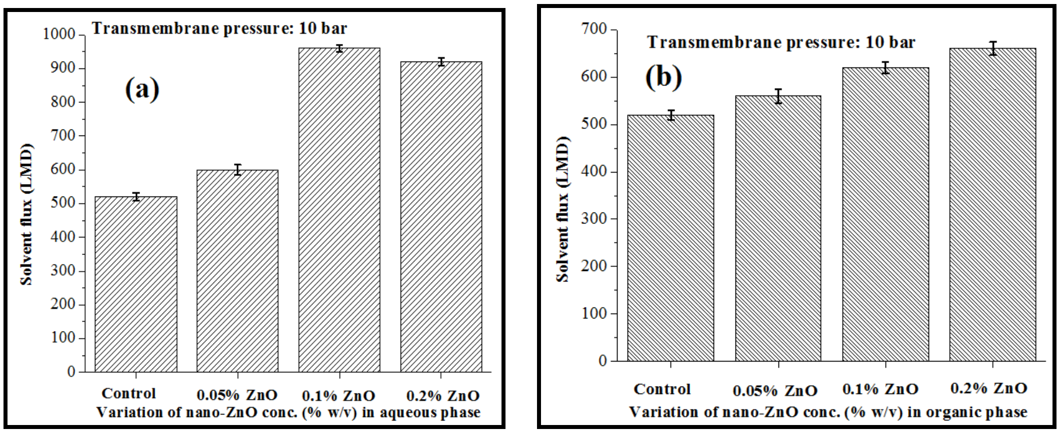

Fig. 5. 22 Effect of variation of nano-ZnO concentration on permeate flux behaviors of (a) Aq-ZnO:TFN-NF and (b) Org-ZnO:TFN-NF class of membranes.

Both the classes of TFN-NF membranes show significant increase in their solvent fluxes, with progressive impregnation of nano-ZnO in making the membranes. Solvent fluxes for the representative solute $MgCl_2$ increase from 520(±12) LMD for Control-NF to 600(±15) LMD for Aq-ZnO:TFN-NF-1, 960(±10) LMD for Aq-ZnO:TFN-NF-2 and 920(±11) LMD for Aq-ZnO:TFN-NF-3 (Fig. 5. 22a). Similarly, the solvent fluxes increase from 520(±12) LMD for

Control-NF to 560(±15) LMD for Org-ZnO:TFN-NF-1, 620(±12) LMD for Org-ZnO:TFN-NF-2 and finally to 660(±14) LMD for Org-ZnO:TFN-NF-3 (Fig. 5. 22b). The increase of solvent fluxes in TFN class of membranes has been widely reported in litereature, where the improvement is attributed to the presence of nanomaterials in the interfacial reaction zone, influencing the kinetics of interfacial polycondensation reaction by factors like change in miscibility of the aqueous and organic phases through release of heat of hydration of nanomaterials, change in diffusion rate of monomers which consequently alter the cross-linking density of the polymer network and hydrophilic/hydrophobic nature of the membrane surfaces [131-133].

For Org-ZnO:TFN-NF class of membranes, the free PEI molecules (since it is devoid of the nano-ZnO) experience a better mobility and diffusivity to migrate from aqueous to the organic phase, across the nascent polymer layer, ensuring an enhanced rate of polymerization in the reaction zone. Also, the heat of hydration of nano-ZnO, which are present in considerable density in the organic phase, could induce an increase of local temperature in the reaction zone as the nanoparticles encounter the hydrated PEI molecules. This thermal impact can additionally contribute to improve the miscibility of the two heterogeneous phases locally and subsequently facilitate the reaction by enhancing the rate of diffusion of the PEI monomers into the organic phase [134]. But, such thermal effect may have some influence in the exothermic type polycondensation reaction to reduce the reactivity. Thus, it can be assumed that impregnation of more nano-ZnO tune the reaction in such a manner that it becomes kinetically more favourable, though thermodynamically adverse. However, the overall effect results in formation of a skin layer with a cross-linked polymer network with an enhanced solvent flux. Simultaneously, as evident from the morphological and topographical analyses, the nanomaterials are less uniformly distributed in the skin layer matrix of the membrane, forming rather discrete clusters, due to an unstable dispersion of nanomaterials in the organic monomeric phase (Fig. 5. 11c). These factors lead to a nanocomposite polymer layer where the clusters of nano-ZnO might block some entrances of the channels for solvent flow in the membranes, resulting in a lesser extent of increase of the solvent fluxes of the Org-ZnO:TFN-NF class of membranes as compared to the Aq-ZnO:TFN-NF class of membranes [135,136].

In the case of Aq-ZnO:TFN-NF class of membranes, bulky nature of the nano-ZnO associated PEI molecules in the aqueous phase leads to restricted mobility and slow rate of diffusion of the monomer from aqueous to the organic phase across the nascent interfacial polymer layer resulting in a reduced reactivity which may result in kinetic inhibition in the growth of the polymer film. Further, an open structure in the polymer network as described in SEM analysis and a probable increase in membranes' pore sizes - reflected in the reduced solute rejection - make the flow of solvent easier [137,138]. The significant peakedness of the membrane, observed in their AFM images, due to nanomaterial incorporation, is supposed to increase the effective surface area of the membranes. These factors collectively account for the increase of solvent fluxes of these membranes prepared by introducing nano-ZnO through aqueous phase. However, a reduced solute rejection with no accompanying increase in solvent flux for the Aq-ZnO:TFN-NF-3 indicates that the increased concentration of the nano-ZnO at this level may be acting as pore blocker residing within the channels of solvent flow, hindering the flow of the solvent through this membrane, and, at the same time, introducing some defects in the skin layer of the membrane lowering its solute rejection ability.

5. 4. Conclusions

Inorganic-polymer hybrid thin film nanocomposite nanofiltration membranes have been prepared and extensively studied. Effects of variation of route specific introduction of nano-ZnO into the skin layer polymer matrix through either aqueous or organic phase route, during *in situ* interfacial polymerization of reactive monomers have been discussed in details. Structural characterizations by XPS and ATR FTIR have probed the interactions of the nano-ZnO and its coexistence in the hybrid nanocomposite material. Morphological and topographical characterizations by SEM and AFM revealed that adoption of these routes yielded membranes with distinctly different surface features. The uniformity in distribution of the nano-ZnO was less in the skin surface of Org-ZnO:TFN-NF membranes than when they were introduced through the aqueous phase. The distinctly positively charged membranes gave differential solute rejections for solutes having varying combinations of cations and anions in the order of $MgCl_2 > NaCl \geq Na_2SO_4$. Introduction of nano-ZnO improved the solvent fluxes of the membranes significantly, particularly in the Aq-ZnO:TFN-NF set of membranes. The study has attempted to establish correlations between the factors leading to dynamic membrane formation and the resulting physicochemical features as well as transport properties.

CHAPTER – 6

Conclusions, Implications
and
Future perspectives

In the present thesis entitled “***Development and Characterization of Charged Membranes for Separation Studies***”, the developments as well as comprehensive physicochemical characterizations of the charged membranes, more particularly both negatively as well as positively charged NF membranes have been accomplished. The thesis delivers the quintessence of generation of novel charged NF membranes, which may achieve a distinct place in the separation industries because of their noticeable physicochemical features and novel separation characteristics. The results of the studies carried out in forming the thesis are summarized in this chapter as:

6. 1. An investigative correlation was carried out between the structural aspects of two different classes of co-polyamides with non-crosslinked and crosslinked molecular architectures, functioning as selective barriers of the negatively charged TFC NF membranes and the changes in membranes’ skin layer morphologies as well as surface topographies with variation in curing conditions during optimization of the membrane preparative conditions. The presence of $–SO_3^-H^+$ groups as the negative charge bearing functionalities, for the skin layers of the TFC NF membranes were substantiated by the ATR FTIR spectroscopic studies of the membranes. Solid state ^{13}C NMR revealed the structural variations as well as local molecular motions of the co-polyamides in terms of distribution of the rotational isomers of the polymer chain. The topographical features of both non-crosslinked and crosslinked co-polyamide based TFC NF membranes, as analyzed through AFM technique exhibited that the surface roughnesses of the membranes were greatly influenced by the change of curing temperature, where elevated temperature for the curing resulted in the rearrangement and redistribution of polymer chains of the thin skin layers due to their increased mobilities, affecting their surface roughnesses. The morphological insights of the skin surfaces, for both the membranes revealed that the merger of

smaller polymer aggregates leading to formation of bigger agglomerates resulting in densification when they were subjected to undergo prolonged curing conditions. Cross sectional SEM images of both types of membranes further revealed that the compactions of skin layers were more prone at higher duration of curing. These observations have suggested that curing is an important process, which, if not properly controlled, could lead to an excessive densification of the skin layer and decrease the solvent fluxes of the membranes. The membranes' performances were also varied with change in polymerization time as well as curing conditions such as curing temperature and its' duration. The membranes provided solute rejection in the order of $Na_2SO_4 > MgSO_4 > CaCl_2 > NaCl$, which seemed to be typical of negatively charged TFC NF membranes. This study furnishes the idea about the sensitivity of the membranes' performances towards the variation of preparation parameters like polymerization time and curing conditions, which can be used to prepare membranes of desired performances.

6. 2. In another study, the development of a novel class of negatively charged polyamide and co-polyamide based TFC NF membranes, by employing two different kinds of diaryl diamine monomers containing multiple sulfonic acid groups (DASDSA and BDSA), either lonely or along with a cyclo-aliphatic diamine monomer (PIP) have been reported. All the membranes provided better selectivity and improved productivity. Extensive physicochemical characterizations of the studied membranes have been done through the techniques of ATR FTIR, AFM, SEM, zeta potentiometer and contact angle measurements. The membranes exhibited very high solute rejection for bivalent anion containing solutes like Na_2SO_4 and $MgSO_4$, and low solute rejection for solutes with monovalent ions like NaCl. The differential rejection patterns of the membranes were attributed to the presence of high negative charges on

the membranes' skin surfaces due to the presence of sulfonic acid groups to a higher extent. The high solute rejection of the bivalent anions and low solute rejection of the monovalent anions make this membrane a potential candidate for use in brackish water conditions to produce potable water. This can be achieved by removing hardness causing components to a large extent and a partial removal of other monovalent ions like NaCl from brackish water/ground water making it suitable for drinking and other applications.

6. 3. We have reported the details of our attempt in developing and characterizing another potential TFC class of NF membranes, but having tethered positive surface charges, made by employing GTACl functionalized branched amine-rich polycationic polymer, BPEI of varying molecular weights and TMC as the crosslinking acid chloride monomer. Structural investigations by ^{1}H–NMR and FTIR established that facile quaternization of BPEIs of varying M.W. by GTACl involved formation of termolecular-oxirane/amine/hydroxyl complex following *in situ* autocatalytic approach during the consecutive non-catalytic and catalytic steps, where inclusion of the hydroxypropyl trimethylammonium groups as quaternized functional-moieties happened in the amine sites of the BPEIs' backbone. The formations of crosslinked-quaternized poly(ethyleneimine amide)s as the synthesized thin skin layers of the TFC-PCNF membranes, following *in situ* interfacial polymerization process were substantiated by FTIR and XPS studies. An extensive investigation of the variations in hydrophilic features of TFC-PCNF membranes implied that the structural orientation as well as organization of the resultant rigid crosslinked poly(ethyleneimine amide) got affected by the enhancement of M.W. of BPEI, since increase in branching density of polymeric backbone of the quaternized BPEI induced constrained mobility in the chain segments and thus, consequently restricted the migration of polar terminal

functional-moieties from the interior to the periphery of the skin layer polymer. The study also signified the effect of inclusion of the quaternized functional-moieties on packing patterns of the polymer chains in structures of crosslinked poly(ethyleneimine amide)s, where the extent of differential hindrance in segmental orientations were dependent on the resultant variation in spacing of the moieties.

Electrokinetic features of the TFC-PCNF membranes, analyzed with variation of pH have revealed that absolute ζ values were enhanced with lowering of pH followed by decline at even higher acidic environment. This signified that the effective streaming current was reasonably reduced by the diffusive back flow of the streaming current due to dragging of the tangentially driven counter-ions from the hydrodynamic slipping plane to the bulk of the membranes stationary positively charged layer. However, progressively enhanced pH condition resulted in non-specific adsorption of the excess counter-ions as well as concentration build up of the counter-ions with subsequent compression in the electrical double layer thickness, leading to screening of the surface positive charges with resultant severe reduction in the positive absolute ζ values of the membranes.

Cross-flow permeation study, performed for all the positively charged TFC-PCNF membranes depicted that the membranes bearing high extent of positive surface charges followed a rejection trend of $MgCl_2 > MgSO_4 > Na_2SO_4 > NaCl$, under iso-osmotic environment of solutes. The higher rejection trend towards $MgCl_2$ and $MgSO_4$ profoundly indicated the effect of Donnan exclusion, governed by the stationary layer of positively charged sites of the membranes. However, the higher rejection efficiency for Na_2SO_4 over NaCl signified the additional and overcompensating contribution of size exclusion phenomena, exhibiting the role of skin layer pore structure formed by the crosslinked architecture of the poly(ethyleneimine amide) in restricting the transport of larger sized hydrated anionic constituents as compared to the smaller sized ones. Based on the trends in obtained solute rejections and solvent fluxes of the investigated membranes, it was proposed through extensive illustrations that factors like incorporation of charges in polymeric structure, extent of charged sites and their impact on the conformations (pore structure) as well as compactness (crosslinking density) of the skin layer polymer collectively played the dominant role in tuning the physicochemical features as well as macroscopic behaviors of the membranes.

6. 4. A study towards development and characterization of a novel class of inorganic-polymer hybrid thin film nanocomposite nanofiltration membranes has been extensively carried out. The effects of variation of route specific introduction of nano-ZnO into the skin layer polymer matrix through either aqueous or organic phase route, during *in situ* interfacial polymerization of reactive monomers have been discussed in details. Structural characterizations by XPS and ATR FTIR have probed the interactions of the nano-ZnO and its coexistence in the hybrid nanocomposite material. Morphological and topographical characterizations by SEM and AFM revealed that adoption of these routes yielded membranes with distinctly different surface features. The uniformity in distribution of the nano-ZnO was less in the skin surface of Org-ZnO:TFN-NF membranes than when they were introduced through the aqueous phase. The distinctly positively charged membranes gave differential solute rejections for solutes having varying combinations of cations and anions in the order of $MgCl_2 > NaCl \geq Na_2SO_4$. Introduction of nano-ZnO improved the solvent fluxes of the membranes significantly, particularly in the Aq-ZnO:TFN-NF set of membranes. The study has attempted to establish correlations between the

factors leading to dynamic membrane formation and the resulting physicochemical features as well as transport properties.

The current research work, carried out in developing the charged NF membranes exhibits the promising ways of inclusion of charges in the very thin active separating layers of TFC membranes, capable of achieving high solute rejection with concurrent differential rejection behavior and high flux, preferable for high pressure nanofiltration application. The challenges attempted in preparation of such membranes illustrate that the successful introduction of charge in the membranes during the *in situ* polymerization process of manufacture thereby can eliminate the post fabrication modification steps and acquire the easy tunability of membrane properties. For this, factors influencing the membrane formations and performances have also been assessed in depth. In the described typical TFC membrane processes, factors like chemical compositions, reaction conditions of *in situ* polymerization, curing conditions have been investigated as important parameters since each of which tune the physicochemical features of the membranes significantly, leading to development of membranes with optimum performances.

The present research work is believed to be a small step towards understanding of the physicochemical features of charged NF membranes and their unique interaction behaviors with the varying mono- and bi-valent cations and anions, as constituents of the iso-osmotic feed solutions. Thus, the efforts have the potential in achieving the importance as a frontier direction of research towards the charged NF membranes. This may draw the attention of the separation scientists or precisely the membranologists worldwide. The endeavor of fulfilling the necessity in development of high-performance novel charged membrane materials, as a crucial step towards a sustainable industrial growth and subsequent beneficial for a large domain of the society has been tried to achieve through this research work, where during the entire period of research a strong motivation has been propagated towards development of indigenous charged NF membranes.

REFERENCES

[1] A. Bhattacharya, P. Ghosh, Nanofiltration and reverse osmosis membranes: theory and application in separation of electrolytes, *Rev. Chem. Eng.*, **2004**, *20*, 111.

[2] R. J. Peterson, Composite reverse osmosis and nanofiltration membranes, *J. Membr. Sci.*, **1993**, *83*, 81–150.

[3] W. J. Lau, A. F. Ismail, N. Misdan, M. A. Kassim, A recent progress in thin film composite membrane: A review, *Desalination*, **2012**, *287*, 190–199.

[4] Wang *et al.*, Internal hydrophilic membranes from blended anionic copolymers, US Patent no. 6,258,272.

[5] Method for preparing negatively charged nanofiltration membrane through grafting induced after plasma radiation, Chinese Patent no.102068912.

[6] Moya *et al.*, Porous composite membrane and process, US Patent no. 5,629,084.

[7] Sclenoff *et al.*, Polyelectrolyte complex films for analytical and membrane separation of chiral compounds, US Patent no. 7,101,947.

[8] Childs *et al*., Composite materials comprising supported porous gels containing metal-affinity ligands, US Patent no. 7,604,749.

[9] X. Tongwen, Y. Weihua, A novel positively charged composite membranes for nanofiltration prepared from poly(2,6-dimethyl-1,4-phenylene oxide) by *in situ* amines crosslinking, *J. Membr. Sci.*, **2003**, *215*, 25–32.

[10] R. Du, J. Zhao, Properties of poly (*N*,*N*-dimethylaminoethyl methacrylate)/polysulfone positively charged composite nanofiltration membrane, *J. Membr. Sci.*, **2004**, *239*, 183–188.

[11] Q. Zhang, H. Wang, S. Zhang, L. Dai, Positively charged nanofiltration membrane based on cardo poly(arylene ethersulfone) with pendant tertiary amine groups, *J. Membr. Sci.*, **2011**, *375*, 191–197.

[12] Y. Su, X. Jian, S. Zhang, G. Wang, Preparation and characterization of quaternized poly(phthalazinone ether sulfone ketone) NF membranes, *J. Membr. Sci.*, **2004**, *241*, 225–233.

[13] B. Tang, T. Xu, M. Gong, W. Yang, A novel positively charged asymmetry membranes from poly(2,6-dimethyl-1,4-phenylene oxide) by benzyl bromination and *in situ* amination: membrane preparation and characterization, *J. Membr. Sci.*, **2005**, *248*, 119–125.

[14] B. Tang, T. Xu, W. Yang, A novel positively charged asymmetry membranes from poly(2,6-dimethyl-1,4-phenylene oxide) by benzyl bromination and *in situ* amination Part II: Effect of charged group species on membrane performance and morphologies, *J. Membr. Sci.*, **2006**, *268***,** 123–131.

[15] B. Tang, T. Xu, P. Sun, W. Yang, A novel of positively charged asymmetry membrane prepared from poly(2,6-dimethyl-1,4-phenylene oxide) by *in situ* amination Part III. Effect of benzyl and aryl bromination degrees of polymer on membrane performance and morphologies, *J. Membr. Sci.*, **2006**, *279***,** 192–199.

[16] S. Zhang, T. Xu, C. Wu, Synthesis and characterizations of novel, positively charged hybrid membranes from poly(2,6-dimethyl-1,4-phenylene oxide), *J. Membr. Sci.*, **2006**, *269*, 142–151.

[17] H. Deng, Y. Xu, Q. Chen, X. Wei, B. Zhu, High flux positively charged nanofiltration membranes prepared by UV-initiated graft polymerization of methacrylatoethyl trimethyl ammonium chloride (DMC) onto polysulfone membranes, *J. Membr. Sci.*, **2011**, *366*, 363–372.

[18] X. Li, L. Zhu, Y. Xu, Z. Yi, B. Zhu, A novel positively charged nanofiltration membrane prepared from N,N-dimethylaminoethyl methacrylate by quaternization crosslinking, *J. Membr. Sci.*, **2011**, *374*, 33–42.

[19] Y. Ji, Q. An, Q. Zhao, H. Chen, C. Gao, Preparation of novel positively charged copolymer membranes for nanofiltration, *J. Membr. Sci.*, **2011**, *376*, 254–265.

[20] C. Gao, D. Yan, Hyperbranched polymers: from synthesis to applications, *Prog. Polym. Sci.*, **2004**, *29*, 183–275.

[21] Y.-C. Chiang, Y.-Z. Hsub, R.-C. Ruaan, C.-J. Chuang, K.-L. Tung, Nanofiltration membranes synthesized from hyperbranched polyethyleneimine, *J. Membr. Sci.*, **2009**, *326*, 19–26.

[22] X.-Z. Wei, L.-P. Zhu, H.-Y. Deng, Y.-Y. Xu, B.-K. Zhu, Z.-M. Huang, New type of nanofiltration membrane based on crosslinked hyperbranched polymers, *J. Membr. Sci.*, **2008**, *323*, 278–287.

[23] T. K. Dey, R. C. Bindal, S. Prabhakar, P. K.Tewari, Development, characterization and performance evaluation of positively charged thin film composite nanofiltration membrane containing fixed quaternary ammonium moieties, *Sep. Sci. Technol.*, **2011**, *46*, 933–943.

[24] D. Wang *et al*., Separation performance of a nanofiltration membrane influenced by species and concentration of ions, *Desalination*, **2005**, *175*, 219-225.

[25] A. E. Childress, M. Elimelech, Effect of solution chemistry on the surface charge of polymeric reverse osmosis and nanofiltration membranes, *J. Memb. Sci.*, **1996**, *119*, 253-268.

[26] J. M. M Peeters, M. H. V. Mulder, H. Strathmann, Streaming potential measurements as a characterization method for nanofiltration membranes, *Colloids and surfaces A: Physicochemical and engineering aspects*, **1999**, *150*, 247–259.

[27] E. S. Gadelmawla, M. M. Koura, T. M. A. Maksoud, I. M. Elewa, H. H. Soliman, Roughness parameters, *J. Mater. Process. Technol.*, **2002**, *123*, 133–145.

[28] J. Schaep, C. Vandecasteele, Evaluating the charge of nanofiltration membranes, *J. Membr. Sci.*, **2001**, *188*, 129–136.

[29] N. Selvakumar, H. C. Barshilia, K. S. Rajam, Effect of substrate roughness on the apparent surface free energy of sputter deposited superhydrophobic polytetrafluoroethylene coatings: A comparison of experimental data with different theoretical models, *J. Appl. Phys.*, **2010**, *108*, 013505-1–013505-9.

[30] L.-Y. Yu, Z.-L. Xua, H.-M. Shen, H. Yang, Preparation and characterization of PVDF–SiO_2 composite hollow fiber UF membrane by sol–gel method, *J. Membr. Sci.*, **2009**, *337*, 257–265.

[31] P. S. Singh, S.V. Joshi, J. J. Trivedi, C. V. Devmurari, A. Prakash Rao, P. K. Ghosh, Probing the structural variations of thin film composite RO membranes obtained by coating polyamide over polysulfone membranes of different pore dimensions, *J.Memb.Sci.*, **2006**, *278*, 19-25.

[32] Z. Yong, Y. Sanchuan, L. Meihong, G. Congjie, Polyamide thin film composite membrane prepared from m-phenylenediamine and m-phenylenediamine-5-sulfonic acid, *J. Memb. Sci.*, **2006**, *270*, 162–168.

[33] Y. Mansourpanah, S. S. Madaeni, A. Rahimpour, Preparation and investigation of separation

properties of polyethersulfone supported poly(piperazinamide) nanofiltration membrane using microwave - assisted polymerization, *Sep. & Purif. Tech.*, **2009**, *69*, 234–242.

[34] Y. Jin, Z. Su, Effect of polymerization conditions on hydrophilic groups in aromatic polyamide thin films, *J. Memb. Sci.*, **2009**, *330*, 175–179.

[35] P. Garidel and H. Schott, Fourier-Transform midinfrared spectroscopy for analysis and screening of liquid protein formulations, *BioProcess International*, **2006**, 48–55.

[36] P. Papanek, J. E. Fischer, N. S. Murthy, Low-frequency amide modes in different hydrogen-bonded forms of Nylon-6 studied by inelastic neutron scattering and density-functional calculations, *Macromolecules,* **2002**, *35*, 4175–4182.

[37] K. J. Kamer, A. Choudhary, R. T. Raines, Intimate interactions with carbonyl groups: dipole−dipole or n→π*?, *J. Org. Chem.*, **2013**, *78*, 2099−2103.

[38] R. Barbucci, P. Ferruti, C. Improta, M. Delfini, A.L. Segre, F. Conti, Protonation studies of multifunctional polymers with a poly(amido-amine) structure, *Polymer*, **1978**, *19*, 1329–1334.

[39] H. R. Kricheldorf, K.H. Rieth, ^{13}C-NMR Sequence Analysis 8. Investigation on Piperazine containing copolyamides, *J. Polym. Sci.: Polymer Letters Edition*, **1978**, *16*, 379.

[40] Y. Miron, B. R. McGarvey, H. Morawetz, Rates of Conformational transitions in Solutions of Randomly Coiled Polymers. I. Nuclear Magnetic Resonance Study of Transitions in the Backbone of Polyamides, *Macromolecules*, **1969**, *2*, 154–161.

[41] S-Y. Kwak, S.G. Jung, Y. S. Yoon, D.W. Ihm, Details of surface features in aromatic polyamide reverse osmosis membranes characterized by scanning electron and atomic force microscopy, *J. Pol. Science: Part B: Polymer Physics*, **1999**, *37*, 1429–1440.

[42] A. K. Ghosh, B-H. Jeong, X. Huang, E.M.V. Hoek, Impacts of reaction and curing conditions on polyamide composite reverse osmosis membrane properties, *J. Memb. Sci.*, **2008**, *311*, 34–35.

[43] D. Wang et al., Separation performance of a nanofiltration membrane influenced by species and concentration of ions, *Desalination*, **2005**, *175*, 219–225.

[44] L. Meihong, Y. Sanchuan, Z. Yong, G. Congjie, Study on thin-film composite nanofiltration membrane for the removal of sulfate from concentrated salt aqueous: Preparation and performance, *J. Memb. Sci.*, **2008**, *310*, 289–295.

[45] A. E. Childress, M. Elimelech, Effect of solution chemistry on the surface charge of polymeric reverse osmosis and nanofiltration membranes, *J. Memb. Sci.*, 1996, *119*, 253–268.

[46] V. Freger, Kinetics of film formation by interfacial polycondensation, *Langmuir*, **2005**, *21*, 1884–1894.

[47] N. K. Saha, S. V. Joshi, Performance evaluation of thin film composite polyamide nanofiltration membrane with variation of monomer type, *J. Memb. Sci.*, **2009**, *342*, 60–69.

[48] I. J. Roh, A. R. Greenberg, V. P. Khare, Synthesis and characterization of interfacially polymerized polyamide thin films, *Desalination*, **2006**, *191*, 279–290.

[49] C. K. Kim, J. H. Kim, I. J. Roh, J. J. Kim, The changes of membrane performance with polyamide molecular structure in the reverse osmosis process, *J. Memb. Sci.*, **2000**, *165*, 189-199.

[50] S. P. Sun, T. A. Hatton,T.-S. Chung, Hyperbranched polyethyleneimine induced cross-linking of polyamide-imide nanofiltration hollow fiber membranes for effective removal of Ciprofloxacin, *Environ. Sci. Technol.*, **2011**, *45*, 4003–4009.

[51] S.-J. Park, R. K. Cheedrala, M. S. Diallo, C. Kim, I. S. Kim, W. A. Goddard III, Nanofiltration membranes based on polyvinylidene fluoride nanofibrous scaffolds and crosslinked polyethyleneimine networks, *J. Nanopart. Res.*, **2012**, *14*, 884–898.

[52] D. R. Holycross, M. Chai, Comprehensive NMR studies of the structures and properties of PEI polymers, *Macromolecules*, **2013**, *46*, 6891−6897.

[53] E. Pedone, G. Cavallaro, S. C. W. Richardson, R. Duncan, G. Giammona, a,b-poly(asparthylhydrazide)–glycidyltrimethylammonium chloride copolymers (PAHy–GTA): Novel polymers with potential for DNA delivery, *J. Control. Release*, **2001**, *77*, 139–153.

[54] G. Nikolic, S. Zlatkovic, M. Cakic, S. Cakic, C. Lacnjevac, Z. Rajic, Fast Fourier Transform IR characterization of epoxy GY systems crosslinked with aliphatic and cycloaliphatic EH polyamine adducts, *Sensors*, **2010**, *10*, 684–696.

[55] L. Schechter, J. Wynstra, R. P. Kurkjy, Glycidyl ether reactions with amines, *Ind. Eng. Chem.*, **1956**, *48*, 94–97.

[56] I. R. Smith, The mechanism of the crosslinking of epoxide resins by amines, *Polymer*, **1961**, *2*, 95–108.

[57] Y. Tanaka, T. F. Mika (1973) In: C. A. May, Y. Tanaka (Eds.) Epoxy Resins Chemistry and Technology, Marcel Dekker, New York 135-239.

[58] L. Xu, J. H. Fu, J. R. Schlup, In situ near-infrared spectroscopic investigation of epoxy resin-aromatic amine cure mechanisms, *J. Am. Chem. Soc.*,**1994**, *116*, 2821–2826.

[59] N. Beyth, I. Yudovin-Farber, R. Bahir, A. J. Domb, E. I. Weiss, Antibacterial activity of dental composites containing quaternary ammonium polyethylenimine nanoparticles against *Streptococcus mutans*, *Biomaterials*, **2006**, *27*, 3995–4002.

[60] K. Horie, H. Hiura, M. Sawada, I. Mita, H. Kambe, Calorimetric investigation of polymerization reactions. III. Curing reaction of epoxides with amines, *J. Polym. Sci. Part A: Polym. Chem.*, **1970**, *8*, 1357–1372.

[61] M. E. Ryan, A. Datta, Kinetics of epoxy cure: A rapid technique for kinetic parameter estimation, *Polymer*, **1979**, *20*, 203–206.

[62] J. Kong, S. Yu, Fourier Transform Infrared spectroscopic analysis of protein secondary structures, *Acta Bioch. Bioph. Sin.*, **2007**, *39*, 549–559.

[63] M-C. Popescu, M. Zanoaga, Y. Mamunya, V. Myahak, C. Vasile, Two dimensional infrared correlation spectroscopy studies of wood-plastic composites with a copolyamide as matrix, *J. Optoelectron. Adv. M.*, **2007**, *9*, 923 – 930.

[64] C. Ba, J. Langer, J. Economy, Chemical modification of P84 copolyimide membranes by polyethylenimine for nanofiltration, *J. Membr. Sci.*, **2009**, *327*, 49–58.

[65] G. Beamson, Conformation and orientation effects in the X-ray photoelectron spectra of organic polymers, *J. Electron. Spectrosc. Relat. Phenom.*, **2001**, *121*, 163–181.

[66] M. J. Ariza, J. Benavente, E. Rodr´ıguez-Castell´on, L. Palacio, Effect of hydration of polyamide membranes on the surface electrokinetic parameters: Surface characterization by X-Ray Photoelectronic Spectroscopy and Atomic Force Microscopy, *J. Colloid Interface Sci.*, **2002**, *247*, 149–158.

[67] C. Y. Tang, Y.-N. Kwon, J. O. Leckie, Effect of membrane chemistry and coating layer on physiochemical properties of thin film composite polyamide RO and NF membranes I. FTIR and XPS characterization of polyamide and coating layer chemistry, *Desalination*, **2009**, *242*, 149–167.

[68] W. T. Godbey, K. K. Wu, A. G. Mikos, Size matters: Molecular weight affects the efficiency of poly(ethylenimine) as a gene delivery vehicle, *J. Biomed. Mater. Res*., **1999**, *45*, 268–275.

[69] A.v. Harpe, H. Petersen, Y. Li, T. Kissel, Characterization of commercially available and synthesized polyethylenimines for gene delivery, *J. Control. Release*, **2000**, *69*, 309–322.

[70] S. H. Anastasiadis, H. Retsos, S. Pispas, N. Hadjichistidis, S. Neophytides, Smart Polymer Surfaces, *Macromolecules*, **2003**, *36*, 1994–1999.

[71] J. A. Orlicki, N. O. L. Viernes, J. S. Moore, Roles of molecular architecture and end-group functionality on the surface properties of branched polymers, *Langmuir*, **2002**, *18*, 9990–9995.

[72] Y. Hu, P. C. Painter, M. M. Coleman, R. J. Butera, Ramifications of chain connectivity in hydrogen-bonded polymer-solutions, *Macromolecules*, **1998**, *31*, 3394–3396.

[73] G. H. Pehlert, P. C. Painter, M. M. Coleman, Functional-group accessibility in hydrogen-bonded polymer blends -3-steric shielding effects, *Macromolecules*, **1998**, *31*, 8423–8424.

[74] T. Takagishi, S. Okuda, N. Kuroki, H. Kozuka, Binding of metal ions by polyethylenimine and its derivatives, *J. Poly. Sci., Poly Chem. Ed.*, **1985**, *23*, 2109–2116.

[75] M. D. Afonso, G. Hagmeyer, R. Gimbel, Streaming potential measurements to assess the variation of nanofiltration membranes surface charge with the concentration of salt solutions, *Separation and Purif. Tech.*, **2001**, *22-23*, 529–541.

[76] E. Spoh, Molecular simulation of the electrochemical double layer, *Electrochim. Acta*, **1999**, *44*, 1697–1705.

[77] J. M. M. Peeters, J. P. Boom, M. H. V. Mulder, H. Strathmann, Retention measurements of nanofiltration membranes with electrolyte solutions, *J. Membr. Sci*., **1998**, *145*, 199–209.

[78] B. Tansel, J. Sager, T. Rector, J. Garland, R. F. Strayer, L. Levine, M. Roberts, M. Hummerick, J. Bauer, Significance of hydrated radius and hydration shells on ionic permeability during nanofiltration in dead end and cross flow modes, *Separation and Purif. Tech.*, **2006**, *51*, 40–47.

[79] E. R. Nightingale, Jr., Phenomenological theory of ion solvation. Effective radii of hydrated ions, *J. Phys. Chem.*, **1959**, *63*, 1381–1387.

[80] A. Szymczyk, P. Fievet, Investigating transport properties of nanofiltration membranes by means of a steric, electric and dielectric exclusion model, *J. Membr. Sci.*, **2005**, *252*, 77–88.

[81] C. Sun, T. Tang, H. Uludag, J. E. Cuervo, Molecular dynamics simulations of DNA/PEI complexes: Effect of PEI branching and protonation state, *Biophys. J.*, **2011**, *100*, 2754–2763.

[82] Y. Xiao, B. T. Low, S. S. Hosseini, T. S. Chung, D. R. Paul, The strategies of molecular architecture and modification of polyimide-based membranes for CO_2 removal from natural gas—A review, *Prog. Polym. Sci.*, **2009**, *34*, 561–580.

[83] R. W. Impey, P. A. Madden, I. R. McDonald, Hydration and mobility of ions in solution, *J. Phys. Chem*., **1983**, *87*, 5071–5083.

[84] C. K. Choudhury, S. Roy, Structural and dynamical properties of polyethylenimine in explicit water at different protonation states: a molecular dynamics study, *Soft Matter*, **2013**, *9*, 2269–2281.

[85] B. H. Jeong, E. M. V. Hoek, Y. Yan, A. Huang, X. Subramani, G. Hurwitz, A. K. Ghosh, A. Jawor, A. Interfacial polymerization of thin film nanocomposites: A new concept for reverse osmosis membranes, *J. Membr. Sci.*, **2007**, *294*, 1–7.

[86] S. Y. Kwa, S. H. Kim, Hybrid organic/inorganic reverse osmosis (RO) membrane for bactericidal anti-Fouling. 1. Preparation and characterization of TiO_2 nanoparticle self-assembled

aromatic polyamide thin-film-composite (TFC) membrane, *Environ. Sci. Technol.*, **2001**, *35*, 2388–239.

[87] S. Sorribas, P. Gorgojo, C. Téllez, J. Coronas, A. G. Li, High flux thin film nanocomposite membranes based on metal–organic frameworks for organic solvent nanofiltration, *J. Am. Chem. Soc.*, **2013**, *40*, 15201–15208.

[88] M. G. Buonomenna, Nano-enhanced reverse osmosis membranes, *Desalination*, **2013**, *314*, 73–88.

[89] J. Shen, H. Ruan, L. Wu, C. Gao, Preparation and characterization of PES–SiO_2 organic–inorganic composite ultrafiltration membrane for raw water pretreatment, *Chemical Engineering Journal*, **2011**, *168*, 1272–1278.

[90] J. Huang, K. Zhang, K. Wang, Z. Xie, B. Ladewig, H. Wang, Fabrication of polyethersulfone-mesoporous silica nanocomposite ultrafiltration membranes with antifouling properties. *J. Membr. Sci.*, **2012**, *423–424*, 362–370.

[91] N. Maximous, G. Nakhla, W. Wan, K. Wong, Preparation, characterization and performance of Al_2O_3/PES membrane for wastewater filtration, *J. Membr. Sci.*, **2009**, *341*, 67–75.

[92] N. Maximous, G. Nakhla, K. Wong, W. Wan, Optimization of Al_2O_3/PES membranes for wastewater filtration, *Sep. Purif. Technol.*, **2010**, *73*, 294–301.

[93] H. S. Lee, S. J. Im, J. H. Kim, H. J. Kim, J. P. Kim, B. R. Min, Polyamide thin-film nanofiltration membranes containing TiO_2 nanocrystals, *Desalination*, **2008**, *219,* 48-56.

[94] Y. Mansourpanah, S. S. Madaeni, A. Rahimpour, A. Farhadian, A. H. Taheri, Formation of appropriate sites on nanofiltration membrane surface for binding TiO_2 photo-catalyst: performance, characterization and fouling-resistant capability, *J. Membr. Sci.*, **2009**, *330*, 297-306.

[95] J. H. Li, Y. Y. Xu, L. P. Zhu, J. H. Wang, C. H. Du, Fabrication and characterization of a novel TiO_2 nanoparticle self-assembly membrane with improved fouling resistance, *J. Membr. Sci.*, **2009**, *326*, 659–666.

[96] M. Sairam, B. V. K. Naidu, S. K. Nataraj, B. Sreedhar, T. M. Aminabhavi, Poly(vinyl alcohol)-iron oxide nanocomposite membranes for pervaporation dehydration of isopropanol, 1,4-dioxane and tetrahydrofuran, *J. Membr. Sci.*, **2006**, *283*, 65–73.

[97] C. P. Leo, W. P. C. Lee, A. L. Ahmad, A. W. Mohammad, Polysulfone membranes blended with ZnO nanocrystals for reducing fouling by oleic acid, *Sep. Purif. Technol.*, **2012**, *89*, 51–56.

[98] L. Shen, X. Bian, X. Lu, L. Shi, Z. Liu, L. Chen, Z. Hou, K. Fan, Preparation and characterization of ZnO/polyethersulfone (PES) hybrid membranes, *Desalination*, **2012**, *293*, 21–29.

[99] M. L. Lind, D. E. Suk, T. V. Nguyen, E. M. V. Hoek, Tailoring the structure of thin film nanocomposite membranes to achieve seawater RO membrane performance, *Environ. Sci. Technol.*, **2010**, *44*, 8230–8235.

[100] M. L. Lind, A. K. Ghosh, A. Jawor, X. Huang, W. Hou, Y. Yang, E. M. V. Hoek, Influence of zeolite crystal size on zeolite-polyamide thin film nanocomposite membranes, *Langmuir,* **2009**, *25*, 10139–10145.

[101] Z. Emami-Karvani, P. Chehrazi, Antibacterial activity of ZnO nanoparticle on gram-positive and gram-negative bacteria, *Afr. J. Microbiol. Res.*, **2011**, *5*, 1368–1373.

[102] J. Sawai, Quantitative evaluation of antibacterial activities of metallic oxide powders (ZnO, MgO and CaO) by conductimetric assay, *J. Microbiol. Methods,* **2003**, *54*, 177–182.

[103] M. Yan, Y. Song, C. P. Wong, K. Hardin, E. Ho, Zinc deficiency alters DNA damage response genes in normal human prostate epithelial cell, *The Journal of Nutrition,* **2008**, *138*, 667–673.

[104] L. K. Adams, D. Y. Lyon, P. J. J. Alvarez, Comparative eco-toxicity of nanoscale TiO_2, SiO_2 and ZnO water suspensions, *Water Research,* **2006**, *40*, 3527–3532.

[105] R. Brayner, R. Ferrari-Iliou, N. Brivois, S. Djediat, M. F. Benedetti, F. Fiévet, Toxicological impact studies based on Escherichia coli bacteria in ultrafine ZnO nanocrystals colloidal medium, *Nano Lett.,* **2006**, *6*, 866–870.

[106] H. A. Jeng, Swanson, J. Toxicity of metal oxide nanocrystals in mammalian cells, *J. Environ. Sci. Health, Part A: Toxic/Hazard. Subst. Environ. Eng.,* **2006**, *41*, 2699–2711.

[107] K. R. Raghupathi, R. T. Koodali, A. C. Manna, Size-dependent bacterial growth inhibition and mechanism of antibacterial activity of zinc oxide nanocrystals, *Langmuir,* **2011**, *27*, 4020–4028.

[108] N. Jones, B. Ray, K. T. Ranjit, A. C. Manna, Antibacterial activity of ZnO nanoparticle suspensions on a broad spectrum of microorganisms, *FEMS Microbiol. Lett.,* **2008**, *279*, 71–76.

[109] J. M. Yousef, E. N. Danial, In vitro antibacterial activity and minimum inhibitory concentration of zinc oxide and nano-particle zinc oxide against pathogenic strains, *Journal of Health Sciences*, **2012**, *2*, 38–42.

[110] Henry Rudolph G.M. C. Bis(2,4-Pentanedionato)zinc (Zinc Acetylacetonate), *Inorganic Syntheses,* **1967**, *10*, 74.

[111] R. Elilarassi, G. Chandrasekaran, Structural, optical and magnetic properties of nanoparticles of ZnO:Ni—DMS prepared by sol–gel method, *Mater. Chem. Phys.,* **2010**, *123, Issue no. 2–3*, 450–455.

[112] T. C. Damen, S. P. S. Porto, B. Tell, Raman Effect in Zinc Oxide, *Phys. Rev.,* **1966**, *142*, 570–574.

[113] Y. J. Xing, Z. H. Xi, Z. Q. Xue, X. D. Zhang, J. H. Song, R. M. Wang, J. Xu, Y. Song, S. L. Zhang, D. P. Yu, Optical properties of the ZnO nanotubes synthesized via vapor phase growth, *Appl. Phys. Lett.*, **2003**, *83*, 1689–1691.

[114] A. A. Ashkarran, S. M. Mahdavi, M. M. Ahadian, Photocatalytic activity of ZnO nanoparticles prepared via submerged arc discharge method, *Appl. Phys. A: Mater. Sci. Process*., **2010**, *100*, 1097–1102.

[115] Z. Li, Y. Xiong, Y. Xie, Selected-control synthesis of ZnO nanowires and nanorods via a PEG-assisted route, *Inorganic Chemistry,* **2003**, *42, Issue No. 24,* 8105–8109.

[116] X. Zhang, J. Qin, Y. Xue, P. Yu, B. Zhang, L. Wang, R. Liu, Effect of aspect ratio and surface defects on the photocatalytic activity of ZnO nanorods, *Nature Scientific Reports,* **2014**, *4*, Article number: 4596.

[117] H. S. Shin, H. C. Choi, Y. Jung, S. B. Kim, H. J. Song, H. J. Shin, Chemical and size effects of nanocomposites of silver and polyvinyl pyrrolidone determined by X-ray photoemission spectroscopy, *Chem. Phys. Lett.,* **2004**, *383*, 418–422.

[118] D. H. Shin, N. Kim, Y. T. Lee, Modification to the polyamide TFC RO membranes for improvement of chlorine-resistance, *J. Membr. Sci.,* **2011**, *376*, 302–311.

[119] M. J. Ariza, E. R. Castell´on, R. Rico, J. Benavente, M. Mu˜noz, M. Oleinikova, X-Ray photoelectron spectroscopy analysis of Di-(2-ethylhexyl) phosphoric acid activated membranes, *J. Colloid Interface Sci.*, **2000**, *226*, 151–158.

[120] D. Maity, J. Ding, Single step synthesis of hydrophobic and hydrophilic nanoparticles via thermal decomposition, *Int. J. of Nanoscience*, **2011**, *10*, 943–947.

[121] K. Namratha, M. B. Nayan, K. Byrappa, Hydrothermal synthesis and photocatalytic properties of modified and unmodified zinc oxide nanoparticles, *Materials Research Innovations*, **2011**, *15*, 36–42.

[122] S. Liufu, H. Xiao, Y. Li, Investigation of PEG adsorption on the surface of zinc oxide nanoparticles, *Powder Technol.*, **2004**, *145*, 20–24.

[123] T. Takagishi, S. Okuda, N. Kuroki, Binding of metal ions by polyethylenimine and its derivatives, *J. Polym. Sci., Part A: Polym. Chem*, **1985**, *23*, 2109–2116.

[124] D. J. Skrovanek, P. C. Painter, M. M. Coleman, Hydrogen bonding in polymers. 2. Infrared temperature studies of Nylon 11, *Macromolecules*, **1986**, *19, Issue no. 3*, 699–705.

[125] E. Rusu, G. Rusu, D. O. Dorohoi, Influence of temperature on structures of polymers with ε-caprolactam units studied by FT-IR spectroscopy, *Polimery*, **2009**, *54*, 347–353.

[126] B. Faure, G. Salazar-Alvarez, A. Ahniyaz, I. Villaluenga, G. Berriozabal, Y. R. De Miguel, L. Bergstr¨om, Dispersion and surface functionalization of oxide nanoparticles for transparent photocatalytic and UV-protecting coatings and sunscreens, *Sci. Technol. Adv. Mater.*, **2013**, *14*, 023001.

[127] G. Fritz, V. Scha¨dler, N. Willenbacher, N. J. Wagner, Electrosteric Stabilization of Colloidal Dispersions, *Langmuir*, **2002**, *18*, 6381–6390.

[128] R. Shenhar, T. B. Norsten, V. M. Rotello, Polymer mediated nanoparticle assembly: Structural control and applications, *Adv. Mater.*, **2005**, *17*, *Issue no. 6*, 657–669.

[129] T. M. Frunze, V. V. Kurashev, L. V. Kozlov, Advances in interfacial polycondensation, *Russian Chem. Rev.*, **1961**, *30*, 252–270.

[130] J. P. Holmberg, E. Ahlberg, J. Bergenholtz, M. Hassellöv, Z. Abbas, Surface charge and interfacial potential of titanium dioxide nanoparticles: Experimental and theoretical investigations, *J. Colloid and Interface Science*, **2013**, *407*, 168–176.

[131] M. L. Lind, B. H. Jeong, A. Subramani, X. Huang, E. M. V. Hoek, Effect of mobile cation on zeolite-polyamide thin film nanocomposite membranes., *J. Mater. Res.*, **2009**, *24*, 1624–1631.

[132] H. Huang, X. Qu, H. Dong, L. Zhang, H. Chen, Role of NaA zeolites in the interfacial polymerization process towards apolyamide nanocomposite reverse osmosis membrane, *RSC Adv.,* **2013**, *3*, 8203–8207.

[133] T. A. Ostomel, P. K. Stoimenov, P. A. Holden, H. B. Alam, G. D. Stucky, Host-guest composites for induced hemostasis and therapeutic healing in traumatic injuries, *J. Thromb.Thrombolysis*, **2006**, *22*, 55–67.

[134] R. Oizerovich-Honig, V. Raim, S. Srebnik, Simulation of thin film membranes formed by interfacial polymerization, *Langmuir*, **2010**, *26(1)*, 299–306.

[135] J. Yin, E. S. Kim, J. Yang, B. Deng, Fabrication of a novel thin-film nanocomposite (TFN) membrane containing MCM-41 silica nanoparticles (NPs) for water purification, *J. Membr. Sci.*, **2012**, *423–424*, 238–246.

[136] R. X. Zhang, L. Braeken, P. Luis, X. L. Wang, B. Van der Bruggen, Novel binding procedure of TiO_2 nanoparticles to thin film composite membranes via self-polymerized polydopamine, *J. Membr. Sci.*, **2013**, *437*, 179–188.

[137] B. Rajaeian, A. Rahimpour, M. O. Tade, S. Liu, Fabrication and characterization of polyamide thin film nanocomposite (TFN) nanofiltration membrane impregnated with TiO_2 nanoparticles, *Desalination*, **2013**, *313*, 176–188.

[138] G. L. Jadav, P. S. Singh, Synthesis of novel silica-polyamide nanocomposite membrane with enhanced properties, *J. Membr. Sci.*, **2009**, *328*, 257–267.